UNIVERSITAT DE BARCELONA

Reaching the tumour: nanoscopy study of nanoparticles biological interactions

Natalia Feiner Gracia

UNIVERSITAT DE BARCELONA

Reaching the tumour: nanoscopy study of nanoparticles biological interactions

Natalia Feiner Gracia

September 2019

Doctoral Thesis

Universitat de Barcelona
Facultat de Física
Departament d' Enginyeria Electrònica i Biomèdica

Reaching the tumour: nanoscopy study of nanoparticles biological interactions

Programa de doctorat:
Nanociències
Cotutela amb TU/e
Línea de Recerca
Nanobiotenología
Directors tesis
Lorenzo Albertazzi
Josep Samitier

Autora
Natalia Feiner Gracia

Index

Chapter 1 .

Cancer Nanomedicine: Understanding the biological interactions of nanocarriers to design effective delivery systems.

Part of this work has been published as:

N. Feiner-Gracia, S. Pujals, P. Delcanale, L. Albertazzi. Smart nanoparticles for Biomedicine. Chapter 15: Advance optical microscopy techniques for the investigation of cell-nanoparticle interactions. Elsevier. 2018

S. Pujals, N. Feiner-Gracia, P. Delcanale, I. Voets & L. Albertazzi Super-resolution microscopy as a powerful tool to study complex synthetic materials Nat. Rev. Chem. 2019, 3, 68-84

1.1. Nanotechnology applied to medicine

Nanotechnology is defined by the European Commission as 'the areas of science in which phenomena taking place at the nanoscale dimension are studied to design, characterize, produce or apply materials, devices or systems'. One of the great challenges that nanotechnology has deeply embraced is the development of medical products, which is commonly known as nanomedicine. **Nanomedicine** emerged more than thirty years ago as a new approach to improve medical diagnosis and treatment, by exploiting unique phenomena occurring at the nanoscale[1–3]. One of the biggest applications of nanomedicine in the area of therapy is the use of nano-sized materials, also known as **nanocarriers**, to deliver bioactive molecules in order to improve their therapeutic efficiency. Nowadays, three principle fields of study can be distinguished: i) **drug delivery** which focuses on the development of nanocarriers to deliver small organic drug molecules[4], ii) **gene delivery** which consists on the use of nanoparticles to transfect cells with genetic materials such as DNA or RNA[5] and iii) **protein delivery** which aims to transport and release proteins with therapeutic or catalytic potential[6].

The main advantages of using nanocarriers as delivery agents are: i) the solubilization of hydrophobic payloads such as small organic drugs; ii) the protection of the encapsulated molecule, very relevant in the case of nucleic acid and proteins; iii) the controlled release of the cargo, reducing dose and multiple administrations and iv) the possibility to target only diseased cells for a more specific treatment[7,8]. Overall each of these properties result in extending the half-life of the molecules inside the body, providing improved biodistribution profiles and significantly reducing side effects. Lastly, the possibility to co-encapsulate different molecules opens exciting possibilities for their co-delivery, to make more efficient combination treatments or to perform a simultaneous diagnostic measurement, an approach known as **theragnostic**[9].

1.1.1. *Materials for nanomedicine*

The first nanocarriers to be used as drug delivery system were liposomes[10], in the early 1970s (Figure 1.1). After 20 years of their introduction, the first drug delivery system, Doxil[11], was approved; after this a few other liposomes were clinically translated. However, it was not until the end of the 2000s that the first gene delivery carriers were introduced into clinical trials, the first translated system being Onpattro in 2018[12].

Currently, a huge array of nanocarriers with precise control of size, shape and surface characteristics are under investigation. We can differentiate between three core families depending on the main material used for their formulation: lipidic, polymeric and inorganic nanosystems as schematically represented in Figure 1.2. The most studied lipidic nanocarriers are **liposomes**, mentioned earlier, which are nano-sized vesicles composed from lipid bilayers

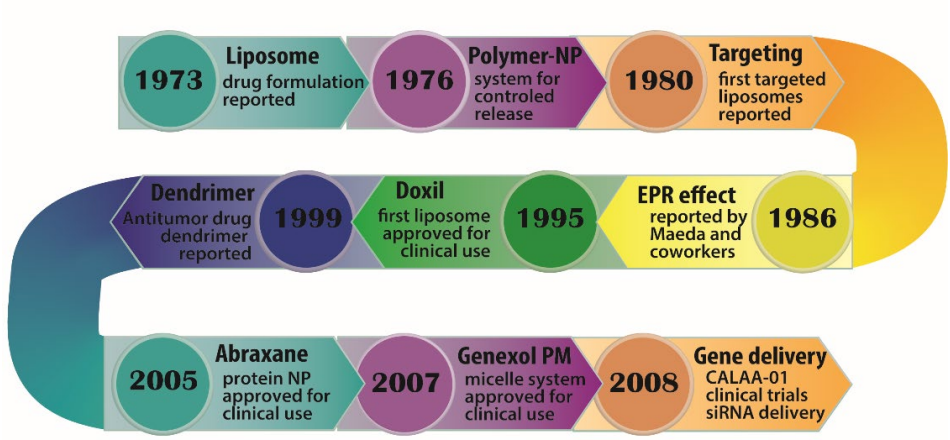

Figure 1.1 Chronogram of nanomedicine evolution. This chronogram shows schematically the more important moments and discovers in the development of nanocarriers for drug and gene delivery, including the formulations introductions or their approval.

to form an inner hydrophilic core. The typical sizes of liposomes comprise of structures from 30 nm to few μm, depending on the formulation method[13], which also grants precise control on the lipid composition, and on the external functionality. A similar vesicular morphology can be synthesised by means of amphiphilic block copolymers, which are known as **polymersomes**[14]**.** This type of nanocarrier is proposed as an improvement over liposomes thanks to the enhanced chemical versatility and the higher stability.

Micelles are supramolecular core-shell systems formulated by the self-assembly of amphiphilic molecules in an aqueous environment[15]. The hydrophobic core of these structures allows the encapsulation of lipophilic molecules while the hydrophilic outside provides water solubility and cargo protection. Moreover, the size, drug loading and release can be tuned by changing the hydrophobic-hydrophilic ratio of the amphiphile. Depending on the material of the amphiphile we can distinguish between lipidic micelles, which are in general composed by phospholipids or cholesterol and polymeric micelles formulated using block co-polymers.

Solid nanoparticles (NPs) are nanostructures characterized by a crystalline or amorphous core and can be classified as a function of their material, that being lipidic, polymeric or inorganic. A wide variety of hydrophobic lipids and polymers can be formulated into nanoparticles with sizes ranging from tens of nanometre to microns[16–18]. Their advantage is easy scale-up and low production costs thanks to their facile formulation. On the other hand, **inorganic nanoparticles** can be formulated using ceramic or metallic materials. **Ceramic nanoparticles** are made of inorganic, non-metallic materials, such as alumina, silica or titania[19]. They can be prepared with the desired size, shape and porosity, as well as modifications with functional groups that can be easily incorporated at their surface. For **metallic nanoparticles**,[20] (eg. iron oxide, gold or silver), the main characteristic is their very small size, less than 50 nm, which provides them with a high surface area. Moreover, thanks

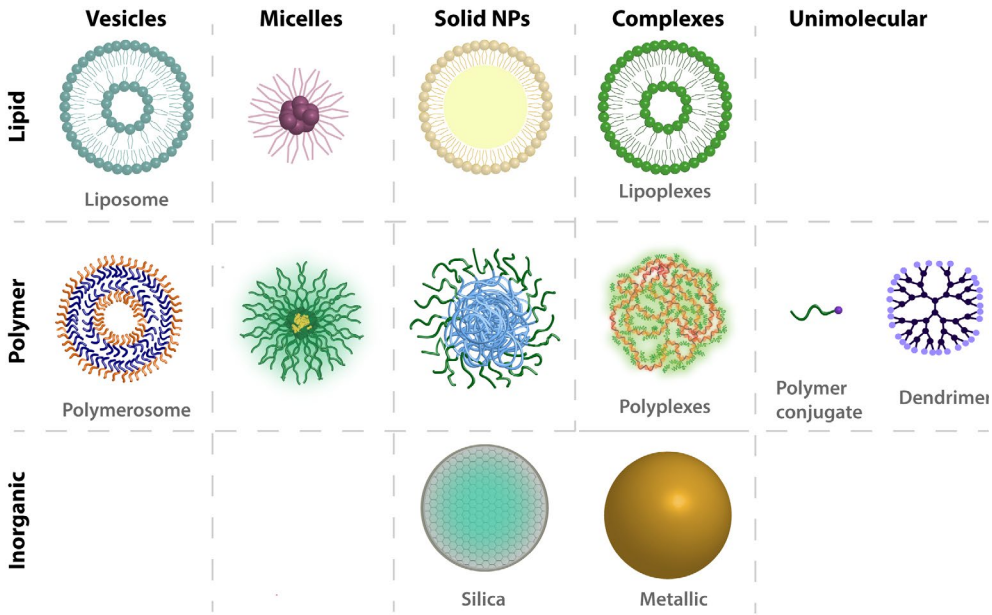

Figure 1.2 Nanosystems based on different structures and materials. Nanocarriers can be classified into lipidic, polymeric and inorganic. Moroever, inside each of these groups a range of nanocarriers can be formulated. By differing their structural properties and morphology we can distinguish between vesicles, micelles, solid NP, complexes and unmilecular systems.

to their intrinsic optical and magnetic properties, these nanoparticles can also be used as imaging agents being a good example of theranostic system, and for direct treatments such as hyperthermia.

Complexes are nanostructure composed of two materials with reciprocal affinity. In particular electrostatic complexes between a cationic molecule and an anionic nucleic acid are employed for gene delivery[21]. We can distinguish between **lipoplexes**, which use cationic lipids, and **polyplexes**[22] which are composed using cationic polymers. Lipoplexes so far have been more explored in the clinic due to their ease of formulation. However, polyplexes are very attractive because of their immense chemical diversity and potential functionalization, representing a promising alternative.

Finally, **unimolecular systems** are among the simplest carriers and consist of single polymeric chains conjugated with therapeutic molecules. They have the advantage of a very small size and low cost. Recently, **dendrimers** have been proposed as new unimolecular carriers. They consist of a perfectly repeating hyperbranched polymer. The main characteristics of these systems are their small sizes from 1 to 20 nm and their low polydispersity[23]. The therapeutic molecule can be incorporated to dendrimers in multiple ways, such as physically encapsulated into the inner core, or covalently linked to the

dendrimer surface as all of the active groups on the branches faces outward, as can be observed in Figure 1.2.

1.2. Nanosystems in cancer treatment

Nanocarriers are being investigated as useful delivery systems in different medical areas. Nanocarriers have recently shown their potential in improving the outcome in **cardiovascular diseases**[24], thanks to the possibility of treating chronic inflammations such as atherosclerosis that currently require surgical intervention. Moreover, nanoparticles have shown to be useful against **infectious diseases**[25]**,** improving the release of antibiotics, as well as for their intrinsic antimicrobial properties (e.g. metallic NPs). In addition, the poor bioavailability of therapeutic molecules in the brain makes nanocarriers attractive to improve treatments of **neurological diseases**[26]**,** such as Alzheimer or Parkinson. In this framework nanocarriers can facilitate the crossing of the Blood Brain Barrier (BBB). BBB is a key barrier for preventing toxins or pathogens to reach the Central Nervous System, but at the same time making it inaccessible to therapeutic drugs. Finally, the field in which the use of nanocarriers as drug or gene delivery systems is more widely exploited is **oncology**[27,28]**.** As this is the application field of this thesis, the use of nanomedicine for oncology will be extensively discussed in the next sections.

1.2.1. *Advantages of nanosystems for cancer therapy*

Cancer is one of the major causes of death worldwide, increasing every year mainly due to the growth in life expectancy. Current treatments beyond surgery include chemotherapy, radiotherapy and immunotherapy which, in many cases, have limited success because of their toxicity or low effectivity. The effectiveness of these drugs are often limited by poor solubility, low half-life and very toxic side effects[27].

If we look at the chemical nature of the therapeutic molecules used in oncology, the potential benefit of nanocarriers clearly appears. Most chemotherapy treatments are performed using very hydrophobic molecules such as paclitaxel or docetaxel. These therapeutic molecules have very strong activity but poor solubility and bioavailability which results in the administration of high doses to achieve the therapeutic dose at the tumour site. The high concnetrations of chemotherapy are responsible for the numerous side effects, due to non-controllable drug distribution through the body and the toxicity of surfactants currently used to increase their bioavailability. In this framework, the use of nanocarriers to encapsulate drug molecules can increase the solubility of the chemotherapeutic drugs, thus, reducing the administered concentrations. In addition, controlled delivery of multiple molecules is a promising therapy, in this sense, the co-encapsulation into the same nanocarrier can improve their coordinated delivery. Recently, new therapies based on silencing oncogenes using small interfering RNA (siRNA) molecules had been described. However,

these molecules are highly susceptible to nucleases degradation and, additionally, are highly negatively charged, preventing their ability to cross negative membranes and so their internalization into cells. The encapsulation of siRNA molecules into nanocarriers offers them high protection, significantly reducing their degradation and increasing the ability to pass over negative barriers. Nowadays, both the use of chemotherapeutic and nucleic acid molecules relate to a high number of side effects due to the non-specificity of the treatment, therefore affecting both healthy and diseased cells (e.g. gene mutations). The possibility to functionalize nanocarriers with targeting moieties that can recognize overexpressed antigens in cancer cells allows us to specifically target those cells. This both reduces toxicity (side effects) and increases the accumulation of delivered molecules into the tumour tissue[29,30]. Immunotherapy is another promising treatment of which the main objective is to induce the activation of the immune system to respond against evading cancer cells. Nanoparticles are generally uptaken by immune cells in blood, thus, the use of nanocarriers combined to immunotherapy can enhance the delivery efficiency of drugs to immune cells, one of the main challenges associated with this therapy[31].

1.2.2. *Current clinical translated nanomedicines for cancer treatment*

The first nanomedicine approved, **Doxil**[32], consisted of a liposome encapsulating Doxorubicin, a chemotherapeutic drug. The main advantage of Doxil versus the free drug is an increased circulation time as well a reduction of side effects such as cardiotoxicity. The approval of this nanocarrier became a milestone in the nanomedicine world, delivering the promised benefits for cancer treatment. Since then, other liposomes based-therapies had been approved for the treatment of different cancers. However, it was only after 10 years of the approval of Doxil for clinical use that the first non-lipid based nanosystem was also authorized, Abraxane, which consists of an albumin-based nanoparticle encapsulating Paclitaxel, another chemotherapeutic drug[33]. A few years later, the first and only polymer-based nanosystem, Genexol-PM[34], a PEG-PLA polymeric micelle, was accepted for clinical use. Overall, all of these systems reduce the side effects or allow a decreased dosage to be administered. Only recently, the first nanocarrier to improve survival rates has been approved, CPX- 351, a combination liposomal formulation shown to improve from 5 to 9 months the life expectancy of patients with leukemia[35].

These successes show the potential of nanomedicine to impact the clinic setting, but the very limited number of approved systems compared to the billions in monetary funds invested for pre-clinical investigations reveals a significant problem in the field. In the last 15 years, the interest in the field has continuously grown, exemplified in the number of publications which have increased from 100 per year to more than 4000 in 2018. The differences in investigations and clinical translated systems demonstrates the importance of identifying and overcoming the challenges that limit nanomedicine application.

1.2.3. *Challenges in clinical translation*

Most of the investigations discovering novel and promising nanocarriers only focus on synthesising novel materials with novel properties that only add to the complexity of the formulation process. Once the nanocarrier is designed to have the desired functionalities and properties in an elemental aqueous solvent such as water, they are tested to treat `a cancer´. However, the current formulation and discovery mechanisms do not focus on the difficulties of the specific cancer type or on the challenges of the current treatment, in conclusion, do not investigate the main problems of the diseases. We believe that this is one of the main reasons of the low number of clinically translated systems compared to the amount of investments and investigations. In our opinion, the correct approach to design effective systems is not by following the chemistry approach, but by understanding the weak points of the illness in combination with the main limitations the nanocarrier will be facing once introduced into the body, and then to use this understanding to formulate effective NPs.

One of the critical points in the complex formulation processes used nowadays is the feasibility of their clinal translation. The volume of nanosystem synthetized on the bench scale to be characterized and to carry out pre-clinical assays is infinitely lower than the quantity needed to be used in a hospital as a daily treatment. Therefore, the scalability of the system should be one of the main focus when synthetizing new nanocarriers[36,37]. The more complex the system, the higher the production cost which will in turn restrict the chances to reach the clinics, as the industrialization will be more difficult. Moreover, it is important to study processes such as long-term stability of large batches, polydispersity and drug release of long-haul storage. Overall, the field should focus in increasing the simplicity of the nanocarriers formulation to increment the chances of their clinical translation.

Another deficiency of the traditional chemistry approach is a low nanocarrier-tumour accumulation. Recently, Chan and coworkers carried out a metadata analysis to determine the advances in the tumour accumulation in the last 20 years[36]. The research did not show any significant increase of NPs tumour delivery in the analysed years. Astonishingly, they pointed out the poor tumour accumulation of both active and passive nanocarriers to be as low as 0.6 *vs* 0.9%, for passive and active respectively. This recent study started an important discussion in the field in order to understand the realistic advantages in the use of nanocarrier delivery systems. For example, it has been argued whether nanoparticle accumulation is the correct parameter to measure the efficiency of nanomedicine[38]. The main aim of nanocarriers is to increase the accumulation of therapeutic molecules in the tumour, which does not necessary correlate with the concentration of the carrier in the tumour cells. In a few studies, it has been proven that tumour accumulation of drugs when using nanosystems is higher than the accumulation of the free chemotherapeutic drugs (see Table 1)[39]. Nevertheless, increasing nanocarrier tumour accumulation will facilitate drug presence and therefore increase the efficiency of the treatment.

Table 1. Overview of tumour accumulation of different anticancer treatment molecules in animal models and patients. The low accumulation of chemotherapeutic molecules is a clear example of the low efficiency of targeting tumour cells specifically. While tumour accumulation in animal models is promising, in humans it is much lower, even though monoclonal antibodies (Ab) have been proven to be effective.

	Animal model	Human
Chemotherapy	0.001-0.05% ID/g	0.001-0.05% ID/gr
Monoclonal Ab	0.05-50% ID/gr	<0.01% ID/gr
Nanosystems	0.01-46% ID/gr ($\bar{X}$ = 3.17%)	N.A

We believe that the main reason of poor tumour accumulation is the difficulties of nanocarriers to reach the tumour cells due to multiple biological interactions occurring in the complex media of the body. These interactions are also the most probable cause why Chan et al. did not observe significantly higher accumulation of active systems compared to the passive. Most of the nanocarriers currently under development rely on the Enhanced Permeability and Retention effect, known as **EPR effect**[40,41]**,** to effectively escape the blood vessels and reach the tumour malignant cells. EPR effect favours the enhanced accumulation of nanocarriers in the tumour site, thanks to a leakier vasculature. However, it has been reported that the EPR effect is oversimplified[42]. Recent investigations have demonstrated this phenomenon is very heterogenous in humans, first between tumour types and secondly among patients with the same illness, which may be due to the huge variety in tumour microenvironment, vascular density and stage of progression (primary, metastatic or replase)[43,44]. These investigations support our approach of understanding first the biology of the cancer type, in order to design specific nanocarriers with the appropriate properties to be effective. Moreover, most of the pre-clinical investigations confirming the success of nanocarriers relying on the EPR effect were performed using subcutaneous tumour xenographs on murine models. These models are characterized by a fast tumour grown which consequently results in a high EPR effect. However, in humans, the huge variability between tumour type induces high heterogeneity in the presence of the EPR effect. These observations point out the need to develop new pre-clinical models that are able to more closely resemble the parameters of the cancer type, which then can be useful to understand the biological challenges and to test newly designed nanocarriers.

More importantly, not only the EPR effect plays a role, but the undesired interactions of nanocarriers with different biological milieu are responsible for their low tumour accumulation. Non-desired interactions play a critical role in the ability of nanocarriers to get

to the tumour site and effectively induce cell death. Moreover, biological barriers are designed to restrict the entering of undesired material. Overall, they are essential systems in the body's defence against pathogens and viruses, but consequently these barriers also restrict the penetration of nanocarriers. All of these interactions dictate the fate of the nanocarrier inside the body. At any moment after injection an adverse interaction can take the material off target (e.g. immune cells), therefore, complete and specific studies on these interactions should be performed to preselect those nanocarriers with increased favourable outcomes.

1.3. Life of a nanocarrier inside the body: biological interactions

Nanocarriers intravenously (i.v.) injected have a long journey inside the body before they can reach the cancer cells, as represented in Figure 1.3. In each step of this voyage, different interactions with biological components may occur[37,39] dictating the nanocarrier performance. In the next paragraphs the key interactions occurring during circulation, tissue diffusion and tumour detection will de detailed.

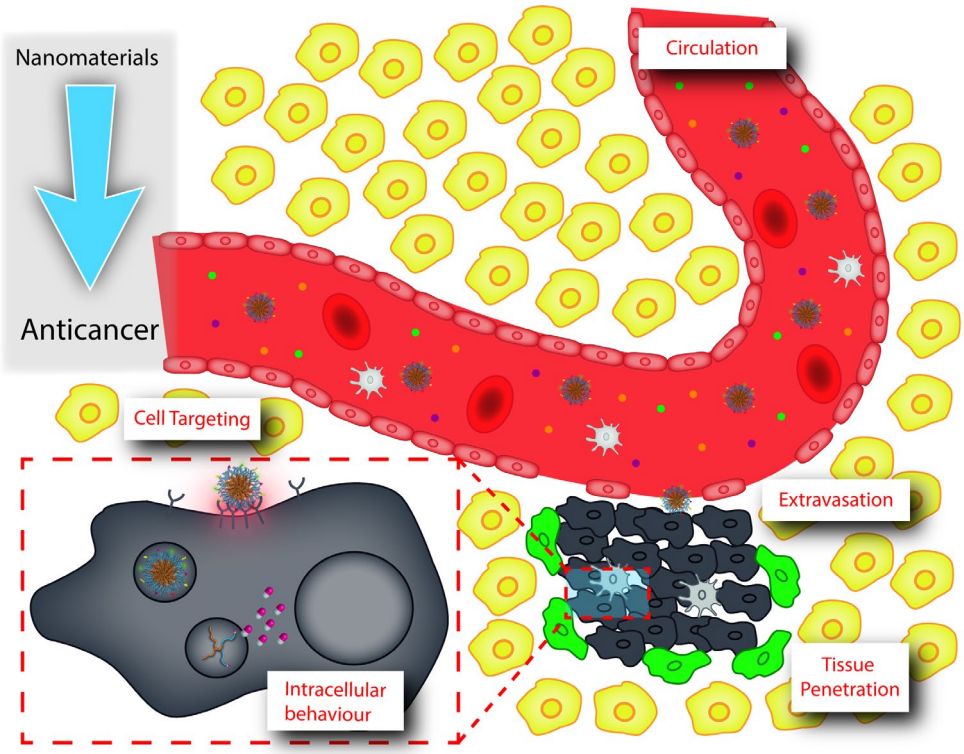

Figure 1.3 Schematic representation of the life of a nanocarrier inside the body. Nanocarrierss are in most cases injected i.v., therefore, they start their journey inside the body in the circulation where multiple interactions can occur. Once they are able to extravasate, they need to penetrate the tumour tissue to reach the cancer cells and then through the tumour mass. Moreover, the detection of cancer cells will help the retention, adding extra interactions. In some cases, nanocarriers need to penetrate the cancer cells and in those cases the intracellular behavior is also very important.

1.3.1. *Interactions of nanoparticles in circulation*

The majority of nanocarriers under investigation are designed to be injected intravenously. This delivery route implicates a number of biological interactions occurring in the blood vessels; as blood is a very complex media which contains proteins, lipids and small metabolites, as well as a variety of circulating cells. In the moment in which a nanocarrier is in contact with this complex environment it starts interacting with it. As schematically represented in Figure 1.4, multiple interactions may occur in the blood vessels, highlighting the need of detailed understanding.

1.3.1.1. Interactions with serum molecules: protein corona formation

The first interaction occurring after administration is mainly with serum proteins and other biomolecules that can adsorb to the nanocarrier's surface due to the high surface free energy of the nanomaterial and the high concentration of proteins and biomolecules in plasma, as shown in Figure 1.4. The adsorption of serum biomolecules on nanocarriers forms a layer known as the **protein corona** (or more recently renamed as biomolecular corona), as shown in scheme of Figure 1.4**.** The proposed theory describes the formation of the corona as a dynamic phenomenon[45,46]. It starts with the initial adsorption of those proteins highly concentrated in the blood (e.g. albumin), followed by an exchange with other species that have a higher affinity but are less concentrated in the media. Moreover, it is hypothesized that the corona consists of a multilayer arrangement of proteins around nanoparticles. The first layer (hard protein corona) is formed by tightly bonded proteins followed by a soft corona multilayer, consisting of an outer layer of weakly interacting proteins which evolves and changes in time as a function of the media environment. Protein corona formation gives a new biological identity to the nanocarrier which will guide the localization, the toxicity and the pharmacological profile of the system[47–49]. The attachment of specific immunogenic proteins can induce the detection of nanocarriers by the immune system and their consequent clearing[50]. The attachment of complement proteins, for example, activates the complement system, which consists on the recruitment and activation of other proteins in a cascade increasing the NP clearance . The unfolding of specific proteins in contact with the nanocarrier surface may induce binding to specific receptors of phagocytes, which also triggers inflammation. Moreover, immunoglobulins, albumin and apolipoprotein adsorption induce phagocytes activation, in turn enhancing the nanocarrier sequestration.

As the protein corona guides the performance of the nanocarrier inside the body, many efforts have been spent to prevent the adsorption of proteins to the nanomaterial surface by functionalizing their surface with anti-fouling materials[51]. PEG or zwitterionic materials have been shown to significantly reduce the adsorption of serum molecules in a large variety of materials, resulting in an increased circulation time. However, there is currently no strategy that allows the complete avoidance of the protein corona. For this reason, in the last decade, focus have been directed to completely characterize, understand and predict the formation as

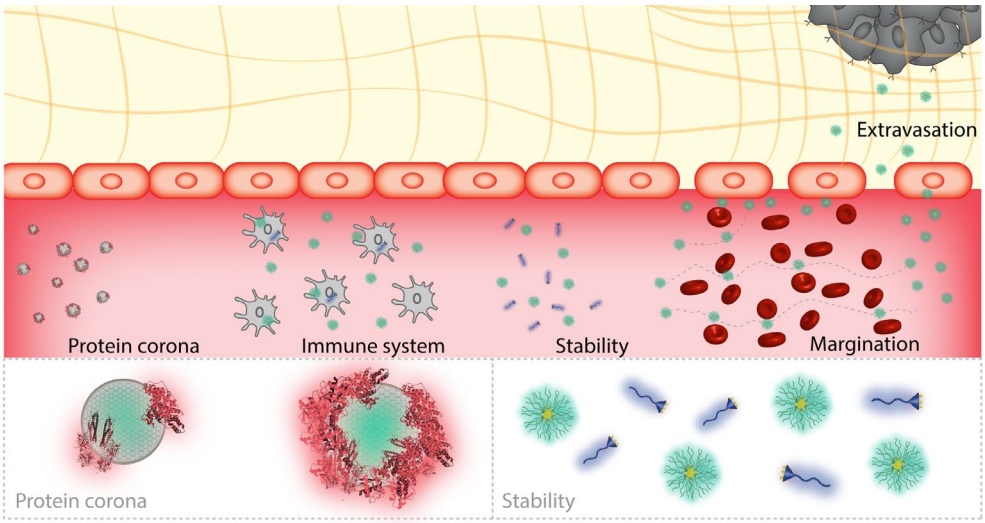

Figure 1.4 The biological interactions of nanocarriers in blood vessels. After introduction into the blood vessels, nanoparticles have to overcome some biological interactions that will determine their effectivness. Such interactions include protein corona formation, escaping immune system phagocytosis, preserve the assembled state of the system, succesfully marginate to blood vessels walls and extravasate to tumour microenvironment.

well as the biological consequences[52–55]. One of the major repercussions of the protein corona formation is the shielding of specific functionalization moieties, and consequently the reduction of specific interactions, as represented in Figure 1.6a. The shielding of active-functionalizing molecules enhances the difficulties of targeting specific cancer cells as the protein layer will be now responsible for guiding the interactions with cells. Due to the difficulties in completely preventing protein adsorption, recent investigations have exploited the use of protein corona formation to enhance the targeting properties of the nanocarrier[56,57]. Different strategies are being exploit such as i) the pre-coating of the surface with specific proteins, reducing the reactivity of the nanocarrier in the blood, ii) the functionalization of NPs with molecules enhancing the protein adsorption of only specific proteins with targeting purposes (e.g. transferrin) iii) the use of self-marker molecules which prevents the immune system recognition and elimination.

Although the knowledge about the protein corona phenomenon has increased in the last decade, it is still of major importance to characterize the formation of the biomolecular corona in order to predict all these interactions, both the undesired and the desired. Multiple investigations have been carried out in order to understand the role of the nanocarrier physicochemical properties on the protein corona formation. Different size, shape, surface charge, among other properties, has been demonstrated to affect the amount and type of protein interactions. Likewise, other factors such as media temperature, time of incubation, plasma source or concentrations dictate the number and type of proteins adsorbed. Distinct methods are used to study the protein corona which can be divided into indirect methods

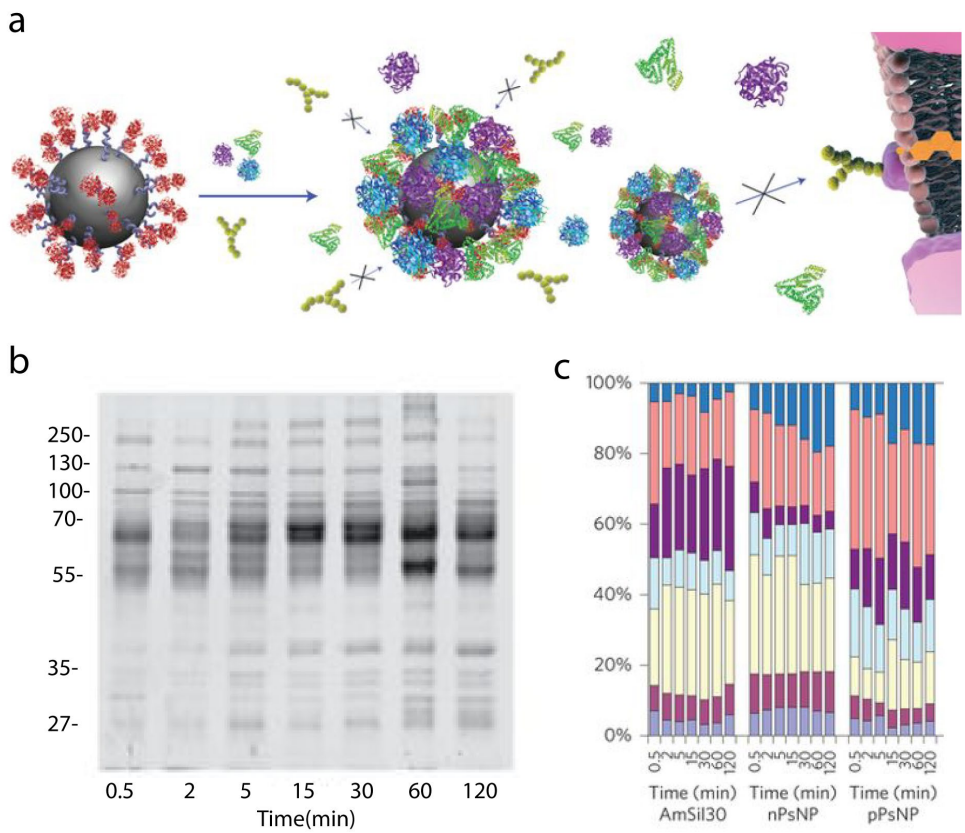

Figure 1.5 Protein corona formation and techniques to characterize adsorbed proteins. a. Proteins present in the blood may adsorb to the nanocarrier surface hiding any functionalization moieties present. This covering will significantly reduce the specific interactions with tumour cells. The most popular techniques to study the molecule species adsorbing to the nanocarrier surface are **b.** Gel electrophoresis SDS-PGAE at different time points, **c.** Quantitative LC-MS at the indicated time points, grouped according to biological processes of the blood system. *Reproduced with permission from Springer Nature, Copyright © 2013.*

(e.g. Dynamic light scattering (DLS), Fluorescence Correlation Spectroscopy (FCS), Isothermal titration calorimetry (ITC)), which measure changes in physicochemical properties of nanocarriers to prove protein adsorption; and direct methods (e.g. sodium dodecyl sulfate polyacrylamide gel electrophoresis (SDS-PAGE), mass spectroscopy, Circular Dichroism (CD)) which qualitatively or quantitatively detect protein adsorption (Figure 1.6b)[53,58,59]. Moreover, direct methods can detect proteins either via ex situ techniques, separating nanoparticles from the proteins, or by in situ techniques which measures the whole complex. Each of these methods have advantages and disadvantages, however they all have a common drawback: they are all ensemble techniques. These studies are carried out over a population of nanocarriers, the main conclusions being extrapolated from an average of the real adsorption occurring on individual nanoparticles. Therefore, it is important to introduce novel techniques to characterized individual nanoparticles to assess possible heterogeneities.

Moreover, the small size of nanoparticles together with the complexity of serum composition and the dynamic nature of the corona make the study of individual nanoparticle-protein interaction and the spatial location and distribution of proteins over nanoparticles challenging. Thus, new methods with high spatial resolution will increase the understanding of the protein adsorption complex phenomenon and guide the design of more effective nanocarriers.

1.3.1.2. Immune clearance

The immune system is the first line of defence of the body against external agents such as chemicals or pathogens and one of the main systems responsible for the low tumour accumulation of nanocarriers. The mononuclear phagocyte system (MPS), a group of phagocyte immune cells circulating in the blood stream, identifies nanocarriers as foreign materials. This generates an immune response, which sequestrates nanocarriers[60,61]. As represented in Figure 1.4. Biodistribution analysis localize most of the injected nanocarrier dose in the liver and spleen, the two main organs of the MPS, demonstrating the significant impact of the immune response on NPs tumour accumulation. This response can differ depending on the physicochemical properties of the nanocarriers e.g. size, shape, surface etc. For example, cationic materials are proven to be more immunogenic. Therefore, once again the physicochemical properties are critical in guiding the nanoparticle biological interaction.

Overall, it is important to minimize the interactions of nanocarriers with the immune system to increase the concentration of nanoparticles in the blood stream, which will help to increase the percentage of injected dose reaching the tumour site. Of notice, a different strategy has recently been introduced consisting of employing the high retention of nanocarriers by the MPS to activate the immune system against cancer cells and exploit their immunotherapy applicability[31]. The encapsulation of antigens to activate the immune response represents a powerful opportunity for cancer nanomedicine and significantly reduces the number of barriers to be overcome.

1.3.1.3. Nanocarrier stability

The complex blood composition also challenges the stability and the integrity of nanocarriers, in particular, self-assembled nanocarriers. Due to their non-covalent nature, supramolecular nanocarriers are more vulnerable to biological interactions and struggle to preserve their assembled state until they reach the cancer cells. The stability of supramolecular systems is dependent on two different parameters: their thermodynamic equilibrium and their dynamic behaviour, i.e. their kinetic stability. Thermodynamic equilibrium is expressed by the critical micelle concentration (CMC) which needs to be tuned to be minimal. Kinetic stability is expressed by the k_{off}, i.e. the rate at which the system disassembles when it is infinity diluted. Notably, both parameters can be affected in physiologically relevant media by not only pH, salt concentration and material dilutions[62–64] but also by the interactions with blood molecules

and cells. Therefore, all of these interactions need to be addressed when designing new supramolecular nanocarriers as *in vitro* stability is not predictive from aqueous stability. Indeed, supramolecular nanosystems are in dynamic equilibrium i.e. they continually assemble and disassemble, exchanging monomers. In the complex blood environment serum components can interact with the monomers, sequestering them, therefore changing the equilibrium and preventing re-assembly, as schematically illustrated in Figure 1.6a. In addition, proteins can also interact with the assembled system by adsorption or penetration which can led to an increase of the K_{off} and therefore to a faster disintegration of supramolecular nanocarriers.

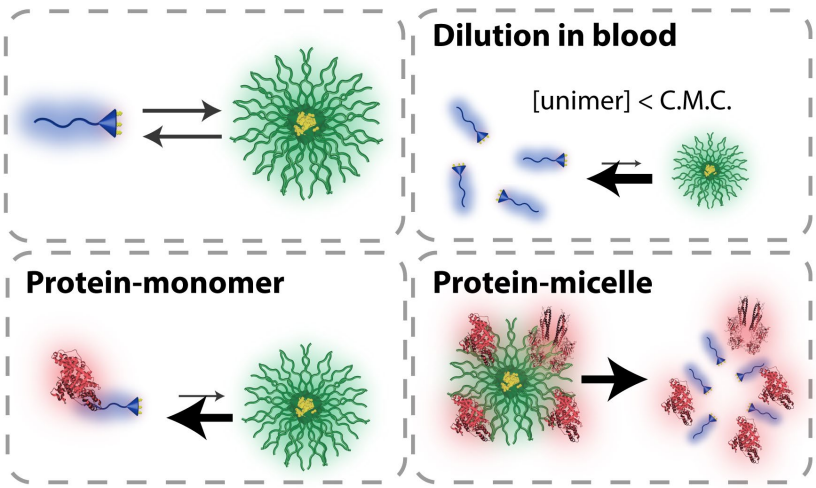

Figure 1.6 Equilibrium of micelles under circulation as an example of supramolecular system stability. **a.** Dynamic equilibrium between the unimer and the self-assembled system. **b.** Upon i.v. injection the high dilution may compromise the stability of the micelle **c.** Interactions bewteen the proteins and the monomer **d.** and/or the micelles. Each interaction may shift the equilibrium to the non-assembled state.

Due to the difficulties of studying such assemblies in complex biological media, the challenges associated with preserving the stability of supramolecular systems are often overlooked in the literature. In the last years, few research groups investigated the stability of micellar systems in contact with serum proteins and under high dilutions using methods such as size exclusion chromatography, DLS or SLS[62]. In these studies, the size of the micelles was measured before and after being incubated with serum protein to understand if they were still forming complexes. FRET studies were also carried out[65–68] to study the release of the dye molecules from micelles after serum incubation. A weakness of those studies if they only focused on the dye release and did not provide information on the assembly state of the micelles.

A particular case in which the stability plays a pivotal role in the success of the nanocarrier is represented by complexes (e.g lipoplexes or polyplexes). These supramolecular materials are composed of two types of molecules that assemble into a kinetically trapped, charged

complex lead by their electrostatic interactions. The upholding of stability is a major issue for complexes because of two main reasons: i) the building blocks are hydrophilic and therefore have higher K_{off}, ii) the highly charged cationic components favour interactions with blood molecules promoting disassembly of the nanocarrier, as schematically illustrated in Figure 1.7.

Up to now, there is little information regarding the integrity of polyplexes in full serum. Therefore, there is a need of suitable quantitative methods to track the stability of the system in a complex biological media[69–71]. Gel electrophoresis can be performed after incubating polyplexes with serum, see an example in Figure 1.7. Using this method, the mobility of nucleic acid molecules through the gel can be visualized which varies depending on their complexation with other molecules. However, when proteins are present the results of the gel are difficult to interpret, as nucleic acid molecules bound to proteins may give similar bands to the genetic material forming the polyplexes. Also, new bands appearing into the gel increases the difficulty of interpretation of the results and therefore the understanding of the interplay between the molecules[71]. A few years ago, a new method based on fluorescence fluctuation spectroscopy was proposed[69,72] to quantify the amount of free labelled siRNA molecules in complex media such as serum. Even though it is possible to follow the decomplexation of the system, it is not possible by using this method to directly quantify the number of nucleic acid molecules in each complex. The method only quantified the free

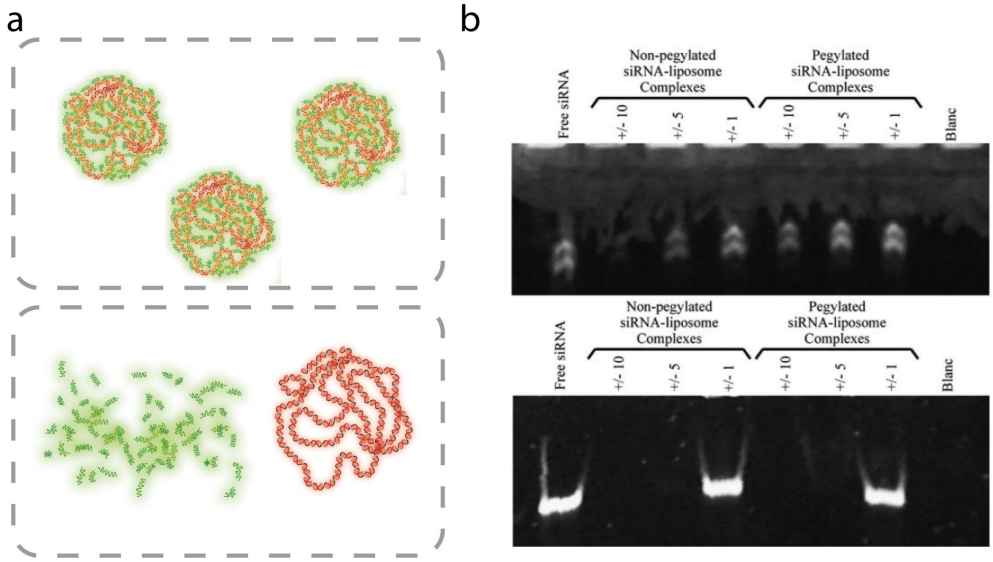

Figure 1.7 Polyplexes stability under circulation. a. Polyplexes are formulated based on electrostatic interactions bewteen cationic polymers and nucleic acid molecules. After being i.v. administered the interactions with serum proteins may induce the decomplexation of the system. **b.** SDS-PAGE is one of the few methods currently used to study the decomplexation of nucleic acid molecules from polyplexes in contact with serum proteins. Bands observed in the gel indicate siRNA molecules which run distinclty through the gel when free compared to complexed polymer molecules. *Reproduced with permission from Elsevier B.V, Copyright © 2007.*

siRNA molecules that are not complexed and it requires a complicated analysis to interpret the results.

Overall, we believe that new methods that allow for a comprehensive study of the stability of drug and gene delivery systems in complex biological media can guide the design of more promising systems and bridge the translational gap.

1.3.2. *Extravasation: the endothelial barrier*

A crucial step to achieve tumour accumulation of NPs is the selective extravasation from the cancer vasculature. Therefore, NPs must reach the vessel wall and be able to cross the endothelial barrier. To achieve this, preferentially in the tumour, two strategies can be employed: i) a passive mechanism based on the different permeability of tumour vasculature or ii) an active pathway exploiting the endothelium transport processes.

The passive accumulation of colloidal particles to tumour cells was first discovered by Maeda and co-workers in 1980's, when they described the Enhanced Permeability and Retention effect (EPR effect)[41]. This phenomenon is based on the fact that tumour vasculature is morphologically different. Normal blood vessels are characterized by the presence of tight junctions between endothelial cells that restrict the permeability of molecules. These structures are disrupted in the vessels surrounding tumours due to rapid and abnormal blood vessel formation during cancer progression which creates fenestrae between endothelial cells with sizes varying from tenths of nm to few microns (~1.5 um). Nanocarriers, thanks to their size, in the order of magnitude of the endothelium fenestrations, can extravasate to tumour sites while they do not escape from healthy vessels. Reports have shown the ability of nanocarriers up to 200 nm to extravasate in animal models with solid tumours. Moreover, the poor lymphatic drainage in the tumour environment induces issue retention of the nanosystems. Overall, the EPR effect favours the enhanced accumulation of nanocarriers in the tumour site, thus, increasing their therapeutic outcome[29].

However, recent investigations have demonstrated EPR is not a universal feature of every tumour but is highly dependent on tumour type, stage and even patient. Likewise, the size of the inter-endothelial cell gaps are also heterogenous, which complicates the prediction of the optimal size of the nanocarrier [44,73]. As a recent example of the importance of this, BIND-014, a targeted nanoparticle that showed great promise in pre-clinical invetsigations, failed clinical trials in phase II[73,74]. The NP was design to passively extravasate to EPR, however Langer and coworkers demonstrated later that the EPR heterogeneity between patients was the main reason of non-tumour recession observed in the clinical trial. Similarly, Harington et. al. had recently proven that the tumour accumulation of liposomes in patients with advanced cancer is very heterogenous, with retention variabilities from 5 to 30%[75]. Following these observations, Merrimack Pharmaceuticals conducted studies to predict the response of patients to liposomes by detecting the accumulation of iron nanoparticles (MRI detected),

which proved to be predictive of liposomes performance[76]. All of the observations raised proves that the existence and extent of EPR effect should be further investigated in humans, and the stratification of patients based on their EPR ability could pre-select patients to be treated and enhance nanomedicine applicability[77]. Another interesting perspective is to artificially enhance EPR through chemical and pharmacological treatments[78].

Recently, active strategies to increase the extravasation of nanosystems have been proposed. They consist on taking advantage of the traditional transport solute pathways: i) the paracellular route (used for small solute transport through intercellular gaps) and ii) the transcellular route (used by nutrient protein transport across the cell via receptor-mediated transcytosis) of endothelial cells[79,80]. The ability of nanoparticles to induce opening of paracellular gaps have been recently highlighted. Tight junction modulators, such as cationic polymers have been demonstrated to induce leakiness of the vascular endothelium which favours nanoparticles extravasation[81]. Moreover, some nanocarriers, such as TiO_2 nanoparticles, interact with VE-cadherin which induces an intercellular gap formation in the range of microns, also granting nanocarriers extravasation[82]. Despite that at first glance these strategies seem very appealing, they also present major complications. Lately, a study demonstrated that the gap opening induced by inorganic nanoparticles promotes cancer cell intravasation that could facilitate metastasis[83]. Therefore, a more mechanistic understanding is needed before being able to exploit these phenomena. A more promising strategy to enhance the extravasation of nanocarriers to tumour tissue is to exploit the transcytosis mechanism. To induce the transcellular pathway, the first step is to induce internalization in the endothelial cells, therefore, physicochemical properties and ligand functionalization will strongly impact on this process. For example, NPs can be modified with ligands promoting receptor-induced transcytosis, which are generally associated with nutrient transport (e.g. albumin, transferrin, insulin)[84]. Noteworthy, some receptors are overexpressed both on the cancer endothelium and in the cancer tissue allowing for dual targeting (e.g. PSMA receptor or integrins).

The extravasation of nanoparticles from the blood vessels is in most cases overlooked, except for the case when nanoparticles are designed to treat glioblastoma. In this last case, nanocarriers must cross the Blood Brain Barrier (BBB) which is known to be a tighter endothelial barrier than the one in the normal vasculature. A lot of efforts have been taken to increase the ability of NPs to cross the BBB. However, the mistaken belief of the existence of an universal EPR effect for any other cancer and any patient is the main cause of the low number of investigations regarding nanoparticles extravasation. We consider that an increase in the understanding of the biological arrangement of tumour vasculature is needed. And together with expanded knowledge about the interactions between specific nanocarriers and the cancer endothelium, it will facilitate the design of nanocarriers with high accumulation rates.

1.3.3. *Tumour tissue penetration*

Once nanocarriers escape the blood vessels they must diffuse through the Extracellular Matrix (ECM) to reach their final target: the tumour cells. This is challenging as the ECM is a dense complex 3d network composed of proteins and carbohydrates which act as a barrier for the freely diffusion of nanocarriers. The main interactions affecting this diffusion are i) the small pore size of the ECM[85] ii) the interactions with the ECM components[57](e.g. collagen, glycosaminoglycan, proteoglycans, etc[88,58]. FRAP experiments and two photons confocal imaging have revealed high variability of the ECM properties depending on the tumour type[88–90]. Moreover, there are evidences that the ECM of the tumour microenvironment is denser than those of healthy tissues, which limits the penetration of the nanocarriers to the initial microns. Therefore, it is important to understand the effect of the nanocarrier physicochemical properties, such as size and surface charge, have on these interactions to rationally design translatable nanocarriers. Confocal studies in mice have revealed a size-dependent penetration across the ECM of solid tumours, which indicates a restricted diffusion of larger carriers[85]. In addition, Jain and collaborators proved that the shape influence can also play a role, demonstrating a faster diffusion of nanorods comparing to nanosphere of similar sizes in a tumour-mimetic collagen gel[91]. Finally, it has been shown that neutral systems have higher diffusion capacities than both anionic or cationic, due to reduced electrostatic interactions with ECM components[92].

Moreover, cancer cells themselves form a tight, densely and packed mass of cells together with a very dense ECM, which decreases the chance of nanocarriers to penetrate to the internal tumour layers. In recent years, this difficulty has been gaining attention, and different studies using 3d cancer cell models (e.g. tumour spheroids) have been used to investigate the effect of physicochemical properties on solid tumour penetration[93]. The size of nanocarriers, for example, is a major parameter determining tumour penetration. An improved penetration of nanoparticles smaller than 100 nm has been proven, while no significant differences were observed when tested in 2d models[47,93–96]. Moreover, shape can also affect the penetration of nanocarriers into solid tumours, where a higher aspect ratio seems to promote an enhanced penetration[93,96,97]. Overall, the need to investigate all of these parameters in more complex pre-clinical 3d models before performing clinical assays is clear. Mainly due to the challenges in predicting and extrapolating the interactions from 2d assays

Overall, ECM and tumour tissue interactions add further limitations in the design space of NPs. Additional restrictions regarding size, shape or surface charge to successfully penetrate the tumour narrow down the optimal physicochemical properties a nanocarrier must possess to be a promising candidate for clinical translation.

1.3.4. *Targeting and intracellular behaviour*

Active targeting consists of functionalizing nanocarriers with moieties that possess a specific affinity for the tumour cells. This strategy has been projected as the magic bullet to effectively differentiate cancer cells from healthy ones and, consequently, provide therapies with absolute selectivity, thus reducing side effects. Frequently, cancer cells overexpress a specific antigen on their surface, which provide a possibility to distinguish them from healthy cells. The first ligands used to functionalize nanocarriers were monoclonal Ab, followed by proteins, peptides, and aptamers. Strikingly, even the increasing interest in functionalizing nanocarriers to actively target cancer cells, there is still no approved system using this approach. The reason for no approved active targeting nanocarrier for clinical use is the complexity of this strategy, which is not as straightforward as it was first believed. The first reason, as previously explained, is the shielding of the ligands due to the adsorption of molecules in blood, which decrease the effectivity of the targeting. Another motive for the low efficiency of active targeting if the fact that overexpression of antigens by cancer cells is not an exclusive condition, in a lesser extent, healthy cells also express these antigens. Therefore, healthy cells are not invisible for the actively-targeted nanocarriers. Moreover, the high variability between patients, and stage of the cancer enhance the difficultly to optimize these systems.

To choose the most effective targeting ligand two major parameters should be considered. The affinity for the cancer antigen, both in terms of thermodynamics (K_d) and kinetics (K_{on} and K_{off}) should be deeply studied. The optimal affinity should be determined as the high binding of nanocarriers to tumour cells which induces high retention rates can reduce the penetration to the inner tumour cells, thus decreasing its effectivity. Secondly, the density of ligands per nanocarrier plays a pivotal role due to possible multivalent interactions. Importantly, the ligand density can not only influence the binding but also perturb the cell, for example through receptor clustering.

Once tumour accumulation is achieved nanocarriers need to release their cargo, thus, it can respond against cancer cells. Depending on the therapeutic molecules encapsulated the release outside the cells is sufficient as chemotherapeutic molecules, for example, can internalize the cells without any extra guidance. However, nucleic acid molecules do not have the ability to penetrate cells on their own therefore the use of vectors, in this case, nanocarrier internalization into cancer cells is essential. Understanding the internalization of these NPs together with the trafficking and intracellular interactions is crucial to design effective systems. Extended information on these interactions can be found elsewhere[98], as it is out of the purpose of the current thesis. Importantly, nanocarriers for drug delivery can increase tumour accumulation if the physicochemical properties of the system minimize their biological interactions. In addition, nanocarriers for gene delivery are essential not only to increase the retention but to deliver the molecules inside the cancer cells to modify protein expression.

1.4. Novel methods to study nanoparticles biological interactions

In the previous sections, complex biological interactions which determine the success or failure of nanomedicine have been reviewed. However, the mechanisms underlying these interactions are poorly understood, limiting the rational design of nanomedicine. Therefore, the development of methods able to dissect the behaviour of NPs in the biological milieu is a key aspect to advance in nanomedicine research. One of the main challenges limiting the information obtained from the available methods is the small size of nanocarriers which requires high spatial resolution. Moreover, the polydispersity within a NP population impel the study of individual nanoparticles, still, the current ensemble techniques do not provide this detailed information. Importantly, the visualization of heterogeneities within a population will help to identify the nanoparticles carrying the properties with the higher chances of success. In addition, the complexity of biological environments represents extra challenges, as there is a need to identify multiple objects within the same measurement. Finally, the evolving environment in the NPs journey demands techniques able to study the biological interactions not only over different time scales, but also spatially. Fluorescence microscopy is a promising technique to overcome the current methodological limitations due to several reasons: i) imaging of nanoparticle-cell interactions can be performed with minimal invasiveness of the specimen (e.g. live cell); ii) it allows for very sensitive and high signal-to-noise measurements, down to single molecule detection; iii) it is endowed with a fairly good spatial resolution (about 200 nm) that can be enhanced down to 10 nm in the case of fluorescence super resolution methods; and iv) fluorescence labelling of molecules gives chemical specificity and multicolour ability. Altogether, these properties render fluorescence imaging among the most powerful tools for the study nanoparticle biological interactions.

In light of the content of this thesis the following paragraphs focus specifically on spectral imaging and super-resolution microscopy, while a more extended review of fluorescence microscopy methods can be found elsewhere[99].

1.4.1. *Spectral imaging*

Spectral imaging is based in the acquisition of the emission spectrum of the fluorophores at each pixel imaged. This is typically achieved with a confocal setup equipped with a prism and able to image the different colours sequentially or simultaneously. The main advantages are the possibility to detect different fluorophores that have overlapping emission spectrum and to perfectly distinguish the signal of interest from background or autofluorescence of the sample being image, see Figure 1.9. Moreover, a very beneficial use of spectral imaging is its combination with sensing molecules able to change their emission wavelength depending on a specific factor (i.e. pH). This is a key feature as it enables functional imaging: providing complementary information about the state and behaviour of NPs and not only its localization in space.

Spectral imaging has been used to understand the uptake mechanisms of different fluorescently labelled nanoparticles into live cancer cells. Arsov et. al. localized and discriminated fluorescent NPs of different sizes from the labelled plasma membrane which was impossible to distinguish using confocal imaging due to emission spectra overlapping[100]. Moreover, in the same work the fusion of lipidic NPs with the membrane was studied. This was possible using a solvatochromic dye, whose emission spectrum shifts depending on the microenvironment. Spectral imaging has been also used to investigate the impact of lipidic nanocapsule internalization on the mitochondria integrity and metabolic activity by using a sensor dye which changes emission spectrum depending on the membrane potential[101]. Confocal spectral imaging was also be used to follow the intracellular release of doxorubicin and to determine its kinetics thanks to different emission spectra of doxorubicin depending on the intracellular microenvironment. [102,103] (Figure 1.9b). Similarly, internalization of nanocarriers and their drug release profile has been measured in skin[104], or in live animals[105,106]. Using spectral imaging the emission fluorescence corresponding to the nanoparticle can be clearly distinguish from the autofluorescence of the tissues or the crosstalk, a main problem when studying biodistribution.

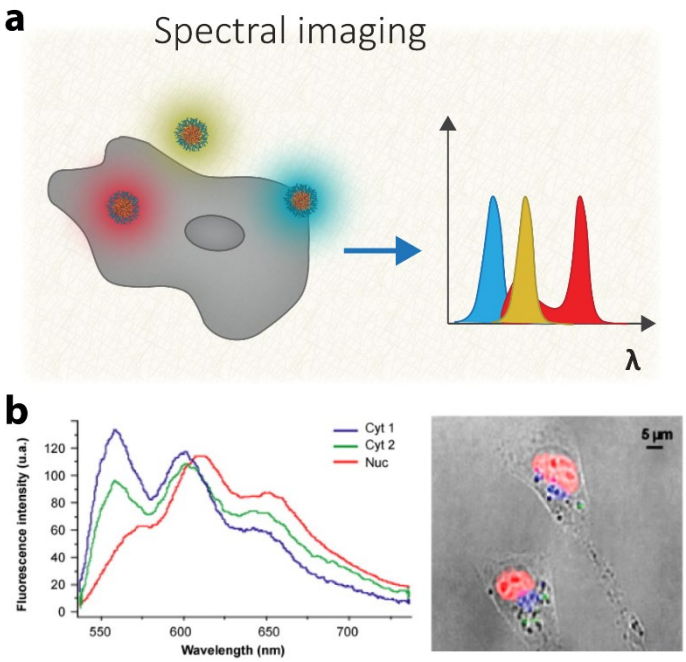

Figure 1.8 Spectral microscopy as an imaging tool to study biological interactions of nanocarriers. a. Spectral confocal measures the fluorescence emission spectra per imaged pixel which allows the distinction of dyes with overlapping spectra. **b.** Example of spectral imaging used to distinguish the different doxorubicin emission depending on the cellular environment performed by Gautier and co-workers. *Reproduced with permission from Elsevier and Copyright Clearance Center.*

Despite these preliminary reports investigating the release kinetics and profile of drugs within cells, spectral imaging can be exploited to answer several questions about the biological interactions of nanocarriers.

1.4.2. *Super resolution microscopy and dSTORM*

Fluorescence microscopy, as stated above, is a powerful technique to analyse the interactions between nanocarriers and biological structures and molecules. However, its spatial resolution is limited by light diffraction to a few hundreds of nanometres according to Abbe's criteria. This restriction hampers the use in the field of nanomedicine as the imaging of nano-sized carriers is impossible. Super resolution microscopy (SRM), or nanoscopy, has recently surfaced as a powerful technique to overcome the diffraction limit, enabling imaging on the nanoscale[107,108]. The SRM family encompasses a range of far-field optical techniques that exploit a number of chemical and physical principles. Three main families can be distinguished: structured illumination microscopy (SIM), stimulated emission depletion (STED) and single- molecule localization microscopy (SMLM). In the present thesis SMLM have been chosen due to its higher spatial resolution, single-molecule sensitivity and its potential in enabling quantitative molecular counting. SMLM achieves sub-diffraction resolution by the accurate localization of individual fluorophores under a wide field illumination, where the detection of each emitter is separated in time[109,110]. The imaging process consists of a series of cycles, in each one, only a small subset of single isolated fluorophores emits, and therefore, can be detected. The fluorescence of single markers can then be fitted with a Gaussian profile and the position of the dye accurately identified from the Gaussian centroid. After multiple iterations a subdiffractional resolved image can be reconstructed by the molecule's positions. Several SMLM methods including Photoactivated Localization Microscopy (PALM), Stochastic Optical Reconstruction Microscopy (STORM), Points Accumulation for Imaging Nanoscale Topography (PAINT) are available and differ in procedure to achieve the temporal separation of emitters.

In direct Stochastic Optical Reconstruction Microscopy (dSTORM) the emission of single fluorophores is achieved thanks to the photoswitching behaviour of the dyes used. During the image acquisition most of the dyes are transferred to an "off" state by a photochemical reaction, allowing the acquisition of sparse single emitters. This reaction is reversible and in the following frames other dyes switch to the "on" state. To control this photoswitching the sample is embedded into a special buffer solution containing redox reagents to induce photochemical reactions and an oxygen scavenging system to reduce photobleaching. dSTORM can achieve among the best spatial resolution attainable with optical techniques, down to 20nm, only limited by the accuracy of the fitting. Moreover, the possibility to localize single molecule events can provide quantitative information such as molecule counting.

dSTORM had a wide impact in cell biology, to molecularly resolve the intracellular structure and organization of different proteins with nanometric detail upon different stimuli.

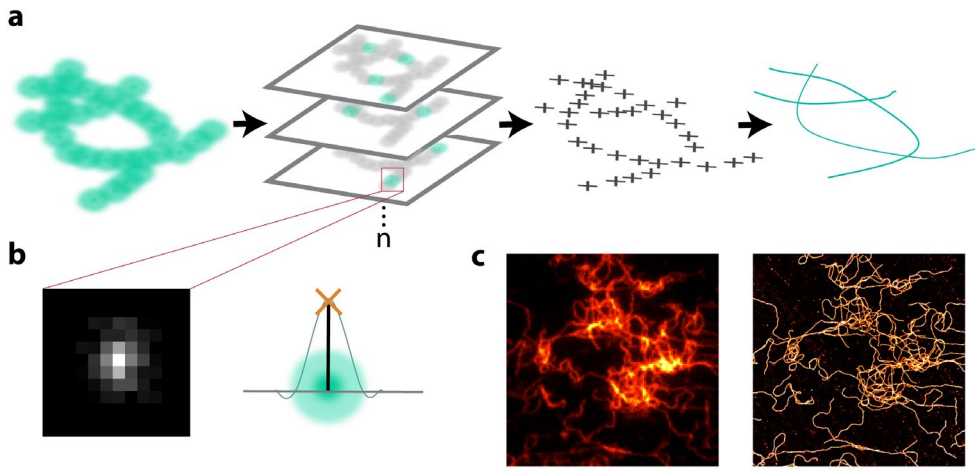

Figure 1.9 Principle of single molecule localization microscopy. a. Fluorescent dyes are difraction limited which limits the resolution of fluorescent imaging. SMLM circumvent this limitation by switching on and off the different dyes in multiple cycles, which allows the specific localization of the emitter in each cycle. This process allows the reconstruction of the structure with nanometric resolution. **b.** Emision of a single dye can be fitted to 2D Gaussian function to accurently localize the position of the dye. **c.** Example of dSTORM image of a synthetic material.

More recently, it has become influential in chemistry and material science as a means to unveil the structure and dynamics of complex materials. As a relevant example of dSTORM Albertazzi and Meijer reported the first example of supramolecular polymer imaging using dSTORM to achieve dynamic information such as the exchange of monomers between fibres [111]. This study was followed by several other reports on the use of the 2-color STORM method to unveil how the dynamics of supramolecular polymers is influenced by hydrophobicity and chirality and by the presence of functional groups[112–114]. Notably, tracking and locating specific monomers in a mixture of different components can be performed only thanks to the combination of nanometric resolution and specific labelling. In parallel, other polymer-based nanostructures were imaged for the first time, Gramlich et al. used STORM to image the nanoscale morphology of polystyrene and polymethyl methacrylate blends. Interestingly, not only the inner structure, but also the surface properties of polymer materials can be investigated with nanoscopy. Moreover, studies on the nanostructure of lipid carriers have been performed to assess their encapsulation and compartmentalization where the precise distribution of drugs was monitored[115].

Since dSTORM was initially developed to study cellular structures, it opens the possibility to study biomaterials *in situ*, for example in cellular environments, Figure 1.11. Recently, the use of this technique to study material–cell interactions have been explored. Internalization of polystyrene particles down to 80 nm by STORM has been assessed in combination with image analysis tools to assess the possibility of accurately measuring their size in different cell

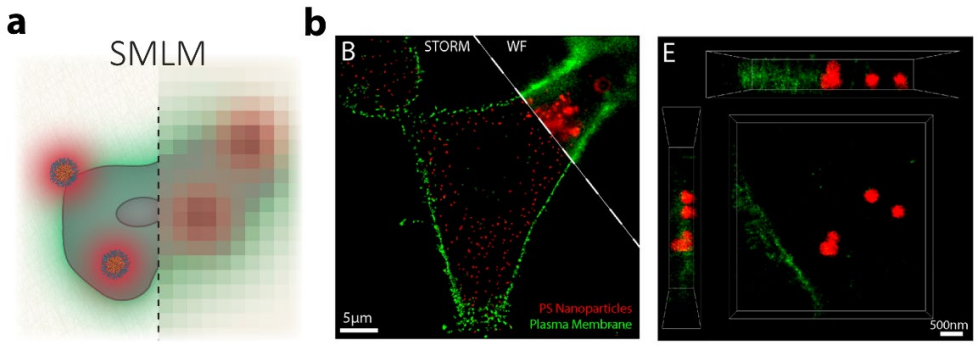

Figure 1.10 Single molecule localization microscopy to image nanocarriers in action. a. Schematic representation demonstrating the improved resolution of the technique. **b.** dSTORM imaging of polystyrene nanoparticle internalization into cells allows determination of the prescie organelle interactions of the system. *Reproduced with permission from Elsevier and Copyright Clearance Center.*

types[116]. The results showed an excellent agreement with *in vitro* TEM measurements for nanoparticles ranging from 80 nm to 800 nm, demonstrating the potential of such techniques to evaluate the nanoparticle interactions inside cells. Moreover 2-color dSTORM has made possible the localization of polystyrene and polymeric nanoparticles in contact with specific subcellular organelles with nanometric precision as observed in Figure 1.11b[117].

Overall, the nanometric resolution of dSTORM, together with the molecular specificity of the multi-colour imaging overcome the limitations of ensemble techniques. Moreover, it presents dSTORM as a suitable technique to investigate nanocarrier biological interactions, both at the molecular and cellular level, also overcoming the challenges of molecular complexity and specificity. The possibility to characterize the physicochemical properties (size, shape or functional ligands) of nanocarriers in complex biological environments can guide the understanding of protein interactions, stability, endothelial interplay during extravasation, as well as the study of ECM component interactions, and targeting precision. Altogether, this knowledge will grant the identification of the most promising nanocarrier to be clinically translated.

1.5. Thesis aim and content

The previous sections have highlighted the need for understanding the nanocarrier biological interactions occurring during their life inside the body. The comprehension of these critical steps together with an in-depth study of the structural composition of nanoparticles will guide a rational design of systems, increasing their translation into the clinics. Currently, one of the main limitations of these investigations is the lack of experimental approaches able to provide information of nanoparticle behaviour on the nanoscale, as well as, those conducted in complex biological media.

Thus, the main aim of this thesis is the use of novel advanced optical microscopy techniques to unveil the biological interactions of nanocarriers in complex biological media at the single particle and single molecule level.

For this purpose, **Chapter 2**, describes the use of dSTORM imaging as a new methodology to obtain an *in-situ* characterization of protein corona on individual nanoparticles. The study unveils the time evolution of the protein corona as a function of surface properties. Overall, it reveals a high interparticle heterogeneity regarding the number of proteins per nanoparticle, which may be one of the causes of their poor clinical performance. Moreover, a relation between corona formation and targeting properties of the nanocarrier is demonstrated.

In **Chapter 3**, dSTORM imaging is used to visualize the exact molecular composition of polyplexes. Using two-colour dSTORM we could detect differences in the stoichiometry of individual polyplexes, revealing a heterogeneity inside the same population. Once the system is fully characterized, this complexation can be followed in serum to study stability. This new method provides mechanistic insights into the disassembly process of polyplexes in blood.

In **Chapter 4**, micelles able to change their fluorescent emission upon disassembly are characterized under different blood-like conditions using a combination of fluorescence spectroscopy and microscopy techniques. The stability of micelles in different biologically relevant conditions (e.g. proteins media, extreme dilutions, temperature) is followed thanks to the use of spectral imaging. Finally, an interplay between stability, interactions with cell and internalization pathway has been discovered using this methodology.

Chapter 5 aims to develop a microfluidic chip mimicking the vascular tumour microenvironment to study the ability and stability of supramolecular structures during extravasation by means of advanced imaging. The stability of the nanocarriers can be correlated to the specific biological interactions occurring thanks the micelles fluorescent properties presented before. The integration of spectral confocal imaging and the 3d microfluidic tumour blood vessel-on-a-chip represents a robust and promising platform to investigate the performance of nanocarriers mimicking *in vivo*. Low penetration of non-targeted micelles into spheroids is observed, together with a destabilization of the system in the tumour surroundings, which cannot be predicted investigating only 2d culture cells.

1.6. References

(1) Koo, O. M.; Rubinstein, I.; Onyuksel, H. Role of Nanotechnology in Targeted Drug Delivery and Imaging: A Concise Review. Nanomedicine Nanotechnol. Biol. Med. 2005, 1 (3), 193–212. https://doi.org/10.1016/j.nano.2005.06.004.

(2) Moghimi, S. M.; Hunter, A. C.; Murray, J. C. Nanomedicine: Current Status and Future Prospects. FASEB J. 2005, 19 (3), 311–330. https://doi.org/10.1096/fj.04-2747rev.

(3) Wagner, V.; Dullaart, A.; Bock, A.-K.; Zweck, A. The Emerging Nanomedicine Landscape. Nat. Biotechnol. 2006, 24 (10), 1211–1217. https://doi.org/10.1038/nbt1006-1211.

(4) LaVan, D. A.; McGuire, T.; Langer, R. Small-Scale Systems for in Vivo Drug Delivery. Nat. Biotechnol. 2003, 21 (10), 1184–1191. https://doi.org/10.1038/nbt876.

(5) Putnam, D. Polymers for Gene Delivery across Length Scales. Nat. Mater. 2006, 5 (6), 439–451. https://doi.org/10.1038/nmat1645.

(6) Morris, M. C.; Depollier, J.; Mery, J.; Heitz, F.; Divita, G. A Peptide Carrier for the Delivery of Biologically Active Proteins into Mammalian Cells. Nat. Biotechnol. 2001, 19 (12), 1173–1176. https://doi.org/10.1038/nbt1201-1173.

(7) Petros, R. A.; DeSimone, J. M. Strategies in the Design of Nanoparticles for Therapeutic Applications. Nat. Rev. Drug Discov. 2010, 9 (8), 615–627. https://doi.org/10.1038/nrd2591.

(8) Lavik, E.; von Recum, H. The Role of Nanomaterials in Translational Medicine. ACS Nano 2011, 5 (5), 3419–3424. https://doi.org/10.1021/nn201371a.

(9) Fang, C.; Zhang, M. Nanoparticle-Based Theragnostics: Integrating Diagnostic and Therapeutic Potentials in Nanomedicine. J. Control. Release Off. J. Control. Release Soc. 2010, 146 (1), 2–5. https://doi.org/10.1016/j.jconrel.2010.05.013.

(10) Gregoriadis, G. Drug Entrapment in Liposomes. FEBS Lett. 1973, 36 (3), 292–296. https://doi.org/10.1016/0014-5793(73)80394-1.

(11) Tardi, P.; Boman, N.; Cullis, P. Liposomal Doxorubicin. J. Drug Target. 1996, 4 (3), 129–140. https://doi.org/10.3109/10611869609015970.

(12) Suhr, O. B.; Coelho, T.; Buades, J.; Pouget, J.; Conceicao, I.; Berk, J.; Schmidt, H.; Waddington-Cruz, M.; Campistol, J. M.; Bettencourt, B. R.; et al. Efficacy and Safety of Patisiran for Familial Amyloidotic Polyneuropathy: A Phase II Multi-Dose Study. Orphanet J. Rare Dis. 2015, 10. https://doi.org/10.1186/s13023-015-0326-6.

(13) Pattni, B. S.; Chupin, V. V.; Torchilin, V. P. New Developments in Liposomal Drug Delivery. Chem. Rev. 2015, 115 (19), 10938–10966. https://doi.org/10.1021/acs.chemrev.5b00046.

(14) Lee, J. S.; Feijen, J. Polymersomes for Drug Delivery: Design, Formation and Characterization. J. Controlled Release 2012, 161 (2), 473–483. https://doi.org/10.1016/j.jconrel.2011.10.005.

(15) Torchilin, V. P. Micellar Nanocarriers: Pharmaceutical Perspectives. Pharm. Res. 2006, 24 (1), 1. https://doi.org/10.1007/s11095-006-9132-0.

(16) Mehnert, W.; Mäder, K. Solid Lipid Nanoparticles: Production, Characterization and Applications. Adv. Drug Deliv. Rev. 2001, 47 (2), 165–196. https://doi.org/10.1016/S0169-409X(01)00105-3.

(17) Banik, B. L.; Fattahi, P.; Brown, J. L. Polymeric Nanoparticles: The Future of Nanomedicine. Wiley Interdiscip. Rev. Nanomed. Nanobiotechnol. 2016, 8 (2), 271–299. https://doi.org/10.1002/wnan.1364.

(18) Kamaly, N.; Xiao, Z.; Valencia, P. M.; Radovic-Moreno, A. F.; Farokhzad, O. C. Targeted Polymeric Therapeutic Nanoparticles: Design, Development and Clinical Translation. Chem. Soc. Rev. 2012, 41 (7), 2971–3010. https://doi.org/10.1039/c2cs15344k.

(19) Singh, D.; Singh, S.; Sahu, J.; Srivastava, S.; Singh, M. R. Ceramic Nanoparticles: Recompense, Cellular Uptake and Toxicity Concerns. Artif. Cells Nanomedicine Biotechnol. 2016, 44 (1), 401–409. https://doi.org/10.3109/21691401.2014.955106.

(20) McCarthy, J. R.; Weissleder, R. Multifunctional Magnetic Nanoparticles for Targeted Imaging and Therapy. Adv. Drug Deliv. Rev. 2008, 60 (11), 1241–1251. https://doi.org/10.1016/j.addr.2008.03.014.

(21) Tros de Ilarduya, C.; Sun, Y.; Düzgüneş, N. Gene Delivery by Lipoplexes and Polyplexes. Eur. J. Pharm. Sci. 2010, 40 (3), 159–170. https://doi.org/10.1016/j.ejps.2010.03.019.

(22) Gebhart, C. L.; Kabanov, A. V. Evaluation of Polyplexes as Gene Transfer Agents. J. Controlled Release 2001, 73 (2), 401–416. https://doi.org/10.1016/S0168-3659(01)00357-1.

(23) Gillies, E. R.; Fréchet, J. M. J. Dendrimers and Dendritic Polymers in Drug Delivery. Drug Discov. Today 2005, 10 (1), 35–43. https://doi.org/10.1016/S1359-6446(04)03276-3.

(24) Park, J. H.; Dehaini, D.; Zhou, J.; Holay, M.; Fang, R. H.; Zhang, L. Biomimetic Nanoparticle Technology for Cardiovascular Disease Detection and Treatment. Nanoscale Horiz. 2019. https://doi.org/10.1039/C9NH00291J.

(25) Zazo, H.; Colino, C. I.; Lanao, J. M. Current Applications of Nanoparticles in Infectious Diseases. J. Controlled Release 2016, 224, 86–102. https://doi.org/10.1016/j.jconrel.2016.01.008.

(26) Srikanth, M.; Kessler, J. A. Nanotechnology—Novel Therapeutics for CNS Disorders. Nat. Rev. Neurol. 2012, 8 (6), 307–318. https://doi.org/10.1038/nrneurol.2012.76.

(27) Ferrari, M. Cancer Nanotechnology: Opportunities and Challenges. Nat. Rev. Cancer 2005, 5 (3), 161–171. https://doi.org/10.1038/nrc1566.

(28) Jain, R. K.; Stylianopoulos, T. Delivering Nanomedicine to Solid Tumors. Nat. Rev. Clin. Oncol. 2010, 7 (11), 653–664. https://doi.org/10.1038/nrclinonc.2010.139.

(29) Bertrand, N.; Wu, J.; Xu, X.; Kamaly, N.; Farokhzad, O. C. Cancer Nanotechnology: The Impact of Passive and Active Targeting in the Era of Modern Cancer Biology. Adv. Drug Deliv. Rev. 2014, 66, 2–25. https://doi.org/10.1016/j.addr.2013.11.009.

(30) Upponi, J. R.; Torchilin, V. P. Passive vs. Active Targeting: An Update of the EPR Role in Drug Delivery to Tumors. In Nano-Oncologicals: New Targeting and Delivery Approaches; Alonso, M. J., Garcia-Fuentes, M., Eds.; Advances in Delivery Science and Technology; Springer International Publishing: Cham, 2014; pp 3–45. https://doi.org/10.1007/978-3-319-08084-0_1.

(31) Riley, R. S.; June, C. H.; Langer, R.; Mitchell, M. J. Delivery Technologies for Cancer Immunotherapy. Nat. Rev. Drug Discov. 2019, 18 (3), 175–196. https://doi.org/10.1038/s41573-018-0006-z.

(32) Barenholz, Y. Doxil®--the First FDA-Approved Nano-Drug: Lessons Learned. J. Control. Release Off. J. Control. Release Soc. 2012, 160 (2), 117–134. https://doi.org/10.1016/j.jconrel.2012.03.020.

(33) Gradishar, W. J.; Tjulandin, S.; Davidson, N.; Shaw, H.; Desai, N.; Bhar, P.; Hawkins, M.; O'Shaughnessy, J. Phase III Trial of Nanoparticle Albumin-Bound Paclitaxel Compared With Polyethylated Castor Oil–Based Paclitaxel in Women With Breast Cancer. J. Clin. Oncol. 2005. https://doi.org/10.1200/JCO.2005.04.937.

(34) Werner, M. E.; Cummings, N. D.; Sethi, M.; Wang, E. C.; Sukumar, R.; Moore, D. T.; Wang, A. Z. Preclinical Evaluation of Genexol-PM, a Nanoparticle Formulation of Paclitaxel, as a Novel Radiosensitizer for the Treatment of Non-Small Cell Lung Cancer. Int. J. Radiat. Oncol. Biol. Phys. 2013, 86 (3), 463–468. https://doi.org/10.1016/j.ijrobp.2013.02.009.

(35) Mayer, L. D.; Tardi, P.; Louie, A. C. CPX-351: A Nanoscale Liposomal Co-Formulation of Daunorubicin and Cytarabine with Unique Biodistribution and Tumor Cell Uptake Properties. Int. J. Nanomedicine 2019, 14, 3819–3830. https://doi.org/10.2147/IJN.S139450.

(36) Wilhelm, S.; Tavares, A. J.; Dai, Q.; Ohta, S.; Audet, J.; Dvorak, H. F.; Chan, W. C. W. Analysis of Nanoparticle Delivery to Tumours. Nat. Rev. Mater. 2016, 1 (5), 16014. https://doi.org/10.1038/natrevmats.2016.14.

(37) Shi, J.; Kantoff, P. W.; Wooster, R.; Farokhzad, O. C. Cancer Nanomedicine: Progress, Challenges and Opportunities. Nat. Rev. Cancer 2017, 17 (1), 20–37. https://doi.org/10.1038/nrc.2016.108.

(38) McNeil, S. E. Evaluation of Nanomedicines: Stick to the Basics. Nat. Rev. Mater. 2016, 1 (10), 1–2. https://doi.org/10.1038/natrevmats.2016.73.

(39) Anchordoquy, T. J.; Barenholz, Y.; Boraschi, D.; Chorny, M.; Decuzzi, P.; Dobrovolskaia, M. A.; Farhangrazi, Z. S.; Farrell, D.; Gabizon, A.; Ghandehari, H.; et al. Mechanisms and Barriers in Cancer Nanomedicine: Addressing Challenges, Looking for Solutions. ACS Nano 2017, 11 (1), 12–18. https://doi.org/10.1021/acsnano.6b08244.

(40) MAEDA, H. Vascular Permeability in Cancer and Infection as Related to Macromolecular Drug Delivery, with Emphasis on the EPR Effect for Tumor-Selective Drug Targeting. Proc. Jpn. Acad. Ser. B Phys. Biol. Sci. 2012, 88 (3), 53–71. https://doi.org/10.2183/pjab.88.53.

(41) Matsumura, Y.; Maeda, H. A New Concept for Macromolecular Therapeutics in Cancer Chemotherapy: Mechanism of Tumoritropic Accumulation of Proteins and the Antitumor Agent Smancs. Cancer Res. 1986, 46 (12 Part 1), 6387–6392.

(42) Chen, H.; Zhang, W.; Zhu, G.; Xie, J.; Chen, X. Rethinking Cancer Nanotheranostics. Nat. Rev. Mater. 2017, 2. https://doi.org/10.1038/natrevmats.2017.24.

(43) Kalyane, D.; Raval, N.; Maheshwari, R.; Tambe, V.; Kalia, K.; Tekade, R. K. Employment of Enhanced Permeability and Retention Effect (EPR): Nanoparticle-Based Precision Tools for Targeting of Therapeutic and Diagnostic Agent in Cancer. Mater. Sci. Eng. C 2019, 98, 1252–1276. https://doi.org/10.1016/j.msec.2019.01.066.

(44) Overchuk, M.; Zheng, G. Overcoming Obstacles in the Tumor Microenvironment: Recent Advancements in Nanoparticle Delivery for Cancer Theranostics. Biomaterials 2018, 156, 217–237. https://doi.org/10.1016/j.biomaterials.2017.10.024.

(45) Barbero, F.; Russo, L.; Vitali, M.; Piella, J.; Salvo, I.; Borrajo, M. L.; Busquets-Fité, M.; Grandori, R.; Bastús, N. G.; Casals, E.; et al. Formation of the Protein Corona: The Interface between Nanoparticles and the Immune System. Semin. Immunol. 2017, 34, 52–60. https://doi.org/10.1016/j.smim.2017.10.001.

(46) Barrán-Berdón, A. L.; Pozzi, D.; Caracciolo, G.; Capriotti, A. L.; Caruso, G.; Cavaliere, C.; Riccioli, A.; Palchetti, S.; Laganà, A. Time Evolution of Nanoparticle–Protein Corona in Human Plasma: Relevance for Targeted Drug Delivery. Langmuir 2013, 29 (21), 6485–6494. https://doi.org/10.1021/la401192x.

(47) Albanese, A.; Walkey, C. D.; Olsen, J. B.; Guo, H.; Emili, A.; Chan, W. C. W. Secreted Biomolecules Alter the Biological Identity and Cellular Interactions of Nanoparticles. ACS Nano 2014, 8 (6), 5515–5526. https://doi.org/10.1021/nn4061012.

(48) Lazarovits, J.; Chen, Y. Y.; Sykes, E. A.; Chan, W. C. W. Nanoparticle–Blood Interactions: The Implications on Solid Tumour Targeting. Chem. Commun. 2015, 51 (14), 2756–2767. https://doi.org/10.1039/C4CC07644C.

(49) Monopoli, M. P.; Walczyk, D.; Campbell, A.; Elia, G.; Lynch, I.; Baldelli Bombelli, F.; Dawson, K. A. Physical–Chemical Aspects of Protein Corona: Relevance to in Vitro and in Vivo Biological Impacts of Nanoparticles. J. Am. Chem. Soc. 2011, 133 (8), 2525–2534. https://doi.org/10.1021/ja107583h.

(50) Cai, R.; Chen, C. The Crown and the Scepter: Roles of the Protein Corona in Nanomedicine. Adv. Mater. 2018, 0 (0), 1805740. https://doi.org/10.1002/adma.201805740.

(51) Schöttler, S.; Landfester, K.; Mailänder, V. Controlling the Stealth Effect of Nanocarriers through Understanding the Protein Corona. Angew. Chem. Int. Ed. 2016, 55 (31), 8806–8815. https://doi.org/10.1002/anie.201602233.

(52) Nel, A. E.; Mädler, L.; Velegol, D.; Xia, T.; Hoek, E. M. V.; Somasundaran, P.; Klaessig, F.; Castranova, V.; Thompson, M. Understanding Biophysicochemical Interactions at the Nano–Bio Interface. Nat. Mater. 2009, 8 (7), 543–557. https://doi.org/10.1038/nmat2442.

(53) Mahmoudi, M.; Lynch, I.; Ejtehadi, M. R.; Monopoli, M. P.; Bombelli, F. B.; Laurent, S. Protein−Nanoparticle Interactions: Opportunities and Challenges. Chem. Rev. 2011, 111 (9), 5610–5637. https://doi.org/10.1021/cr100440g.

(54) Walkey, C. D.; Chan, W. C. W. Understanding and Controlling the Interaction of Nanomaterials with Proteins in a Physiological Environment. Chem. Soc. Rev. 2012, 41 (7), 2780–2799. https://doi.org/10.1039/C1CS15233E.

(55) Docter, D.; Westmeier, D.; Markiewicz, M.; Stolte, S.; Knauer, S. K.; Stauber, R. H. The Nanoparticle Biomolecule Corona: Lessons Learned – Challenge Accepted? Chem Soc Rev 2015, 44 (17), 6094–6121. https://doi.org/10.1039/C5CS00217F.

(56) Anselmo, A. C.; Mitragotri, S. A Chemical Engineering Perspective of Nanoparticle-Based Targeted Drug Delivery: A Unit Process Approach. AIChE J. 2016, 62 (4), 966–974. https://doi.org/10.1002/aic.15189.

(57) Caracciolo, G.; Cardarelli, F.; Pozzi, D.; Salomone, F.; Maccari, G.; Bardi, G.; Capriotti, A. L.; Cavaliere, C.; Papi, M.; Laganà, A. Selective Targeting Capability Acquired with a Protein Corona Adsorbed on the Surface of 1,2-Dioleoyl-3-Trimethylammonium Propane/DNA Nanoparticles. ACS Appl. Mater. Interfaces 2013, 5 (24), 13171–13179. https://doi.org/10.1021/am404171h.

(58) Carrillo-Carrion, C.; Carril, M.; Parak, W. J. Techniques for the Experimental Investigation of the Protein Corona. Curr. Opin. Biotechnol. 2017, 46, 106–113. https://doi.org/10.1016/j.copbio.2017.02.009.

(59) Pederzoli, F.; Tosi, G.; Vandelli, M. A.; Belletti, D.; Forni, F.; Ruozi, B. Protein Corona and Nanoparticles: How Can We Investigate On? Wiley Interdiscip. Rev. Nanomed. Nanobiotechnol. 2017, 9 (6), e1467. https://doi.org/10.1002/wnan.1467.

(60) Najafi-Hajivar, S.; Zakeri-Milani, P.; Mohammadi, H.; Niazi, M.; Soleymani-Goloujeh, M.; Baradaran, B.; Valizadeh, H. Overview on Experimental Models of Interactions between Nanoparticles and the Immune System. Biomed. Pharmacother. 2016, 83, 1365–1378. https://doi.org/10.1016/j.biopha.2016.08.060.

(61) Dobrovolskaia, M. A.; Shurin, M.; Shvedova, A. A. Current Understanding of Interactions between Nanoparticles and the Immune System. Toxicol. Appl. Pharmacol. 2016, 299, 78–89. https://doi.org/10.1016/j.taap.2015.12.022.

(62) Kim, S.; Shi, Y.; Kim, J. Y.; Park, K.; Cheng, J.-X. Overcoming the Barriers in Micellar Drug Delivery: Loading Efficiency, in Vivo Stability, and Micelle–Cell Interaction. Expert Opin. Drug Deliv. 2010, 7 (1), 49–62. https://doi.org/10.1517/17425240903380446.

(63) Owen, S. C.; Chan, D. P. Y.; Shoichet, M. S. Polymeric Micelle Stability. Nano Today 2012, 7 (1), 53–65. https://doi.org/10.1016/j.nantod.2012.01.002.

(64) Miller, T.; Hill, A.; Uezguen, S.; Weigandt, M.; Goepferich, A. Analysis of Immediate Stress Mechanisms upon Injection of Polymeric Micelles and Related Colloidal Drug Carriers: Implications on Drug Targeting. Biomacromolecules 2012, 13 (6), 1707–1718. https://doi.org/10.1021/bm3002045.

(65) Lu, J.; Owen, S. C.; Shoichet, M. S. Stability of Self-Assembled Polymeric Micelles in Serum. Macromolecules 2011, 44 (15), 6002–6008. https://doi.org/10.1021/ma200675w.

(66) Aguilar-Castillo, B. A.; Santos, J. L.; Luo, H.; Aguirre-Chagala, Y. E.; Palacios-Hernández, T.; Herrera-Alonso, M. Nanoparticle Stability in Biologically Relevant Media: Influence of Polymer Architecture. Soft Matter 2015, 11 (37), 7296–7307. https://doi.org/10.1039/C5SM01455G.

(67) Gravier, J.; Sancey, L.; Hirsjärvi, S.; Rustique, E.; Passirani, C.; Benoît, J.-P.; Coll, J.-L.; Texier, I. FRET Imaging Approaches for in Vitro and in Vivo Characterization of Synthetic Lipid Nanoparticles. Mol. Pharm. 2014, 11 (9), 3133–3144. https://doi.org/10.1021/mp500329z.

(68) Chen, H.; Kim, S.; He, W.; Wang, H.; Low, P. S.; Park, K.; Cheng, J.-X. Fast Release of Lipophilic Agents from Circulating PEG-PDLLA Micelles Revealed by in Vivo Förster Resonance Energy Transfer Imaging. Langmuir 2008, 24 (10), 5213–5217. https://doi.org/10.1021/la703570m.

(69) Buyens, K.; Lucas, B.; Raemdonck, K.; Braeckmans, K.; Vercammen, J.; Hendrix, J.; Engelborghs, Y.; De Smedt, S. C.; Sanders, N. N. A Fast and Sensitive Method for Measuring the Integrity of SiRNA-Carrier Complexes in Full Human Serum. J. Controlled Release 2008, 126 (1), 67–76. https://doi.org/10.1016/j.jconrel.2007.10.024.

(70) Zelphati, O.; Uyechi, L. S.; Barron, L. G.; Szoka, F. C. Effect of Serum Components on the Physico-Chemical Properties of Cationic Lipid/Oligonucleotide Complexes and on Their Interactions with Cells. Biochim. Biophys. Acta BBA - Lipids Lipid Metab. 1998, 1390 (2), 119–133. https://doi.org/10.1016/S0005-2760(97)00169-0.

(71) Scomparin, A.; Polyak, D.; Krivitsky, A.; Satchi-Fainaro, R. Achieving Successful Delivery of Oligonucleotides — From Physico-Chemical Characterization to in Vivo Evaluation. Biotechnol. Adv. 2015, 33 (6, Part 3), 1294–1309. https://doi.org/10.1016/j.biotechadv.2015.04.008.

(72) Buyens, K.; Meyer, M.; Wagner, E.; Demeester, J.; De Smedt, S. C.; Sanders, N. N. Monitoring the Disassembly of SiRNA Polyplexes in Serum Is Crucial for Predicting Their Biological Efficacy. J. Controlled Release 2010, 141 (1), 38–41. https://doi.org/10.1016/j.jconrel.2009.08.026.

(73) Hrkach, J.; Hoff, D. V.; Ali, M. M.; Andrianova, E.; Auer, J.; Campbell, T.; Witt, D. D.; Figa, M.; Figueiredo, M.; Horhota, A.; et al. Preclinical Development and Clinical Translation of a PSMA-Targeted Docetaxel Nanoparticle with a Differentiated Pharmacological Profile. Sci. Transl. Med. 2012, 4 (128), 128ra39-128ra39. https://doi.org/10.1126/scitranslmed.3003651.

(74) Autio, K. A.; Dreicer, R.; Anderson, J.; Garcia, J. A.; Alva, A.; Hart, L. L.; Milowsky, M. I.; Posadas, E. M.; Ryan, C. J.; Graf, R. P.; et al. Safety and Efficacy of BIND-014, a Docetaxel Nanoparticle Targeting Prostate-Specific Membrane Antigen for Patients With Metastatic Castration-Resistant Prostate Cancer: A Phase 2 Clinical Trial. JAMA Oncol. 2018, 4 (10), 1344–1351. https://doi.org/10.1001/jamaoncol.2018.2168.

(75) Harrington, K. J.; Mohammadtaghi, S.; Uster, P. S.; Glass, D.; Peters, A. M.; Vile, R. G.; Stewart, J. S. W. Effective Targeting of Solid Tumors in Patients With Locally Advanced Cancers by Radiolabeled Pegylated Liposomes. Clin. Cancer Res. 2001, 7 (2), 243–254.

(76) Lee, H.; Gaddy, D.; Ventura, M.; Bernards, N.; de Souza, R.; Kirpotin, D.; Wickham, T.; Fitzgerald, J.; Zheng, J.; Hendriks, B. S. Companion Diagnostic 64Cu-Liposome Positron Emission Tomography Enables Characterization of Drug Delivery to Tumors and Predicts Response to Cancer Nanomedicines. Theranostics 2018, 8 (9), 2300–2312. https://doi.org/10.7150/thno.21670.

(77) Hare, J. I.; Lammers, T.; Ashford, M. B.; Puri, S.; Storm, G.; Barry, S. T. Challenges and Strategies in Anti-Cancer Nanomedicine Development: An Industry Perspective. Adv. Drug Deliv. Rev. 2017, 108, 25–38. https://doi.org/10.1016/j.addr.2016.04.025.

(78) Golombek, S. K.; May, J.-N.; Theek, B.; Appold, L.; Drude, N.; Kiessling, F.; Lammers, T. Tumor Targeting via EPR: Strategies to Enhance Patient Responses. Adv. Drug Deliv. Rev. 2018, 130, 17–38. https://doi.org/10.1016/j.addr.2018.07.007.

(79) Murugan, K.; Choonara, Y. E.; Kumar, P.; Bijukumar, D.; Toit, L. C. du; Pillay, V. Parameters and characteristics governing cellular internalization and trans-barrier trafficking of nanostructures https://www.dovepress.com/parameters-and-characteristics-governing-cellular-internalization-and--peer-reviewed-article-IJN (accessed Sep 18, 2019). https://doi.org/10.2147/IJN.S75615.

(80) Setyawati, M. I.; Tay, C. Y.; Docter, D.; Stauber, R. H.; Leong, D. T. Understanding and Exploiting Nanoparticles' Intimacy with the Blood Vessel and Blood. Chem. Soc. Rev. 2015, 44 (22), 8174–8199. https://doi.org/10.1039/C5CS00499C.

(81) Deli, M. A. Potential Use of Tight Junction Modulators to Reversibly Open Membranous Barriers and Improve Drug Delivery. Biochim. Biophys. Acta BBA - Biomembr. 2009, 1788 (4), 892–910. https://doi.org/10.1016/j.bbamem.2008.09.016.

(82) Setyawati, M. I.; Tay, C. Y.; Chia, S. L.; Goh, S. L.; Fang, W.; Neo, M. J.; Chong, H. C.; Tan, S. M.; Loo, S. C. J.; Ng, K. W.; et al. Titanium Dioxide Nanomaterials Cause Endothelial Cell Leakiness by Disrupting the Homophilic Interaction of VE–Cadherin. Nat. Commun. 2013, 4 (1), 1–12. https://doi.org/10.1038/ncomms2655.

(83) Peng, Q.; Mu, H. The Potential of Protein–Nanomaterial Interaction for Advanced Drug Delivery. J. Controlled Release 2016, 225, 121–132. https://doi.org/10.1016/j.jconrel.2016.01.041.

(84) Akita, H.; Fujiwara, T.; Santiwarangkool, S.; Hossen, N.; Kajimoto, K.; El-Sayed, A.; Tabata, Y.; Harashima, H. Transcytosis-Targeting Peptide: A Conductor of Liposomal Nanoparticles through the Endothelial Cell Barrier. Small 2016, 12 (9), 1212–1221. https://doi.org/10.1002/smll.201500909.

(85) Dreher, M. R.; Liu, W.; Michelich, C. R.; Dewhirst, M. W.; Yuan, F.; Chilkoti, A. Tumor Vascular Permeability, Accumulation, and Penetration of Macromolecular Drug Carriers. JNCI J. Natl. Cancer Inst. 2006, 98 (5), 335–344. https://doi.org/10.1093/jnci/djj070.

(86) Lieleg, O.; Baumgärtel, R. M.; Bausch, A. R. Selective Filtering of Particles by the Extracellular Matrix: An Electrostatic Bandpass. Biophys. J. 2009, 97 (6), 1569–1577. https://doi.org/10.1016/j.bpj.2009.07.009.

(87) Stylianopoulos, T.; Poh, M.-Z.; Insin, N.; Bawendi, M. G.; Fukumura, D.; Munn, L. L.; Jain, R. K. Diffusion of Particles in the Extracellular Matrix: The Effect of Repulsive Electrostatic Interactions. Biophys. J. 2010, 99 (5), 1342–1349. https://doi.org/10.1016/j.bpj.2010.06.016.

(88) Ramanujan, S.; Pluen, A.; McKee, T. D.; Brown, E. B.; Boucher, Y.; Jain, R. K. Diffusion and Convection in Collagen Gels: Implications for Transport in the Tumor Interstitium. Biophys. J. 2002, 83 (3), 1650–1660.

(89) Alexandrakis, G.; Brown, E. B.; Tong, R. T.; McKee, T. D.; Campbell, R. B.; Boucher, Y.; Jain, R. K. Two-Photon Fluorescence Correlation Microscopy Reveals the Two-Phase Nature of Transport in Tumors. Nat. Med. 2004, 10 (2), 203–207. https://doi.org/10.1038/nm981.

(90) Pluen, A.; Boucher, Y.; Ramanujan, S.; McKee, T. D.; Gohongi, T.; Tomaso, E. di; Brown, E. B.; Izumi, Y.; Campbell, R. B.; Berk, D. A.; et al. Role of Tumor–Host Interactions in Interstitial Diffusion of Macromolecules: Cranial vs. Subcutaneous Tumors. Proc. Natl. Acad. Sci. 2001, 98 (8), 4628–4633. https://doi.org/10.1073/pnas.081626898.

(91) Chauhan, V. P.; Popović, Z.; Chen, O.; Cui, J.; Fukumura, D.; Bawendi, M. G.; Jain, R. K. Fluorescent Nanorods and Nanospheres for Real-Time In Vivo Probing of Nanoparticle Shape-Dependent Tumor Penetration. Angew. Chem. Int. Ed Engl. 2011, 50 (48), 11417–11420. https://doi.org/10.1002/anie.201104449.

(92) Rudnick, S. I.; Lou, J.; Shaller, C. C.; Tang, Y.; Klein-Szanto, A. J. P.; Weiner, L. M.; Marks, J. D.; Adams, G. P. Influence of Affinity and Antigen Internalization on the Uptake and Penetration of

Anti-HER2 Antibodies in Solid Tumors. Cancer Res. 2011, 71 (6), 2250–2259. https://doi.org/10.1158/0008-5472.CAN-10-2277.

(93) Lazzari, G.; Couvreur, P.; Mura, S. Multicellular Tumor Spheroids: A Relevant 3D Model for the in Vitro Preclinical Investigation of Polymer Nanomedicines. Polym. Chem. 2017, 8 (34), 4947–4969. https://doi.org/10.1039/C7PY00559H.

(94) Tchoryk, A.; Taresco, V.; Argent, R. H.; Ashford, M.; Gellert, P. R.; Stolnik, S.; Grabowska, A.; Garnett, M. C. Penetration and Uptake of Nanoparticles in 3D Tumor Spheroids. Bioconjug. Chem. 2019, 30 (5), 1371–1384. https://doi.org/10.1021/acs.bioconjchem.9b00136.

(95) Lu, H.; Stenzel, M. H. Multicellular Tumor Spheroids (MCTS) as a 3D In Vitro Evaluation Tool of Nanoparticles. Small 2018, 14 (13), 1702858. https://doi.org/10.1002/smll.201702858.

(96) Agarwal, R.; Jurney, P.; Raythatha, M.; Singh, V.; Sreenivasan, S. V.; Shi, L.; Roy, K. Effect of Shape, Size, and Aspect Ratio on Nanoparticle Penetration and Distribution inside Solid Tissues Using 3D Spheroid Models. Adv. Healthc. Mater. 2015, 4 (15), 2269–2280. https://doi.org/10.1002/adhm.201500441.

(97) Millard, M.; Yakavets, I.; Zorin, V.; Kulmukhamedova, A.; Marchal, S.; Bezdetnaya, L. Drug Delivery to Solid Tumors: The Predictive Value of the Multicellular Tumor Spheroid Model for Nanomedicine Screening. Int. J. Nanomedicine 2017, 12, 7993–8007. https://doi.org/10.2147/IJN.S146927.

(98) Donahue, N. D.; Acar, H.; Wilhelm, S. Concepts of Nanoparticle Cellular Uptake, Intracellular Trafficking, and Kinetics in Nanomedicine. Adv. Drug Deliv. Rev. 2019, 143, 68–96. https://doi.org/10.1016/j.addr.2019.04.008.

(99) Feiner-Gracia, N.; Pujals, S.; Delcanale, P.; Albertazzi, L. 15 - Advanced Optical Microscopy Techniques for the Investigation of Cell-Nanoparticle Interactions. In Smart Nanoparticles for Biomedicine; Ciofani, G., Ed.; Micro and Nano Technologies; Elsevier, 2018; pp 219–236. https://doi.org/10.1016/B978-0-12-814156-4.00015-X.

(100) Arsov, Z.; Urbančič, I.; Garvas, M.; Biglino, D.; Ljubetič, A.; Koklič, T.; Štrancar, J. Fluorescence Microspectroscopy as a Tool to Study Mechanism of Nanoparticles Delivery into Living Cancer Cells. Biomed. Opt. Express 2011, 2 (8), 2083–2095. https://doi.org/10.1364/BOE.2.2083.

(101) Weyland, M.; Manero, F.; Paillard, A.; Grée, D.; Viault, G.; Jarnet, D.; Menei, P.; Juin, P.; Chourpa, I.; Benoit, J.-P.; et al. Mitochondrial Targeting by Use of Lipid Nanocapsules Loaded with SV30, an Analogue of the Small-Molecule Bcl-2 Inhibitor HA14-1. J. Controlled Release 2011, 151 (1), 74–82. https://doi.org/10.1016/j.jconrel.2010.11.032.

(102) Gautier, J.; Munnier, E.; Paillard, A.; Hervé, K.; Douziech-Eyrolles, L.; Soucé, M.; Dubois, P.; Chourpa, I. A Pharmaceutical Study of Doxorubicin-Loaded PEGylated Nanoparticles for Magnetic Drug Targeting. Int. J. Pharm. 2012, 423 (1), 16–25. https://doi.org/10.1016/j.ijpharm.2011.06.010.

(103) Gautier, J.; Munnier, E.; Soucé, M.; Chourpa, I.; Eyrolles, L. D. Analysis of Doxorubicin Distribution in MCF-7 Cells Treated with Drug-Loaded Nanoparticles by Combination of Two Fluorescence-Based Techniques, Confocal Spectral Imaging and Capillary Electrophoresis. Anal. Bioanal. Chem. 2015, 407 (12), 3425–3435. https://doi.org/10.1007/s00216-015-8566-9.

(104) Stracke, F.; Weiss, B.; Lehr, C.-M.; König, K.; Schaefer, U. F.; Schneider, M. Multiphoton Microscopy for the Investigation of Dermal Penetration of Nanoparticle-Borne Drugs. J. Invest. Dermatol. 2006, 126 (10), 2224–2233. https://doi.org/10.1038/sj.jid.5700374.

(105) Gao, H.; Yang, Z.; Cao, S.; Xiong, Y.; Zhang, S.; Pang, Z.; Jiang, X. Tumor Cells and Neovasculature Dual Targeting Delivery for Glioblastoma Treatment. Biomaterials 2014, 35 (7), 2374–2382. https://doi.org/10.1016/j.biomaterials.2013.11.076.

(106) Kenesei, K.; Murali, K.; Czéh, Á.; Piella, J.; Puntes, V.; Madarász, E. Enhanced Detection with Spectral Imaging Fluorescence Microscopy Reveals Tissue- and Cell-Type-Specific Compartmentalization of Surface-Modified Polystyrene Nanoparticles. J. Nanobiotechnology 2016, 14. https://doi.org/10.1186/s12951-016-0210-0.

(107) Huang, B.; Bates, M.; Zhuang, X. Super-Resolution Fluorescence Microscopy. Annu. Rev. Biochem. 2009, 78 (1), 993–1016. https://doi.org/10.1146/annurev.biochem.77.061906.092014.

(108) Schermelleh, L.; Heintzmann, R.; Leonhardt, H. A Guide to Super-Resolution Fluorescence Microscopy. J. Cell Biol. 2010, 190 (2), 165–175. https://doi.org/10.1083/jcb.201002018.

(109) Hess, S. T.; Girirajan, T. P. K.; Mason, M. D. Ultra-High Resolution Imaging by Fluorescence Photoactivation Localization Microscopy. Biophys. J. 2006, 91 (11), 4258–4272. https://doi.org/10.1529/biophysj.106.091116.

(110) Rust, M. J.; Bates, M.; Zhuang, X. Sub-Diffraction-Limit Imaging by Stochastic Optical Reconstruction Microscopy (STORM). Nat. Methods 2006, 3 (10), 793–796. https://doi.org/10.1038/nmeth929.

(111) Albertazzi, L.; Zwaag, D. van der; Leenders, C. M. A.; Fitzner, R.; Hofstad, R. W. van der; Meijer, E. W. Probing Exchange Pathways in One-Dimensional Aggregates with Super-Resolution Microscopy. Science 2014, 344 (6183), 491–495. https://doi.org/10.1126/science.1250945.

(112) Baker, M. B.; Albertazzi, L.; Voets, I. K.; Leenders, C. M. A.; Palmans, A. R. A.; Pavan, G. M.; Meijer, E. W. Consequences of Chirality on the Dynamics of a Water-Soluble Supramolecular Polymer. Nat. Commun. 2015, 6, 6234. https://doi.org/10.1038/ncomms7234.

(113) Baker, M. B.; Gosens, R. P. J.; Albertazzi, L.; Matsumoto, N. M.; Palmans, A. R. A.; Meijer, E. W. Exposing Differences in Monomer Exchange Rates of Multicomponent Supramolecular Polymers in Water. Chembiochem Eur. J. Chem. Biol. 2016, 17 (3), 207–213. https://doi.org/10.1002/cbic.201500606.

(114) Aloi, A.; Vargas Jentzsch, A.; Vilanova, N.; Albertazzi, L.; Meijer, E. W.; Voets, I. K. Imaging Nanostructures by Single-Molecule Localization Microscopy in Organic Solvents. J. Am. Chem. Soc. 2016. https://doi.org/10.1021/jacs.5b13585.

(115) Boreham, A.; Volz, P.; Peters, D.; Keck, C. M.; Alexiev, U. Determination of Nanostructures and Drug Distribution in Lipid Nanoparticles by Single Molecule Microscopy. Eur. J. Pharm. Biopharm. 2017, 110, 31–38. https://doi.org/10.1016/j.ejpb.2016.10.020.

(116) van der Zwaag, D.; Vanparijs, N.; Wijnands, S.; De Rycke, R.; De Geest, B. G.; Albertazzi, L. Super Resolution Imaging of Nanoparticles Cellular Uptake and Trafficking. ACS Appl. Mater. Interfaces 2016, 8 (10), 6391–6399. https://doi.org/10.1021/acsami.6b00811.

(117) De Koker, S.; Cui, J.; Vanparijs, N.; Albertazzi, L.; Grooten, J.; Caruso, F.; De Geest, B. G. Engineering Polymer Hydrogel Nanoparticles for Lymph Node-Targeted Delivery. Angew. Chem. Int. Ed Engl. 2016, 55 (4), 1334–1339. https://doi.org/10.1002/anie.201508626.

Chapter 2 .
Super-resolution Microscopy Unveils Dynamic Heterogeneities in Nanoparticle Protein Corona

The adsorption of serum proteins, leading to the formation of a biomolecular corona, is a key determinant of the biological identity of nanoparticles in vivo. Therefore, gaining knowledge on the formation, composition and temporal evolution of the corona is of utmost importance for the development of nanoparticle-based therapies. Here, we show that the use of super-resolution optical microscopy enables the imaging of the protein corona on mesoporous silica nanoparticles with single protein sensitivity. Particle-by-particle quantification reveals a significant heterogeneity in protein adsorption under native conditions. Moreover, the diversity of the corona evolves over time depending on the surface chemistry and degradability of the particles. We investigate the consequences of protein adsorption for specific cell targeting by antibody-functionalized nanoparticles providing a detailed understanding of corona-activity relations. The proposed methodology is widely applicable to a variety of nanostructures and complements the existing ensemble approaches for protein corona study.

Part of this work has been published as:

N. Feiner-Gracia, M. Beck, S. Pujals, S. Tosi, T. Mandal, C. Buske, M. Linden, L. Albertazzi. Super-Resolution Microscopy Unveils Dynamic Heterogeneities in Nanoparticle Protein Corona. Small, 2017, 13, 1701631.

2.1. Introduction

Nanoparticles (NPs) interact with biological fluids after in vivo injection, leading to the formation of a biomolecular corona that determines the biological identity of the nanomaterial. The adsorption of serum proteins, lipids and small metabolites affects the stability, targeting abilities and immunogenicity of injected NPs with dramatic consequences for their therapeutic potential as already explained in Chapter 1[1–5]. Therefore, it is of major importance to understand the formation and the dynamics of nanoparticle protein corona, permitting the design of effective nanostructures for biomedical applications[6–9]. Up to date, the most commonly used methods to quantify protein adsorption are gel electrophoresis (SDS-PAGE) and liquid chromatography mass spectrometry (LC-MS)[10–15] that allow for high-throughput identification of corona composition. However, both are ensemble techniques that do not allow the study of inter-particle variation. Moreover, the small size of nanoparticles together with the complexity of serum composition make challenging the study of nanoparticle-protein interaction[3]. Likewise, the corona is believed to be dynamic, changing in composition in time[3,10]. For these reasons advanced techniques are required to investigate the composition of the corona of biomedical nanomaterials, thence, imaging-based methodologies have been very recently proposed[14–17]. In particular, the pioneering work of Dawson and co-workers made use of transmission electron microscopy to image the distribution of serum protein epitopes enabling the understanding of the spatial organization of the corona[14]. Despite these advances, the small size and polydispersity of NPs together with the complexity of serum composition make the study of nanoparticle-protein interaction very challenging and new methods are required to achieve a full understanding of such relevant phenomenon. Recently super resolution microscopy and single molecule imaging are emerging as powerful tool to probe the formation and composition of protein corona in microparticles[16–18]. The high sensitivity, resolution and the ability to measure particle-by-particle are particularly suitable to complement the existing techniques and extend our understanding of the biomolecular corona and the use of super resolution microcopy to nanoparticles.

In this chapter, we introduce the use of super-resolution optical microscopy for the imaging of the heterogeneity and dynamics of nanoparticle protein corona. dSTORM imaging revealed that the formation of the biomolecular corona is highly heterogeneous inside the same nanoparticle population and this heterogeneity evolves in time depending on the physicochemical properties of the NPs. This is a crucial finding as this variability will strongly influence the *in vivo* behavior of therapeutic particles. Moreover, we show that adsorption and degradation processes are of great relevance for the targeting ability of these NPs. The high resolution, molecular specificity and the ability to measure on a particle-by-particle basis make dSTORM a powerful technique to look at the fine details of the protein corona, complementing the existing high-throughput methods in the identification of the nanoparticle biological identity. Here dSTORM allows highlighting hidden features of nanoparticles

behavior in biological fluids contributing to the understanding of drug delivery and to the rational design of novel and improved nanocarriers.

2.2. dSTORM imaging of nanoparticles protein corona

2.2.1. Mesoporous Silica Nanoparticles

Mesoporous silica nanoparticles (MSN)[a], a relevant nanostructure for medical applications[19–21], are gaining wide interest for biomedical applications such as targeted drug delivery[19]. MSN are based on inorganic material which exhibit beneficial properties over other inorganic NPs. The possibility to highly tune their pore and particle size allows a fine control of drug encapsulation and release, as well as, an easy functionalization thanks to the high specific surface area. Moreover, distinct studies have shown a remarkable high biocompatibility, as well as, biodegradability in physiological conditions[22]. Despite the promising pre-clinical studies, the clinical translation of this systems is still a challenge which needs to be further investigate. Therefore, we aimed to characterize the protein corona formation into individual MSNs to provide tools to finely tune the system to improve its clinical benefits.

MSNs with an average diameter of 170 nm and different surface chemistries (MSN1-3), varying in hydrophilicity and charge were prepared. Amino-functionalized MSNs (MSN1), synthesized according to literature procedures by dr. M. Beck[23], were obtained from our collaborators. Two additional particles, MSN2 and MSN3, were synthesized by partial conversion of amino-groups to carboxylic acid groups in order to tune the surface charge of the particles keeping the particle size identical in all cases.

2.2.2. Optimizing STORM imaging of MSN protein corona formation

In this Chapter, a new methodology was optimized to be able to prove the interactions of blood proteins with MSN, Figure 2.1a schematically shows the super-resolution method applied. First, nanoparticles and proteins were labelled with two spectrally separated STORM dyes, Alexa488 and Cy5, respectively. Then, nanoparticles were incubated at 37 °C with fluorescently labelled proteins for a desired amount of time, and subsequently imaged with STORM. Following previously reported studies we imaged NP either in full serum[24–26] or in single protein solution[14,16,27], e.g. bovine serum albumin (BSA). In both cases, we spiked the native solution with a low fraction (1-10%) of fluorescently labelled protein of interest. After

[a] MSN formulation, functionalization and characterization was performed by M. Berck in Ülm University.

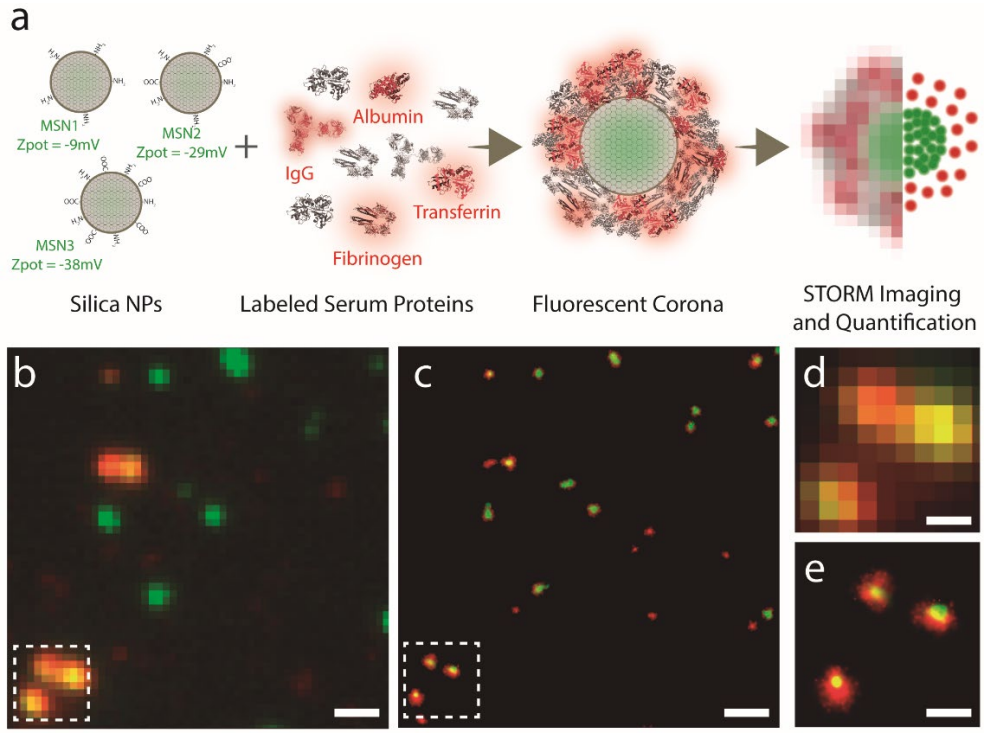

Figure 2.1. STORM imaging of protein corona formation in mesoporous silica nanoparticles. a, Schematic representation of the protocol followed: i) labelling of nanoparticles (green) and proteins (red); ii) incubation of nanoparticles in serum to form protein corona; iii) STORM imaging and iv) protein quantification. **b-c,** MSN1 NPs (green) incubated with 10%mol BSA-Cy5 (red) in full serum imaged using conventional wide-field (**b**) and STORM (**c**). Scale Bar: 1 μm. (**d**) Zoom of the wide-field image and (**e**), Zoom of the STORM image. Scale Bar: 400 nm.

the desired incubation time NPs were deposited on a glass coverslip for STORM imaging without the need of sample manipulation such as centrifugation or surfactant addition used in other techniques when studying protein corona formation. Figure 2.1b-c shows a conventional fluorescence image (b) of MSN1 incubated with Cy5-labelled BSA in full serum, compared to the corresponding dSTORM image (c). Due to the increased resolution of dSTORM microscopy, it is possible to resolve individual nanoparticles and to visualize the surrounding protein layer. Figure 3.1d-e shows a section containing three nanoparticles in conventional (d) and dSTORM (e) images, highlighting the structural details of the protein corona and allowing determining its size on a single particle basis.

To achieve optimal dSTORM imaging of nanoparticles-protein corona different parameter regarding sample preparation needed to be optimize. As stated in Chapter 1, dSTORM good image reconstruction is determined by the photoswhitching behavior of the dye, which can limit the resolution achieved[28,29]. In the present work, we used Cyanine5 and Alexa488

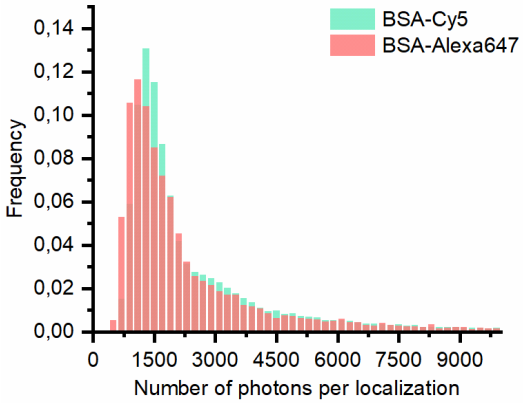

Figure 2.2. Histogram of number of photons per localization. MSN1 incubated for 1 hour in 1% BSA-labelled/BSA either with Cy5 or Alexa647. The number of photons obtained for each 647 localization in each condition are plotted.

although, Alexa647 and Atto488 are normally considered the best performing far-red and green dyes respectively. It is worth noting, that most of the investigations on dSTORM imaging have been performed in biological samples, such as cells[28]. However, the photophysical properties of the dyes are different when interacting with synthetic materials as published recently[30–32]. Synthetic materials offer to the dye a different microenvironment for example a different hydrophobicity and charge than an antibody used for immunolabelling of biological samples. This difference in the microenvironment can affect the dSTORM performances. As an example, we observed that the performance of Alexa 647 was not improved compared to Cy5. Figure 2.2 shows that the photon counts of BSA-Alexa647 is similar to the photon counts of BSA-Cy5, also demonstrated in the work of Dempsey et. al. Another significant issue we observe when using Alexa647 labelled BSA was an impact of the labeling on the behavior of corona formation (that do not match with our label-free controls). Moreover, the choice of the dyes should take in account the effect on the nanoparticles properties. In particular, we did not use Atto488 because of its hydrophobicity, which would be more impactful on the NP surface, as well as, because other biological studies where in the past performed on these nanoparticles with Alexa488.

Another important parameter which had to be optimize is the amount of fluorescent protein in order i) to optimize STORM imaging and obtain the most realistic image reconstruction and ii) to minimize the effect of the labeling on the corona formation[15]. Different percentages of labelled and non-labelled protein were used, and the corona formed studied. First, we aimed to minimize the background signal due to the non-corona-bound proteins that are adsorbed onto the glass slide. At 1% of labelled-protein, the corona was clearly distinguishable from the surrounding background while at higher concentrations the background influenced the accuracy in the identification of proteins forming the corona

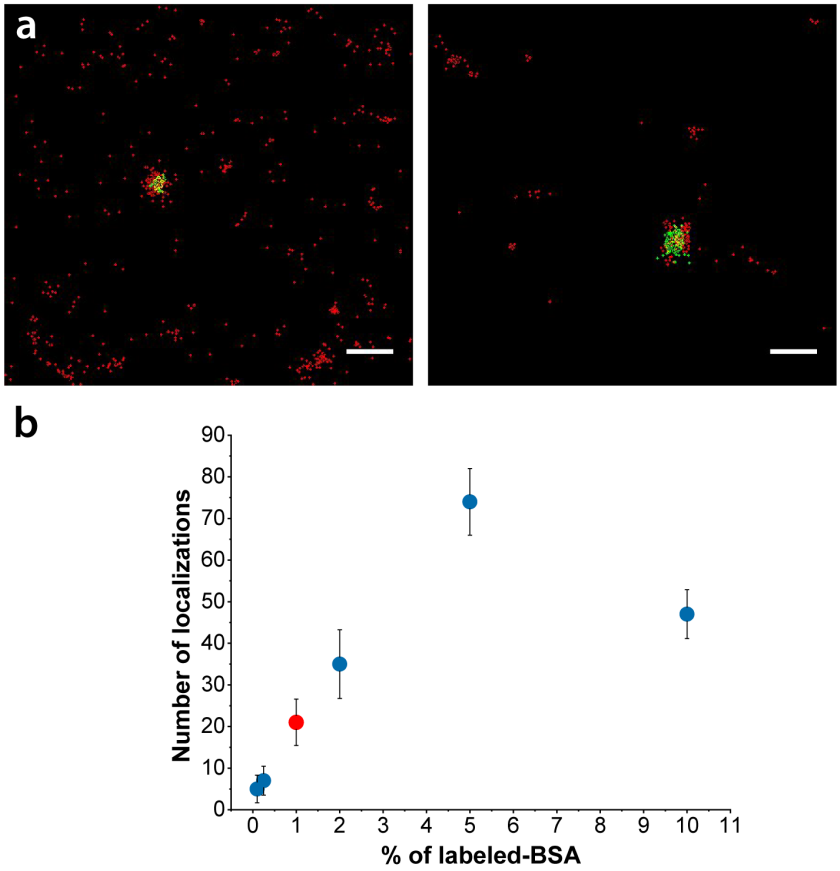

Figure 2.3. The percentage of labeled protein was tuned to distinguish the protein corona form the free protein in the solution. a. Representative images of MSN1 incubated with 10% BSA-Cy5/BSA v/v during 30 minutes (left) or incubated with 1% BSA-Cy5/BSA v/v during 30 minutes, at this percentatge it is possible to distinguish the localizations of the protein corona from those of the free protein. Scale bar 200 nm. **b**. Median number of localizations with increasing percentages of labeled BSA (±S.E.) detected in MSN1 incubated for 1 hour at 37ºC with BSA-Cy5/BSA.

(Figure 2.3a). Notably, we corroborated the linearity in number of localizations detected at increasing concentrations of labeled protein, which is crucial for quantification as shown in Figure 2.3b. Linearity was tracked down between 0.1% and 5% BSA-Cy5/BSA, for this reason 1% of labelled protein perfectly sits in the linearity range, whereas, we observed a sublinear number of localizations at 10% of labeled protein. We attributed the latter to multiple simultaneous blinking events that are discarded during the analysis among other photophysical effects.

Finally, we verified that under the proposed conditions the use of labelled proteins does not significantly alter the protein corona formation. DLS analysis demonstrated the size of the

complex MSN-protein corona was the same when using labelled and non-labelled proteins, Figure 2.4a. Moreover, Bradford Protein assay (BCA) test was used as a bulk method to quantify the concentration of proteins which turn out to be also similar for both conditions as shown in Figure 2.4b.

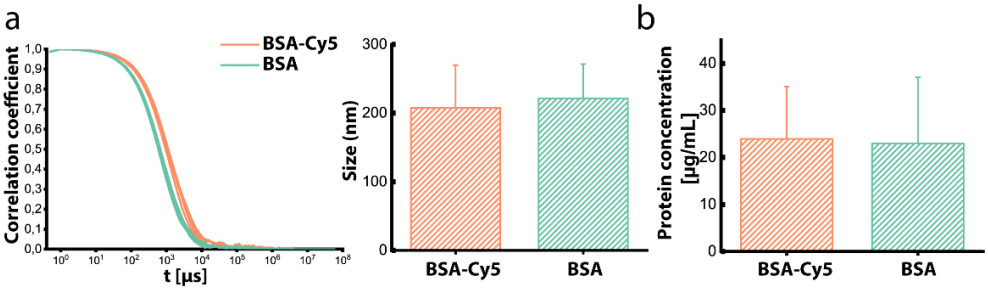

Figure 2.4 Labelling of protein does not affect protein corona-nanoparticle complex formation. a. DLS measurements of MSN incubated with 10% BSACy5/FBS and 10% BSA/FBS for 1 hour at 37ºC, following 3 washing steps. Correlation coefficients (left) were obtained from 3 independent runs for each condition and hydrodynamic size (right) was calculated by number based in 3 independent runs for each condition. **b.** Protein quantification based on a BCA test on MSN with 10%BSA-Cy5/FBS for 1h a 37ºC compared to MSN incubated with 10%BSA/FBS. The mean of 4 independent samples is shown together with an error bar of the S.D.

2.3. STORM quantification of protein corona

2.3.1. Quantitative approach for nanoparticle and protein localization

In dSTORM, the image reconstruction is based on single molecule localization, allowing us not only to visualize the molecular organization of the protein corona, but also to estimate the number of proteins interacting with each nanoparticle[30,33,34]. To allow for automatic quantification of the dSTORM images, we developed an analysis tool able to extract the number of localizations obtained from proteins attached to each NP and to measure the thickness of the corona[b].

The image analysis procedure, schematically represented in Figure 2.5, first separated and plot both channels, nanoparticle localizations (green) and protein localizations (red). Next, Figure 2.5b, MSN were localized by applying the mean shift cluster algorithm[35] only to the localization of the channel corresponding to the nanoparticles. The result from the algorithm was a set of clusters, each expected to correspond to a given MSN (further details on parameters used are described in Experimental Section). After that, nanoparticles were validated according to their geometry; they were expected to be spheres of about 170 nm in

[b] The software was developed in collaboration of S. Tosi from IRB.

diameter, but we allowed some deviation both in size and shape to account for NP synthesis and experimental variability. Too large or too elongated NPs were likely clusters of NPs, or NPs that rolled during acquisition, therefore, they were discarded from the quantification. To further limit the risk of grouping several close NPs and hence assign wrong protein corona localizations to them, any valid NP which center of mass was closer than 300 nm to the center of mass of another valid NP is also discarded. Finally, valid NPs were fitted a disk to accurately estimate their size and NPs, adapting a previously described procedure developed by Zwaag et.al.[36]

Once MSN were localized, analyzed and validated, the molecule localizations in the protein channel are assigned to each validated NP. To this end, we considered a distance equal

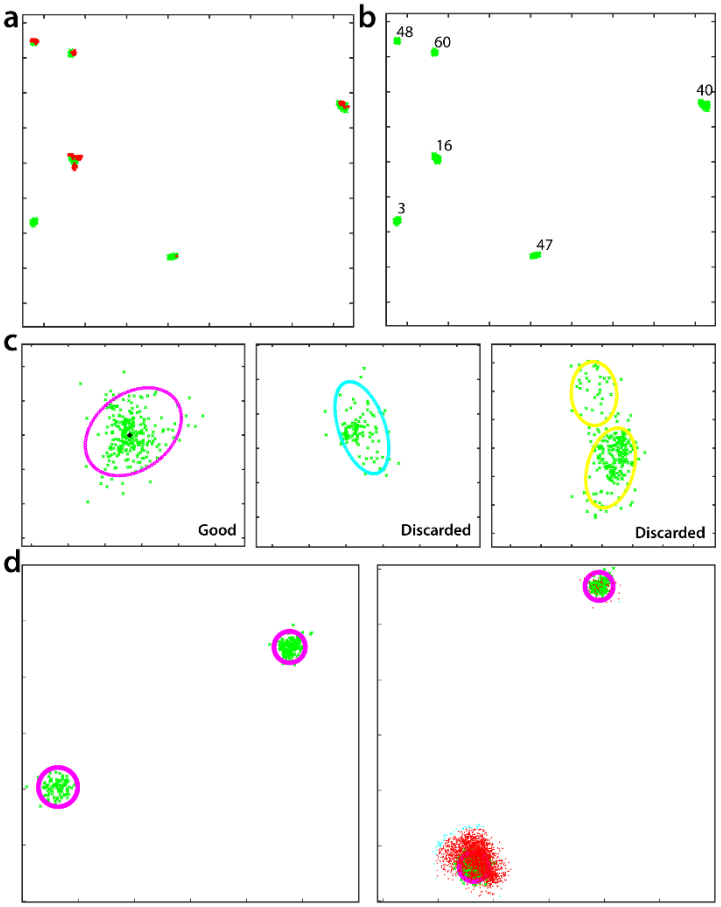

Figure 2.5 Schematic representation of the analysis procedure to quantify proteins localization per nanoparticle. a. Plot of MSN (green) and protein (red) localizations. **b.** Clustering of localizations and identification of individual nanoparticles. **c.** Nanoparticles validation as a function of elongation, size and aggregates. Pink ellipse indicates valid nanoparticle, cyan ellipse indicates big or elongated particle and yellow ellipse aggregates. **d.** Two field of views of nanoparticles fitted to a sphere to obtain their size together with the protein localizations (in red).

to 3 times the estimated cluster size corresponding to a NP from its center of mass and assigned it the closest protein localizations up to 98% of the total number of protein localizations falling in this region. Finally, the radius of the complexes (NP-protein corona) was estimated as the distance between the center of mass of the nanoparticle and the farthest protein localization that was assigned to it.

2.3.2. Blinking behavior of single proteins

To estimate the number of proteins adsorbed on each nanoparticle one must consider that its associated dye (Cy5) can be localized several times during acquisition since fluorophores are subject to blinking[29]. To take this effect into account it is necessary to calibrate the measurements by estimating the statistical distribution of these blinking events. A schematically representation of the procedure used is shown in Figure 2.6. Since this phenomenon is known to highly depend on the chemical environment[37] the number of localizations per individual molecule were estimated from measurements performed under same conditions than during the main experiments (i.e. with nanoparticles and serum). Nevertheless, proteins were this time labelled at a ratio of 0.01% instead of 1% and 10% for the main experiments. At this concentration protein localizations appeared as clearly isolated clusters, facilitating the analysis.

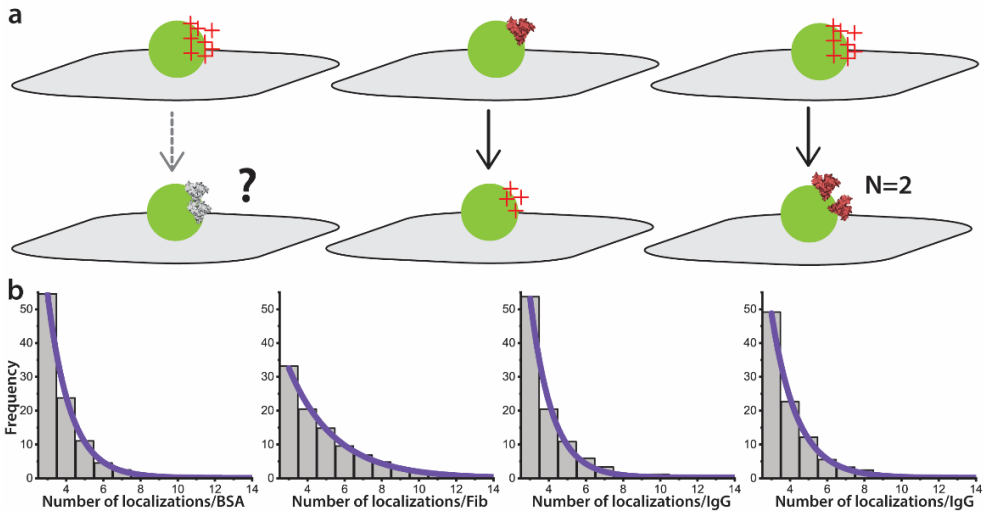

Figure 2.6. Single protein estimation. a. Schematic representation of the challenge in estimating number of proteins from number of localizations. From a single protein on a nanoparticle the number of localizations per protein can be estimated, being easier to extrapolate then the number of proteins in other experiments. **b.** Frequency histograms showing the number of localizations per protein, from left to right, BSA, Fib, IgG, Tf.

The images obtained for this experiment were analyzed using the NIS-Elements Nikon software configured with the exact same parameters as for the main experiments. The list of localizations was exported and analyzed by another Matlab script as illustrated in Figure 2.6 implementing the following steps. i)The proteins localizations were clustered applying the meanshift clustering algorithm[35]. ii)The size of the cluster is estimated by measuring the distance between the two farthest localizations it has been assigned. Clusters larger than 50 nm were discarded as this distance is quite larger than the expected accuracy of STORM for such sample. Then, we built a histogram of localizations per single protein from thousands of measurements (Figure 2.6b). Since blinking follows a geometric distribution[38,39] we estimated the average number of localizations per single protein as the mean of a decreasing exponential function fitted to this histogram[34].

2.3.3. Estimating number of proteins per nanoparticle

The number of localizations per single labeled protein obtained in the previous section was used to estimate the total number of proteins in the corona, following similar methods previously reported for the dSTORM-based quantification of molecules in biological structures[34,37,40]. The number of proteins adsorbed by a NP was estimated by dividing the number of protein localizations assigned to each MSN by the corresponding mean number of recurring localizations due to blinking for this protein (as estimated from the histograms of Figure 2.6b). Notably, we acknowledge that due to the stochastic nature of dye blinking there is an uncertainty for the measurements of nanoparticles with a very low number of proteins

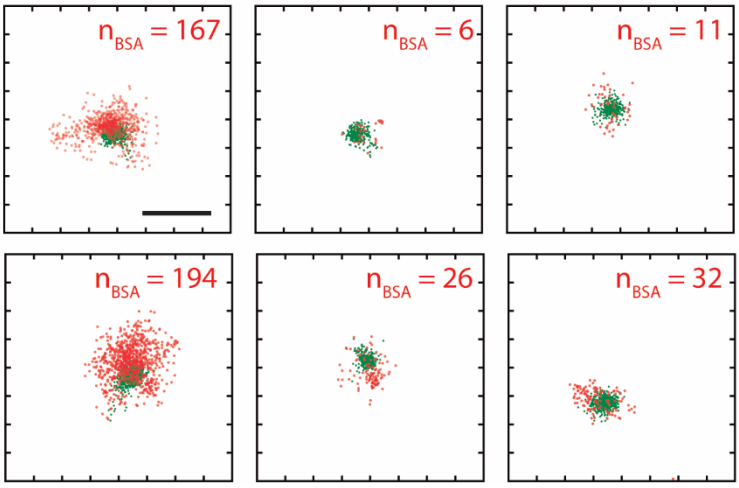

Figure 2.7 Representative images of MSN1 incubated with BSA. Reconstruction of different MSN1 nanoparticles with the corresponding protein corona, showing the heterogeneity present. The number of labelled-proteins counted on the surface on the surface of each nanoparticle is indicated. Scale bar: 200 nm.

adsorbed while this effect is minimized for larger corona. Thanks to the automatic detection and quantification, a large number of NPs can be identified, providing an estimation of the average number of proteins per particle, of the particle-by-particle distribution and of the dependency of the corona on time and surface chemistry.

Figure 2.7 shows six representative MSN1 NPs identified and quantified by the software. As it can be observed in these images, the same nanoparticle type displays a very heterogeneous behavior where some of the nanoparticles have none or a very small corona and others have a considerable amount of proteins adsorbed onto their surface. The heterogeneity in protein adsorption has been hypothesized[2] but, due to the lack of suitable techniques, poorly investigated experimentally. In the next sections, the dSTORM methodology was used to unveil the effect of nanoparticle structure on the time evolution of this molecular diversity.

2.4. Time-dependent growth of the protein corona

Having established this powerful methodology, we studied the time evolution of the protein corona, a key factor considering the different *in vivo* circulation time of NPs. Recent proteomics analysis reported that the corona is formed within seconds after exposure to serum and grows over time both in thickness and protein amount[11]. Here we expand the scope of these ensemble studies using dSTORM to investigate the time evolution of the corona on a particle-by-particle basis.

Figure 2.8 shows representative super-resolution images of different MSN1 nanoparticles (green) after exposure to 10 mg/mL of BSA (1%mol labelled, red) for different incubation times. As clearly shown in Figure 2.8, the quantity of adsorbed BSA per nanoparticle rises in time with a maximum at the longest incubation time studied (12 hours), in good agreement with previous studies[11]. We utilized our automated analysis tool to quantitatively investigate the evolution of the protein corona on a particle-by-particle basis. Figure 2.9a-c shows the distributions of the number of proteins adsorbed (b), NP size (c) and NP-corona size (d) for

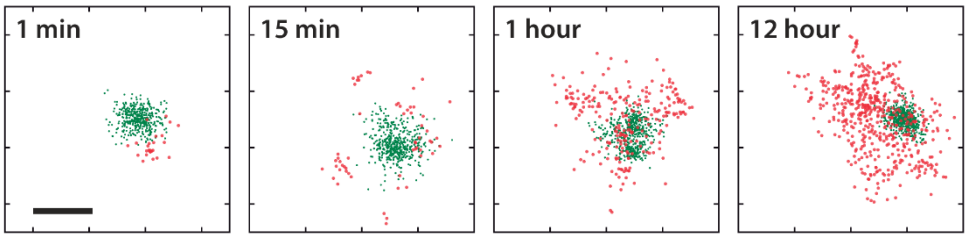

Figure 2.8. Protein corona evolution in time. MSN1s were incubated at 37°C with 1%mol BSA-Cy5 in a 10 mg/mL BSA solution and the complexes imaged at different times. Representative images of the evolution of the corona from 1 minute to 12 hours (left to rigth). Scale bar: 100 nm.

each time point studied. The number of proteins adsorbed did not significantly increase in the first 15 minutes but subsequently rised at 1h and 12h time points. Knowing the surface area of both, BSA molecules (28 nm^2 and 32 nm^2, rectangular and triangular cross section)[41] and the mean outer surface area of the MSNs (90,792 nm^2/particle), we calculated the theoretical number of BSA required to cover the whole NP surface[42] to be around 3,000 molecules . From dSTORM data, we detected 42 labelled BSA molecules (mean value) after 1 hour of incubation, from which, taking into account the labeling ratio of 1%, we estimated a total of 4,200 BSA molecules forming the protein corona. This is an indication that already at this time point the nanoparticle surface is fully covered and the formation of a protein multilayer occurs. Notably we cannot rule out unfolding processes occurring during the formation of the protein corona which modifies the surface area of the BSA[7].

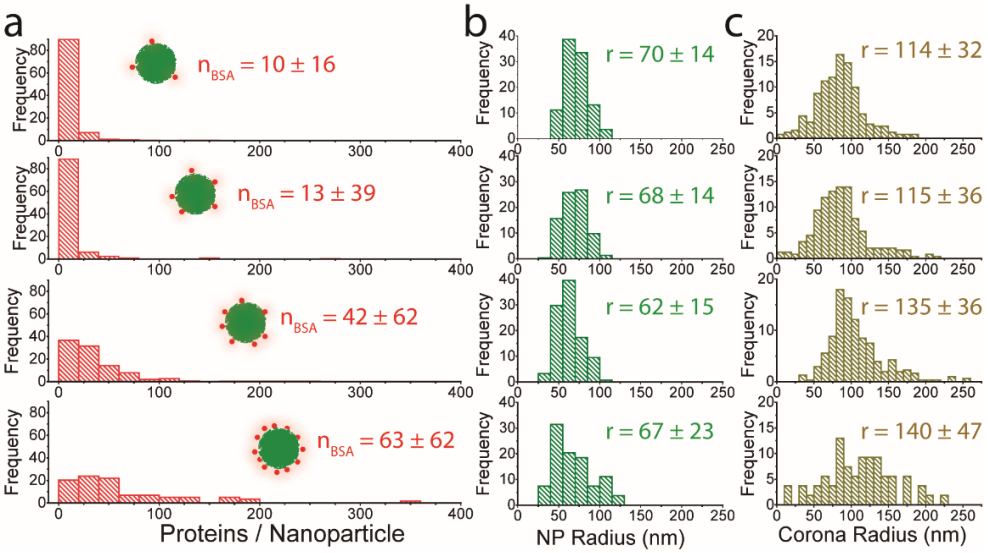

Figure 2.9. Kinetics of the BSA protein corona formation over time on MSN1. a. Distribution of the number of labelled BSA molecules detected per nanoparticle at each time point studied (1 minute , 1 5 minutes, 1 hour and 12 hours, top to bottom). The mean and standard deviation of the number of BSA molecules at each time point is indicated. **b.** Size distribution of MSN **c.** Size distribution of MSN-protein corona complex

Interestingly, the inter-particle differences increased tremendously after 1h as demonstrated by the broader distribution of the protein-per-particle histogram. This was even stronger after 12h incubation where particles with almost no corona (< 20 labelled BSA per particle) coexisted with particles with very large corona (> 200 labelled BSA per particle). This heterogeneity is also observed in the thickness of the corona that showed a broader distribution after 12h of incubation (see Figure 2.9c). Recent studies postulated the heterogeneity of protein absorption on NPs.[2] Here, the direct observation of this

heterogeneity highlights the importance of studying the biomolecular corona on a single particle level and provides crucial information about the biological behavior of these particles, which will reflect this molecular diversity[43].

Most of the studies carried out to determine the protein corona composition require purification steps of the nanoparticle-protein complex, allowing the detection of strongly adsorbed proteins only. It is known that different layers of proteins, varying in adhesion strength, are present; this can be simplified assuming a strong layer of high-affinity proteins known as hard corona[44] and a layer of loosely bound proteins indicated as soft corona as already explained in Chapter 1. Due to the difficulties in preserving the soft corona its biological relevance is poorly understood[11,27,45,46]. The method we propose quantifies proteins adsorbed to the nanoparticles surface with minimal processing, allowing the investigation of loosely adsorbed proteins. Figure 2.10a shows representative dSTORM images of MSN1 nanoparticles after the centrifugation procedure commonly used in the literature[24,27,44] (left, hard corona) and without any centrifugation (right, hard+soft corona). As quantified in Figure

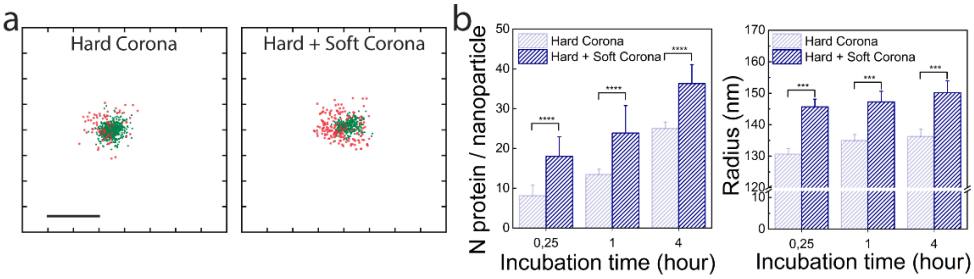

Figure 2.10. dSTORM imaging of both soft and hard corona. a. Representative MSN1–protein corona STORM images comparing the corona observed with washing steps to remove the loosely bound proteins (hard corona) and without the washing steps, in situ, (hard + soft corona). **b**. Median and standard error of the number of BSA molecules quantified (left) and size of the complexes protein corona-MSN (right) for both conditions, non-centrifuged and centrifuged in each time point.

2.10b we identified significantly more labelled BSA proteins in the non-centrifuged samples (pvalue<0.0001 in all cases) (see Figure 2.11 for the frequency histograms), as well as, a small increase in the average thickness. The difference in the number of proteins present in the total corona and the number of proteins present in the hard corona remained constant for different incubation periods. Whereas, the total amount of adsorbed protein increased with time, indicating a constant soft corona present on a growing hard corona.

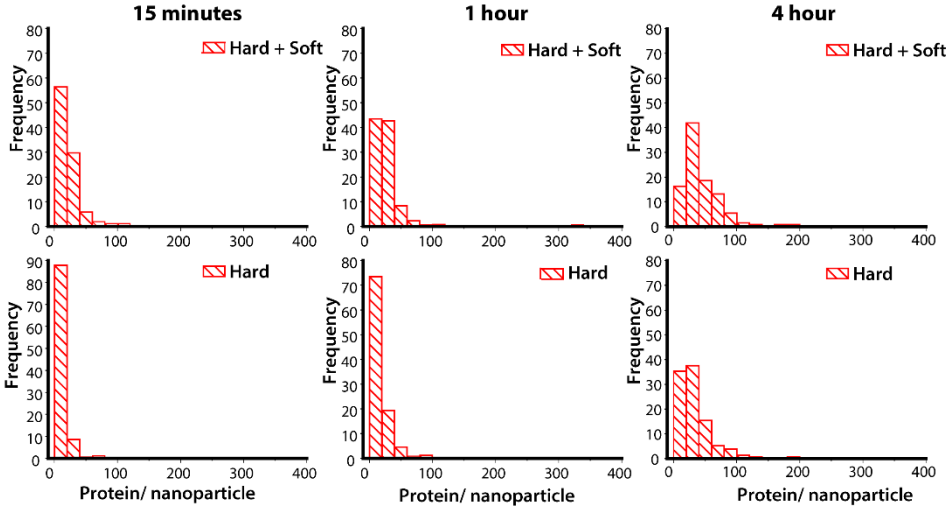

Figure 2.11 Histograms of number of BSA molecules comparing Hard vs Hard + Soft corona. The histograms represent the normalized frequency of the number of proteins detected for MSN1 after being incubated at 37ºC with 1% BSA-Cy5/BSA. Top graphs were measured just after the incubation time and bottom graphs MSN were centrifugated to eliminate the soft corona.

2.5. Nanoparticle surface chemistry influence on corona formation

Several studies have shown that physicochemical properties such as size, shape, surface chemistry and hydrophobicity determine the type and the number of proteins adsorbed to the nanoparticle surface[3,8]. In this framework, the hydrophilicity and the charge of the NP surface play a pivotal role. To identify whether the surface charge of MSN particles influences the corona formation in time, we studied 3 different types of nanoparticles with different zeta potentials: amino-functionalized MSNs (MSN1 – ζ =-9mV); and two MSNs where the amino-groups were carboxylated to different extents (MSN2 – ζ =-29mV and MSN3 – ζ =-38mV).

Figure 2.12a shows representative dSTORM images of nanoparticles of each type after being incubated for 1 hour with 10 mg/mL BSA solution (1mol% labeling). dSTORM imaging proved a clear correlation between the number of proteins adsorbed and the surface charge of the NPs. The presence of carboxylic acids surface groups implies a more negative zeta potential but also a more hydrophilic nature, reducing protein adsorption to MSN2 and MSN3 particles in comparison to MSN1 particles. Figure 2.12b shows the quantification of protein adsorption for each particle type over time. At the 1 minute time point the number of proteins detected was very low for the three studied NPs. However, after 1 hour MSN1 adsorbed significantly more proteins than MSN2 and MSN3 (pvalues<0.0001). MSN1, as described before, showed a very heterogeneous distribution. These results are in good agreement with the literature, which shows that nanoparticles with positive surface charge adsorb more proteins (e.g. BSA molecules) than negatively charged particles[24,47]. Interestingly, also for

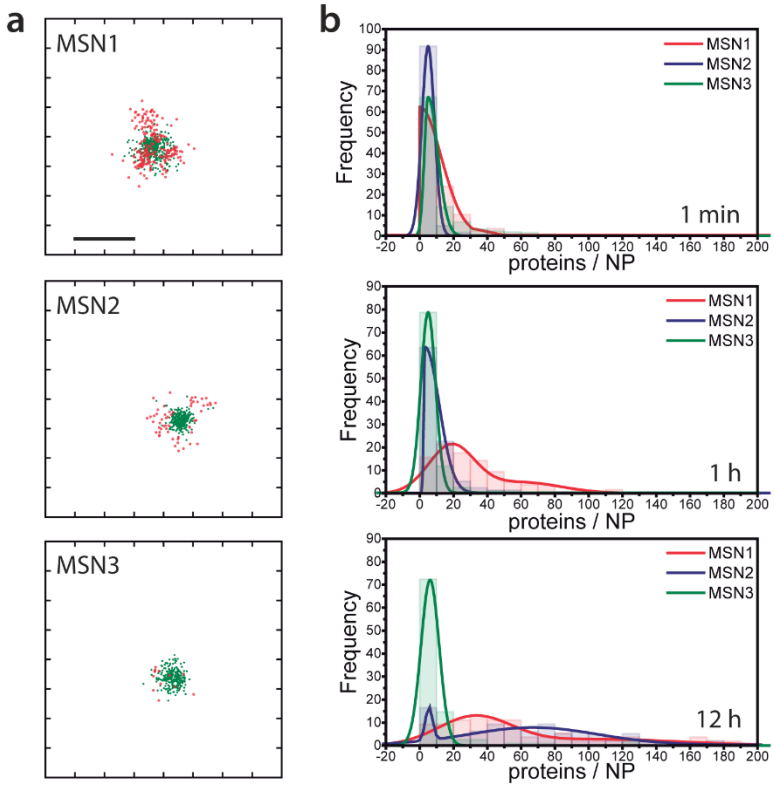

Figure 2.12 Surface charge strongly influences corona composition. Comparing protein corona formation between NPs with different surface charges. All 3 types of NPs were incubated at 37ºC with 1%mol BSA-Cy5 in a 10 mg/mL BSA solution during 1 minute, 1 hour and 12 hours and the complexes obtained were imaged in situ. **a.** Images of MSN1, MSN2 and MSN3 after incubation with BSA for 1 hour. Scale bar: 200 nm. **b.** Distribution of the number of labelled-BSA molecules detected in each NPs type at 1 min, 1 hour, 12 hours (top to bottom). Distributions are fitted to single or double Gaussians. Distributions are normalized to the total number of nanoparticles quantified in each condition to simplify the comparing.

MSN2 a dramatic change in protein adsorption behavior was observed after 12h of incubation in the direction of a very heterogeneous population with larger coronas. After 12h MSN1 and MSN2 displayed a similar behavior while MSN3 still showed a negligible increase in the number of adsorbed proteins. We therefore hypothesized that the particle underwent changes in their chemistry over time influencing the extent of the protein adsorption.

Figure 2.13a shows the zeta potential evolution of the three particles measured in protein-free HEPES buffer as a function of time. Notably, all particles showed a relatively rapid change in zeta potential towards less negative values during the initial hours of incubation. However, while the zeta potential values measured for MSN1 and MSN2 after 3 days of incubation reached very similar values of about 11 mV, the zeta potential of MSN3 remained strongly negative during the whole course of the experiment. We propose that this change is

related to the degradable nature of silica materials which leads to detachment of some of the silane molecules, and/or to time-dependent changes in the degree of counter-ion adsorption. Strikingly, the evolution of zeta potential in time of the three nanoparticles followed the same trend than the change in the protein adsorption behavior as shown in Figure 2.13b. As an example, only when the zeta potential of MSN2 raised towards neutral we observed an increase in the protein corona. While MSN3 maintained a pronounced negative zeta potential within the whole observation window, and consistently exhibited a low extent of protein adsorption. These results indicate that the formation and dynamics of the protein corona strongly depend on the surface charge and that changes in the surface chemistry of the nanoparticles due to hydrolysis clearly affect the composition of the corona. We anticipate that this phenomenon will affect not only the amount of biomolecules adsorbed but also the relative affinity for different serum proteins. We highlight for the first time that changes in corona composition occur over time due to the degradation of the nanoparticle surface adding a further element of complexity towards increased understanding of the biological identity of nanomaterials. The alteration of the NP surface chemistry with time introduces a further factor of heterogeneity to the corona formation – i.e. a dynamic heterogeneity. We speculate that this is a general phenomenon for degradable particles and suggest that the evolution of the properties of resorbable nanoparticles should be taken into account when studying biomolecular corona formation.

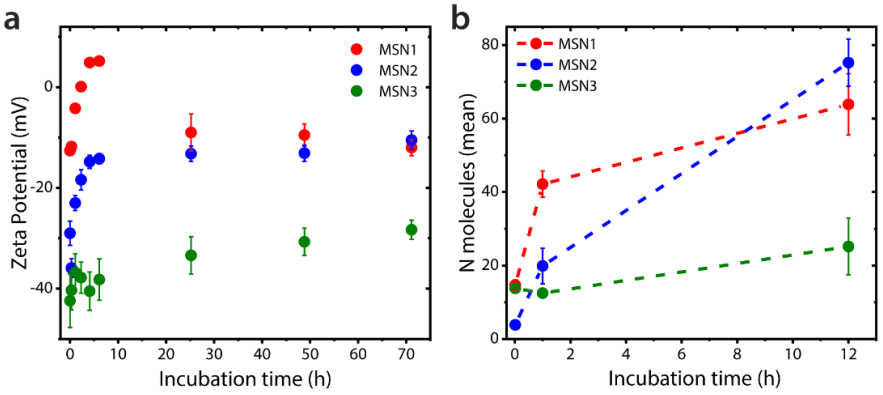

Figure 2.13. Changes on surface charge over time guides changes in protein corona. a. Changes in zeta potential for each type of NP as a function of time in aqueous solution. **b.** Kinetic of corona formation in each nanoparticle type, the mean of the distribution is represented ± Standard Error (S.E.).

2.6. Evolution of the protein corona composition

The blood serum comprises thousands of distinct proteins that compete for binding to the nanoparticle surface. The establishment of the protein corona depends on both the affinity

and the abundance of individual serum components. It has been proposed that most abundant proteins (e.g. albumin) are absorbed first but in time displaced by proteins with higher surface affinity[8,12,13,48,49]. However, a recent report using proteomic analysis showed that the corona is qualitatively established within minutes and its composition (i.e. the ratio of the different proteins) does not change in time for several types of nanoparticles[11]. The understanding of this controversial issue is of great importance for the control of nanoparticle behavior in vivo. Here, we made use of our STORM methodology to investigate the time-dependent changes in protein corona composition. We therefore incubated MSNs with serum containing a specific labelled protein (10%mol of the physiological serum concentration: i) BSA at 10 mg/mL, ii) Transferrin (Tf) at 3 mg/mL, iii) Fibrinogen at 1 mg/mL and iv) Immunoglobulin G (IgG) at 10 mg/mL) and acquired dSTORM images at two different time points (1 minute and 1 hour). This method allowed us to follow single protein species in a complete serum medium (fetal bovine serum, FBS) with single molecule and single particle sensitivity. Therefore, it represents an ideal complement to the high throughput proteomic methods. Albumin, fibrinogen, IgG and transferrin were chosen because of their high concentration in blood, their biological relevance (e.g. binding to transferrin receptor, or activation of immune system) and their reported affinity for silica nanoparticles[50–53].

Figure 2.14 shows the dynamic changes in the corona composition of MSN2 in time indicating an interplay between fast-adsorbing and strongly-adsorbing species. BSA molecules adsorbed on the surface of MSN2 at short exposure times, but their concentration significantly decreased (pvalue<0.0001) after one hour of incubation. This supports the idea that abundant serum proteins are the first interacting with nanoparticles after injection, which is accepted by the community. In contrast, the mean number of transferrin molecules adsorption increased with exposure times indicating a stronger affinity for the MSN2 surface than those of BSA. It is worth mentioning that the analysis of individual nanoparticles instead of the full population studied (see the histogram of frequency in Figure 2.14) indicated the

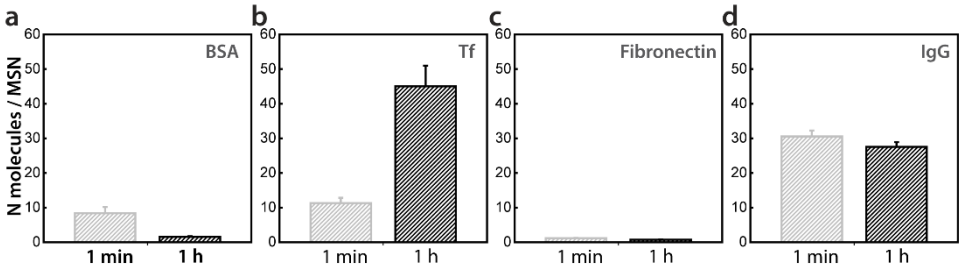

Figure 2.14. Dynamics of protein corona in full serum. The composition of the protein corona was studied at 2 different time points to understand the dynamics of its formation. **a.** BSA, **b.** Tf, **c.** Fibrinogen and **d.** IgG were labelled and incubated separately with MSN2 at 37ºC in full serum (FBS) to study the dynamics of each protein in blood-mimic medium. Bars indicate the mean number of molecules detected after 1 minute and 1 hour of incubation for each protein type; BSA, Tf, Fibrinogen, IgG (from left to right). Error bars represent the S.E.

increase in the mean value is mostly due to a low percentage of nanoparticles which displayed a very high adsorption of transferrin, while most of the nanoparticles had little or none. These observations highlight the importance of studying corona formation on a single-particle basis and again points towards a heterogeneity in protein corona formation which may lead to different behavior *in vivo*.

Lastly, the concentrations of fibrinogen and IgG remained largely constant over time, having a low adsorption of fibrinogen molecules and a higher number of IgG molecules per nanoparticle. Similar kinetic trends were observed for MSN1 and MSN3 as shown in Figure 2.16 where the adsorption of BSA, Transferrin and Fibrinogen in full media was studied. Fibrinogen, despite being one of the most abundant proteins in blood, displayed low

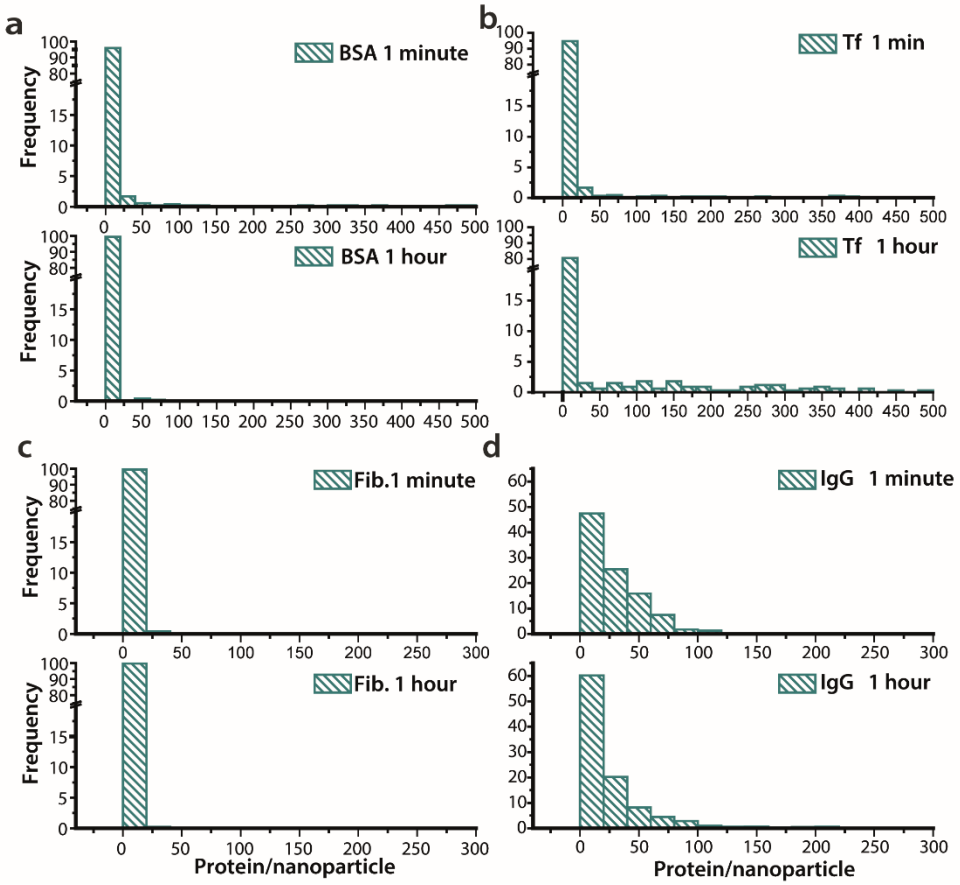

Figure 2.15 Heterogeneity of protein corona formation in full serum. The composition of the corona was studied at two different time points to understand the dynamic of its formation. 10%vol labelled BSA, Tf, Fibrinogen or IgG in full FBS with MSN2 for one minute and one hour and STORM images were acquired. Histograms show the number of the specific labelled protein detected in each condition **a.** BSA **b.** Transferrin **c.** Fibrinogen **d.** IgG. Data were normalized for the total number of nanoparticles quantified.

adsorption. This feature is in agreement with previous studies which revealed that fibrinogen binds to NPs only under less competitive conditions (e.g. 10% FBS)[53] and it is displaced by other proteins in full serum. On the contrary, Tf and Immunoglobulins are reported to have high affinity[53] resulting in higher adsorption under competitive conditions. It is worth noting that the high abundance of Tf could be advantageous to target cancer cells, due to the fact that multiple cancer types overexpress Tf receptors at early stages of cancer progression[54].

These results resemble previous observations on the binding competition occurring during the corona formation where more abundant proteins adsorbed first but are later displayed by proteins with high affinity[48]. Nevertheless, the dynamic composition changes detected in this work are probably due not only to the binding competition between the different species but also to the degradation of the particles over time we previously demonstrated (Figure 2.13). The combination of all these phenomena results in a complex and heterogeneous evolution of the nanoparticle biological identity which is important to determine to rationally design effective systems.

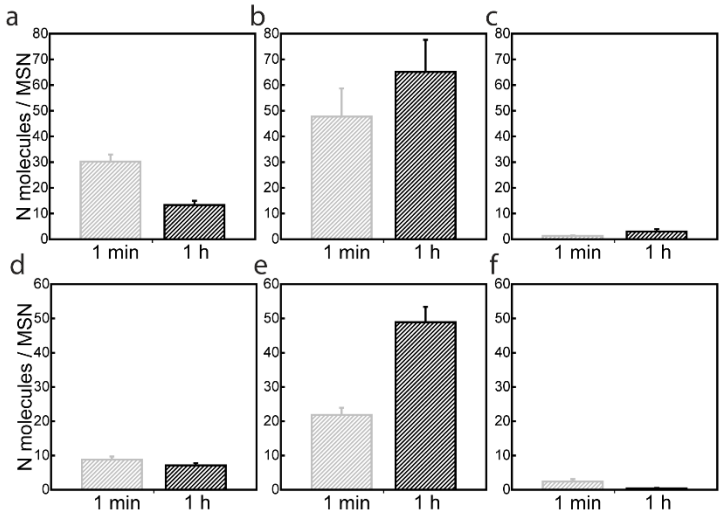

Figure 2.16 Protein corona composition changes in time. The composition of the protein corona was studied at 2 different time points to understand its dynamic formation. BSA, Tf and Fibrinogen were labelled and incubated separately with MSN1 (a,b,c) or MSN3 (d,e,f)at 37ºC at a concentration of 10%vol in full serum (FBS) to study the dynamic of each protein in a complete serum media to mimic blood. Mean number of molecules detected per nanoparticles after incubation with a. and d. BSA b. and e. Transferrin c. and f. Fibrinogen

2.7. Proteins adsorbed to NPs affect their targetability

The ability of functional nanomaterials to target specific cell types is of utmost importance in nanomedicine. Recent studies showed a strong effect of protein adsorption on nanoparticle

selectivity towards different cell types[26,55–57]. The protein corona may shield NPs functionalities, reduce cell selectivity[55,57] and influence cell uptake efficiency and kinetics[5,56]. Therefore, it is of major importance to study the uptake of nanoparticles in presence of serum and to understand the effects of corona formation on NPs internalization by the cell.

In the present study, we correlated the results from our super-resolution investigation of the protein corona with the targeting capabilities of antibody-functionalized mesoporous silica nanoparticles. Interestingly, we first observed that corona formation was influenced by the presence of antibodies (Ab) on the NP surface. Figure 2.17a shows a comparison of protein adsorption on MSN2 and MSN2 functionalized with an antibody to confer targeting properties (Ab-MSN2) after 1 hour of incubation with 10%v/v BSA-Cy5/FBS. The Ab-MSN2s adsorbed about twice the amount of BSA due to the physicochemical changes of the surface induced by the presence of the large targeting ligand (e.g. change of zeta potential: ζMSNB220= -17.8 mV, ζMSN2 = -29 mV). These results proved the importance of studying the corona formation directly on the biologically relevant-nanoparticles; because changes in the surface composition upon functionalization can strongly affect the corona formation. In parallel, we studied the loss of Ab over time, we hypothesized the biodegradable nature of the MSN surface may induce changes in the number of Ab per MSN in time. We functionalized MSNs particles with an Alexa488-labelled Ab and we quantified with dSTORM the amount of Ab attached to the nanoparticles as a function of incubation time. Figure 2.17b shows a minimal loss of Ab during the first 12 hours (around 10%) which became more significant (up to 40%, pvalue<0.0001) after 18 hours of incubation.

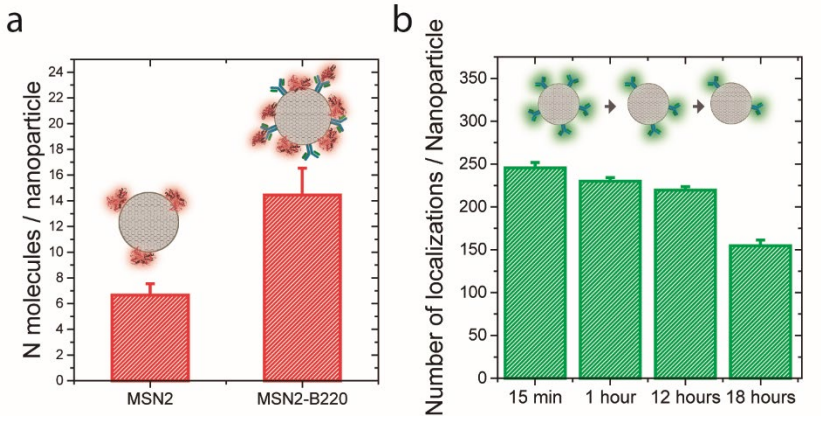

Figure 2.17 Influence of Ab functionalization on protein corona formation in MSN2 particles. (a) Comparison of the BSA protein corona formed (10% labelled-BSA in FBS) after 1 hour of incubation between functionalized (right) and non-functionalized MSN2s (left) in 10%BSA/FBS. (b) Antibody detachment kinetics for MSN2 in fetal bovine serum (FBS) due to degradability of the nanoparticles.

The formation of a significant corona together with the loss of the Ab foreboded a serum-induced effect on targetability. To verify this hypothesis, we compared the targeting ability of Ab-functionalized MSN2 particles pre-incubated with serum for different amounts of time, as schematically shown in Figure 2.18a. Specifically, we measured the ability of MSN2 to target leukemia cells when functionalized with an antibody against B220 (anti-human/mouse B220, 60% cells positive), an antigen overexpressed in B cells during lymphoproliferative disorders[c].

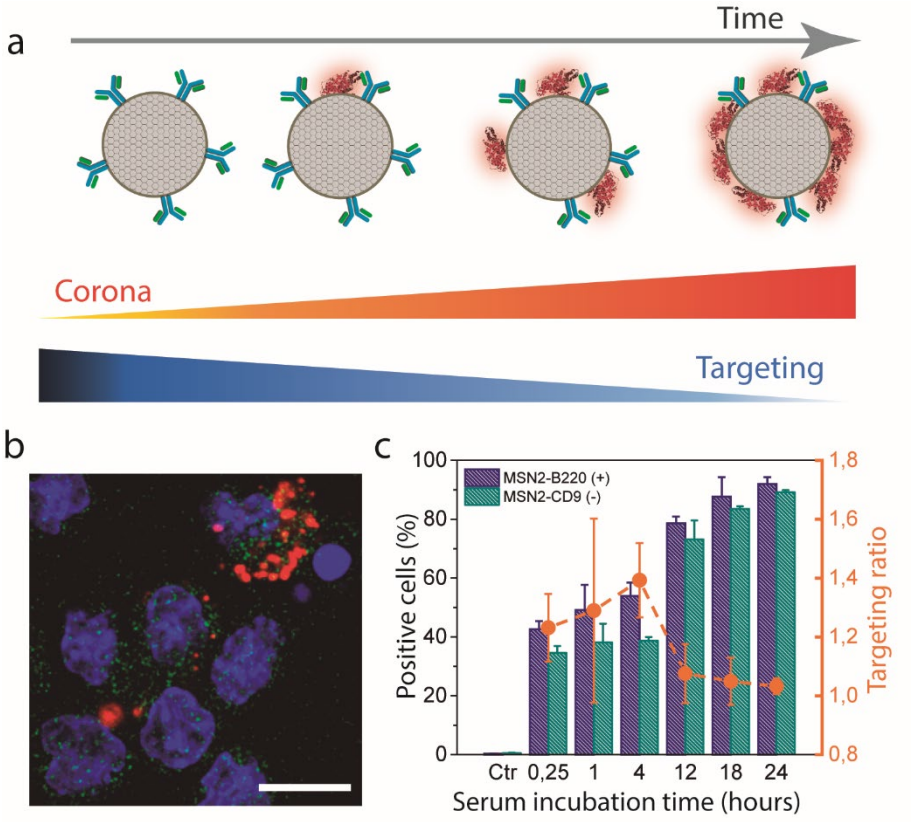

Figure 2.18 Influence of protein corona formation on the selectivity of Ab-functionalized MSN2 particles. a. Schematic representation of the corona formation over functionalized MSNs in time and its consequences for their targeting ability. b. Representative image of MSN2-B220 nanoparticles taken up by CALM/AF10 cells (B cells) after 12 hours, nucleus is shown in blue, eGFPs proteins in green (indicating CALM/AF10 gene positive) and MSNs in red. Scale bar = 10 μm. e. Quantification of MSN2-B220 and MSN2-CD9 taken up by cells after being pre-incubated different times with serum to mimic different states of the corona formation (left axis) and targeting ratio of the MSN2-B220, calculated by dividing the percentages of cells with MSN2-B220 and MSN2-CD9. Both experiments were carried out independently.

[c] Targeting studies were performed by T. Mandal in University Hospital Ulm, Germany.

As a control, we studied the same particle functionalized with less specific Ab against murine CD9 (anti-human CD9, 10% cells positive). MSN2-B220 were taken up in murine B cells (see confocal microscopy image in Figure 2.18b) and a quantification of nanoparticles internalized or strongly bound to the membrane, performed by means of flow cytometry, as shown in Figure 2.18c. The uptake of both NPs raised with increasing serum pre-incubation time, suggesting that the new biological identity of the NPs improved their level of cellular uptake. Moreover, the targeting ratio, i.e. the ratio between the specific internalization of MSN-B220 versus the non-specific uptake of MSN-CD9, decreased dramatically after 12h of pre-incubation in serum when the two NPs show the same uptake efficiency, i.e. complete loss of selectivity. It is striking that the decrease of targeting efficacy occurred at 12 hours, as we previously showed a strong increase in protein adsorption on MSN2 at that time point (see Figure 3d). This suggests that serum proteins covered the surface of the MSNs hiding the Ab and making the targeting ligand ineffective. This is crucial information for the *in vivo* use of such nanosystems, providing information about the "targeting lifetime" in serum, i.e. the time during which the NPs retain their targeting ability, and offering design rules for novel and more effective NPs. An interesting perspective is the synchronization of the *in vivo* circulation time of the NPs with the "targeting lifetime" that will maximize selective localization over non-specific detrimental accumulation in healthy tissues.

2.8. Conclusions

In the present Chapter, a new method based on dSTORM super-resolution imaging has been presented to investigate the interactions between silica nanoparticles and serum proteins at the single particle level with nanometric accuracy. Despite here we focused on the study of protein corona formation on silica nanoparticles, the method is widely applicable to both organic and inorganic materials. However, plasmonic materials such as gold may quench fluorescence, therefore, special considerations should be taken when working with these types of nanomaterials. The ability of our methodology to measure inter-particle variability allowed us to unveil heterogeneity in corona formation over time and to relate it to the surface chemistry and degradability of the nanoparticles studied. We speculate that small initial differences in surface chemistry among particles could lead to different protein adsorption amplifying particle diversity and resulting in the co-existence of particles with very different protein layers. This heterogeneity dramatically increased in time and it was enhanced by particle degradability. We showed the relevance of corona formation for nanoparticle cancer cell targeting, showing the importance of understanding these phenomena to design targeted nanoparticles, a key issue of nanomedicine[1]. Super-resolution microscopy represents a complementary tool to the current ensemble techniques for the study of protein corona formation.

2.9. Perspectives

2.9.1. Versatility of dSTORM protein quantification

The versatility of the method developed in this Chapter allows to study the protein corona formation on a variety of other nanocarrier types. Following the previous studies, we investigated the protein corona formation on lipid nanoparticles (Quatsomes[58]) and polymeric nanoparticles (PEG-PLGA-based). Full serum was used to investigate the possibility to follow the overall growth of the protein corona in time. Figure 2.19 shows the number of localizations corresponding to the serum proteins detected per nanoparticle after few minutes or 1 hour for each particle type. We can observe that in the case of lipidic nanoparticles (Figure 2.18a) the amount of proteins attached is lower compared to the polymeric NPs and that protein corona did not grow in time. In contrast, the amount of protein adsorbed to polymeric nanoparticles increased significantly after 1 hour of incubation. Overall, we demonstrate the possibility to use dSTORM image to understand and quantify the protein corona formation in time for different nanoparticle types.

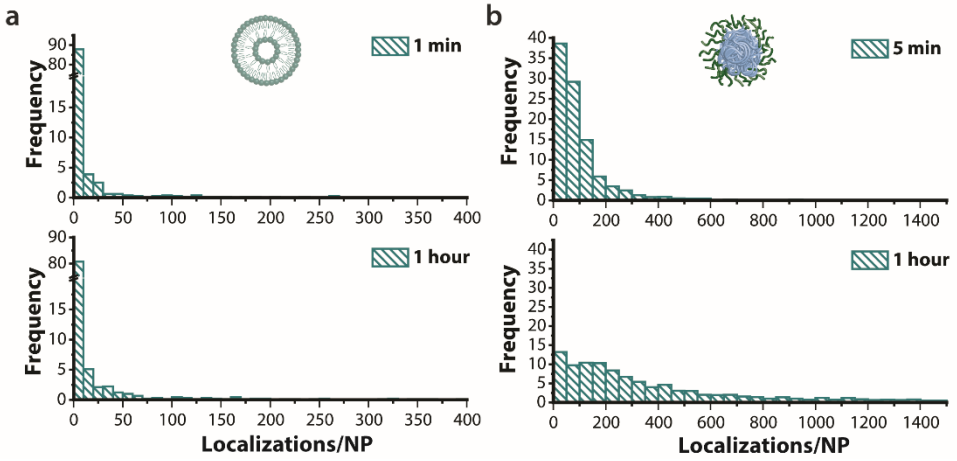

Figure 2.19 Protein corona formation on lipid NPs and polymeric NPs. a. Histogram of frequency of number of protein localizations detected per lipidic nanoparticle. Quatsomes were incubated with 1%FBS-Cy5/FBC v/v for 1 minute and 1 hour. b. Histogram of frequency of number of protein localizations detected per polymeric nanoparticle. PLGA-PEG nanoparticles were incubated with 1% FBS-Cy5/FBS v/v for 5 minutes and 1 hour.

2.9.2. Dynamic environment affects corona formation

An important difference between *in vitro* and *in vivo* is that the nanoparticles are exposed to the serum under flow upon injection while most of the *in vitro* corona experiments fail to recapitulate this. Studies have recently showed differences in number and molecule species forming the protein corona of nanocarriers under flow[59,60]. To verify this, we quantified the amount of proteins adsorbed to the surface of nanoparticles when incubated in static

conditions compared to dynamic conditions, using a fluidic system to mimic blood flow. In figure 2.19 the results obtained after 30 minutes of incubation proved a small but significant difference between the adsorption of serum proteins in the two conditions. Similarly to previous literature reports, the number of proteins localized in the protein corona under flow were lower than the static one. This preliminary data demonstrates the importance of testing our nanosystems using more realistic conditions in order to predict more accurately the *in vivo* behavior. We envision future experiments to characterize the molecular diversity of adsorbed proteins in dynamic or static environments to help in the rational design of stealth's carriers.

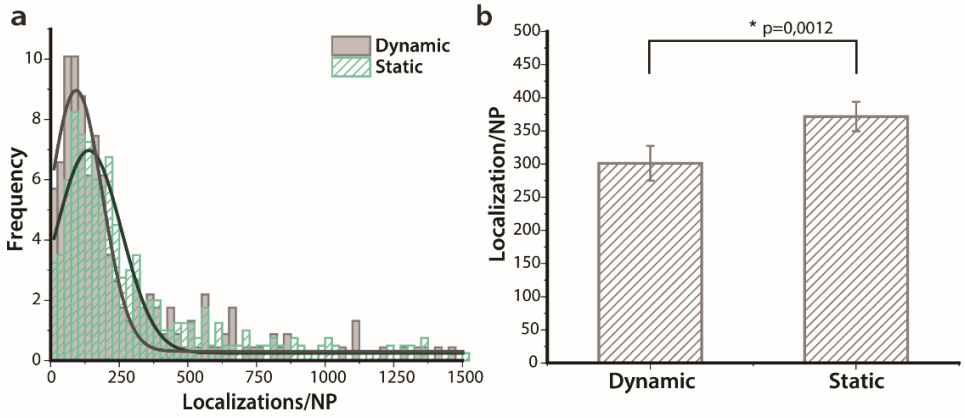

Figure 2.20 Different protein corona formation occur in dynamic enviroment. For dynamic conditions MSN were flow througth a PTFE tubing and mixed using a cross conector with 10% FBS-Cy5/FBS v/v at continous flow of 250 µL/min mimicking blood flow for 10 minutes. a. Frequency histogram of number of localizations per MSN compring dynamic vs static conditions. b. Mean number of localizations ±S.E.

2.9.3. Characterization of heterogenous protein corona using CLEM

The heterogeneity in the protein corona formation revealed in the present study suggest a single nanoparticle batch does not contain a monodisperse population of particles, but a rather polydisperse one. We hypothesis that polydispersity in the physiochemical properties of the nanoparticles may be leading to distinct interactions with serum proteins resulting in a heterogenous corona formation. Therefore, it is of interest to understand which features are the responsible of the diversity, in order to predict the population of nanocarriers with high chances to succeed in the clinic. To further investigate this, we propose the use of correlative light and electron microscopy (CLEM). We believe electron microscopy can give insights on the nanoparticles' size, shape and surface morphology, which may be correlated to a heterogenous number of proteins, detected using fluorescence microscopy. Here, we exploited the possibility to obtain CLEM images of mesoporous silica nanoparticles

interacting with serum proteins using AiryScan and Scanning Electron Microscopy (SEM). Figure 3.20 demonstrates the potential use of this technique to further investigate on the origin of the protein corona heterogeneity. The fluorescence of both the MSN (in green) and the protein (magenta) can be detected, and the morphology of the nanoparticle can be observed in the SEM image. Future experiments will be performed to correlate the fluorescence intensity with morphological differences of each nanoparticle and determine those physicochemical properties more relevant on the protein corona formation.

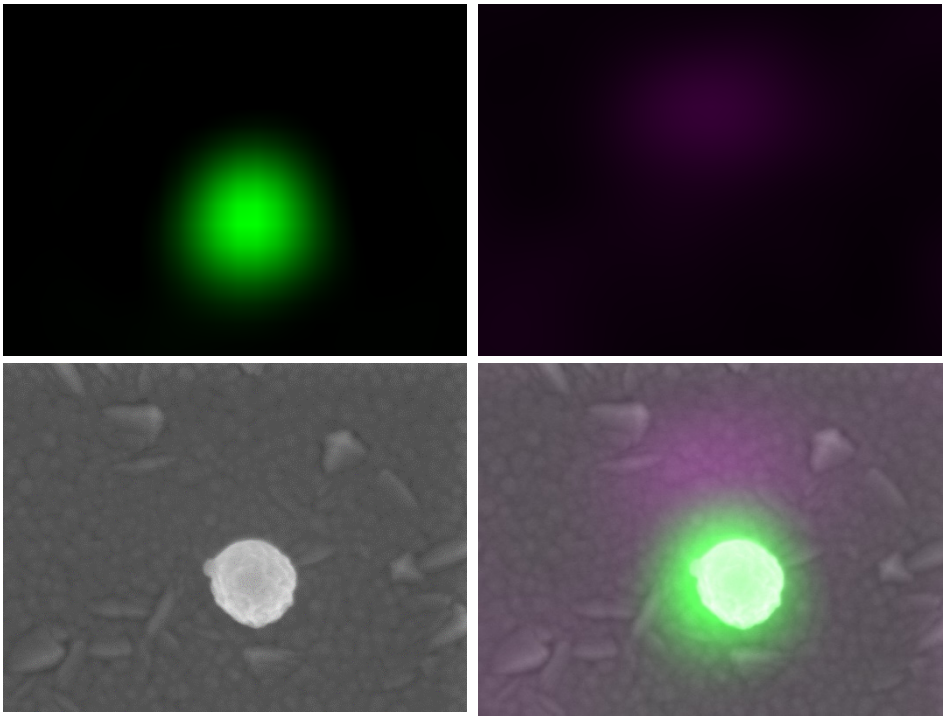

Figure 2.21 CLEM imaging of protein corona formation on MSN. MSN (green) were incubated with 10% FBS-Cy5/FBS (magenta) O/N. Samples were prepared using the same protocol than dSTORM imaging but adsorbed to an ITO coated glass coverslip. First Airy-Scan Imaging was performed, following by air-drying of the sample and SEM imaging. The images were correlated manually.

2.10. Experimental section

2.10.1. Nanoparticles synthesis, functionalization and characterization

Synthesis. Particles (MSN1) were synthesized according to literature.[32] Cetyltrimethylammonium bromide (CTAB) (7.9 g; 21.6 mmol) was dissolved in a solution of methanol (640.0 g; 20.0 mol), water (962.3 g; 53.5 mol) and caustic soda (2.3 mL; 2 M; 4.6 mmol). Tetramethoxysilane (TMOS) (2.2 mL; 14.8 mmol) and 3-aminopropyltrimethoxysilane (APTMS) (360.0 μL; 2.1 mmol) were mixed under inert conditions and added to the solution

while stirring (500 rpm). Reaction mixture was stirred for 45 min at 500 rpm and 24 h at 300 rpm at room temperature and particles were separated via centrifugation. Surfactant removal was performed via three times extraction with ammonium nitrate in ethanol (6 g L-1) for 1 h in an ultrasonic bath. Particles were washed three times with ethanol afterwards and dried overnight at 60 °C. Succinic anhydride functionalization (to obtain MSN2 and MSN3) was performed in dry ethanol at room temperature. Therefore, amino functionalized particles (MSN1) were dried in vacuum at 80 °C for 3 h prior to functionalization. The dried particles were dispersed in ethanol (15 mg mL-1) and a solution of succinic anhydride in ethanol (MSN2: 40.0 μg mg-1; 0.4 mmol g-1; MSN3: 400.3 μg mg-1; 4 mmol g-1) was added. After 24 h of continuous shaking at room temperature the particles were separated via centrifugation, washed three times with ethanol and dried in vacuum for 24 h at room temperature.

Functionalization. Particles were labelled either with Alexa Fluor® 488 (for STORM imaging) or ATTO 594 (for in vitro analysis). Therefore, particles were dispersed in HEPES buffer solution (pH 7.2; 25 mM) (20.0 mg mL-1) and either a solution of Alexa Fluor® 488 tetrafluorophenyl ester (1.0 μg mg-1; 1.1 nmol mg-1) or ATTO 594 NHS ester (1.8 μg/mg particles; 1.3 nmol mg-1 particles) in DMSO (1 mg mL-1) was added. After a reaction time of 30 minutes the particles were separated via centrifugation, washed twice with ethanol and dried overnight in vacuum at room temperature.

Antibody functionalization (MSN2-B220, MSN2-CD9) was performed in HEPES buffer solution (pH 7.2; 25 mM) by EDC and NHS coupling. The COOH groups of the antibodies anti-human/mouse CD45R (B220), anti-human CD9 and anti-human/mouse CD45R (B220) labelled with Alexa Fluor® 488 was activated by suspending the antibody in HEPES buffer solution (pH 7.2; 25 mM) (10 μg mg-1; 20 μg mL-1) followed by the addition of N-hydroxysuccinimide (NHS) (2,3 mg mL-1; 19,9 μmol mL-1) and N-(3-dimethylaminopropyl)-N′-ethylcarbodiimide (EDC) (3.4 μL mL-1, 19.2 μmol mL-1). After 30 minutes of rotation at room temperature a dispersion of MSN2 in HEPES buffer solution (pH 7.2; 25 mM) (2 mg mL-1) was added and rotated for another 90 minutes. Particles were washed twice with HEPES buffer solution (pH 7.2; 25 mM) and directly used without further drying steps.

Characterization. For dynamic light scattering and zeta potential measurements particles were dispersed in HEPES buffer solution (pH 7.2; 25 mM) (100 μg mL-1) in a focused ultrasonicator (Covaris, USA) for 10 minutes prior to analysis. Measurements were performed on a Zetasizer Nano-ZS ZEN 3600 (Malvern Instruments, Germany).

Transmission electron microscopy imaging was performed on a JEM-1400 (Jeol, Japan) with a working voltage of 120 kV.

To compare antibody functionalized particles and particles without Ab, MSN1, MSN2 and MSN3 were treated the same as during the functionalization step (90 min incubation in HEPES at room temperature; 1 mg mL-1) prior to dissolution studies. Dissolution studies of

MSN2-B220, MSN1, MSN2 and MSN3 were performed in DMEM + 15 % FCS at 37 °C, particles were dispersed (100 μg mL-1). Silicon concentration in the supernatant was measured via ICP-OES and resulting silica concentration was calculated based on these measurements.

2.10.2. Protein labelling

The proteins were dispersed in Sodium Bicarbonate (pH=8.5, Sigma Aldrich) at different concentrations depending on the protein: BSA at 10 mg mL-1 (Bovine Serum Albumin from Sigma Aldrich,purity ≥96%), Tf at 3 mg mL-1 (Human Transferrin from Sigma Aldrich, purtity ≥95%), IgG at 10 mg mL-1 (IgG from Human Serum from Sigma Aldrich, purity ≥98%) and Fibrinogen at 1 mg mL-1 (Fibrinogen from Human plasma from Sigma Aldrich, purity 50-70% protein) following by the addition of 1.5 eq. of Cy5-NHS (Lumiprobe). All the reactions were shaken at 300 r.p.m. for 4 hours at room temperature. The proteins were then dialyzed with 1kDa pore size (Spectrum Lab) against PBS pH= 7.4 during 24 hours. The concentration of dye per protein was then quantified using a Nanodrop ND-1000 Spectrophotometer, by measuring the adsorption at 280 nm (protein) and 650 nm (dye), to be 1.09 molecules Cy5/molecule BSA, 1.46 molecules Cy5/molecule Tf, 1.53 molecules Cy5/molecule IgG and 1.85 molecules Cy5/molecule Fib.

2.10.3. Protein corona formation

To study the protein corona formation MSNs were dissolved in DMSO at a concentration of 1 mg/mL and sonicated in a bath sonicator during 5 minutes to disperse the particles. Then MSNs were dissolved in a pre-warmed protein solution (final MSNs concentration 100 μg mL-1), gently mixed, and incubated at 37ºC for the desired time (from 1 minute to 12 hours depending on the experiment).

The protein solutions used were solutions of single BSA (10 mg mL-1) or full fetal bovine serum (FBS, Thermo Fisher), with a percentage of a labelled protein depending on each experiment. Specifically, for the experiments studying the time evolution of the protein corona and the influence of the surface chemistry on the formation of the corona, the solution used were 1%mol BSA-Cy5/BSA (10 mg mL-1). While for the studies of the corona composition the solutions used were 10% BSA-Cy5/FBS v/v (BSA at 10 mg mL-1, 100% FBS), 10% Tf-Cy5/FBS v/v (Tf at 3 mg mL-1, 100% FBS), 10% IgG-Cy5/FBS v/v (IgG at 10 mg mL-1, 100% FBS), 10% Fibrinogen-Cy5/FBS v/v (Fibrinogen at 1 mg mL-1, 100% FBS).

In some experiments, those where FBS was used, the non-attached proteins were removed by washing 3 times by centrifuging the mixture at 16,100 g for 5 minutes and redispersing the NPs-complexes with PBS (pH 7.4).

For protein quantification, a Pierce™ BCA Protein Assay Kit (from Thermo Fisher) was used following the enhanced protocol described in the kit, together with the protocol of

Monopoli et. al. [60] MSN2 were incubated with 10% BSA-Cy5/FBS v/v and 10% BSA/FBS v/v for 1 hour at 37ºC, following 3 washing steps consisting on 5 min centrifugation at 16100 g and redispersion of the pellet in PBS to obtain the complexes hard corona-MSN. Samples were mixed with the Working reagent (A:B, 50:1) at a ratio 1:15 and incubated at 60ºC for 30 minutes. The samples were then cooled at RT for 45 minutes and centrifuged 5 minutes at 16100g. The absorbance of the supernatant was measured at 562 using an Infinite M200 PRO Multimode Microplate Reader from Tecan.

2.10.4. Kinetic of antibody detachment

The loss of the antibodies present in the nanoparticles due to the degradation of the particles was determined in full FBS media. MSN2-B220-Alexa488® (100 μg mL-1) were incubated at 37ºC in complete FBS for different time points (15 minutes, 1 hour, 12 hours and 18 hours) and then the samples were imaged under STORM microscope (see protocol below). The change in the number of localizations upon increasing incubation times was analyzed.

2.10.5. STORM sample preparation and imaging

To perform direct STORM (dSTORM) imaging NP-protein complexes, or NP alone, were immobilized by adsorption onto the surface of a flow chamber assembled from a glass slide and a coverslip (24mm x 24 mm, thickness 0.15 mm) separated by double-sided tape. After being incubated for 10-15 minutes unbound complexes and proteins were removed by washing the chamber twice with PBS. Then, TetraSpeck™ Microspheres (0.1 μm, Life Technology) were added and immobilized by adsorption onto the surface to correct the drift during acquisition. Finally, non-adsorbed TetraSpeck™ Microspheres were removed by washing the chamber twice with STORM buffer. STORM buffer contains PBS, an oxygen scavenging system (0.5 mg mL-1 glucose oxidase, 40 μg mL-1 catalase), glucose (5% w/v) and cysteamine (100 mM).

STORM images were acquired using a Nikon N-STORM system configured for total internal reflection fluorescence (TIRF) imaging. Cy5 labelled proteins were imaged by means of a 647nm laser (160 mW) and MSNs-Alexa488 were imaged by means of a 488nm (80 mW). The TetraSpeck™ Microspheres were imaged by a 561nm laser (80 mW). No activation UV light was employed. Fluorescence was collected by means of a Nikon 100x, 1.49 NA oil immersion objective and passed through a quad-band pass dichroic filter (97335 Nikon). Images were acquired onto a 256x256 pixel region (pixel size 0.16μm) of a Hamamatsu ORCA-Flash 4.0 camera at 10 ms integration time. For the protein corona measurements 20,000 frames were acquired for the 647 channel and 10,000 frames for the 488 channel, the total time required to acquire one image was about 5 minutes. And for the antibody losing measurements 20,000 frames were acquired for the 488 channel. In both experiments every 100 frames a frame for the 561 channel (drift correction) was acquired. The absence of background localization was checked recording images of NPs with unlabeled proteins (see

Figure S143). STORM images were analyzed with the STORM module of the NIS element Nikon software.

2.10.6. Data analysis

During STORM-imaging, the NIS elements Nikon software generates a list of localizations by Gaussian fitting of blinking dyes in the acquired movie of conventional microscopic images. This analysis takes around 2 minutes per image, and can be run in a batch mode. To avoid overcounting blinkings detected in consecutive frames are counted as single by the software. The number of photons per localization was quantified in different conditions to be sure of the reproducibility of the imaging resolution between conditions (see Figure S154). The generated localization list was filtered to remove background due to free protein attached to the glass, by applying a density filter of 50 localization in a radius of 60 nm on both channels together (see Figure S165). The list of filtered localizations was imported and analyzed by a Matlab script we developed to quantify the number of molecules forming the corona of each nanoparticle as well as the size of the complexes. The code is extensively described in supporting material.

The total number of nanoparticles analyzed in each experiment is reported in its corresponding figure capture. The time required to process each image using the Matlab code (extensively described in Supporting Information), goes from seconds to 1-2 minutes per image, obtaining the number of localizations and sizes of both nanoparticles and complexes.

2.10.7. In vitro analysis

B220 positive CALM/AF10 ex vivo murine suspension cells were created according to Deshpande et al. [61] These murine leukemic cell line was derived by single-cell-sorted B220+/Mac1- cells. Cell culture was performed in Dulbecco's modified eagle medium (DMEM) supplemented with 15 % fetal bovine serum (FBS) containing 1 % Penicillin/Streptomycin and recombinant mouse interleukin3 (RMIL310, 10 ng mL-1) at 37 °C with a relative humidity of >80 % and a CO2 level of 5 %.

To study the influence of protein adsorption on the selectivity of antibody conjugated particles, ATTO 594 labelled particles (MSN2-B220 and MSN2-CD9) were incubated for several hours (0.25, 1, 4, 12, 18 and 24 h) in 100 % FCS at 37 °C (1 mg mL-1). The particles/FCS mixture was then diluted with DMEM supplemented with 5.5 % FCS to gain dispersions containing 200 μg mL-1 particles and 15 % FCS. CALM/AF10 ex vivo murine cells were seeded at an initial density of 106 mL-1 and treated with the pre-incubated particle dispersions for 24 h (100 μg particles mL-1). Afterwards the cells were washed with 1x Dulbecco's phosphate buffered saline (DPBS) (w/o Mg2+/Ca2+) containing 0.01 % Tween-20 and twice with DPBS.

Particle uptake was quantified by flow cytometry.Fluorescence activated cell sorting for B220+/Mac1- cells was performed on a BD FACS ARIA II (BD Bioscience, USA) and particle uptake was quantified) on a BD LSRFortessa cell analyzer (BD Bioscience, USA). Analysis of the data was done using BD FACSDiva software v8.0.1 (BD Bioscience, USA).

Confocal laser microscopy was performed on cells treated with ATTO 594 labelled MSN2-B220. An initial density of CALM-AF10 ex vivo cells of 106 mL-1 was treated with ATTO 594 labelled MSN2-B220 (10 μg mL-1) for 24 h. Cells were washed once with DPBS containing 0.01 % Tween-20 and twice with DPBS before fixed with 4 % paraformaldehyde in DPBS for 30 minutes at room temperature. Afterwards cells were washed twice with DPBS and fixed to positively charged slides (Fisherbrand™ Superfrost™ Plus Microscope Slides). The coverslips were mounted with Vectashield® containing DAPI (Vector Labs, USA) and visualized with a Leica TCS SP8 (Leica Microsystems, USA) (Leica Application Suite X (LAS X)).

2.10.8. dSTORM imaging of protein corona on lipid nanoparticles

Quatsomes (QS) were incubated in a BSA-Cy5 solution of 10 mg/mL containing 1% v/v of labelled protein (at 37ºC) for 1 minute and 1 hour. Then, QS were immobilized by adsorption onto the surface of a flow chamber assembled from a glass slide and a coverslip (24mm x 24 mm, thickness 0.15 mm) separated by double-sided tape. After being incubated for 10-15 minutes unbound complexes and proteins were removed by washing the chamber twice with PBS. Then, TetraSpeck™ Microspheres (0.1 μm, Life Technology) were added and immobilized by adsorption onto the surface to correct the drift during acquisition. Finally, non-adsorbed TetraSpeck™ Microspheres were removed by washing the chamber twice with STORM buffer. STORM buffer contains PBS, an oxygen scavenging system (0.5 mg mL-1 glucose oxidase, 40 μg mL-1 catalase), glucose (5% w/v) and cysteamine (100 mM). STORM images were acquired using a Nikon N-STORM system configured for total internal reflection fluorescence (TIRF) imaging. Cy5 labelled proteins were imaged by means of a 647nm laser (160 mW) and DiI-QS were imaged by means of a 561 nm (80 mW). The TetraSpeck™ Microspheres were imaged by a 488 nm laser (80 mW). For the protein corona measurements 20,000 frames were acquired for the 647 channel and 20,000 frames for the 561 channels. The images were analyzed using the NIS Nikon software and proteins quantified using the same Matlab software.

2.10.9. STORM imaging of protein corona on PLGA-PEG nanoparticles

Nanoparticle preparation. Block copolymers PLGA-PEG (PolySciTech AK102, Mw PEG: PLGA 5:30 kDa, L: G in PLGA 50:50. Lot: 50331SMS) and PLGA (PolySciTech AP082, L:G 50:50, acid endcap, Mw. 25–35 kDa. Lot: 70201AMS-A) were used at a ratio 65/35 PLGA-PEG/PLGA. Polymers were dissolved in ACN at a final concentration of 10 mg/mL. DiI was firstly dissolved in Acetonitrile to obtain a 1.1 mM stock solution, which was then added to the solvent phase, reaching a final concentration of about 7.1 μM. Nanoparticles were

prepared using the nanoprecipitation method: 300 μL of solvent phase (polymer solution) was injected dropwise into a solution of 3 mL of anti-solvent phase (aqueous solution) under continuous stirring to provide constant mixing of water (100-200 rpm). The solution was maintained under magnetic stirring for about 5-6 hours to accelerate the solvent extraction. Afterwards the vial was capped, and the sample was stored in the fridge at 4°C until further experiments.

Nanoparticles were diluted 1:100 into a solution of 1%FBS-Cy5/FBS v/v and incubated at 37 ºC for 5 minutes or 1 hour. The complexes where centrifugated 3 times at 16000g for 10 minutes to remove unbound proteins. Then they were immobilized into a glass coverslip and sample preparation and dSTORM imaging performed following the same protocol explained for MSN and lipid-naoparticles. PLGA-PEG nanoparticles were imaged using 561nm laser and FBS-Cy5 proteins using 647 nm laser, while Fiducial Markers for drift correction were imaged using 488 nm laser. 20000 frames of each channel were acquired. NIS elements and the custom-made Matlab software were used to process the images.

2.10.10. Dynamic protein corona formation

MSN2 at a concentration of 0.5 mg/mL were incubated into a solution of 10% FBS-Cy5/FBS v/v for 10 minutes for static conditions. To mimic the dynamic environment of blood flow the solution of MSN2 was loaded into a 1 mL syringe and the solution of proteins into another 1 mL syringe. Each syringe was connected to a PTFE tube of 0.75mm inlet diameter, both tubes were connected using a T connector were the solutions were mixed. Flow was applied using a syringe pump at 250 μL/min mimicking blood flow in arteria. After 10 minutes of continuous flow the MSN2 were collected and purified to separate from unbound proteins washing 3 times by centrifuging the mixture at 16,100 g for 5 minutes and redispersing the NPs-complexes with PBS (pH 7.4). dSTORM imaging was performed as described in section 2.10.5. and analyzed as MSN in static conditions.

2.10.11. CLEM of protein corona on MSN

MSN were incubated O/N at 37°C in continuous agitation with a solution of 10% FBS-Cy5/FBS v/v. The mixture was then centrifugated 3 times at 16,100 g for 5 minutes and redispersed in PBS (pH 7.4). To immobilize the nanoparticles 20 μL of solution was added to an ITO coated glass coverslip where a defined scratch was made to help in the correlation. After 15 minutes the coverslip was washed 3 times with water and mounted into a self-designed low drift magnetic imaging chamber. Airyscan images were acquired using a Zeiss LSM 900, MSN were excited using 488 nm laser and proteins using 633 nm laser. Bright field images of the same field of view were acquired to facilitate the correlation of the images.

After Airyscan images the coverslip were air dried O/N and SEM images where acquired without any coating. SEM imaging was performed in a Zeiss Sigma 300 microscope (Carl

Zeiss AG, Jena, Germany) equipped with the ATLAS 5 external scanner and software (Fibics, Canada) and the shuttle and find option in the Zeiss ZEN Blue software. SEM images were acquired using 3 kV voltage, 7 mm working distance. Big field of view images including the scratch in the coverslip where acquired together with magnified images of individual nanoparticles in order to localize each nanoparticle and facilitate the correlation with the AiryScan images. Both images were manually aligned using ImageJ.

2.11. References

1. Lazarovits, J., Chen, Y. Y., Sykes, E. A. & Chan, W. C. W. Nanoparticle–blood interactions: the implications on solid tumour targeting. *Chem. Commun.* **51**, 2756–2767 (2015).
2. Monopoli, M. P., Åberg, C., Salvati, A. & Dawson, K. A. Biomolecular coronas provide the biological identity of nanosized materials. *Nat. Nanotechnol.* **7**, 779–786 (2012).
3. Schöttler, S., Landfester, K. & Mailänder, V. Controlling the Stealth Effect of Nanocarriers through Understanding the Protein Corona. *Angew. Chem. Int. Ed.* **55**, 8806–8815 (2016).
4. Nel, A. E. *et al.* Understanding biophysicochemical interactions at the nano–bio interface. *Nat. Mater.* **8**, 543–557 (2009).
5. Albanese, A. *et al.* Secreted Biomolecules Alter the Biological Identity and Cellular Interactions of Nanoparticles. *ACS Nano* **8**, 5515–5526 (2014).
6. Mahmoudi, M. *et al.* Protein−Nanoparticle Interactions: Opportunities and Challenges. *Chem. Rev.* **111**, 5610–5637 (2011).
7. Saptarshi, S. R., Duschl, A. & Lopata, A. L. Interaction of nanoparticles with proteins: relation to bio-reactivity of the nanoparticle. *J. Nanobiotechnology* **11**, 26 (2013).
8. Setyawati, M. I., Tay, C. Y., Docter, D., Stauber, R. H. & Leong, D. T. Understanding and exploiting nanoparticles' intimacy with the blood vessel and blood. *Chem. Soc. Rev.* **44**, 8174–8199 (2015).
9. Walkey, C. D., Olsen, J. B., Guo, H., Emili, A. & Chan, W. C. W. Nanoparticle Size and Surface Chemistry Determine Serum Protein Adsorption and Macrophage Uptake. *J. Am. Chem. Soc.* **134**, 2139–2147 (2012).
10. Docter, D. *et al.* Quantitative profiling of the protein coronas that form around nanoparticles. *Nat. Protoc.* **9**, 2030–2044 (2014).
11. Tenzer, S. *et al.* Rapid formation of plasma protein corona critically affects nanoparticle pathophysiology. *Nat. Nanotechnol.* **8**, 772–781 (2013).
12. Göppert, T. M. & Müller, R. H. Adsorption kinetics of plasma proteins on solid lipid nanoparticles for drug targeting. *Int. J. Pharm.* **302**, 172–186 (2005).
13. Barrán-Berdón, A. L. *et al.* Time Evolution of Nanoparticle–Protein Corona in Human Plasma: Relevance for Targeted Drug Delivery. *Langmuir* **29**, 6485–6494 (2013).
14. Kelly, P. M. *et al.* Mapping protein binding sites on the biomolecular corona of nanoparticles. *Nat. Nanotechnol.* **advance online publication**, (2015).
15. Bertoli, F., Garry, D., Monopoli, M. P., Salvati, A. & Dawson, K. A. The Intracellular Destiny of the Protein Corona: A Study on its Cellular Internalization and Evolution. *ACS Nano* (2016). doi:10.1021/acsnano.6b06411
16. Dominguez-Medina, S. *et al.* Adsorption and Unfolding of a Single Protein Triggers Nanoparticle Aggregation. *ACS Nano* **10**, 2103–2112 (2016).
17. Doorley, G. W. & Payne, C. K. Nanoparticles act as protein carriers during cellular internalization. *Chem. Commun.* **48**, 2961–2963 (2012).
18. Clemments, A. M., Botella, P. & Landry, C. C. Spatial Mapping of Protein Adsorption on Mesoporous Silica Nanoparticles by Stochastic Optical Reconstruction Microscopy. *J. Am. Chem. Soc.* **139**, 3978–3981 (2017).
19. Mamaeva, V., Sahlgren, C. & Lindén, M. Mesoporous silica nanoparticles in medicine—Recent advances. *Adv. Drug Deliv. Rev.* **65**, 689–702 (2013).

20. Slowing, I. I., Vivero-Escoto, J. L., Wu, C.-W. & Lin, V. S.-Y. Mesoporous silica nanoparticles as controlled release drug delivery and gene transfection carriers. *Adv. Drug Deliv. Rev.* **60**, 1278–1288 (2008).
21. Datz, S. *et al.* Genetically designed biomolecular capping system for mesoporous silica nanoparticles enables receptor-mediated cell uptake and controlled drug release. *Nanoscale* **8**, 8101–8110 (2016).
22. Owens, G. J. *et al.* Sol–gel based materials for biomedical applications. *Prog. Mater. Sci.* **77**, 1–79 (2016).
23. Rosenholm, J. M. *et al.* Targeting of Porous Hybrid Silica Nanoparticles to Cancer Cells. *ACS Nano* **3**, 197–206 (2009).
24. Clemments, A. M., Muniesa, C., Landry, C. C. & Botella, P. Effect of surface properties in protein corona development on mesoporous silica nanoparticles. *RSC Adv.* **4**, 29134–29138 (2014).
25. Lesniak, A. *et al.* Effects of the Presence or Absence of a Protein Corona on Silica Nanoparticle Uptake and Impact on Cells. *ACS Nano* **6**, 5845–5857 (2012).
26. Fleischer, C. C. & Payne, C. K. Secondary Structure of Corona Proteins Determines the Cell Surface Receptors Used by Nanoparticles. *J. Phys. Chem. B* **118**, 14017–14026 (2014).
27. Winzen, S. *et al.* Complementary analysis of the hard and soft protein corona: sample preparation critically effects corona composition. *Nanoscale* **7**, 2992–3001 (2015).
28. Dempsey, G. T., Vaughan, J. C., Chen, K. H., Bates, M. & Zhuang, X. Evaluation of fluorophores for optimal performance in localization-based super-resolution imaging. *Nat. Methods* **8**, 1027–1036 (2011).
29. Dempsey, G. T. *et al.* Photoswitching Mechanism of Cyanine Dyes. *J. Am. Chem. Soc.* **131**, 18192–18193 (2009).
30. Albertazzi, L. *et al.* Probing exchange pathways in one-dimensional aggregates with super-resolution microscopy. *Science* **344**, 491–495 (2014).
31. Beun, L. H., Albertazzi, L., van der Zwaag, D., de Vries, R. & Cohen Stuart, M. A. Unidirectional Living Growth of Self-Assembled Protein Nanofibrils Revealed by Super-resolution Microscopy. *ACS Nano* **10**, 4973–4980 (2016).
32. da Silva, R. M. P. *et al.* Super-resolution microscopy reveals structural diversity in molecular exchange among peptide amphiphile nanofibres. *Nat. Commun.* **7**, 11561 (2016).
33. Sengupta, P., Jovanovic-Talisman, T. & Lippincott-Schwartz, J. Quantifying spatial organization in point-localization superresolution images using pair correlation analysis. *Nat. Protoc.* **8**, 345–354 (2013).
34. Letschert, S. *et al.* Super-Resolution Imaging of Plasma Membrane Glycans. *Angew. Chem. Int. Ed.* **53**, 10921–10924 (2014).
35. Fukunaga, K. & Hostetler, L. The Estimation of the Gradient of a Density Function, with Applications in Pattern Recognition. *IEEE Trans Inf Theor* **21**, 32–40 (2006).
36. van der Zwaag, D. *et al.* Super Resolution Imaging of Nanoparticles Cellular Uptake and Trafficking. *ACS Appl. Mater. Interfaces* **8**, 6391–6399 (2016).
37. Ehmann, N. *et al.* Quantitative super-resolution imaging of Bruchpilot distinguishes active zone states. *Nat. Commun.* **5**, 4650 (2014).
38. Lee, S.-H., Shin, J. Y., Lee, A. & Bustamante, C. Counting single photoactivatable fluorescent molecules by photoactivated localization microscopy (PALM). *Proc. Natl. Acad. Sci.* **109**, 17436–17441 (2012).
39. Nino, D., Rafiei, N., Wang, Y., Zilman, A. & Milstein, J. N. Molecular Counting with Localization Microscopy: A Bayesian Estimate Based on Fluorophore Statistics. *Biophys. J.* **112**, 1777–1785 (2017).
40. Nair, D. *et al.* Super-Resolution Imaging Reveals That AMPA Receptors Inside Synapses Are Dynamically Organized in Nanodomains Regulated by PSD95. *J. Neurosci.* **33**, 13204–13224 (2013).

41. Yu, S. *et al.* Albumin-coated SPIONs: an experimental and theoretical evaluation of protein conformation, binding affinity and competition with serum proteins. *Nanoscale* **8**, 14393–14405 (2016).
42. Dominguez-Medina, S., McDonough, S., Swanglap, P., Landes, C. F. & Link, S. In situ measurement of bovine serum albumin interaction with gold nanospheres. *Langmuir* **28**, 9131–9139 (2012).
43. Lartigue, L. *et al.* Nanomagnetic Sensing of Blood Plasma Protein Interactions with Iron Oxide Nanoparticles: Impact on Macrophage Uptake. *ACS Nano* **6**, 2665–2678 (2012).
44. Lundqvist, M. *et al.* Nanoparticle size and surface properties determine the protein corona with possible implications for biological impacts. *Proc. Natl. Acad. Sci.* **105**, 14265–14270 (2008).
45. Pederzoli, F. *et al.* Protein corona and nanoparticles: how can we investigate on? *Wiley Interdiscip. Rev. Nanomed. Nanobiotechnol.* **9**, (2017).
46. Docter, D. *et al.* The nanoparticle biomolecule corona: lessons learned – challenge accepted? *Chem Soc Rev* **44**, 6094–6121 (2015).
47. Foroozandeh, P. & Aziz, A. A. Merging Worlds of Nanomaterials and Biological Environment: Factors Governing Protein Corona Formation on Nanoparticles and Its Biological Consequences. *Nanoscale Res. Lett.* **10**, (2015).
48. Cedervall, T. *et al.* Understanding the nanoparticle–protein corona using methods to quantify exchange rates and affinities of proteins for nanoparticles. *Proc. Natl. Acad. Sci.* **104**, 2050–2055 (2007).
49. Cedervall, T. *et al.* Detailed identification of plasma proteins adsorbed on copolymer nanoparticles. *Angew. Chem. Int. Ed Engl.* **46**, 5754–5756 (2007).
50. Hata, K. *et al.* Evaluation of silica nanoparticle binding to major human blood proteins. *Nanoscale Res. Lett.* **9**, (2014).
51. Tenzer, S. *et al.* Nanoparticle Size Is a Critical Physicochemical Determinant of the Human Blood Plasma Corona: A Comprehensive Quantitative Proteomic Analysis. *ACS Nano* **5**, 7155–7167 (2011).
52. Aggarwal, P., Hall, J. B., McLeland, C. B., Dobrovolskaia, M. A. & McNeil, S. E. Nanoparticle interaction with plasma proteins as it relates to particle biodistribution, biocompatibility and therapeutic efficacy. *Adv. Drug Deliv. Rev.* **61**, 428–437 (2009).
53. Monopoli, M. P. *et al.* Physical–Chemical Aspects of Protein Corona: Relevance to in Vitro and in Vivo Biological Impacts of Nanoparticles. *J. Am. Chem. Soc.* **133**, 2525–2534 (2011).
54. Högemann-Savellano, D. *et al.* The Transferrin Receptor: A Potential Molecular Imaging Marker for Human Cancer. *Neoplasia N. Y. N* **5**, 495–506 (2003).
55. Mirshafiee, V., Kim, R., Park, S., Mahmoudi, M. & Kraft, M. L. Impact of protein pre-coating on the protein corona composition and nanoparticle cellular uptake. *Biomaterials* **75**, 295–304 (2016).
56. Ritz, S. *et al.* Protein Corona of Nanoparticles: Distinct Proteins Regulate the Cellular Uptake. *Biomacromolecules* **16**, 1311–1321 (2015).
57. Salvati, A. *et al.* Transferrin-functionalized nanoparticles lose their targeting capabilities when a biomolecule corona adsorbs on the surface. *Nat. Nanotechnol.* **8**, 137–143 (2013).
58. Ferrer-Tasies, L. *et al.* Quatsomes: Vesicles Formed by Self-Assembly of Sterols and Quaternary Ammonium Surfactants. *Langmuir* **29**, 6519–6528 (2013).
59. Pozzi, D. *et al.* The biomolecular corona of nanoparticles in circulating biological media. *Nanoscale* **7**, 13958–13966 (2015).
60. Palchetti, S. *et al.* The protein corona of circulating PEGylated liposomes. *Biochim. Biophys. Acta BBA - Biomembr.* **1858**, 189–196 (2016).

Chapter 3 .

Studying the molecular composition and stability in serum of single oligonucleotide polyplexes

The successful application of gene therapy relies on the development of safe and efficient delivery vectors. Cationic polymers like cell-penetrating peptides (CPPs) can condense genetic material into nanoscale particles – polyplexes – and induce cellular uptake. To this point, several aspects of the nanoscale structure of polyplexes have remained elusive due to the difficulty to visualize the molecular arrangement of the two components with nanometer resolution. This limitation has hampered the rational design of polyplexes based on direct structural information. Here, we used super-resolution imaging to study the structure and molecular composition of individual CPP-mRNA polyplexes with nanometer accuracy. We use two-color direct stochastic optical reconstruction microscopy to unveil the impact of peptide stoichiometry on polyplex structure and composition and to assess their destabilization in blood serum. Our method provides information about the size and composition of individual polyplexes allowing the study of such properties on a single polyplex basis. Furthermore, the differences in stoichiometry readily explain differences in cellular uptake behavior. Thus, quantitative dSTORM of polyplexes is complementary to the currently used characterization techniques for understanding the determinants of polyplexes activity in vitro and inside cells.

This work has been published as:

N. Feiner-Gracia, R. A. Olea, R. Fitzner, N. El Boujnouni, A.H. van Asbeck, R. Brock and L. Albertazzi, *Nano Lett.*, 2019, **19** (52) 784-2792.

3.1. Introduction

Protein interactions are not only responsible of reducing specific interactions (as shown in Chapter 2) but can also dramatically affect the stability of nanosized delivery systems. Therefore, it is important to study their stability in the blood complex environment to predict their behavior *in vivo*. A field of application particularly affected by this is the use of gene delivery systems such as polyplexes. As presented in Chapter 1, polyplexes are nanocarriers characterized by the electrostatic interactions between the polymer and the nucleic acid which guides the formation of complexes. The design of the polyplexes is still very challenging and activity varies greatly among different studies and systems[1]. Nowadays, mainly their physicochemical structure is investigated, and *in vitro* cell studies are performed to determine their ability to transfect cells. Surprisingly, a great number of these investigations are performed in serum free medium to optimize their functionality. The differences in transfection abilities may be attributed to the interplay between blood proteins or other blood molecules and polyplexes, which can lead to a reduction of the polyplexes stability. Therefore, to be able to design successful polyplexes is of utmost importance to understand the complexation efficiency of these systems in blood like conditions.

The study of the complexation efficiency of polyplexes in complex biological media requires a previous deep understanding of the structural properties and variations of the formulated polyplexes. Nowadays, the knowledge on these structural properties is very limited, in fact, only a handful of methods for polyplex characterization are currently available. The average hydrodynamic size and charge of the polyplexes can be measured using DLS and Zeta-potential or electrophoretic shift assays, respectively[2]. Also, images from EM or AFM can indicate the polyplex size and shape[3], thus providing information on morphological changes[4,5]. The efficiency of complexation is evaluated using gel electrophoresis, by detecting the presence of free oligonucleotides, while the affinity is currently measured using dye exclusion assay[1]. Overall, each of the current methods brings valuable information; however, they exhibit two main limitations: i) they are mostly ensemble techniques providing an average information of the polyplexes; ii) they are not able to distinguish between the two components of the polyplex and therefore miss quantitative and qualitative aspects of the composition and inner organization of individual polyplexes. Therefore, only very limited data is available to compose molecular models of the structure and composition of polyplexes[6–8]. Even less information is available regarding the integrity of polymer carriers and genetic material in full serum. Some attempts have been made either using electrophoretic shift assays or method based on fluorescence fluctuation spectroscopy, as detailed in Chapter 1. However, following these techniques is not possible to directly quantify the exact composition of individual polyplexes, which will help to optimize their design.

In this chapter I report the use of two-color dSTORM to unveil the structure and composition of polyplexes on a single particle basis to be able to follow they complexation on

complex media such as serum. In Chapter 2 we have demonstrated the possibility to image single nanocarriers as well as they interactions with serum proteins. Here, we want to exploit the possibility to understand the organization of single nanocarriers and use this information to predict their stability in blood like conditions. With the appropriate knowledge of the photophysical properties of the dye such as duty cycle and bleaching rate, STORM provides the possibility to obtain quantitative information about stoichiometries and absolute molecular numbers. In this framework membrane receptors[9–11], DNA origami DNA strands[12], and accessible binding sites on endocytic/endosomal vesicles[13] were quantified. Therefore, dSTORM can also contribute to the quantitative understanding of polyplexes. Despite this potential, to the best of our knowledge, the use of super-resolution for the study of gene delivery carriers has not been explored.

3.2. dSTORM imaging of polyplexes

3.2.1. Cell-penetrating peptides based polyplexes

Cell-penetrating peptides (CPPs), also known as protein transduction domains, are a very promising class of vectors for gene delivery[14] because of their ability to facilitate cell entry of conjugated molecules[15,16]. Moreover, due to their positive charge, CPPs are ideal candidates for non-covalent complexation of negatively charged oligonucleotides into nano-sized particles named polyplexes[3]. The potential of polyplexes to deliver different oligonucleotide cargo such as plasmid DNA or RNA into cells for gene therapy has been widely explored[2,17,18]. Only recently, mRNA has been emerging as another promising option[19–21]. Polyplexes of mRNA only need to penetrate cells and escape from the endosomes or lysosomes to the cytoplasm, where mRNA gets translated immediately into proteins. This route avoids the complicate nuclear penetration that DNA therapies need. Furthermore, mRNA is only transiently active, without risk of insertion into the host genome and it is fully degraded via physiological mechanisms. Therefore, mRNA loaded polyplexes have recently been proposed as efficient carriers for oligonucleotide therapy[19–21].

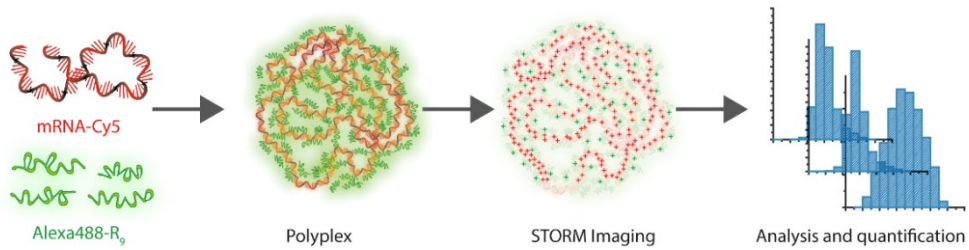

Figure 3.1 Schematic illustration of the followed procedure. Representation of polyplex formation from mRNA-Cy5 and Alexa488-R9, imaging and analysis.

3.2.2. Optimizing dSTORM imaging of polyplexes

For our dSTORM analysis we prepared polyplexes formed by the CPP L-nona-arginine (r9) with a 1929 nucleotide long mRNA coding for firefly luciferase, as a model system to investigate the power of our methodology. R9 is a well-known cell-penetrating peptide and its capacity to complex and induce the cellular uptake of oligonucleotides has been previously studied[1,22,23] An overview of our procedure is reported in Fig. 3.1a. To perform dSTORM imaging, both components were labeled using the dSTORM-compatible, spectrally well-separated dyes, AlexaFluor488 and Cyanine 5 for R9 and mRNA, respectively. The peptide was labeled at the N-terminus. The mRNA was stochastically labeled with Cy5-UTP with an average labeling ratio of 27 dyes per molecule, estimated from Uv/Vis absorption measurements (as detailed in Experimental Section). After complexation, the polyplexes were deposited on a glass coverslip for dSTORM imaging. Figures 3.2a and show representative images of R9-mRNA polyplexes. The direct comparison between conventional (a) and dSTORM (b) microscopy images shows how the improvement of resolution allows individual

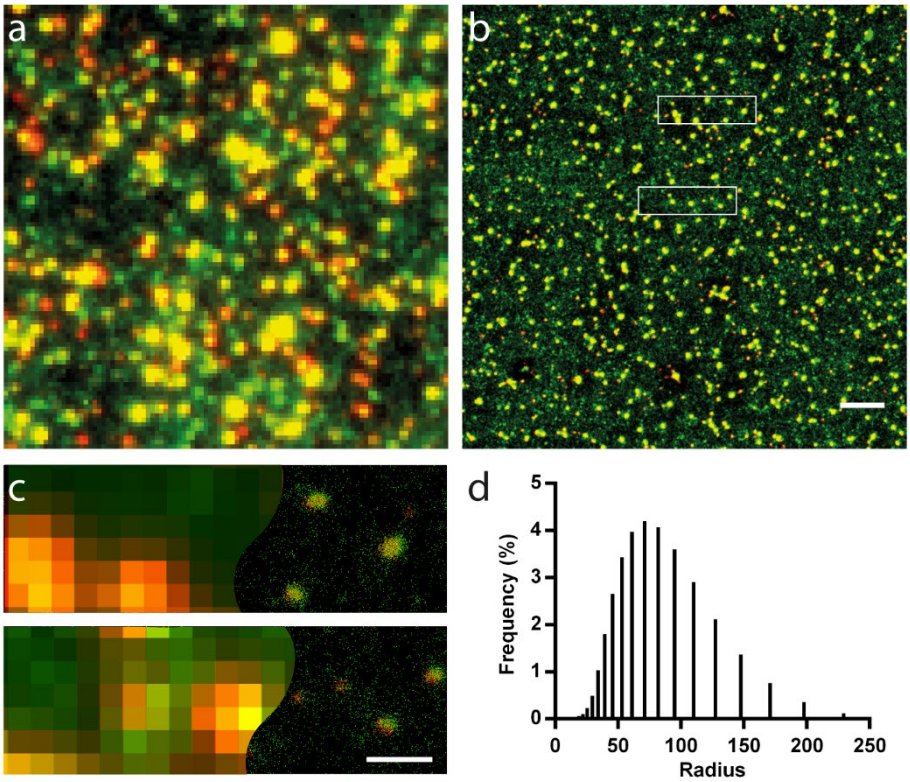

Figure 3.2 Imaging of polyplexes using dSTORM microscopy. a. Conventional fluorescence image of polyplexes at N/P 5 (red represents mRNA molecules and green R9 molecules) **b.** dSTORM imaging of polyplexes, same field of view as in a. **c.** Zoom-in of three different areas of a. and b. to distinguish single polyplexes structure. **d.** Hydrodynamic radius of polyplexes prepared at N/P **5**.

polyplexes to be resolved, while in the conventional image it is impossible to distinguish a single polyplex from clusters. Images revealed complexes of 50-75 nm in radius, in agreement with DLS measurements (Figure 3.2d). The labeling ratio, i.e. the proportion of labeled molecules, was optimized to obtain an optimal signal density for dSTORM, moreover, dSTORM images of polyplexes with non-labelled molecules were acquired as a control, showing almost no localizations (Figure 3.3).

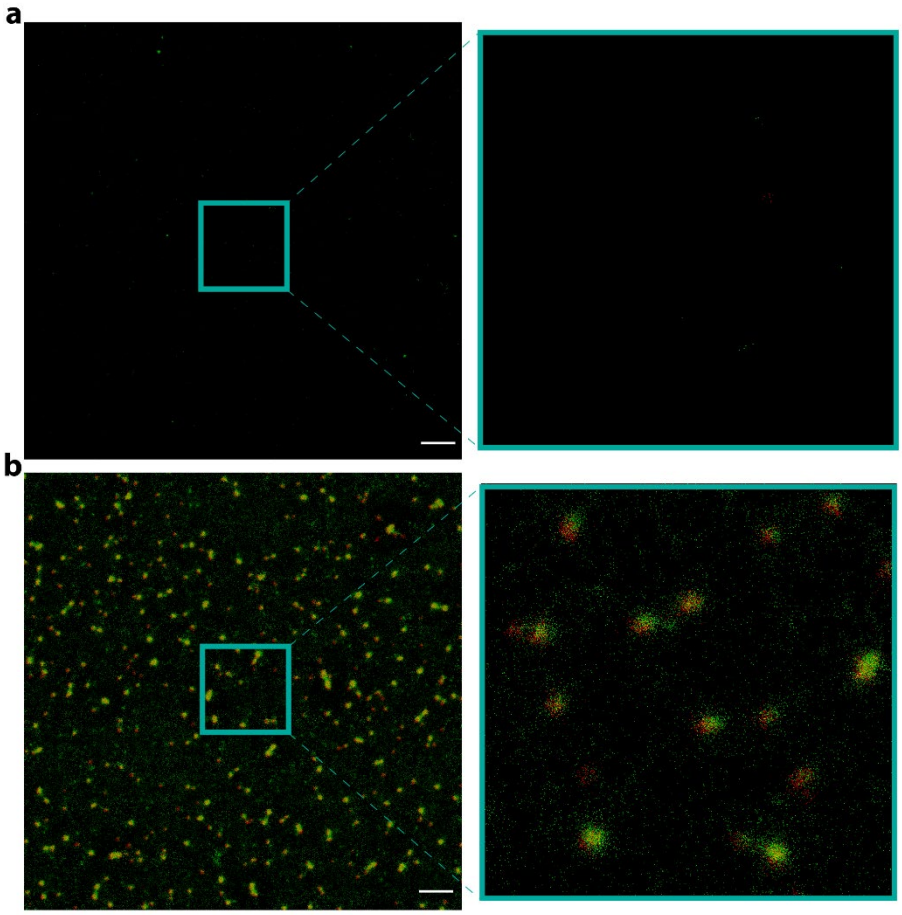

Figure 3.3 dSTORM control of images of a. non-labelled vs **b.** labelled polyplexes**.** Polyplexes at N/P 5 were prepared with non-labelled mRNA and non-labelled r9 and image using dSTORM (a) and compared to dSTORM images of labelled polyplexes (b) to demonstrate the signal detected was specific of our labelled-structures.

Interestingly, from the dSTORM images of Figure 3.2 we detected a large amount of green signal (which corresponds to the peptide) which was not associated with the polyplexes but freely distributed into the slide. This observation indicates that not all the peptide used in the complexation procedure was incorporated into the polyplexes' structure. Moreover, it is of special interest because most of the other characterization methods, e.g. DLS, TEM, AFM and

gel electrophoresis, cannot detect individual peptides and are strongly biased towards the macromolecular assemblies. Notably, free cationic moieties may have a role in the transfection and/or toxicity. As an example, previous studies of Vaidyanathan et al. proved enhanced pDNA endosomal escape of polyplexes due to the addition of free PEI polymer[24]. In addition, for acylated TP10 analogs, non-incorporated peptide at higher N/P ratios showed enhanced toxicity[25]. Therefore, being able to visualize the non-complex materials is of crucial importance.

In addition, dSTORM imaging allowed studying the distribution of the peptide and the mRNA within the polyplexes as magnified in Figure 3.2c. The observed overlap of the two colors indicated that mRNA and R9 molecules are homogenously intertwined inside the polyplex, at least within the resolution of dSTORM. A STORM 3D image was acquired to

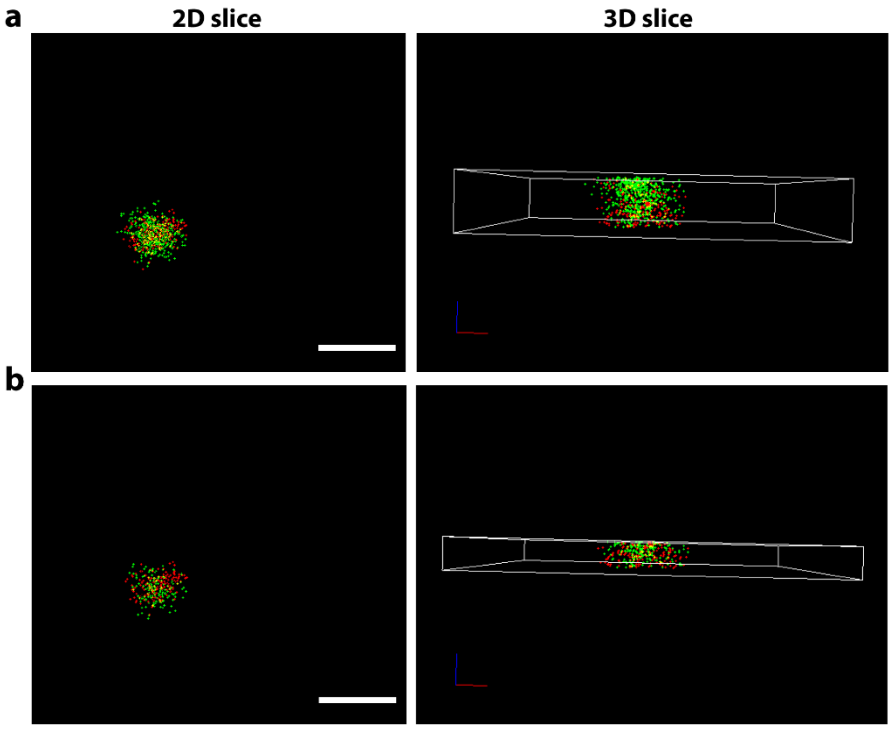

Figure 3.4 mRNA and r9 are homogenously entwined inside polyplexes. a. Localizations of a center Z slice of 100 nm of a 3D dSTORM image **b.** Localizations of a center Z slice of 50 nm

prove these observations and rule out the effect of the projection, a middle stack of a polyplex is shown in Figure 3.4 showing both molecules are indeed intertwined. This result proves that mRNA molecules are not exposed on the polyplexes surface but shielded within the structure. This information is of utmost importance when designing effective gene delivery systems, as

confined mRNA will be more stable than exposed[26] and cannot easily be determined with other characterization techniques introducing dSTORM as a new tool in the field.

3.2.3. Imaging structural differences between N/P ratios

One of the most important experimental degrees of freedom in polyplex generation is the ratio of cationic moiety and nucleic acids, which determines the N/P ratio, the ratio of positive over negative charge carriers. The N/P ratio determines several key properties of the formed polyplexes such as net charge, size and stability[1,27]. We considered the N/P ratio an ideal test case to establish a direct quantitative analysis of polyplex composition using super-resolution dSTORM microscopy. Therefore, having successfully obtained super-resolution images of polyplexes formed at N/P **5**, we further aimed to compare the structure and distribution of mRNA and R9 molecules for different N/P ratios.

For this purpose, we imaged polyplexes formed at N/P **1**, **3**, **5** and **7**. The mRNA concentration was maintained constant in order to follow the complexation of the same number of oligonucleotides. In Figure 3.5a a representative image of each condition is shown.

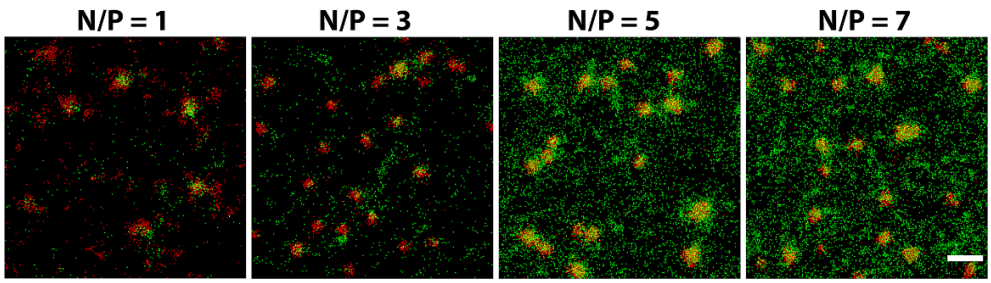

Figure 3.5 Polyplexes structural differences at varying N/P ratios. dSTORM images of polyplexes prepared at N/P ratios **1**, **3**, **5** and **7** from left to right.

At N/P **1**, the mRNA-Cy5 signal was not clustered, resulting in more spread structures compared to the images obtained for N/P 5. Moreover, only minimal mRNA signal colocalized with the Alexa488-R9 signal and mostly free mRNA and free peptides were present, suggesting that the amount of R9 present at N/P **1** was not sufficient to condense mRNA into polyplexes. The distribution of mRNA changed dramatically at N/P **3**, for which clear rounded clusters of mRNA-Cy5 were present. Therefore, we concluded that the R9 concentration present at N/P **3** was enough to compact the mRNA into polyplexes. The N/P **5** and N/P **7** polyplexes clearly contained more R9 than the N/P **3** ones. Both, N/P **5** and N/P **7** were very similar to each other, which indicates that the charges of the mRNA were already saturated and the extra r9 remained in solution and was not incorporated into the polyplexes. Overall, this qualitative evaluation of dSTORM images of polyplexes formed at different N/P ratios already provided important structural information regarding the mRNA and r9 interplay in the formation of polyplexes.

3.3. Molecular composition of polyplexes: quantitative dSTORM

In dSTORM the image reconstruction is based on single molecule localizations detected during the imaging as introduced in Chapter 1. Therefore, dSTORM provides a highly powerful approach to analyze the polyplexes not only qualitatively but also quantitatively[28]. Using an adapted version of the previously developed MatLab script, explained in detail in Chapter 2, the localizations in the mRNA-Cy5 channel were clustered in order to remove the free R9 localizations on the glass coverslip and to provide an estimation of the localizations of mRNA and CPP molecules per polyplex at different complexation ratios (the exact procedure is described in Experimental section). Moreover, the size of the polyplexes could be estimated for each N/P ratio, which in all conditions matched the DLS data (Figure 3.2d). In Figure 3.6 the size of the polyplexes quantified for each N/P ratio are plotted into a frequency histogram. The radius of the polyplexes was between 60 and 80 nm for all conditions, however, the polydispersity of N/P **1** was significantly higher compared to the one of the other ratios. N/P **1** polyplexes had a significant population of polyplexes exceeding 100 nm in size indicating that at this condition most of the mRNA molecules were not packaged. For N/P **3** to **7** the formation of polyplexes reduced the size of the structures obtaining also more monodisperse populations with no significant differences between N/P **3-7**.

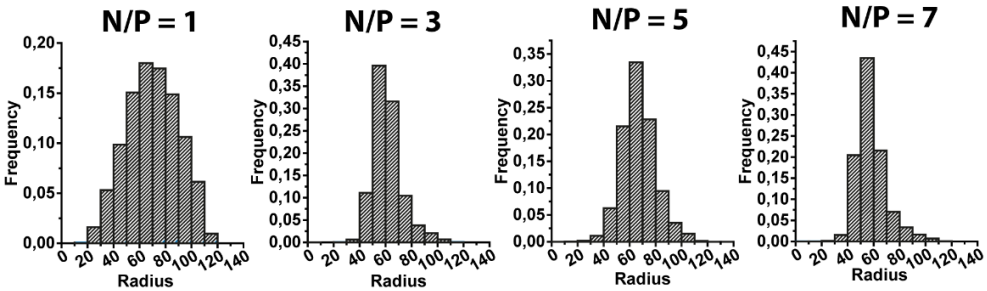

Figure 3.6 Size of polyplexes at different N/P. Frequency histograms of the radius of the polyplexes quantified from the dSTROM images for each N/P ratio.

3.3.1. Stochastic simulation to predict number of molecules

As previously shown[29], stochastic simulations can predict the expected number and distribution of localizations of a set number of molecules. Therefore, comparing the number of localizations per polyplex that were experimentally detected to simulated data can provide a more accurate estimation of the composition of individual polyplexes. To gain further insight we designed and implement a program that can simulate the underlying process of stochastic photoactivation to compare its output to our imaging measurements [a], as shown in

[a] The simulation program was developed by R. Fitzner based on our inputs and suggestions

Figure 3.7. We modeled each polyplex as a cluster of dyes considering they were all at the same spot. We made the reasonable assumptions that each dye within the cluster behaves independently and each will randomly be active, deactivate or bleach. We simulated the blinking of dyes that are allocated within polyplexes. The radii of the polyplexes are smaller than the optical resolution limit:; while dSTORM can distinguish the location of individual dyes, it can do so only when just one dye is blinking within one frame. If more than one dye in the same polyplex are blinking in the same frame, the image processing will register that the detected light comes from more than one sources and will discard the localization. For this reason, the precise location of a dye within the polyplex is irrelevant for our result which only focusses on the detection likelihood. In all our simulations of polyplexes we used a Poisson distribution to account for the heterogeneity across different polyplexes. Also, we assumed the number of peptides and mRNA are independent from one another to simplify the simulation.

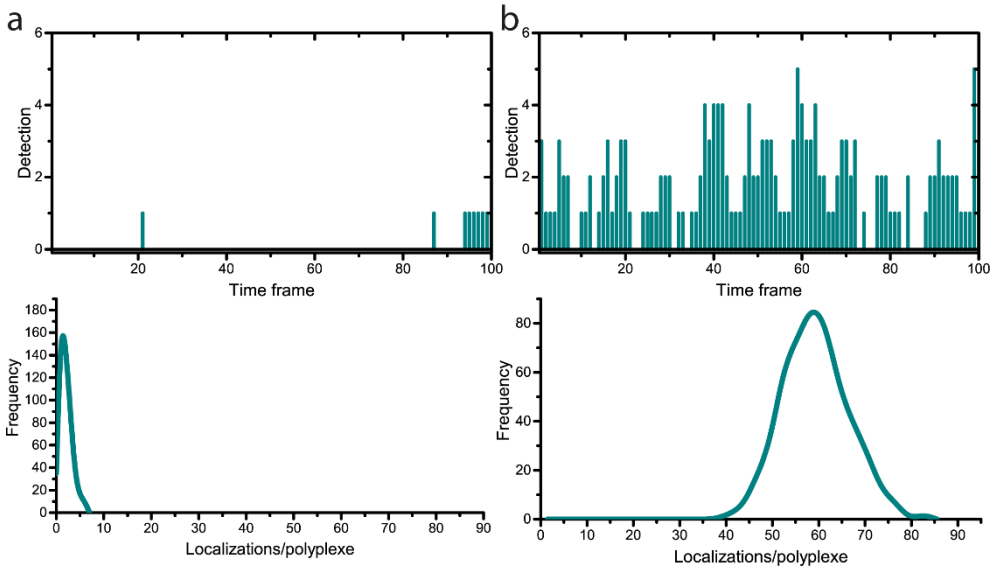

Figure 3.7 Output generated from the Simulator of the r9 dye blinking in our structures. The simulator provides information about the number of detected localizations per frame (upper graphs), as well as, the number of localizations per single polyplexes detected in the whole time simulated (lower graphs). Here two different conditions are represented a. 1 dye per polyplex and b. 50 dyes per polyplex.

To obtain the simulated data presented in Figure 3.8 the following steps were performed: i) we acquired dSTORM images of polyplexes with a single labeled r9 molecule from which we estimated the photophysical parameters of the AlexaFluor488 dye; ii) we introduced these parameters together with the known experimental data such as number of frames, number of polyplexes to be simulated; iii) we simulated the blinking behavior of a single-r9 molecule and verified that the output number of localizations per cluster corresponded to the

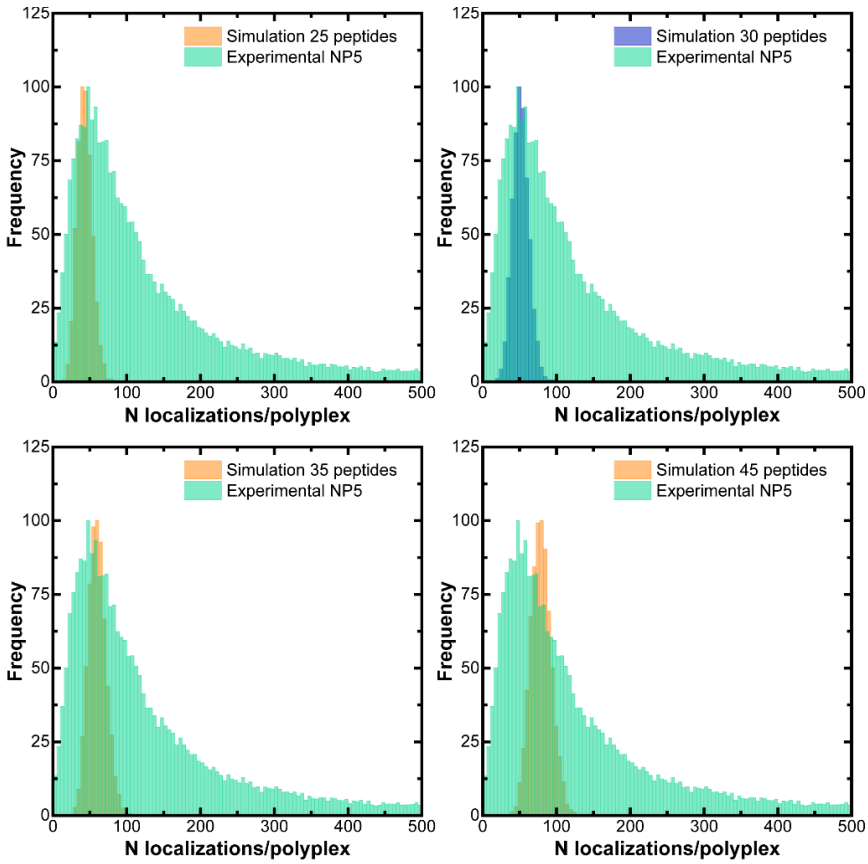

Figure 3.8 Comparation of experimental data of polyplexes prepared at N/P 5 with simulated data of polyplexes with different number of r9 molecules. Each graph represents a histogram of frequency of the number of localizations per polyplexes comparing the simulated with the experimental data (green). The simulated condition which fits better our experimental data is represented in blue, while other simulated conditions are represented in orange.

experimental one (detailed information on the simulation can be found in the Experimental Section).The distributions of simulated and experimentally detected localizations were compared to determine which simulated peptide number matched the peak of the experimental data (Figure 3.8). Notably, for mRNA no simulation was conducted due to the heterogenous labeling of the mRNA which together with the stochastic nature of the detection could not be approximated.

3.3.2. Revealing molecular composition differences for each N/P ratio

As stated before, after our quantitative analyses we could estimate the number of localizations of each component, mRNA and CPP, for each imaged condition. In Figure 3.9 the median number of localizations per polyplex detected for each N/P ratio, which is proportional to the number of molecules of the specific component, is plotted to unveil the

composition of the polyplexes for the different conditions. More than 15,000 polyplexes were measured per N/P ratio. In order to better understand the data in Figure 3.9 the median number of localizations per polyplex was plotted together with two more conditions: i) data of polyplexes with only one labeled mRNA molecule or only one labeled r9 molecule; ii) simulated data obtained from the stochastic blinking model. The results for polyplexes with only one labeled molecule are crucial to interpret the data from the measured polyplexes as they provided a reference for the estimation of the number of molecules per polyplex, e.g. distinguish single uncomplexed RNA strands from multiple RNAs in a particle. On the other hand, the simulations could unmask the stochastics of the dSTORM blinking, one of the main issues of STORM quantification, and provided the possibility to compare the median number of localizations that was detected experimentally with a theoretical framework.

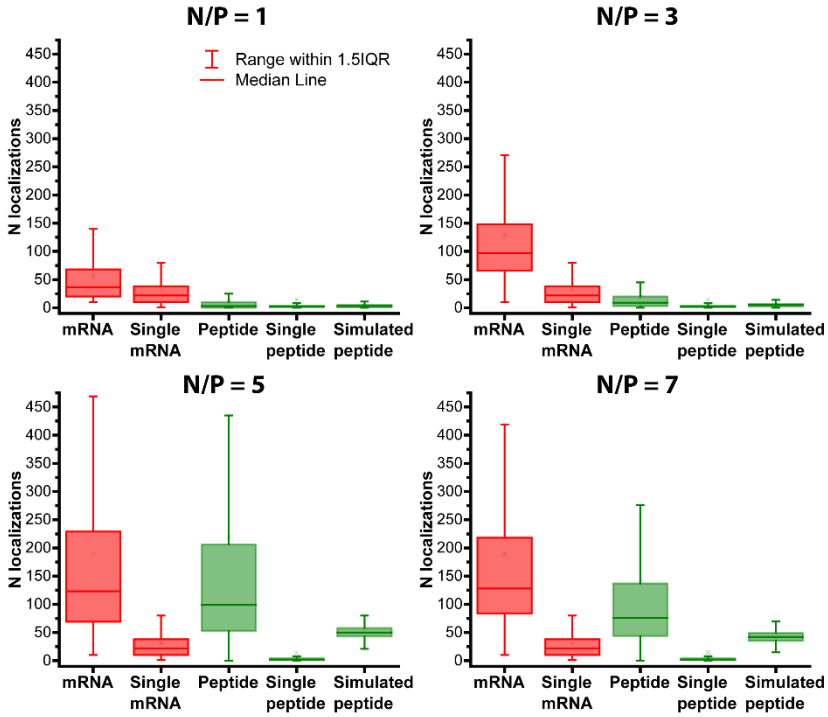

Figure 3.9 Stoichiometry differences of polyplexes at distinct N/P ratios. Box plot comparing the number of localizations of mRNA and peptide quantified for each N/P ratio (**1**, **3**, **5** and **7**) together with the quantification of single molecules and the number of localizations obtained from the simulations. Statistical analyses were run (Mann-Whitney test) showing significant differences between the peptide content in NP3 and NP5 ($p<0.0001$) and the mRNA content between NP1 and NP3 ($p<0.0001$).

From the experimental and simulated data presented in Figure 3.9 comprehensive information on the polyplexes structure and composition was obtained. For N/P **1** the number of mRNA localizations was comparable to the one for a single molecule supporting the hypothesis that single mRNA molecules were present which were not able to be complexed

into polyplexes. From N/P **3** the experimentally determined median number of mRNA localizations significantly increased to about 2-3 times the single molecule and remained more or less stable at N/P ratios **5** and **7**. These results indicate that inside each polyplex there were only few mRNA molecules. Interestingly, from N/P **3** to N/P **5** the box width was enlarged which indicates a high polydispersity with respect to the number of encapsulated mRNAs. The exact number of mRNA molecules per polyplexes could not be obtained due to the heterogenous labelling of the mRNA molecules which was not represented by the simulation.

In contrast, the density of the peptides followed a different behavior than the one of the mRNA molecules. At N/P **1** the number of R9 localizations per polyplex was very low and similar to the one of a single peptide. Considering the labeling density (about 1.25 % of labeled

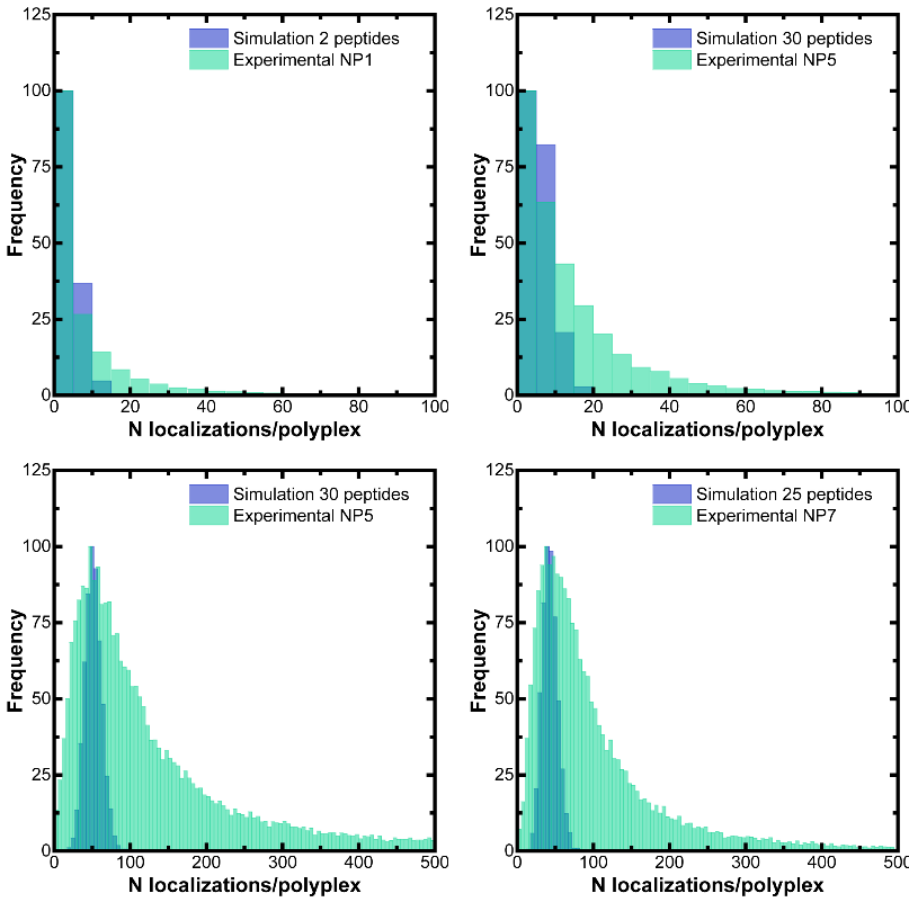

Figure 3.10 Simulation vs experimental data of polyplexes at different N/P. For each experimental condition different number of r9 molecules per polyplex were simulated to approximate the number of molecules per structure. In all cases a central population of the experimental data could be fitted to a simulated data, however, the experimental data had always a broader population which increases with higher N/P.

peptides were mixed with 98.75 % unlabeled ones) this is compatible with individual mRNA molecules with about one hundred peptides attached, an insufficient number to compact the oligonucleotides into a polyplex. At N/P **3** the number of R9 localizations slightly increased but it was not until N/P **5** that the number abruptly grew and remained stable for higher ratios. At N/P **5** and N/P **7** also the box widths were similar and again larger than the one at N/P **3**. The median number of simulated localizations matched the experimental data, demonstrating the validity of our model. The number of peptides for which the simulated number of localizations best matched the experimental data were about 25-30 labeled peptides per polyplexes; considering that 1.25% of the peptides were labeled we could estimate approximately 2000-2400 peptides per polyplex. Still, for N/P **5** and **7** the box plot was very broad. The simulated data always corresponded to the lower range of the plots. Frequency histograms of the number of localizations of experimental and simulated data are plotted in Figure 3.10. From the graphs the presence of a major population in the experimental sample, which fits the simulated data, together with a tail of polyplexes with higher number of molecules that cannot be fitted to the simulated data is observed. The fact that the experimental data was always broader demonstrates heterogeneity in the samples which the simulation did not recapitulate. Thus, the measured heterogeneity cannot be simply explained with the stochastic behavior of the dye blinking. Therefore, it can be concluded that the polyplex formulation does not consists of a single monodisperse population but to a rather mixture where polyplexes of different sizes and molecules number co-exist.

To summarize these data into a molecular picture, r9 binds mRNA at N/P **1** but only from N/P **3** this binding is sufficient to condense the mRNA into polyplexes. Polyplexes from N/P **3** to N/P **7** are similar in size and amount of mRNA but change significantly with respect to the amount of peptide present in the particles. Moreover, a significant heterogeneity of the molecular composition is present, especially at N/P **5** and **7**. Notably, the differences between the last three conditions and the heterogeneity in the samples would have been difficult or impossible to measure with other methods, showing the potential of dSTORM to complement existing technique for polyplexes characterization.

3.3.3. Correlation between the number of mRNA and CPP localizations

Above, the median number of localizations per component and condition was analyzed to determine the approximate number of molecules per polyplex and the polydispersity of the samples. However, dual color dSTORM simultaneously provides information regarding the number of localizations for each component and the size for each individual polyplex. Figure 3.11 show a correlative analysis of these three variables. The scatter plots in Figure 3.11a represents the data from over 15,000 polyplexes: every dot in the chart represents one polyplex that is positioned in the graph depending on its amount of r9 or mRNA localizations. Moreover, every point was plotted in a different color depending on the size of the polyplex. With this representation, we could draw conclusions on the relationship between size and

amount of the two components on a single particle basis, and thus, on the heterogeneity of the sample.

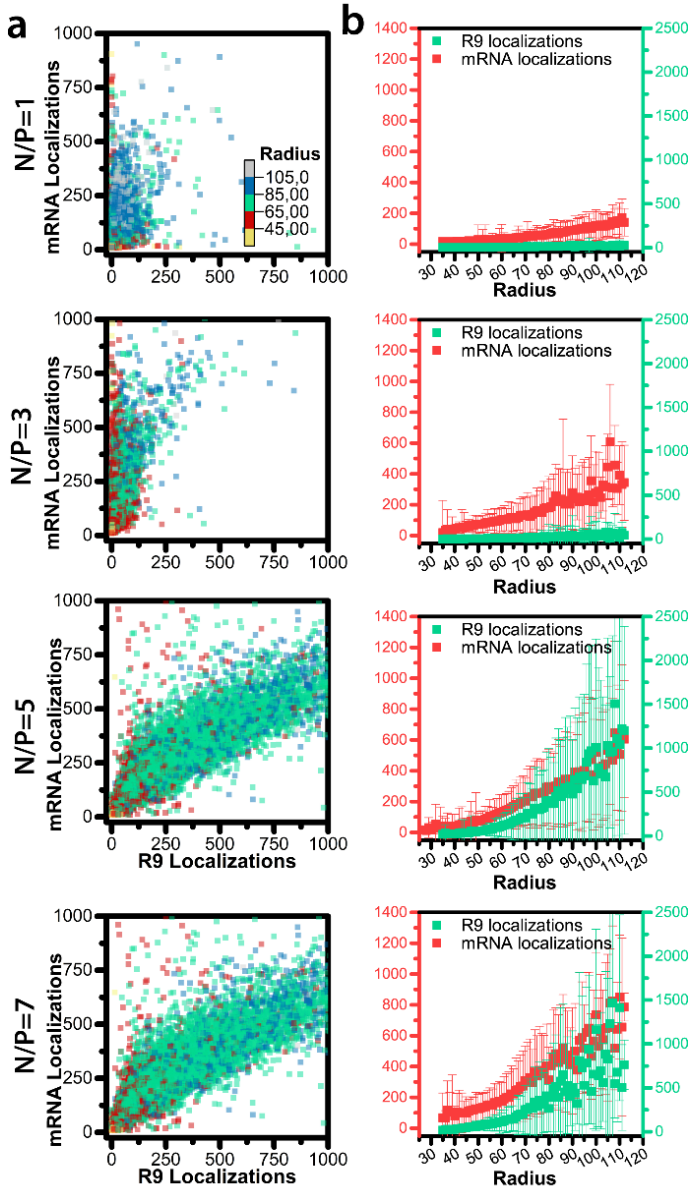

Figure 3.11 Correlation between the number of mRNA localizations and R9 localizations. **a.** Scatter plots of the number of mRNA localizations versus number of R9 localizations, together with a color code representing the size for each polyplex. **b.** Number of localizations is plotted as a function of polyplexes size for both mRNA (red) and r9 (green).

At N/P **1** the mRNA localizations were rather monodisperse compared to other samples, corresponding to the presence of single mRNA molecules. At N/P **3** the number of mRNA localizations significantly increased as well as the polydispersity of the mRNA content, indicating the existence of polyplexes with multiple RNA molecules. Moreover, a correlation between the amount of R9 and mRNA is present. This is even more evident for the N/P ratios **5** and **7** where the number of R9 localizations increased overall. In particular, the polyplexes with higher mRNA localizations were the ones that show a pronounced increase in the number of R9 localizations. Following this pattern, at N/P **5** the polyplexes with high mRNA localizations displayed an increase in the R9 localizations and at N/P **7** similar correlation was observed suggesting the charges were saturated at N/P **5**. These results prove a clear correlation in the number of molecules of each component inside individual polyplexes. Moreover, the color code provided information on the interplay between composition and size. In all the N/P studied, higher amounts of mRNA and R9 were found in polyplexes with larger size (green-blue color). The plots in Fig. 3.11b, where the RNA and R9 content is plotted against size, also confirm this. However, the data also indicate that the density of the packing inside the polyplexes must be heterogeneous. Within the size category of 65 – 85 nm radius, polyplexes differed in volume by a factor of maximally 2.2 while the number of localizations varied by up to a factor of eight. Similarly, with increasing N/P more localizations for both mRNA and peptide were found for polyplexes of the same size.

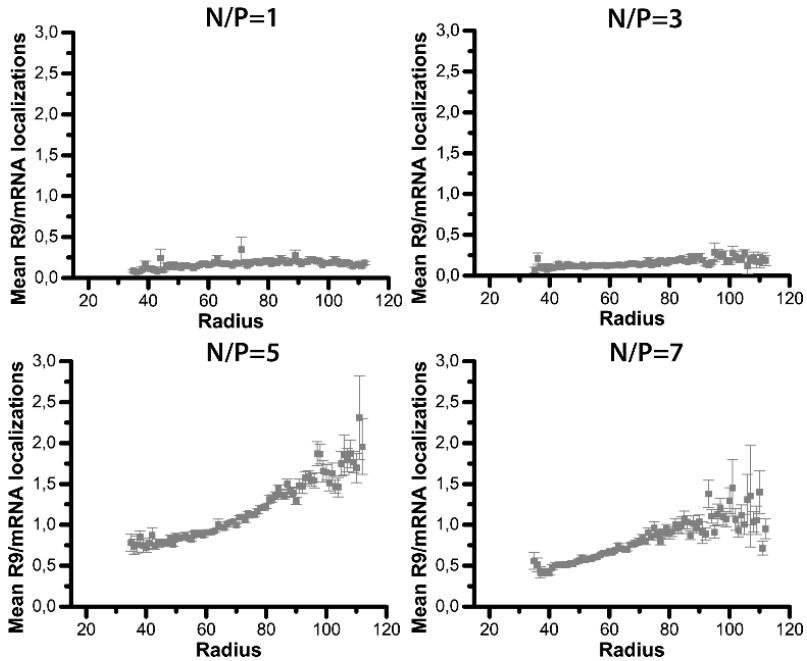

Figure 3.12 Dependence of cellular nanoparticle uptake on N/P ratio. HeLa cells were incubated for 1 hour with polyplexes consisting of Cy5-mRNA and fluorescein-labeled R9 at the indicated N/P ratios followed by washing and confocal microscopy of living cells. Scale bar 20 μm.

Moreover, we calculated the ratio of R9 localizations per mRNA localizations and found that it was constant for N/P **1** and **3**, but slightly increased with higher radius at N/P **5** and **7** (Figure 3.12). These results indicate that the density of polyplexes prepared at the same N/P is overall similar, although there is a trend of higher ratios at higher radii. Altogether our measurements depict some important structural aspects of polyplexes: i) a significant heterogeneity is present, with polyplexes varying significantly in size and composition; ii) a correlation between the two component is present, with more R9 necessary to pack a higher copy number of mRNA inside the same polyplex; iii) higher mRNA content results in larger sizes.

3.4. Bio-interactions of polyplexes

3.4.1. N/P ratio formulation guides cell internalization

Next, we aimed to assess whether the STORM analyses could lead to a better understanding of cell biological experiments. For this purpose, polyplexes were formed with Cy5-mRNA and fluorescein-labeled R9. We had shown before that fluorescein and alexa488-labeled r9 yield equivalent results[30]. Hela cells were incubated with polyplexes at constant concentrations of mRNA resulting in increasing concentrations of peptide. Then, intracellular fluorescence was recorded by confocal microscopy after 1 h incubation (Figure 3.13). This concentration was proved to be non-cytotoxic for cells at any of the N/P (Figure 3.14). For N/P

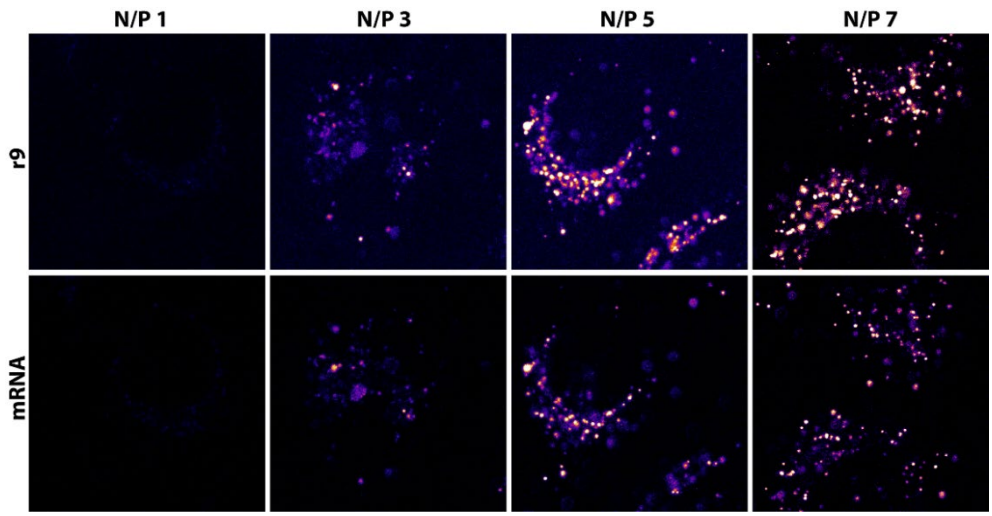

Figure 3.13 Mean number of R9 localizations/mRNA per polyplex as a function of the radius. For each polyplex the number of R9 localizations was divided by the number of mRNA localizations in the same polyplex; then all the polyplexes with the same radius were clustered and the mean number of R9 localizations/mRNA localizations was calculated and plotted.

1, corresponding to a concentration of fluorescein labeled peptide of 0.05 μM hardly any cell-associated fluorescence could be detected. From N/P 3 vesicular fluorescence was presented that further increased to an N/P ratio of 5 with no further increase to N/P 7 (Figure 3.13a). Quantitative image analysis demonstrated that both, the mean intensity of vesicular fluorescence (Figure 3.13b) as well as the total number of vesicular pixels per cell as a measure for the number of endosomes increased from N/P 1 to N/P 5 (Figure 3.13c). At N/P 1 almost no polyplex was internalized while at N/P 3 the amount increased, and it further did at N/P 5 and 7. These data demonstrate that from N/P 5 the polyplexes had the right composition to be internalized. Even though the cells were washed in order to reduce extracellular out-of-focus fluorescence, there was still some fluorescence left.

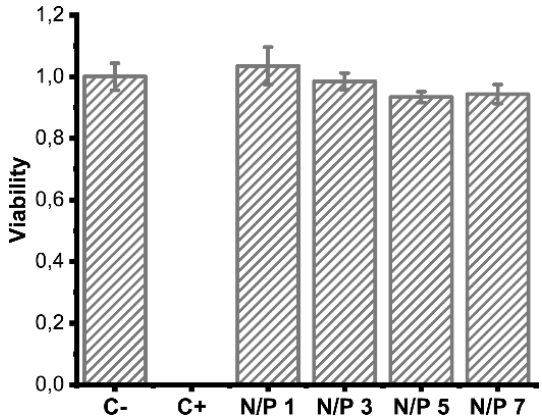

Figure 3.12 Cytotoxicity study of polyplexes at different N/P. The polyplexes were incubated with cells for 1 hour and cytotoxicity was tested after 24 hours, controls were added where cells were incubated with PBS (C-) and 30% ethanol (C+).

For the peptide, this extracellular fluorescence strongly increased with increasing N/P ratio, consistent with the STORM results that had demonstrated incomplete incorporation of peptide from N/P ratios larger than 3 (Figure 3.13d). Moreover, we divided both mean fluorescence intensities (peptide vs mRNA) to assess the ratio of peptide per mRNA in the internalized poyplexes (Figure 3.13e). Interestingly, from N/P 3 to 7 this value remained constant. This observation proves that a specific composition of the polyplexes is needed to be internalized by the cells. From our dSTORM data we demonstrated that at N/P 3 most of the polyplexes did not have enough peptide incorporated to pack the mRNA; therefore, we hypothesis that only a small population of polyplexes at N/P 3 had the right composition which corresponds to the lower internalization observed. Finally, the higher ratio at N/P 1 was consistent with the absence of polyplex formation so that only free peptide was being internalized.

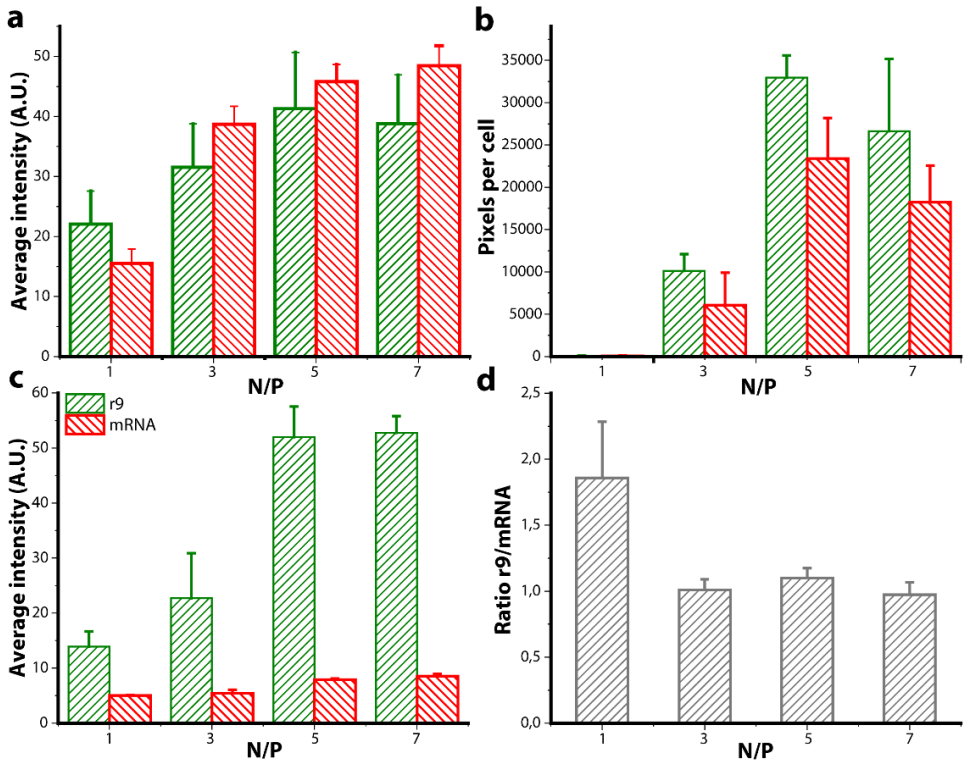

Figure 3.13 N/P ratio of polyplexes guides cellular uptake. a. Average pixel intensities for vesicular fluorescence. **b.** Fluorescent pixels per cell as a measure for the number of endocytic vesicles with polyplexes. **c.** Average pixel intensity for fluorescence outside cells, recorded at higher detector gain. **d.**Ratio of peptide over mRNA fluorescence intensity inside cell. Ratios were calculated for the vesicular intensities of each analyses image and averaged. Error bars correspond to the standard deviation for normalized data of four independent experiments.

3.4.2. Serum proteins induce polyplexes decomplexation

Having established the methodology to measure polyplex size and composition, we exploited the ability of dSTORM to perform analyses in complex media such as blood serum. Polyplexes are designed to be intravenously injected into the blood stream, being in contact with proteins and other biomolecules that can destabilize the complex. Therefore, it is of major importance to understand the stability of the polyplexes in serum. Classically, gel retardation assays are used to assess the release and decomposition of polyplexes[1]. Using dSTORM imaging we expected to obtain information on the mechanism of decomplexation because we are able to track the composition and size of polyplexes.

To this end, we incubated polyplexes formulated at N/P 5 at 37ºC with FBS at concentrations of 1%, 20% and 100% for 1 minute and 1 hour followed by deposition on cover

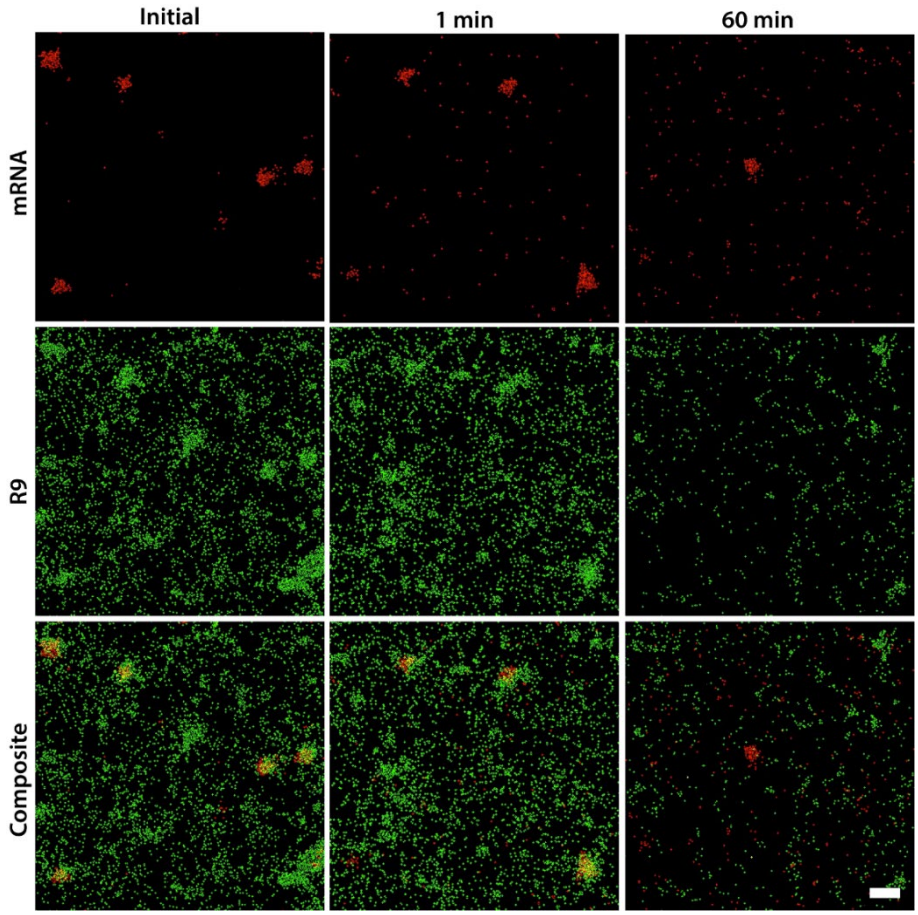

Figure 3.14 Imaging stability of polyplexes in complex medium. dSTORM image of the N/P 5 polyplexes were acquired before and after the polyplexes were incubated with 20% FBS for 1 minute and 1 hour. Scale bar 200 nm.

slips. Then, dSTORM images of the complexes were acquired (Figure3.15 shows representative images of polyplexes behavior with 20% FBS). We observed that after 1 minute complexed polyplexes were still observed together with free peptide while after 1 hour of incubation only free mRNA and free peptide was observed. To understand the behavior of polyplexes in serum all the images were quantitatively analyzed in order to approximate the molecular composition in each condition (Figure 3.16). Interestingly, the behavior of the polyplexes was similar when incubated with 1% or 20% of FBS. In these conditions, after 1 minute the mRNA content in the polyplexes remained stable compared to the initial composition, indicating that the polyplexes were not releasing their payload. However, we observed a decrease in the number of peptide molecules. After 1 min of serum incubation only half of the initial peptide localizations were detected. In contrast, after 1 hour of FBS incubation both the number of mRNA and R9 molecules abruptly dropped (Figure 3.116). In

contrast, polyplexes incubated with 100% of serum where immediately destabilized and any intact polyplex was detected after 1 minute neither 1 hour of incubation.

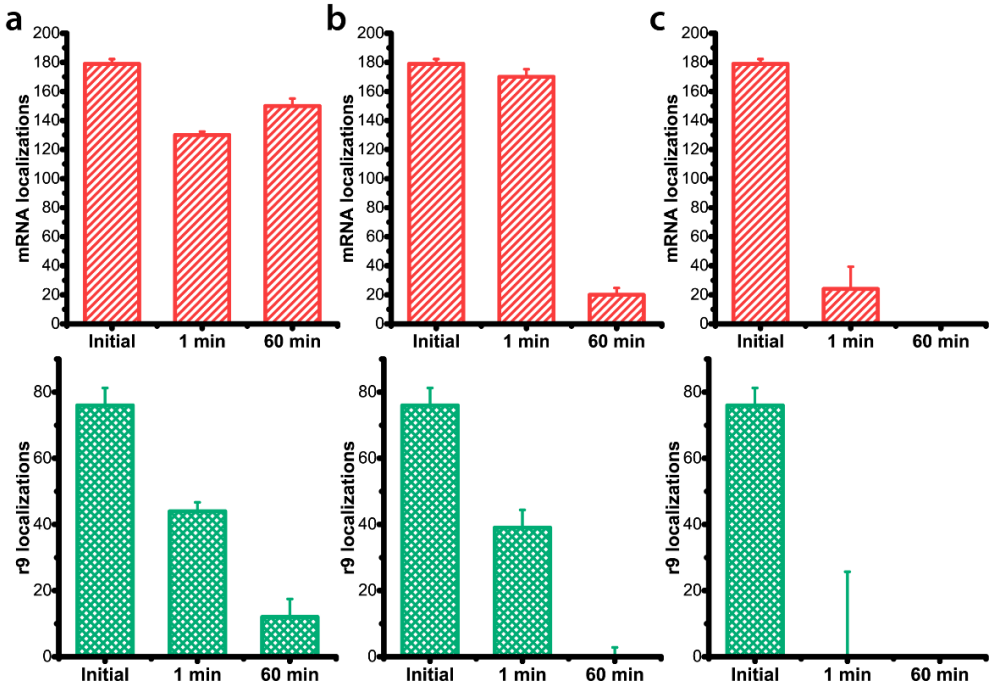

Figure 3.15 Stability of N/P 5 polyplexes in serum at different concentrations. Number of localizations after 1 and 60 min of incubation with (a) 1% FBS, (b) 20% FBS, and (c) 100% FBS in comparison to the initial polyplexes. Upper graphs correspond to the median number of mRNA localizations (± S.D.) and lower graphs to the median number of R9 localizations (± S.D.).

Altogether, these results indicate that the serum proteins interact with the polyplexes in two stages as schematically represented in Figure 3.17: i) serum rapidly removes peptides from the polyplexes without compromising the mRNA compacted inside the particle (minute time-scale); ii) proteins destabilize the complexes causing the release of mRNA molecules (hour time-scale). This mechanistic study proves the importance of understanding the stability of polyplexes, or other nanocarriers formulated based on electrostatic interactions, in complex media mimicking *in vivo* environments. The pre-screening of systems *in vitro* will improve the rational design of systems and select more relevant nanocarriers to be further studied. We envision that the ability of dSTORM to provide additional information about the mechanism of polyplex disassembly will support the study and design of gene carriers with improved serum stability.

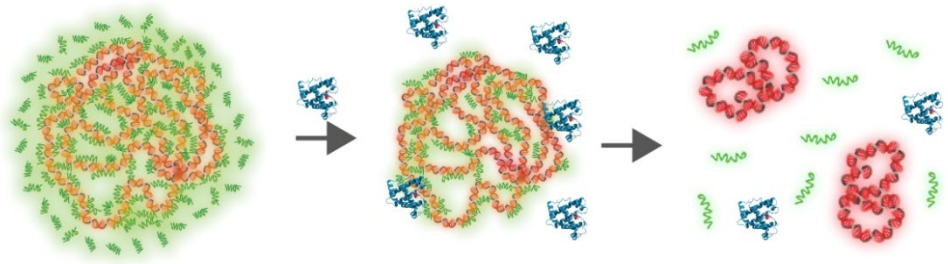

Figure 3.16 Schematic representation of the destabilization of the polyplexes in time in the presence of serum. First serum proteins adsorb to the complex and displace few r9 localizations, but the structure of the complex is preserved. With increasing incubation times or serum concentrations the polyplexes are totally decomplexed.

3.5. Conclusions

In this Chapter, an in-depth study of the structure and composition of polyplexes containing mRNA and the cell-penetrating peptide R9 using dSTORM imaging has been presented as a new tool to study polyplexes stability in complex media. The results show both, qualitative and quantitative differences in the mRNA and peptide content of individual polyplexes formed at different N/P ratios. Importantly, a minimum excess of peptide was required to condense the mRNA into polyplexes as at N/P 1 no distinct clusters could be observed. At N/P 3 the number of peptides was sufficient to pack the mRNA into compact polyplexes. With an increase of N/P to 5 the R9 content and peptide to mRNA ratio in the polyplexes further increased reaching a plateau around N/P 5. The possibility to image individual polyplexes allowed us to dissect the relationship between the relative content of the two components and the size of the polyplexes demonstrating next to a positive correlation of both components also with respect to size, also some heterogeneity in packing density and an increase in packing density with increasing N/P ratio. Our analyses clearly demonstrate that the insights gained through the STORM analysis of the polyplexes directly translate into a better understanding of cellular uptake experiments. From N/P 5 to N/P 7 the characteristics of the polyplexes were the same which explains why they showed the same cellular uptake efficiency. At N/P 3 sufficient mRNA encapsulation was achieved for only a fraction of polyplexes as evident from the large heterogeneity of polyplexes at the molecular level, demonstrated by STORM. Finally, the imaging of the destabilization of polyplexes in the presence of serum provided mechanistic insights into the disassembly mechanism, a crucial aspect for the *in vivo* performance of gene carriers. Our study highlights the potential of multicolor super-resolution microscopy to shed new light onto the nanoscale structure and stoichiometry of polyplexes in complex media, a key aspect for the understanding of gene delivery carriers.

3.6. Perspectives

To provide insights into the broad applicability of dSTORM to understand the stability of polyplexes in the presence of serum, polyplexes formulated with amphiphilic alkylated poly(α)glutamate amine (APA) complexed with siRNA or siRNA and miRNA were studied. Both formulations were imaged after being incubated for 1 hour with 10% FBS and 75% FBS and compared to the plain polyplexes, as shown in Figure 3.19. Interestingly, polyplexes formulated with both siRNA and miRNA were forming bigger aggregates than those formulated using just siRNA. After being incubated for 1 hour in 10% FBS the big aggregates of miRNA/siRNA polyplexes disappeared and smaller complexes were observed. Moreover, in 75% FBS there were still complexed polyplexes, however, also free siRNA was observed. In contrast, polyplexes formulated only with siRNA were stable for 1 hour in 10% FBS but mostly free siRNA was observed when incubated with 75% FBS. Of notice, both formulations were more stable than R9-peptide polyplexes which after 1 hour completely decomplexed at any FBS content.

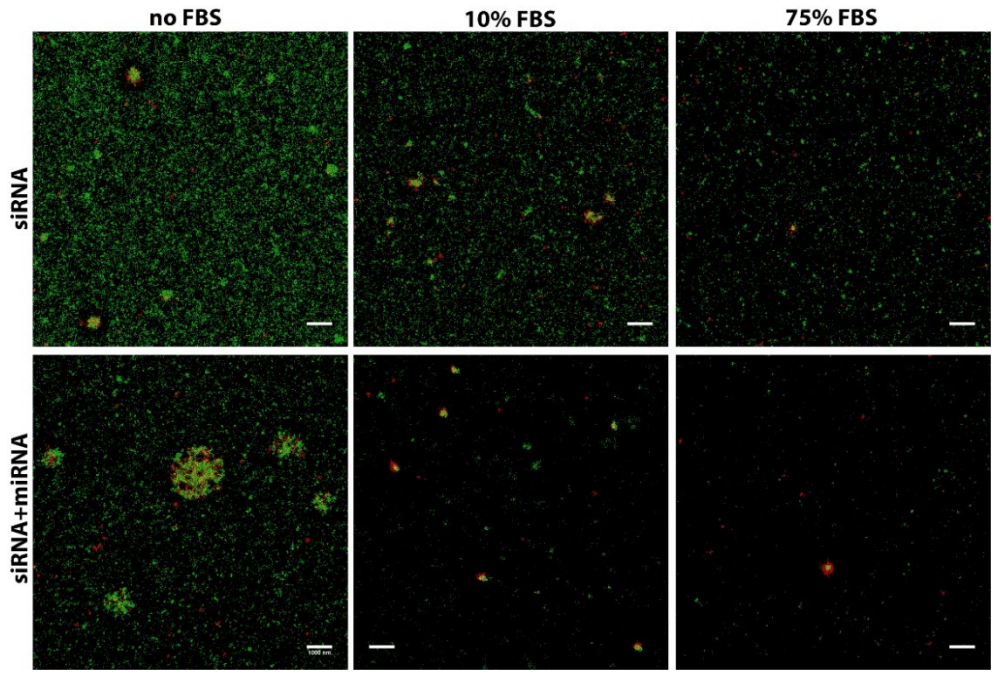

Figure 3.17 Stability of APA polyplexes in complex medium. APA polyplexes formulated using only siRNA or a mixture of siRNA and miRNA were images before and after serum incubation (either 10% or 75% v/v). Red corresponds to siRNA molecules and green to APA molecules. Scale bar 1 μm.

Overall, our studies demonstrate the applicability of dSTORM to follow the stability of another polyplexes type in complex media. In addition, the low stability observed for all investigated systems at high FBS concentrations evidences the need of understanding the

stability of polyplexes in serum prior to cell internalization and *in vitro* and *in vivo* transfection studies.

Another interesting applicability of dSTORM imaging is to correlate the release of nucleic acid molecules with the transfection efficiency of the system. In this framework, it has to be considered that dSTORM imaging is possible only in fixed cells and therefore optimization of the fixation procedure to retain the polyplex structure is necessary. Therefore, the study of r9- mRNA polyplexes internalization was not possible due to the poor fixability of the peptide. This observation on CPPs has already been reported elsewhere before (Richard et at., 2002). We therefore concluded that r9 polyplexes are not suitable for cell analysis. However, we exploited the possibility to perform similar measurements using polymer-based polyplexes, specifically Poly(β-amino ester)s. In these cases, the polymers are fixable and the structure of the polyplexes preserved, allowing for stoichiometry quantification in cells in time. dSTORM images acquired after a pulse of 30 minutes and different chase times are shown in Figure 3.20, where the polymer is represented in red and DNA molecules in green. At time 0 we can observe clusters of both colors mainly in the membrane or close to it. With

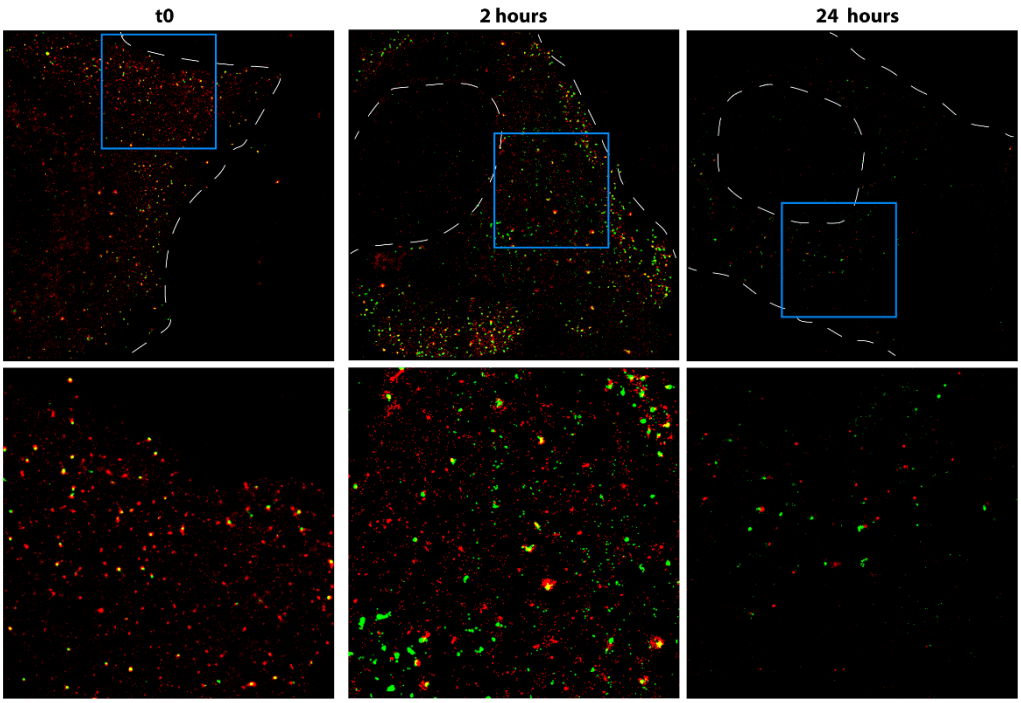

Figure 3.18 Polyplexes decomplexed in time inside cells. Polyplexes were incubated for 30 minutes with Cos7 cells, followed by washing steps to remove non-internalized nanostructures. To follow the decomplexation of the polyplexes, cells were further culture and fixed at different time points. Representative images of internalized polyplexes (red-polymer, green-DNA) obtained after the washing step (t0), after 2 hours and after 24 hours. Lower row corresponds to a zoom in section of the upper row. Membrane and nucleus of the cells are indicated using dashed lines.

time we can see that polyplexes were trafficking towards a region closer to the nucleus, and that the polymer was lost or degraded. This experiment proves the applicability of dSTORM to study not only stability of polyplexes in complex media but decomplexation of the system inside the cells, which could be correlated with the transfection efficiency of the nanocarrier. In conclusion, we believe that super-resolution microscopy can nicely complement the current techniques for polyplexes characterization contributing to guide the design of more effective oligonucleotide therapeutics.

3.7. Experimental section

3.7.1. Reagents

N-terminally acetylated R9 and AlexaFluor488-R9 were purchased as peptide amides from EMC microcollections (Tübingen, Germany). Firefly luciferase-coding mRNA (L6107 and L6401 from Trilink, San Diego, USA) was 1929 nucleotides in length, capped with Cap 0, polyadenylated and modified with 5-methylcytidine and pseudouridine, with or without Cyanine 5 fluorescent labeling (Cyanine5-UTP:Pseudo-UTP 1:3). The mRNA was kept in the original 10 mM Tris-HCl buffer, pH 7.5. The approximate number of Cy5 labels per mRNA was determined from the ratio of Cy5 and mRNA concentrations extrapolated from measuring the extinction of a 10x dilution in water using a NanoDrop ND-1000 (Thermo Fisher, Massachusetts, USA) detailed information can be found in the Supplementary Information. The mRNA and Cy5 concentrations in the sample were calculated from the absorption profile using the MicroArray function of the NanoDrop 1000 (Thermo Fisher).

3.7.2. Polyplex preparation

The N/P ratio was calculated by dividing the positive charges of the side-chain amino groups of the peptides (9 for R9) through the number of negative charges of the mRNA phosphate backbone (1929). For R9 polyplexes of N/P 5, the final peptide concentration was set to 50 μM. The N/P ratio for nona-arginine polyplexes was varied by maintaining the mRNA concentration at 0.045 μM (1160 ng).

For polyplex formation, equal volumes of diluted solutions of CPP and mRNA were prepared in water. The mixing was performed by simultaneous expulsion of the fluid from two identical micro-pipettes arranged to create an obtuse angle on the wall of an Eppendorf tube. For optimal imaging of R9 polyplexes, the AlexaFluor488 labeled R9 was pre-mixed with unlabeled R9 at 1.25% final labeling percentage.

3.7.3. DLS measurements

Several dilutions were prepared from non-fluorescently labeled polyplexes in RNase-free water and measured using a Zetasizer Nano-ZS ZEN 3600 (Malvern Instruments, Germany).

3.7.4. Microscopy sample preparation

Oxygen depleting dSTORM buffer was prepared fresh for every experiment using RNase-free MilliQ water, glucose (5% w/v), glucose oxidase (0.5 mg/mL), catalase (40 μg/μL) and β-mercaptomethylamine (100 mM; all Sigma Aldrich).

The microscopy slide was prepared using two stripes of double-sided adhesive tape that secured the coverslip on the glass slide. Polyplex solution was pipetted in the remaining space, requiring ~ 35 μL of sample solution. After 10-15 min incubation at room temperature, unbound polyplexes were washed by flushing 2 times 40 μL STORM buffer, followed by the addition 35 μL water-based solution of TetraSpeck Microspheres (0.1 μm, Life Technologies/Thermo Fisher, Massachusetts, USA) for drift-tracking. After 5-10 min of incubation, unbound particles were removed by flushing again 2 times 40 μL of dSTORM buffer. The sample was placed in the microscope upside-down, for imaging through the cover-slip (150 μm thickness, 24x24 mm size).

3.7.5. dSTORM microscopy

Microscopy was performed on a Nikon N-STORM system (Nikon Europe, Amsterdam) using three laser-lines: 488 nm (~80 mW) for AlexaFluor488, 561 nm (~80 mW) for TetraSpec Microspheres, and 647 nm (~160 mW) for Cy5 fluorescence. The sample was illuminated using a total internal reflection fluorescence (TIRF) alignment system and the z-level was kept constant by Nikon perfect focus system. Fluorescence was captured using a 100x Nikon oil-immersion objective with 1.49 NA and passed through a quad-band pass dichroic filter (9733 Nikon). Images were captured by the in-built Hamamatsu ORCA-Flash 4.0 camera on a 256x256 pixels field (170 nm/pixel) at a rate of 20 ms/frame. dSTORM images contained 20,000 and 40,000 frames for the 647 nm and 488 nm channels respectively at 100% laser power. TetraSpec Microspheres were imaged once every 100 frames using 5% laser power in the 561 nm channel. Total imaging time was approx. 25 min/image.

3.7.6. Image analysis

Identification of individual blinks in each frame was performed by fitting a 2D Gaussian function on the intensity profile in NIS Elements software (Nikon). For all experiments, the identification thresholds (the difference between the number of photons of the detected pixel and the surrounding pixels) were kept constant: 250 photons for the 647 nm channel (mRNA-Cy5), 200 photons for the 488 nm channel (R9-Alexa Fluor 488) and 700 photons for the 561 nm channel (TetraSpec Microspheres for drift correction). In order to exclude non-blinking molecules from consecutive frames, the trace length was set from 1 to 5, meaning that a molecule "on" for less than five consecutive frames was counted as a single localization, while a molecule "on" for more than five consecutive frames was discarded. No filter for the number of photons was applied.

The dSTORM image was exported as a list of localizations in ".txt" format and analyzed using a MatLab script previously described in Chapter 2. The first 500 frames of the Cy5-mRNA and 1000 of the Alexa488-R9 were excluded to let the blinking equilibrate after the initial sample illumination. The mRNA-Cy5 localizations were clustered using a mean shift cluster algorithm with a bandwidth of 65 nm. An ellipse was fitted on the obtained clusters in order to apply filtering with the following parameters: minimum 10 localizations, minimum 10 nm for the small diameter, maximum 225 nm diameter for the longest axis, maximum elongation factor of 2.3 (representing the ratio of the long and short axes of the ellipse) and minimum 150 nm distance between cluster density centers. Using the cluster centers, circles to determine the polyplex size were fitted on the mRNA-Cy5 localizations to contain 90% of the points in each cluster. The circle radius was further checked to be minimum 5 nm and maximum 125.5 nm. The analysis output consisted of the number of localizations per cluster for mRNA-Cy5 (all clustered points) and Alexa488-R9 (the localizations within 1.2 times the circle radius) as well as the radius of the fitted circle for each identified cluster.

3.7.7. Polyplex internalization experiments

For cell biological experiments, a 10-fold lower mRNA concentration than for the dSTORM analysis was used. Polyplexes were formed at an mRNA concentration of 45 pM and peptide concentrations of 5, 15, 25 and 35 μM in increasing order of N/P ratio. For cellular uptake studies, the polyplexes were diluted 1:10. Fluorescein-labeled R9 was pre-mixed with unlabeled R9 at a ratio of 1:10. Polyplexes were formed as described previously and a 1:10 dilution of polyplex solution in RNase-free water was used for DLS measurements.

HeLa cells (DSMZ ACC-57) were maintained in sterile conditions in Dulbecco's Modified Eagle's medium (DMEM,Gibco) supplemented with 10% fetal calf serum (FCS, PAN-biotech, Aidenbach, Germany). HeLa cells were seeded in an 8-well chambered coverslip one day prior to the experiment (4.5*104 cells/well). On the day of the experiment, cells were incubated with 250 μL of polyplex solution in FCS-free DMEM for 60 minutes at 37 °C, 5% CO2. Cells were then washed three times with FCS-free DMEM and kept in Opti-MEM 1 reduced serum medium. Live cells were imaged directly using a Leica SP5 + FCS confocal microscope (Leica Microsystems), equipped with an HCX PL APO 63x 1.2 water immersion lens. Fluorescein was excited at 488 nm using an Argon ion laser and emission was collected between 495 and 545 nm. Cy5 was excited at 633 nm using a HeNe laser and emission was collected between 640 and 720 nm.

Images were quantitated with Fiji image analysis software37. In brief, noise was reduced with a low pass filter followed by generation of threshold-based binary masks for extraction of vesicular fluorescence. Thresholds were adjusted independently for both channels. The pixel numbers of the binary masks were divided by the number of cells to determine average cellular pixel numbers. Average extracellular intensities were extracted from regions-of-interest outside cells from images acquired at higher detector sensitivity. Data for both

independent experiments were normalized to the sum of all conditions and averaged. Error bars correspond to standard deviations of the means.

3.7.8. Quantification of the number of Cy5 molecules per mRNA molecule

First, the theoretical number of Cy5 molecules per mRNA molecules were calculated based on the data obtained from the provider. The mRNA contains a ratio of 1 pseudo-UTP: 3 UTP; the total number of mRNA bases is 1929 and considering 1 in every 4 bases is UTP we obtain 482 UTP bases. Therefore, theoretically we should have 125 Cy5 per mRNA molecule.

To experimentally verify the number of Cy5 dyes per molecule, a solution of mRNA-Cy5 at 20 ng/μL in MiliQ water was prepared and the absorbance at 260 nm and 280 nm (to calculate the real mRNA concentration) and at 647 nm (to calculate the Cy5 concentration) was measured in triplicates using a Nanodrop. We measured to have 0.973 μg/mL mRNA in the stock solution, which was close to the theoretical 1 μg/mL, and 40.5 μM Cy5. Then, using these concentrations we calculated the mean number of Cy5 molecules per mRNA molecule to be 27, therefore we have one labeled base every 70 bases.

3.7.9. Polyplexes with single labelled-molecules

To get to quantitative molecules count per polyplexes using dSTORM, one must consider that the dye can be localized several times during acquisition since fluorophores are subject to blinking. To take this effect into account it is necessary to calibrate the measurements by estimating the statistical distribution of these blinking events. Since this phenomenon is known to highly depend on the environment the number of localizations per individual molecule were estimated from measurements performed under similar conditions than during the main experiments. In the present work, to independent measurements were done, the first to detect single mRNA molecules and the second to detect single R9 molecules. In these experiments, the labeled mRNA-Cy5 or Alexa488-R9 respectively were diluted with unlabeled mRNA or R9 molecules until reaching a concentration where only one labeled molecule remained per polyplex. In each sample, the opposite compound, which was not diluted, was used as a reference for polyplex identification during image quantification.

3.7.10. Simulation. Parameters estimation

To gain further insight we designed and implement a program that can simulate the underlying process of stochastic photoactivation to compare its output to the measurements. Agreement of simulation and experiment for a particular condition demonstrates that the correct assumptions on likelihood of photoactivation were made, a prerequisite for a quantitative analysis.

The simulation requires the input of parameters, that should be chosen in a reasonable manner. Here we discuss how we estimated the required parameters, see Figure S2. Most of

these parameters are straight forward to estimate, such as i) number of frames for each kind of dyes, ii) number of clusters = polyplexes to be simulated in one run, iii) number of green-dyes = labeled peptides in each cluster, iv) number of mRNA on average in each cluster. These quantities can be chosen to be deterministic for each polyplexes or to follow a possion distribution, where in this case the input corresponds to mean. In all our simulations of polyplexes we use a Poisson distribution to account for the heterogeneity across different polyplexes. Also, we assumed the number of peptides and mRNA are independent from one another to simplify the simulation. Only the probabilities of changing the state of a dye remain to be estimated.

For the peptide for which each peptide carried exactly one label, the probability of activation of the dye was calculated by using the data obtained from imaging polyplexes containing a single AlexaFluor488-R9. This was achieved by diluting the AlexaFluor488-R9 sample with non-labelled R9 down to 0.0002%. We compute the average number of times these single dyes were active and divide this by the total number of frames to obtain a probability of activation of 0.0000548. The probability of deactivation was estimated using the average number of consecutive frames a dye stays ON once it is activated, which is one of the outputs of the NIS-elements software used to process the images. This number was estimated from the experimental data of the single AlexaFluor488-R9 and found to be 1.85 frames. Then, we used the simulator to simulate the blinking behavior of single peptides and we calculated the cumulative mean of this same value (number of consecutive frames a dye stays ON once it is activated) using different deactivation probabilities from 0.25 to 0.8. After comparing the different simulations, the probability of deactivation was estimated to be 0.37, as the cumulative mean number of consecutive frames was stable at 1.855 close to the experimentally calculated one 1.85.

Having establish the probability of activation and deactivation the probability of bleaching was determined. The number of detected dyes per time frame of experimental and simulated data considering 0.1 as the probability of bleaching were plotted and compared. The data was binned every 1000 frames and a linear fitting was applied to compare simulation and experimental data. The slope of the curve was similar for both being -0.008 and -0.006 for the simulated and experimental data, respectively, Therefore, 0.1 was considered the bleaching probability of the Alexa488 dye in r9 molecules.

3.7.11. dSTORM imaging APA polyplexes in FBS

Eighty-four μL (0.84 mg) of APA (from a 10 mg/mL stock) were diluted in a mixture of 1037 μL ultra-pure water (UPW) and 1120 μL of filtered 20% glucose solution in UPW and pipetted. One hundred and seventy one μL (34.2 nmol) of siRNA from a stock solution of 200 μM were diluted in 2070 μL UPW and pipetted. Both solutions were mixed and incubated for 10 minutes before further experiments. Incubation with FBS was carried out at 37ºC for 1 h.

To perform direct STORM (dSTORM) imaging polyplexes were immobilized by adsorption onto the surface of a flow chamber assembled from a glass slide and a coverslip (24mm x 24 mm, thickness 0.15 mm) separated by double-sided tape. The flow chamber was previously treated with unlabeled APA for 1 h to favor polyplexes adsorption, and washed 3 times with PBS to remove the unbound APA before polyplexes addition. After polyplexes being incubated for 10-15 min unbound structures were removed by washing the chamber with STORM buffer. Then, TetraSpeck™ Microspheres (0.1 μm, Life Technology) were added and immobilized by adsorption onto the surface to correct the drift during acquisition. Finally, non-adsorbed TetraSpeck™ Microspheres were removed by washing the chamber twice with STORM buffer. The STORM buffer used was a new imaging buffer, OxEA, described by Nahidiazar et al.

STORM images were acquired using a Nikon N-STORM system configured for total internal reflection fluorescence (TIRF) imaging. APA-FITC was imaged by means of a 488nm laser (80 mW), siRNA Rac1-Cy5 was imaged by means of a 647nm laser (160 mW) and TetraSpeck™ Microspheres were imaged by means of a 561nm (80 mW). No activation UV light was employed. Measurements of 20,000 frames for the 488 channel and 12,000 frames for the 647 channel were acquired and every 100 frames a frame for the 561 channel (drift correction) was acquired. Fluorescence was collected by means of a Nikon 100x, 1.49 NA oil immersion objective and passed through a quad-band pass dichroic filter (97335 Nikon). Images were acquired onto a 256x256 pixel region (pixel size 0.16μm) of a Hamamatsu ORCA-Flash 4.0 camera at 10 ms integration time. STORM images were analyzed with the STORM module of the NIS element Nikon software. The NIS elements Nikon software generates a list of localizations by Gaussian fitting of blinking dyes in the acquired movie of conventional microscopic images.

3.7.12. dSTORM image of pBAE polyplexes cell internalization

Polyplexes were prepared as detailed before[31]. In brief, they were formulated by mixing equal volumes of pGFP and pBAE polymer at a 1 : 25 weight ratio (w/w) in NaOAc buffer solution (12.5 mM, pH 5.0). pGFP was added over the polymer solution, mixed vigorously by pipetting, and the mixture was incubated for 30 minutes at 25 °C. Then, the mixture was added into an equal volume of Milli-Q H2O, followed by another equal volume of HEPES buffer (20 Mm, pH 7.4) with 4 wt% of sucrose. Polyplexes were lyophilized and stored at −20 °C. On the day of use, they were redispersed in the initial preparation volume of Milli-Q water. For optimal dSTORM imaging, polyplexes were prepared using 1% Cy5 labelled pBAE and 25% Cy3 labelled pDNA.

COS-7 cells (ATCC® CRL-1651™) were cultured in DMEM containing 10% FBS, 2 mM l-glutamine, 100 units per mL penicillin and 100 μg mL−1 streptomycin. Cells were seeded at a density of 30 000 cells per well with 400 μL of media in an 8-well Nunc™ Lab-Tek™ (Thermo Fisher Scientific®) and were allowed to grow overnight at 37 °C and 5% CO2, to reach 70–

90% confluence. Cells were incubated with 400 μL of diluted polyplexes at a concentration of 3.75 ng pGFP μL−1 in full media for 30 minutes in a standard CO2 incubator, washed with PBS and grown for 0 h, 2 h, and 24 h before fixation. Then, cells were fixed for 15 minutes using 4% PFA at room temperature under stirring conditions and washed 3 times with PBS. For imaging purposes, 200 μL of dSTORM buffer was added to each well.

Images were acquired using NIS-Elements software in a Nikon Eclipse Ti microscope (Nikon Europe, Amsterdam). Cy5-labelled pBAE was imaged with a 647 nm laser (160 mW), Cy3-labelled pDNA was imaged with a 561 nm laser (80 mV) and GFP was imaged with a 488 nm laser (1.6 mW). The sample was illuminated using a total internal reflection fluorescence (TIRF) alignment system and the z-level was kept constant using a Nikon perfect focus system. Fluorescence was recorded using a Nikon 100×, 1.49 NA oil immersion objective and passed through a quad-band pass dichroic filter (97335 Nikon). Images were acquired onto a 256 × 256 pixel region (pixel size 0.16 μm) of a Hamamatsu 19 ORCA-Flash 4.0 camera at 10 and 50 ms integration time for dSTORM and GFP imaging, respectively. For dSTORM images, 21 000 and 20 000 frames were obtained for the 647 nm and the 567 nm channels, respectively. NIS Elements software was used to obtain the super resolution image.

.

3.8. References

(1) van Asbeck, A. H.; Beyerle, A.; McNeill, H.; Bovee-Geurts, P. H. M.; Lindberg, S.; Verdurmen, W. P. R.; Hällbrink, M.; Langel, Ü.; Heidenreich, O.; Brock, R. Molecular Parameters of SiRNA–Cell Penetrating Peptide Nanocomplexes for Efficient Cellular Delivery. ACS Nano 2013, 7 (5), 3797–3807. https://doi.org/10.1021/nn305754c.

(2) Scomparin, A.; Polyak, D.; Krivitsky, A.; Satchi-Fainaro, R. Achieving Successful Delivery of Oligonucleotides — From Physico-Chemical Characterization to in Vivo Evaluation. Biotechnol. Adv. 2015, 33 (6, Part 3), 1294–1309. https://doi.org/10.1016/j.biotechadv.2015.04.008.

(3) Lee, J. B.; Hong, J.; Bonner, D. K.; Poon, Z.; Hammond, P. T. Self-Assembled RNA Interference Microsponges for Efficient SiRNA Delivery. Nat. Mater. 2012, 11 (4), 316–322. https://doi.org/10.1038/nmat3253.

(4) Patil, M. L.; Zhang, M.; Taratula, O.; Garbuzenko, O. B.; He, H.; Minko, T. Internally Cationic Polyamidoamine PAMAM-OH Dendrimers for SiRNA Delivery: Effect of the Degree of Quaternization and Cancer Targeting. Biomacromolecules 2009, 10 (2), 258–266. https://doi.org/10.1021/bm8009973.

(5) Ofek, P.; Fischer, W.; Calderón, M.; Haag, R.; Satchi-Fainaro, R. In Vivo Delivery of Small Interfering RNA to Tumors and Their Vasculature by Novel Dendritic Nanocarriers. FASEB J. 2010, 24 (9), 3122–3134. https://doi.org/10.1096/fj.09-149641.

(6) García-Sosa, A. T.; Tulp, I.; Langel, K.; Langel, Ü. Peptide-Ligand Binding Modeling of siRNA with Cell-Penetrating Peptides https://www.hindawi.com/journals/bmri/2014/257040/ref/ (accessed May 24, 2018). https://doi.org/10.1155/2014/257040.

(7) Meneksedag-Erol, D.; Tang, T.; Uludağ, H. Molecular Modeling of Polynucleotide Complexes. Biomaterials 2014, 35 (25), 7068–7076. https://doi.org/10.1016/j.biomaterials.2014.04.103.

(8) Majzoub, R. N.; Ewert, K. K.; Safinya, C. R. Cationic Liposome–Nucleic Acid Nanoparticle Assemblies with Applications in Gene Delivery and Gene Silencing. Phil Trans R Soc A 2016, 374 (2072), 20150129. https://doi.org/10.1098/rsta.2015.0129.

(9) Burgert, A.; Schlegel, J.; Bécam, J.; Doose, S.; Bieberich, E.; Schubert-Unkmeir, A.; Sauer, M. Characterization of Plasma Membrane Ceramides by Super-Resolution Microscopy. Angew. Chem. 2017, 129 (22), 6227–6231. https://doi.org/10.1002/ange.201700570.

(10) Letschert, S.; Göhler, A.; Franke, C.; Bertleff-Zieschang, N.; Memmel, E.; Doose, S.; Seibel, J.; Sauer, M. Super-Resolution Imaging of Plasma Membrane Glycans. Angew. Chem. Int. Ed. 2014, 53 (41), 10921–10924. https://doi.org/10.1002/anie.201406045.

(11) Fricke, F.; Beaudouin, J.; Eils, R.; Heilemann, M. One, Two or Three? Probing the Stoichiometry of Membrane Proteins by Single-Molecule Localization Microscopy. Sci. Rep. 2015, 5, 14072. https://doi.org/10.1038/srep14072.

(12) Zanacchi, F. C.; Manzo, C.; Alvarez, A. S.; Derr, N. D.; Garcia-Parajo, M. F.; Lakadamyali, M. A DNA Origami Platform for Quantifying Protein Copy Number in Super-Resolution. Nat. Methods 2017, 14 (8), 789–792. https://doi.org/10.1038/nmeth.4342.

(13) Puchner, E. M.; Walter, J. M.; Kasper, R.; Huang, B.; Lim, W. A. Counting Molecules in Single Organelles with Superresolution Microscopy Allows Tracking of the Endosome Maturation Trajectory. Proc. Natl. Acad. Sci. 2013, 110 (40), 16015–16020. https://doi.org/10.1073/pnas.1309676110.

(14) Koren, E.; Torchilin, V. P. Cell-Penetrating Peptides: Breaking through to the Other Side. Trends Mol. Med. 2012, 18 (7), 385–393. https://doi.org/10.1016/j.molmed.2012.04.012.

(15) Collado Camps, E.; Brock, R. An Opportunistic Route to Success: Towards a Change of Paradigm to Fully Exploit the Potential of Cell-Penetrating Peptides. Bioorg. Med. Chem. 2017. https://doi.org/10.1016/j.bmc.2017.11.004.

(16) Heitz Frederic; Morris May Catherine; Divita Gilles. Twenty Years of Cell-penetrating Peptides: From Molecular Mechanisms to Therapeutics. Br. J. Pharmacol. 2009, 157 (2), 195–206. https://doi.org/10.1111/j.1476-5381.2009.00057.x.

(17) Zhang, P.; Wagner, E. History of Polymeric Gene Delivery Systems. Top. Curr. Chem. 2017, 375 (2), 26. https://doi.org/10.1007/s41061-017-0112-0.

(18) Lächelt, U.; Wagner, E. Nucleic Acid Therapeutics Using Polyplexes: A Journey of 50 Years (and Beyond). Chem. Rev. 2015, 115 (19), 11043–11078. https://doi.org/10.1021/cr5006793.

(19) Debus, H.; Baumhof, P.; Probst, J.; Kissel, T. Delivery of Messenger RNA Using Poly(Ethylene Imine)–Poly(Ethylene Glycol)-Copolymer Blends for Polyplex Formation: Biophysical Characterization and in Vitro Transfection Properties. J. Controlled Release 2010, 148 (3), 334–343. https://doi.org/10.1016/j.jconrel.2010.09.007.

(20) Meng, Z.; O'Keeffe-Ahern, J.; Lyu, J.; Pierucci, L.; Zhou, D.; Wang, W. A New Developing Class of Gene Delivery: Messenger RNA-Based Therapeutics. Biomater. Sci. 2017, 5 (12), 2381–2392. https://doi.org/10.1039/C7BM00712D.

(21) Sahin, U.; Karikó, K.; Türeci, Ö. MRNA-Based Therapeutics — Developing a New Class of Drugs. Nat. Rev. Drug Discov. 2014, 13 (10), 759–780. https://doi.org/10.1038/nrd4278.

(22) Wu, R. P.; Youngblood, D. S.; Hassinger, J. N.; Lovejoy, C. E.; Nelson, M. H.; Iversen, P. L.; Moulton, H. M. Cell-Penetrating Peptides as Transporters for Morpholino Oligomers: Effects of Amino Acid Composition on Intracellular Delivery and Cytotoxicity. Nucleic Acids Res. 2007, 35 (15), 5182–5191. https://doi.org/10.1093/nar/gkm478.

(23) Futaki, S.; Ohashi, W.; Suzuki, T.; Niwa, M.; Tanaka, S.; Ueda, K.; Harashima, H.; Sugiura, Y. Stearylated Arginine-Rich Peptides: A New Class of Transfection Systems. Bioconjug. Chem. 2001, 12 (6), 1005–1011. https://doi.org/10.1021/bc015508l.

(24) Vaidyanathan, S.; Chen, J.; Orr, B. G.; Banaszak Holl, M. M. Cationic Polymer Intercalation into the Lipid Membrane Enables Intact Polyplex DNA Escape from Endosomes for Gene Delivery. Mol. Pharm. 2016, 13 (6), 1967–1978. https://doi.org/10.1021/acs.molpharmaceut.6b00139.

(25) Lehto, T.; Vasconcelos, L.; Margus, H.; Figueroa, R.; Pooga, M.; Hällbrink, M.; Langel, Ü. Saturated Fatty Acid Analogues of Cell-Penetrating Peptide PepFect14: Role of Fatty Acid Modification in Complexation and Delivery of Splice-Correcting Oligonucleotides. Bioconjug. Chem. 2017, 28 (3), 782–792. https://doi.org/10.1021/acs.bioconjchem.6b00680.

(26) Jekhmane, S.; de Haas, R.; Paulino da Silva Filho, O.; van Asbeck, A. H.; Favretto, M. E.; Hernandez Garcia, A.; Brock, R.; de Vries, R. Virus-Like Particles of MRNA with Artificial Minimal Coat Proteins: Particle Formation, Stability, and Transfection Efficiency. Nucleic Acid Ther. 2017, 27 (3), 159–167. https://doi.org/10.1089/nat.2016.0660.

(27) Ezzat, K.; EL Andaloussi, S.; Zaghloul, E. M.; Lehto, T.; Lindberg, S.; Moreno, P. M. D.; Viola, J. R.; Magdy, T.; Abdo, R.; Guterstam, P.; et al. PepFect 14, a Novel Cell-Penetrating Peptide for Oligonucleotide Delivery in Solution and as Solid Formulation. Nucleic Acids Res. 2011, 39 (12), 5284–5298. https://doi.org/10.1093/nar/gkr072.

(28) Coltharp, C.; Yang, X.; Xiao, J. Quantitative Analysis of Single-Molecule Superresolution Images. Curr. Opin. Struct. Biol. 2014, 0, 112–121. https://doi.org/10.1016/j.sbi.2014.08.008.

(29) Albertazzi, L.; Zwaag, D. van der; Leenders, C. M. A.; Fitzner, R.; Hofstad, R. W. van der; Meijer, E. W. Probing Exchange Pathways in One-Dimensional Aggregates with Super-Resolution Microscopy. Science 2014, 344 (6183), 491–495. https://doi.org/10.1126/science.1250945.

(30) Wallbrecher, R.; Ackels, T.; Olea, R. A.; Klein, M. J.; Caillon, L.; Schiller, J.; Bovée-Geurts, P. H.; van Kuppevelt, T. H.; Ulrich, A. S.; Spehr, M.; et al. Membrane Permeation of Arginine-Rich Cell-Penetrating Peptides Independent of Transmembrane Potential as a Function of Lipid Composition and Membrane Fluidity. J. Controlled Release 2017, 256, 68–78. https://doi.org/10.1016/j.jconrel.2017.04.013.

(31) Segovia, N.; Dosta, P.; Cascante, A.; Ramos, V.; Borrós, S. Oligopeptide-Terminated Poly(β-Amino Ester)s for Highly Efficient Gene Delivery and Intracellular Localization. Acta Biomater. 2014, 10 (5), 2147–2158. https://doi.org/10.1016/j.actbio.2013.12.054.

Chapter 4 .
Micellar stability in biological media dictates internalization in living cells

The dynamic nature of polymeric assemblies makes their stability in biological media a crucial parameter for their potential use as drug delivery systems in vivo. Therefore, it is essential to study and understand the behavior of self-assembled nanocarriers under conditions that will be encountered in vivo such as extreme dilutions and interactions with blood proteins and cells. Herein, using a combination of fluorescence spectroscopy and microscopy, we studied four amphiphilic PEG-dendron hybrids and their self-assembled micelles in order to determine their structure-stability relations. The high molecular precision of the dendritic block enabled us to systematically tune the hydrophobicity and stability of the assembled micelles. Using micelles that change their fluorescent properties upon disassembly, we observed that serum proteins bind to and interact with the polymeric amphiphiles in both their assembled and monomeric states. These interactions strongly affected the stability and enzymatic degradation of the micelles. Finally, using spectrally-resolved confocal imaging, we determined the relations between the stability of the polymeric assemblies in biological media and their cell entry. Our results highlight the important interplay between molecular structure, micellar stability, and cell internalization pathways, pinpointing the high sensitivity of stability-activity relations to minor structural changes and the crucial role that these relations play in designing effective polymeric nanostructures for biomedical applications.

This work has been published as:
N. Feiner-Gracia, M. Buzhor, E. Fuentes, S. Pujals, R. Amir and L. Albertazzi, *j. Am. Chem. Soc.*, 2017, **139** (46), 16677-16687.

4.1. Introduction

Recently, self-assembled nanomaterials such as micelles and other polymeric assemblies have been gaining increasing attention as smart drug delivery systems,[1,2] as introduced in Chapter 1. The use of micelles as delivery systems presents several advantages: i) improved solubility of lipophilic drugs; ii) sustained release of encapsulated molecules in the body, and iii) the ability to target cells and/or tissues of interest in order to reduce side effects and increase therapeutic effectiveness. The potential and feasibility of using polymeric delivery systems has been recently demonstrated by the clinical approval of a micellar system: Genexol-PM.[3] The system is used in Europe and Asia for the delivery of paclitaxel in patients with metastatic breast cancer and small cell lung cancer. Despite this clinical success, Genexol remains the only clinically approved micellar delivery system and new strategies to enhance the performances of micellar nanocarriers are currently under investigation.[4]

One of the crucial challenges in using self-assembled nanomaterials is their stability in the biological media, (e.g., blood and serum). The importance of studying the stability of nanocarriers in complex media has been evidenced in Chapter 3, where we demonstrated that electrostatic interactions forming polyplexes can be disrupted due to blood proteins adsorption. Supramolecular stability of micelles may be also affected by the interactions of multiple biomolecular species present in the blood with the polymeric assemblies which may affect their structure and functionality.[5,6] Moreover, serum proteins can prematurely disassemble the micelle and lead to non-selective release of the cargo in healthy tissues. These issues are often overlooked in the literature, most likely due to the difficulties of studying micellar assemblies in complex biological media, as reflected in Chapter 1. Previous studies on stability of micelles in FBS, globulin, and BSA solutions were carried out by spectral analysis of two dyes, which form a FRET pair, encapsulated in polymeric micelle.[7–10] However, this study focused only on the dye release and did not provide information on the assembly state of the micelles. Due to the dynamic nature of self-assembled delivery systems, another key parameter that needs to be addressed when designing supramolecular nanocarriers is the extreme dilution that these self-assembled systems face when administrated intravenously.[11] Whereas many studies report the CMC values as an indicator of stability, these values are often measured in water or PBS and hence they do not provide information on the behavior in serum. Therefore, understanding how dilution and blood proteins affect micellar stability and degradation is of crucial importance for designing the next generation of delivery systems.

It is clear that in addition to high micellar stability, nanocarriers should also have a well-defined release mechanism that will allow them to selectively release their molecular cargo in a controlled manner only at the target site of disease. One very interesting possibility is to use enzymes or proteins to trigger the degradation and disassembly of micellar assemblies and re-lease of active cargo. The overexpression of enzymes such as matrix metalloproteinases (MMPs)[12] and cathepsin B6 in tumors can potentially be used to design micelles that will

effectively release drugs only in the disease tissues but not in healthy ones.[13] MMPs, for example, were used to release paclitaxel covalently linked to micelles formed from diblock copolymers[14,15] and polymers coupled to metalloprotease sensitive peptide (PVGLIG).10 In addition, several groups, including the Wooley,[16,17] Heise,[18,19] Thayumanavan[20–22] and Amir[23–25] groups, have independently reported the utilization of esterase and amidase degradable amphiphiles to trigger micelle disassembly and cargo release. The Thayumanavan group has also explored specific protein binding for triggering the disassembly of dendritic amphiphiles.[26,27]

In Chapter 4, we study the interactions of a series of four different enzymatically degradable amphiphiles and their micellar assemblies with serum proteins to understand the stability of these systems in serum and the consequent effect on cellular internalization. Carrying out a variety of fluorescence spectroscopy measurements in protein solutions and serum allowed us to understand the stability of the different micelles in the biological media, as well as, the differences in enzymatic responses of the nanosystems induced by the presence of proteins. In Chapter 2 and 3, super resolution imaging was used which provided high resolution but only static information. In this chapter we aimed to study the time evolution of micelles' stability, therefore, we used confocal microscopy which can be performed on live cells. Using spectral confocal microscopy, we were able to determine whether the labeled polymeric hybrids were internalized in their self-assembled (micellar) or disassembled (monomeric) forms, to track their intracellular localization, and to follow micelle disassembly inside the cell in real time. These data reveal the interactions of dynamic supramolecular systems with cells, paving the way for better understanding of these interactions and for rational design of micelle-based delivery systems with high stability, controllable release rates, and adjustable cellular internalization mechanisms.

4.2. Design and synthesis of enzyme-responsive micelles

The micelles used in this work were composed from PEG-dendron amphiphiles with enzymatically cleaved dendritic end-groups. Enzymatic degradation of the hydrophobic end-groups can increase the hydrophilicity of the hybrids, leading to their disassembly. The utilization of PEG-dendron hybrids as the polymeric amphiphiles granted us ultimate control over the mono-dispersity of the hydrophobic dendritic block,[28,29] allowing fine tuning of the amphiphilicity of the hybrids to enable a high-resolution study of structure-stability relations. A series of four fluorescently labeled amphiphilic PEG dendron hybrids that can report their self-assembly and disassembly through spectral response were synthesized following a previously reported methodology[a] (Figure 4.1).[30] The hybrids were labeled with 7-

[a] Synthesis and characterization of all hybrids was performed by M. Buzhor of R. Amir group in Tel Aviv University after designing together with them the structures of interest.

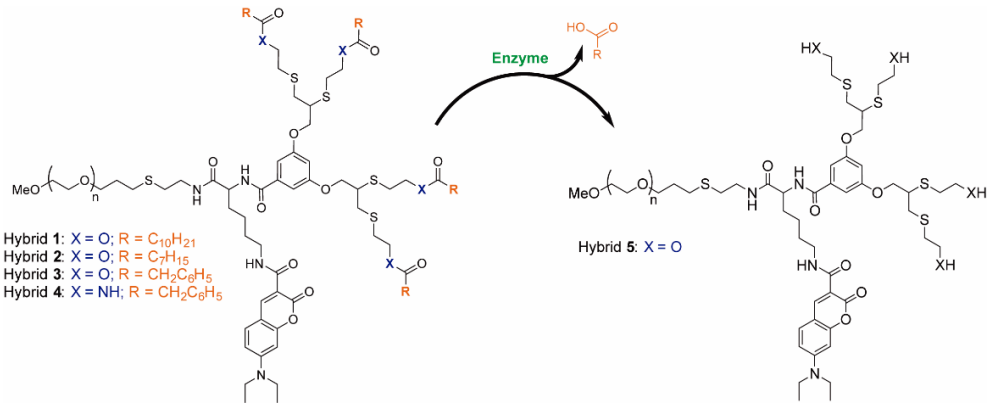

Figure 4.1 Molecular structure of the amphiphilic PEG-dendron hybrids and the hydrophilic hybrids formed after enzymatic degradation of the hydrophobic end-groups. PEG used was 5 kDa.

diethylamino-3-carbocy coumarin, which was shown to form excimers when the hybrids self-assemble into micelles, leading to a significant red-shift of the emission peak, from 480 nm to approximately 560 nm. Hence labeling the polymeric hybrids with this dye allowed us to distinguish easily between the micelles (Em ~ 560 nm) and the non-assembled monomeric hybrids (Em ~ 480 nm) even in complex biological media by obtaining fluorescent spectral information (Figure 4.2c). All hybrids were composed of dendrons with four lipophilic end-groups and differed by the type of enzymatically cleavable end-groups. Hybrids **1 – 3** had undecanoate, octanoate, or phenyl-acetate end-groups, respectively, which could be cleaved by an esterase (PLE) (Figure 4.2b). The undecanoate end-groups of hybrid 1 were selected based on previous results for non-labeled hybrids with similar end-groups, which showed remarkable stability toward enzymatic degradation.19 To systemically decrease the hydrophobicity of the dendrons, we synthesized hybrids 2 and 3,36 which had eight carbon

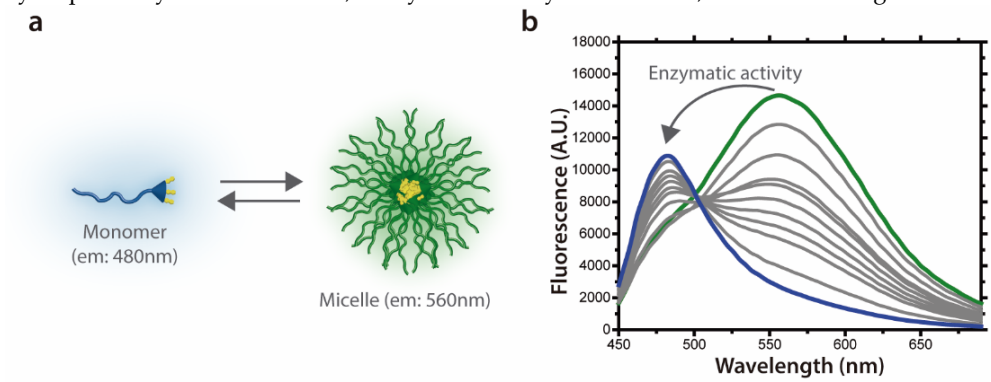

Figure 4.2 Hybrids' properties a. Schematic presentation of the monomer-micelle equilibrium and the difference in fluorescent emission wavelength due to formation of excimers only at the assembled state. **b**. Fluorescence spectra example at different time intervals during the enzymatic disassembly of hybrid **3** in PBS showing the differences in the emission spectrum of assembled and non-assembled hybrid.

atoms in each of their end-groups; the end-group of 2 was aliphatic end-groups, and that of 3 was aromatic. We expected that the dendron with the aromatic end-groups would be slightly less hydrophobic due to the higher polarity of the aromatic rings in comparison with the aliphatic chains.

In addition to the esterase-responsive hybrids, we prepared hybrid 4,[30] which had four phenyl acetamide end-groups that could be cleaved by the enzyme penicillin G amidase (PGA).[31] All hybrids were synthesized following a recently reported modular approach based on accelerated divergent growth of the dendron. In general, the synthetic methodology was based on growing the dendron from PEG-Lysine(Boc)Fmoc after deprotection of the Fmoc group, followed by conjugation of the labeling dye at the last step of the synthesis. All hybrids were synthesized in high overall yields and their characterization data correlated well with the expected theoretical values (more information can be obtained in the Experimental Section, Figure 4.3). Besides the four amphiphiles, hybrids **1 - 4**, we also synthesized hybrid 5 with four hydroxyl end-groups,[30] which is the expected degradation product of the three

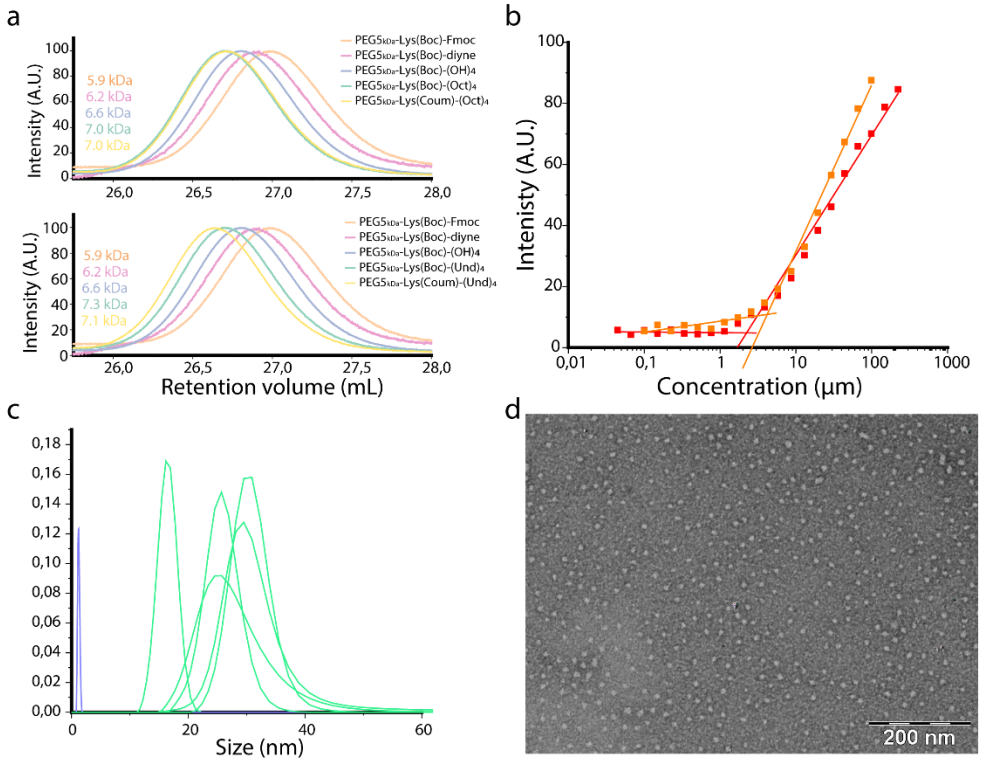

Figure 4.3 Characterization PEG-dendron hybrids. a, Gel permeation chromatography of hybrids 1 (top graph) and 2 (bottom graph). **b,** CMC characterization using Nile Red of hybrids 1 and 2. **c,** DLS data to characterize the hydrodynamic size of the hybrids 1-4 (green) and 5 (blue, monomer form). **d,** TEM image of hybrid 1 at 160 μM

esterase-responsive hybrids **1**, **2**, and **3** after complete enzymatic hydrolysis of all the hydrophobic end-groups. After the synthesis of the hybrids was completed, we determined their CMCs (Figure 4.3b) by using the solvatochromic dye Nile red.[32] The obtained values (in the range of 2 to 6 μM) were found to increase as the hydrophobicity of the dendrons decreased. DLS and TEM were then used to measure the size of the formed assemblies for hybrids **1** - **4**, and diameters of 22 - 36 nm were observed (Figure 4.3c-d), fitting well with the expected diameters of core-shell micellar assemblies. Importantly, DLS data for hydrophilic hybrid **5**, showed the sizes of around 3 nm (Figure S12), which correlate well with the expected size of individual non-assembled polymeric hybrid.

4.3. Stability of micelles in complex serum media

4.3.1. *Interactions of monomers and micelles with serum albumin*

In supramolecular systems, such as micelles, monomers and assemblies are in equilibrium and are both always present during their use as drug delivery systems; therefore, it is important to study the interactions of serum proteins with both the assembled and non-assembled states. In this sense, our system is unique as the coumarin label allows identification and study of both states of the system. First, we wanted to study whether there are any interactions between serum proteins and the micelles and/or the monomeric state (Figure 4.4a and b). To do this we designed two different assays, based on either solvatochromism or FRET. These assays aimed to dissect the interactions of serum proteins

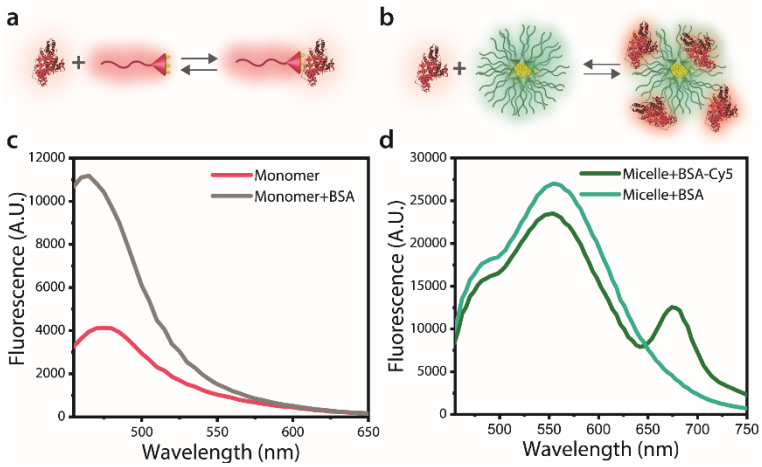

Figure 4.4 Albumin interacts with both monomer and micelles. a. Scheme of interaction BSA with the monomer. **b.** Scheme of interaction of BSA with micelle. **c.** Fluorescence emission spectra of hybrid **4** at a concentration of 2 μM in the absence or presence of BSA showing a solvatochromic effect. **d.** Fluorescence emission spectra of micelles of hybrid **3** (160 μM) in the presence of Cy5-labeled and unlabeled BSA show energy transfer from coumarin excimers in the micelles to the Cy5 on the BSA.

with the monomers and the assemblies, respectively. To examine the interaction of monomers with BSA we used hybrid **4**, which should have the highest hydrolytic stability of hybrids synthesized due to its amidic bonds, at a concentration slightly below its CMC. We mixed BSA (360 μM, close to blood concentration) with the hybrid and measured changes in fluorescence spectrum. At this low concentration of hybrid 4, the polymeric amphiphile was only in its monomeric form as confirmed by the emission at 480 nm in its fluorescence spectra (Figure 4.4cc), which is characteristic for the non-assembled state.[30] After BSA addition, we observed a significant increase in fluorescence emission intensity and a 15-nm blue-shift in the spectra. These alterations in the fluorescence spectra of the coumarin dye can be attributed to a solvatochromic effect due to the direct interaction between the monomer and BSA molecules. The interactions may be causing changes in the polarity of the microenvironment surrounding the dye upon protein binding which cause the spectra shift. Interestingly, our observations are in good agreement with previous reports using coumarin dyes as protein sensors.[33] In addition, similar studies using the hydrophilic hybrid **5**, which can only be in the monomer form, further confirmed the interactions of the labeled hybrid with the protein (Figure 4.5).

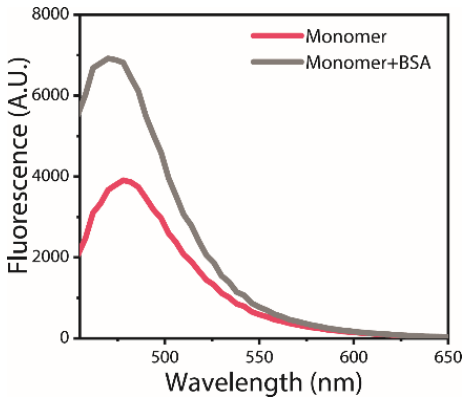

Figure 4.5 Interaction of monomer with BSA. Hybrid 5 at a concentration of 160 μM was incubated with BSA at a concentration of 400 μM. An increase in the emission intensity can be observed attributed to the solvathocromic effect of coumarin when interact with the monomer.

Next, to investigate the interactions of BSA with the micellar state, we labeled BSA with the dye Cy5, which serves as a FRET acceptor for the excimer of the coumarin dyes. An energy transfer would indicate that the assembled hybrids interact with the BSA molecules, due to overlap of the fluorescence emission spectra of the coumarin excimer with the excitation spectra of the Cy5. Micelles of hybrid **3** were incubated with either native BSA or Cy5-labeled BSA (Figure 2b), and the emitted fluorescence after micelle excitation was measured. The fluorescence spectra in Figure 2d, clearly showed the appearance of a new emission peak at 675 nm when the micelles were incubated with the Cy5-labeled BSA. This peak was produced by the energy transfer from the coumarin excimers inside the micelles to the Cy5 dye on the BSA, which were in close proximity. The energy transfer was further supported by the

observed decrease in intensity in the fluorescence emission of the micelles only in the presence of labeled BSA as well as by the non-fluorescence emission of BSA-Cy5 alone when excited in the same conditions. Due to FRET's high dependence on distance (1-10 nm), this experiment proves the direct interaction of BSA with micelles. This interaction may be produced by i) protein penetration inside the micelle due to the flexibility of the PEG shell or ii) proteins adsorption onto the PEG shell forming a protein corona.[34,35]

Based on both the increase in fluorescent emission of the non-assembled hybrids and the FRET results, we conclude that the BSA molecules directly and effectively interact in close proximity with both the monomeric hybrids and their micelles. We envision that these interactions may influence the stability of the system.

4.3.2. *Supramolecular stability in contact with serum proteins*

Supramolecular stability toward disassembly of micelles in serum-like conditions is of major importance to optimize the in vivo performance of nanocarriers. To evaluate the potential of the studied polymeric micelles to serve as delivery vehicles for *in vivo* experiments in the future, we aimed to study their micellar stability by mimicking these conditions *in vitro*. First, we determined the stability of the four types of micelles in the presence of increasing concentrations of BSA, as albumin is the most abundant protein in the blood. The concentration of BSA was systematically increased up to 1000 μM (two-fold higher than its concentration in blood), while the concentration of hybrids was kept constant at 160 μM. Fluorescence emission spectra were collected, and the ratios of the emission intensities for monomer to micelle were calculated (Figure 4.6).

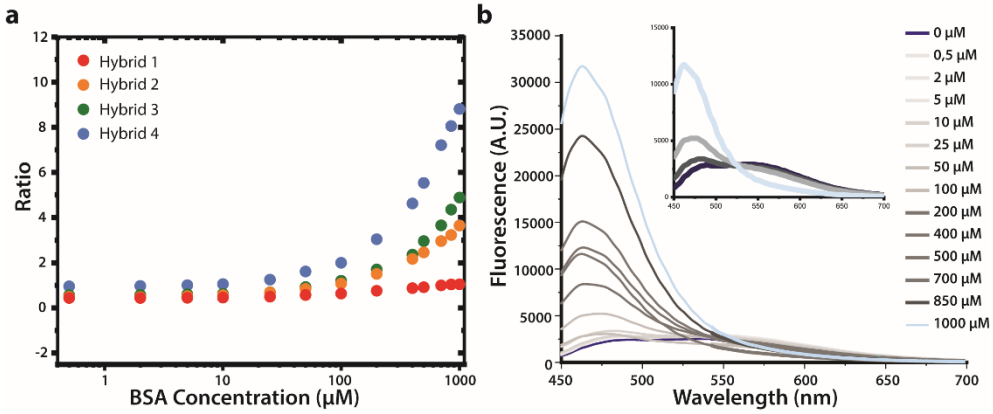

Figure 4.6 Supramolecular stability of the micelles as a function of BSA con-centration. a. Ratio of emitted fluorescence of monomer (~ 480 nm) versus micelle (~ 560 nm) at increasing concentrations of BSA of all hybrids subtypes. **b.** Fluorescence emission spectrum of hybrid **4** at increasing concentrations of BSA, from 0 to 1000 μM.

The obtained results showed that at low BSA concentrations (<10 μM of BSA, 160 μM of hybrid), all hybrid subtypes showed similar low ratios due to a major presence of micelles. Upon further increase in BSA concentration, the ratios for hybrids **2**, **3**, and **4** slightly increased, which may indicate that the BSA molecules started to interact with the monomer, leading to the solvatochromic effect that enhanced the fluorescence intensity of the monomer as discussed above. Interestingly, at concentrations higher than 100 μM, the ratios for hybrids **2**, **3**, and **4** in-ceased more profoundly as the micelles started to disassemble. The complete disappearance of the excimer peak at 560 nm (Figure 4.6b) confirmed that the disassembly of micelles formed by **2**, **3**, and **4** took place at around 100 μM BSA. In contrast, the ratio for hybrid **1** started to slightly increase only above 100 μM BSA, indicating that these micelles were resistant toward disruption by the interaction with BSA. These findings also suggest that micelles with aliphatic groups are more stable than those having aromatic groups, as micelles of hybrid **2** were found to be more stable than the micelles of hybrid **3**. Although a plateau was expected to be obtained in these experiments indicative of the full disassembly of the micelles, it was not observed, most likely due to the solvatochromic effect of the coumarin dye in the monomeric form. The solvatochromic effect can continuously enhance the emitted fluorescence intensity as discussed earlier.

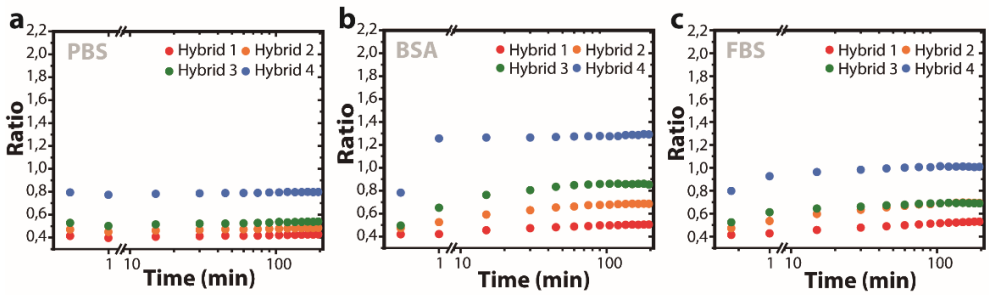

Figure 4.7 Supramolecular stability of the micelles as a function of time. Ratio of emitted fluorescence of monomer versus micelle of all hybrid's subtypes at different time intervals in **a.** PBS, **b.** 10 mg/mL BSA, and **c.** 10% FBS.

Next, we investigated the supramolecular stability of the micelles in time in the presence of serum (Figure 4.7). The experiments were performed either in 10% FBS, mimicking cellular assays conditions, or in BSA solution (10 mg/mL, 151.52 μM), mimicking its concentration in the blood. The stability of the micelles in PBS was measured as control, and the emission fluorescence spectra of micelles were recorded over time in the different conditions for all the hybrids subtypes. All four types of micelles were stable for more than 14 hours in PBS, whereas in 10% FBS and in BSA conditions they slightly disassembled, and micelles of different subtypes had different behaviors.

In both cellular assay mimicking and blood mimicking conditions, we observed an increase in the ratio as a function of time for all the micelles, corresponding to a mild disassembly of the structures. Interestingly, for hybrids **4** and **3** in BSA media, it resulted in slightly higher monomer/micelle ratio than it did in FBS. Moreover, kinetics of disruption were different for each hybrid. A rapid disassembly was observed for hybrid **4**, which reach the equilibrium state within 15 minutes, after which changes in the monomer/micelle ratio were less than 7.5% the total change. Hybrids **3** and **2** showed slower kinetics and need longer times to equilibrate, 45 and 75 minutes respectively, after the addition of the proteins' solutions. The ratio of hybrid **1** showed no significant change over time, confirming the previous results and demonstrating that hybrid **1** is not only the most thermodynamically stable but also kinetically the most stable. Lastly, the same experiment was performed at 37 ºC, mimicking body conditions, and we observed a reduction in stability at the higher temperature, but the same behaviors in PBS and FBS (Figure 4.8). Overall, these results illustrate how relatively small changes in molecular structure can lead to substantial

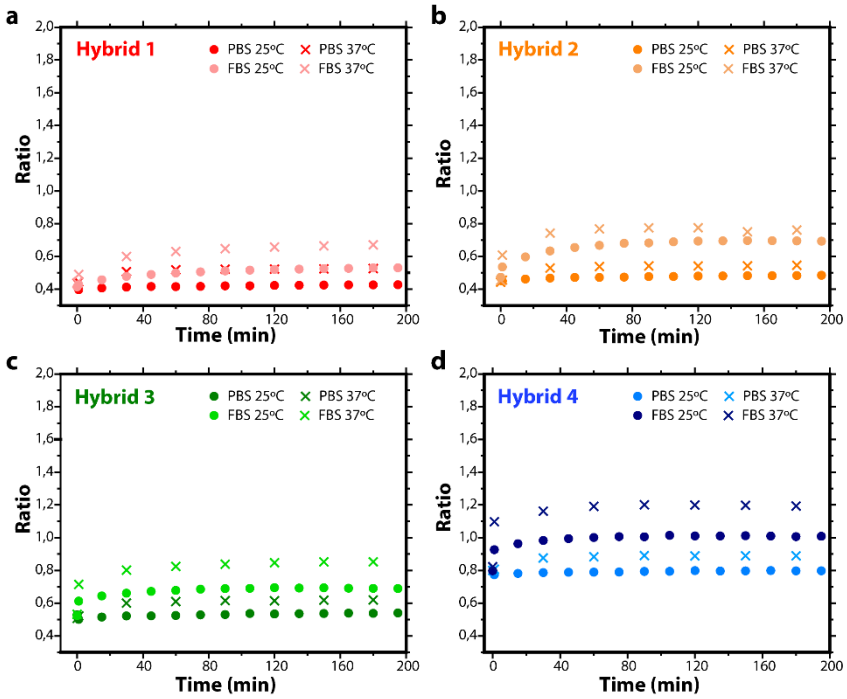

Figure 4.8 Stability as a function of time in PBS and 10% v/v FBS at 37ºC shows a smooth reduction of the stability in every condition compared to the stability at 25ºC. The graphs represent the ratio of monomer emitted fluorescence vs micelle emitted fluorescence **a.** Hybrid **1 b.** Hybrid **2 c.** Hybrid **3** and **d.** Hybrid **4**.

differences in micellar stability, with hybrid **1** being the most stable, followed by hybrids **2**, **3**, and **4**.

4.3.3. *Supramolecular stability upon extreme dilution*

When micelles are administered intravenously, they undergo a strong dilution in blood, which may severely affect their supramolecular stability. However, PBS, which is often used as the solvent in testing the effects of dilution and determining the CMC as reported in the literature,[11] does not mimic *in vivo* conditions. Hence, it is of crucial importance to investigate the effect of dilution in biologically relevant media. Taking advantage of the fluorescent reporting mechanism, we investigated the resistance of micelles, formed by hybrids tested here, to dilution into two different media: PBS and 10% FBS. As detailed before, we measured the fluorescence spectra to determine the stability of micelles and plotted the ratio between the monomer peak and the micelle peak for different concentrations as shown in Figure 4.9. Notably, we did not use an external probe for measuring the micellar stability as typically reported (e.g., Nile red or pyrene) but measured directly the intrinsic fluorescence of the

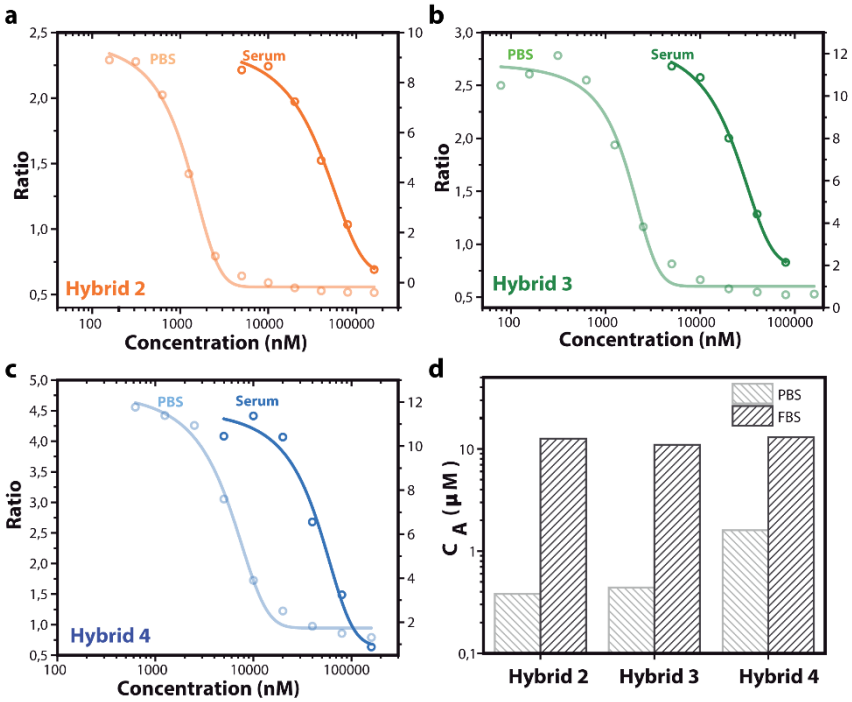

Figure 4.9 Supramolecular stability of the micelles upon dilution into PBS or 10% FBS. a-c. Ratio of emitted fluorescence of monomer versus micelle as a function of micelle concentration when diluted either with PBS or 10% FBS for hybrids **a. 2**, **b. 3**, and **c. 4**. **d.** Representation of the concentrations of aggregation (CA), concentration in which hybrids start to assemble in both PBS and FBS for hybrids **2**, **3**, and **4**.

labeled monomers as indication of the aggregation state of the system. The data obtained show a sigmoidal profile with three characteristic regions: i) at low concentrations of the hybrids, the structures were completely disassembled and showed constant ratio of monomer to micelle and the lack of the peak of the micelles; ii) as the concentrations increased, the structures self-assembled and the ratio of monomer to micelle de-creased; and iii) at high concentrations the ratios were again stable and characteristic of the excimer equilibrium. As expected, the data showed dramatic differences between diluting the micelles into PBS or 10% FBS. In FBS the disassembly began at much higher concentrations than in PBS (Figure 4.9). The disassembly of hybrid **1** could not be followed as it was under the limit of detection of the technique. The resistance of the micelles to dilution in PBS followed the expected trend, with hybrid **1** being the most stable, followed by hybrids **2**, **3**, and **4**, with aggregation

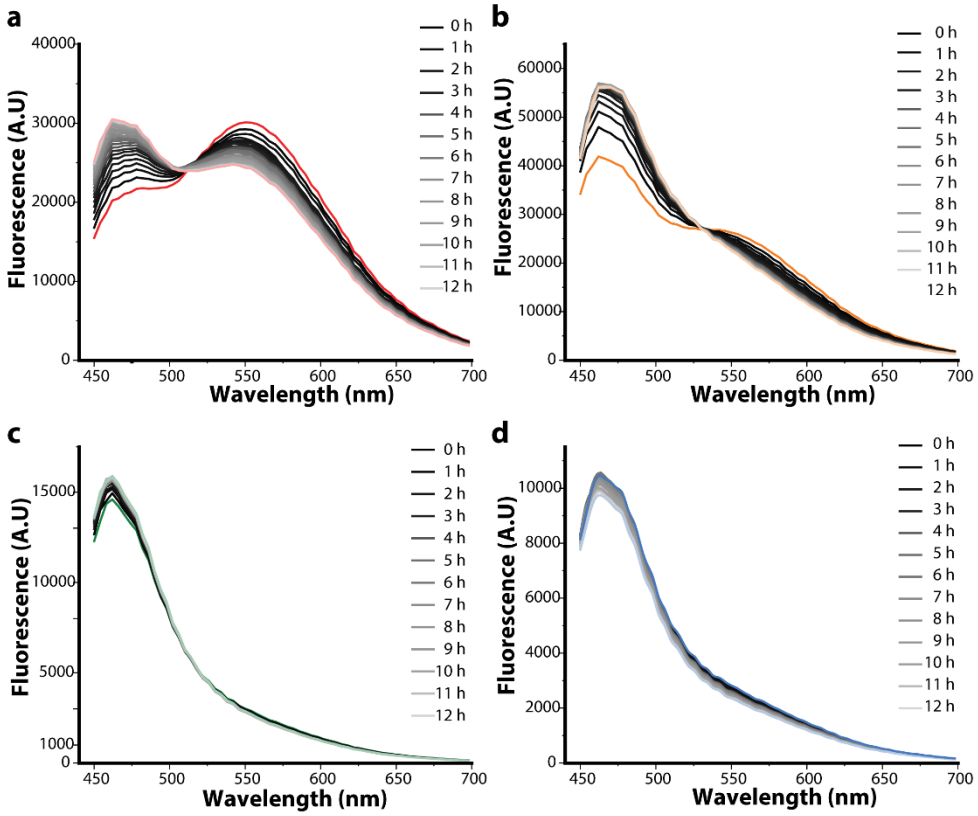

Figure 4.10 Kinetics of disassembly upon dilution, Stability of the micelles upon dilution (in 10% v/v FBS) showed hybrid **4** and hybrid **3** disassembly occurs immediately after dilution but hybrid **2** and hybrid **1** disassemble is much slower. Graphs represent the emission fluorescence spectra at different time points after dilution from 0h to 12h. **a**. Hybrid **1** at 80 μM in FBS **b**. Hybrid **2** at 80 μM in FBS **c**. Hybrid **3** at 40 μM and **d.** Hybrid **4** at 80 μM.

concentrations of 380 nM, 440 nM, and 1,6 μM respectively. Interestingly, in FBS the observed differences between hybrids **2**, **3**, and **4** were significantly attenuated, and all the three types of micelles showed an aggregation concentration of around 10-20 μM (Figure 4.9d). These results highlight the importance of studying the stability of the micelles toward dilution under blood-like conditions as our data confirms that the resistance of the micelles to dilution can dramatically change due to the interactions with serum proteins. In the case of FBS, the interaction pushes the equilibrium toward the disassembled state. Moreover, the observed kinetic behaviors of the four micelles were very different (Figure 4.10). Whereas hybrids **3** and **4** disassembled rapidly upon their dilution, hybrids **1** and **2** took 12 hours to reach their equilibrium state, demonstrating higher kinetic stability. Under the measured conditions, we conclude that hybrid **1** is both kinetically and thermodynamically stable, hybrid **2** is kinetically stable but not thermodynamically, and hybrids **3** and **4** are not stable, as indicated by their rapid disassembly.

4.3.4. *Covalent stability*

As previously discussed, the polymeric amphiphiles synthesized in this work present dendritic end-groups that can be enzymatically degraded in order to trigger the disassembly of the micellar nanocarrier. This principle has been extensively proven for similar amphiphiles in buffer solutions;[24,25,30,36] however, from the previous results is clear the importance of studying the enzymatic response of the micelles in complex media as a better mimic of the *in vivo* behavior. To verify if serum proteins affect the enzymatic-responsiveness, we compared the enzymatic degradation rates (i.e., the covalent stability of the amphiphilies) of all micelles in three different environments: PBS, BSA, and FBS. The monomer/micelle ratios as a function of time obtained from fluorescence emission spectra are plotted in Figure 4.11. A marked difference in the kinetic responsiveness between the different micelles was observed. Interestingly, the enzymatic degradation rates followed the same trend observed for micellar stability. Hybrids **1** and **2** did not fully disassemble even after 40 days at the enzyme concentration used (270 nM PLE), whereas micelles formed from hybrids **3** and **4** disassembled in about 4 and 2 hours, respectively. To further evaluate the enzymatic degradability of hybrids **1** and **2**, we carried out a control degradation experiment with significantly higher concentration of PLE (2 μM PLE) and followed the degradation and disassembly by HPLC and fluorescence spectroscopy, respectively. The results showed that at this high concentration of the activating enzyme, hybrid **2** was degraded in 160 hours (Figure 4.12c and d), whereas for hybrid **1** micelles almost no degradation or disassembly was observed (Figure 4.12a and b), further supporting its high micellar stability.

This result supports the hypothesis that enzymatic degradation takes place in the monomeric state, therefore, the disassembly of the micelles and enzymatic cleavage follow the same trend.[24,36,37] In light to future *in vivo* studies, it is important to note that in all cases both BSA and FBS in the medium accelerated the enzymatic degradation, although in different magnitude depending on the hybrid type. This enhancement of the micelle

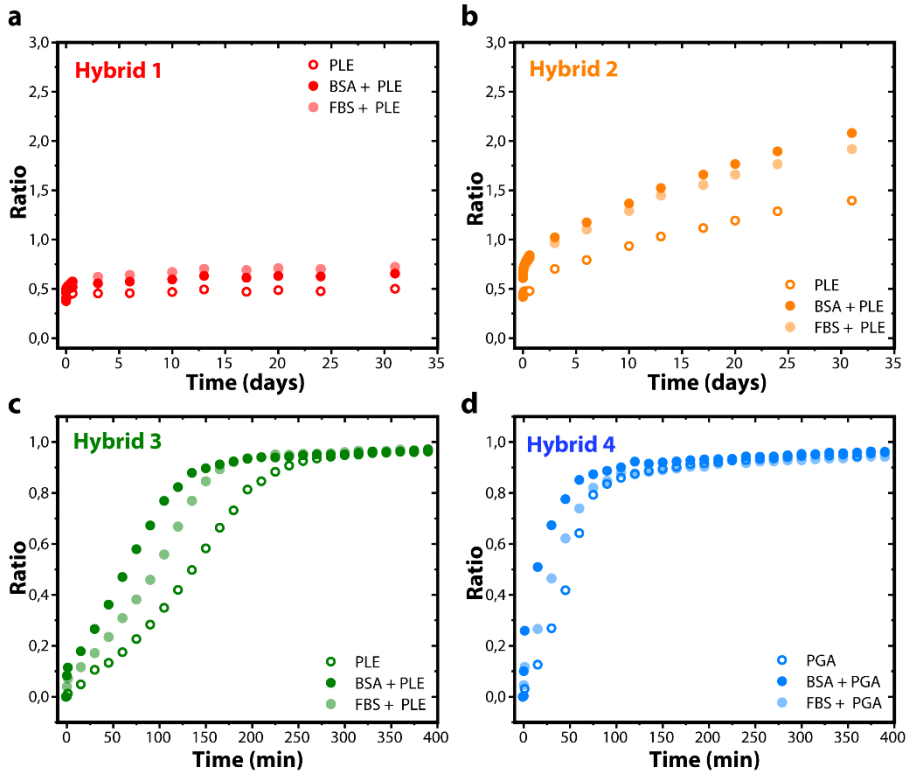

Figure 4.11 Changes in enzymatic response of micelles due to the presence of serum proteins. Ratio of emitted fluorescence of the monomer and the micelle in presence of PGA (910 nM) or PLE (270 nM) and PBS, 10 mg/mL BSA, or 10% FBS for micelles formed from **a**. hybrid **1, b.** hybrid **2**, **c.** hybrid **3**, and **d**. hybrid **4**. Data for hybrids **3** and **4** were normalized to follow the disassembly, 1 indicate the ratio were the micelles were fully disassembled and 0 the ratio of the micelles prior to any enzymatic activity.

degradation also supports the hypothesis that the enzymatic degradation occurs in the monomer form, and hence due to the displacement of the equilibrium by the serum proteins, the enzymatic cleavage is accelerated in comparison with the PBS conditions. Once again, the observed results highlight the importance of studying micellar assemblies and other nanocarriers in *in vivo*-like conditions to screen for the most suitable systems prior to any animal study. Moreover, this data suggests reasons that could induce *in vivo* failure of supramolecular systems in animal models when not tested pre-clinically.

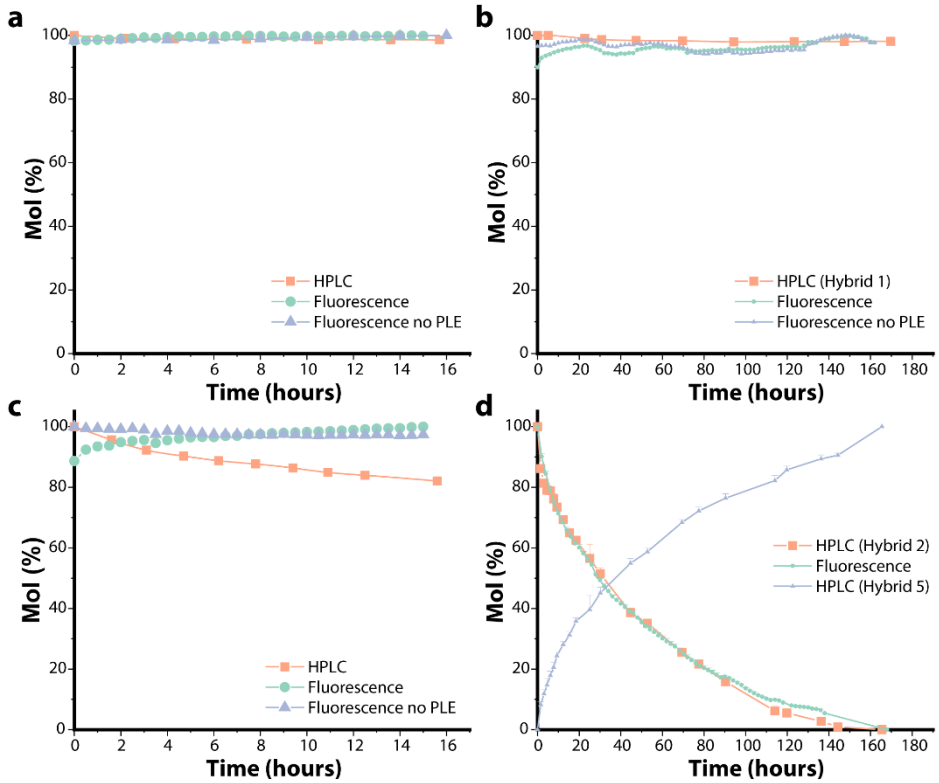

Figure 4.12 Overlays of the change in fluorescence (λ=540nm) and HPLC analysis of the enzymatic degradation. a. Hybrid **1**, 685 nM PLE **b.** Hybrid **1**, 2 μM **c.** Hybrid **2**, 685 nM PLE **d.** Hybrid **2**, 2 μM.

4.4. Stability of micelles upon internalization

Finally, we explored the role of micellar stability in cell internalization, a key step in drug delivery. We first confirmed the lack of toxicity of the hybrids at the concentration to be used (160 μM in PBS, see Figure 4.13). Then, we studied internalization into cells using spectral confocal laser scanning microscopy. This tool allowed us to obtain the full fluorescence spectra and the monomer/micelle ratio for every pixel of the confocal image and, therefore, to identify the two states of the different systems in space and time. After a 30-minute incubation we observed internalization of all micelles, however, with very different subcellular localizations as shown in Figure 4.13. Hybrid **1**, which formed the most stable micelles, was mostly observed in intracellular vesicle-like structures, whereas hybrid **2** was observed both in vesicle-like structures and also showed significant accumulation on the membrane of the cells. Interestingly, hybrids **3**, **4**, and **5** showed mostly diffuse perinuclear fluorescence, attributed to localization on the endoplasmic reticulum (ER, see also co-localization

experiments in the next section). Moreover, hybrids **3** and **4** were also observed in smaller amounts in a vesicular localization, whereas hybrid **5** was not. These notable differences in localization are striking when one takes into account the relatively small structural changes between the different hybrids and the very similar sizes and surface chemistry (PEG5000k) of the various micelles. We therefore hypothesize that the variations in intracellular trafficking are related to the differences in monomer/micelle equilibrium and micellar stability.

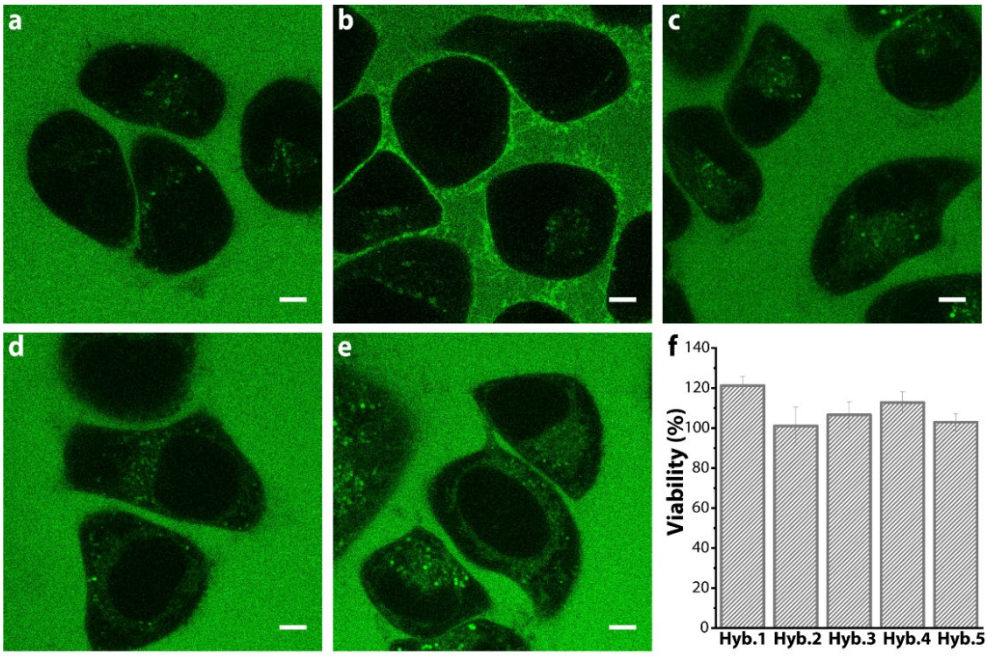

Figure 4.13 Internalization of hybrids 1 - 5 into HeLa cells. Confocal images obtained after 1 hour of continuous incubation with hybrids at a concentration of 160 μM **a.** Hybrid **1 b.** Hybrid **2 c.** Hybrid **3 d.** Hybrid **4 d.** Hybrid **5 e.** Viability of HeLa cells incubated with hybrids **1-5** for 24 hours at a concentration of 160 μM**.**

To shed more light on the origin of the observed differences in cell internalization, we performed spectral imaging to follow the monomers and micelles separately. In this technique the fluorescence emission of the monomer and micelle were collected using a multichannel photomultiplier detection technology and the following were determined: i) the overall signal localization (Figures 4.14a); ii) a ratiometric map highlighting the monomer/micelle ratio for every pixel (Figure 4.14b) using a pseudocolor map, and iii) a full fluorescent spectra for every pixel of the image (Figure 4.14c). This detailed information provided a full picture of the assembly behavior in space and time. We discuss in detail the spectral imaging for hybrid **2** as an example. The confocal image in Figure 4.14 shows the presence of the hybrids outside the cell as well as their accumulation in the membrane and in intracellular vesicles. Both the ratiometric map (Figure 4.14b) and the fluorescence spectra (Figure 4.14c) highlight that the

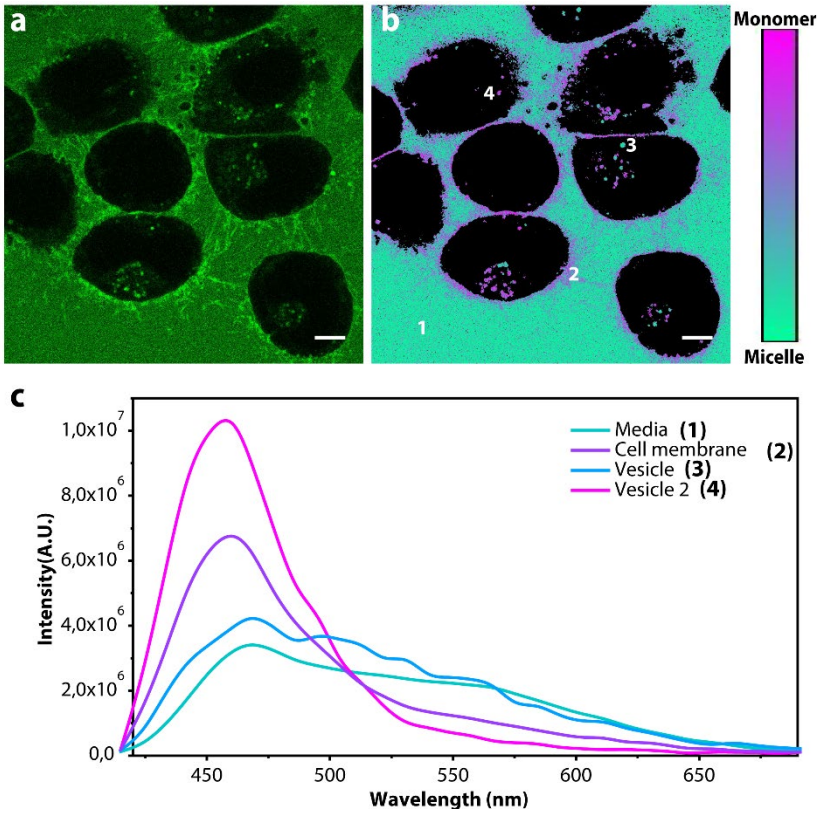

Figure 4.14 Stability of micelles in space. a. Internalization of hybrid **2** into HeLa cells **b.** Ratiometric image obtained by analysis of monomer signal and micelle signal in image shown in panel a **c.** Spectra measured outside and inside cells obtained from spectral images of the cells in image 5b.

different localizations correlate with different assembly states. Outside the cell, the micelles were fully assembled; both 470 nm and 560 nm peaks were present, similarly to the in vitro results. Interestingly, in the membrane the hybrids seemed to be in their monomeric form as indicated by the fluorescent spectra (major peak at 470 nm and slight component at 560 nm). We attribute this disassembly of the micelles to intercalation of the monomeric hybrids into the bilayer membrane of the cells. We were then fascinated to see that inside the intracellular vesicles, we could distinguish between vesicles with only monomer (peak at 470 nm) and vesicles with micelle (both 470 nm and 560 nm components present). This coexistence was also observed in the ratiometric image (Figure 4.14c).

Motivated by the comparable detailed results of ratiometric imaging and spectral imaging, we obtained ratiometric images of all the hybrids after different incubation times with cells (10 and 30 minutes) to compare their behavior as shown in Figure 4.15. As expected, hydrophilic hybrid **5** was in its monomeric form at both time points and regardless of its

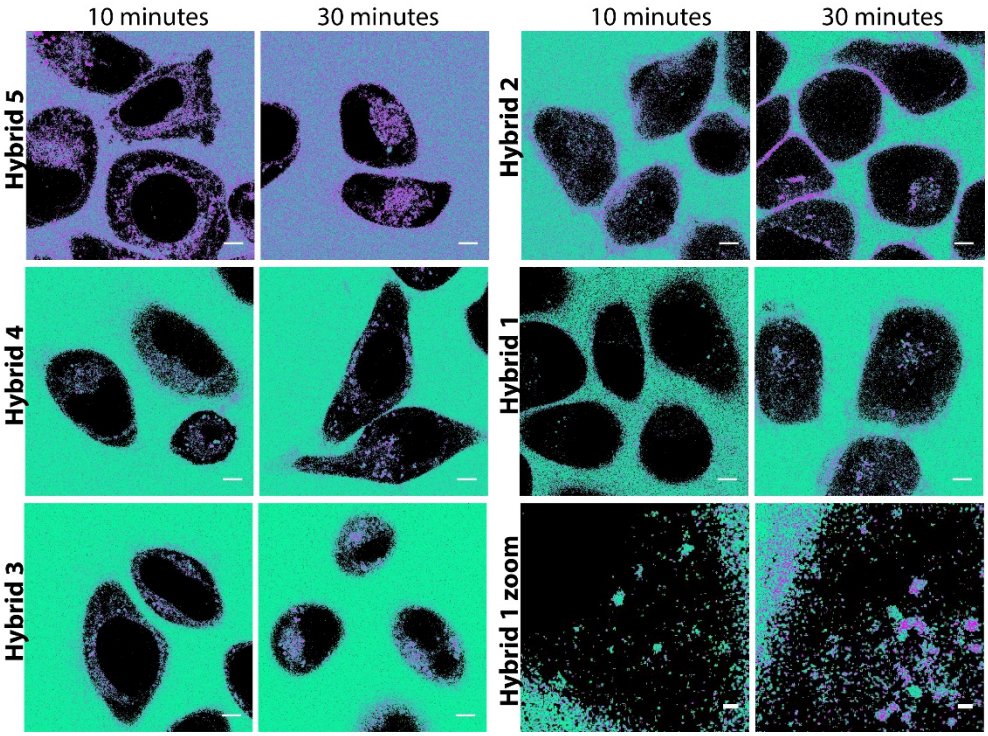

Figure 4.16 Stability of the micelles inside the cells. Ratiometric images of the different hybrid subtypes **1-5** in HeLa cells after 10 and 30 minutes of incubation. Green indicates micelle assembled ang magenta monomer. Scale bar 5 μm. Zoom in scale bar 1 μm.

localization. Hybrids **3** and **4** were mostly in their monomeric state after 10 minutes with some vesicle-like regions in the cell containing the self-assembled hybrids (blue-green color), which is in good agreement with their poor micellar stability as discussed before. After 30 minutes, all the internalized hybrids **3** and **4** were in their disassembled monomeric form. These results suggest that the hybrids enter the cells both in their monomeric state, probably by intercalation into the membrane, and in their assembled micellar state, probably by endocytosis and then disassemble inside the endocytic vesicles. Very differently, hybrid **2** was observed in the membrane both as a monomer and micelle after a 10-minute incubation, which may indicate that the system disassembled once in contact with the cell. However, the images also clearly showed the presence of assembled micelles inside vesicle-like structures in the intracellular region. After 30 minutes, the amount of disassembled hybrids detected in the membrane strongly increased and most of the hybrids inside the cell were disassembled into their monomeric form. Finally, hybrid **1**, after 10 minutes of incubation, was internalized significantly less than the other hybrids. Moreover, all the internalized hybrids were in vesicle-like structures and seemed to be in their assembled micellar state. After 30 minutes, the amount of internalized hybrids increased and both assembled and disassembled

structures were detected inside the cells. These results further confirm the high micellar stability of hybrid **1**. The observed disassembly after 30 minutes inside the cells highlight its potential to specifically release cargo intracellularly.

To assign the localization of the hybrids inside cells to specific organelles, we performed co-localization studies with cellular markers of the Endoplasmic Reticulum (ERtracker Red) or lysosomes (Lysotracker Red). We focused on the hybrids **1** and **4**, due to their diverse behaviors as described above. HeLa cells were incubated 1 hour with the micelles before

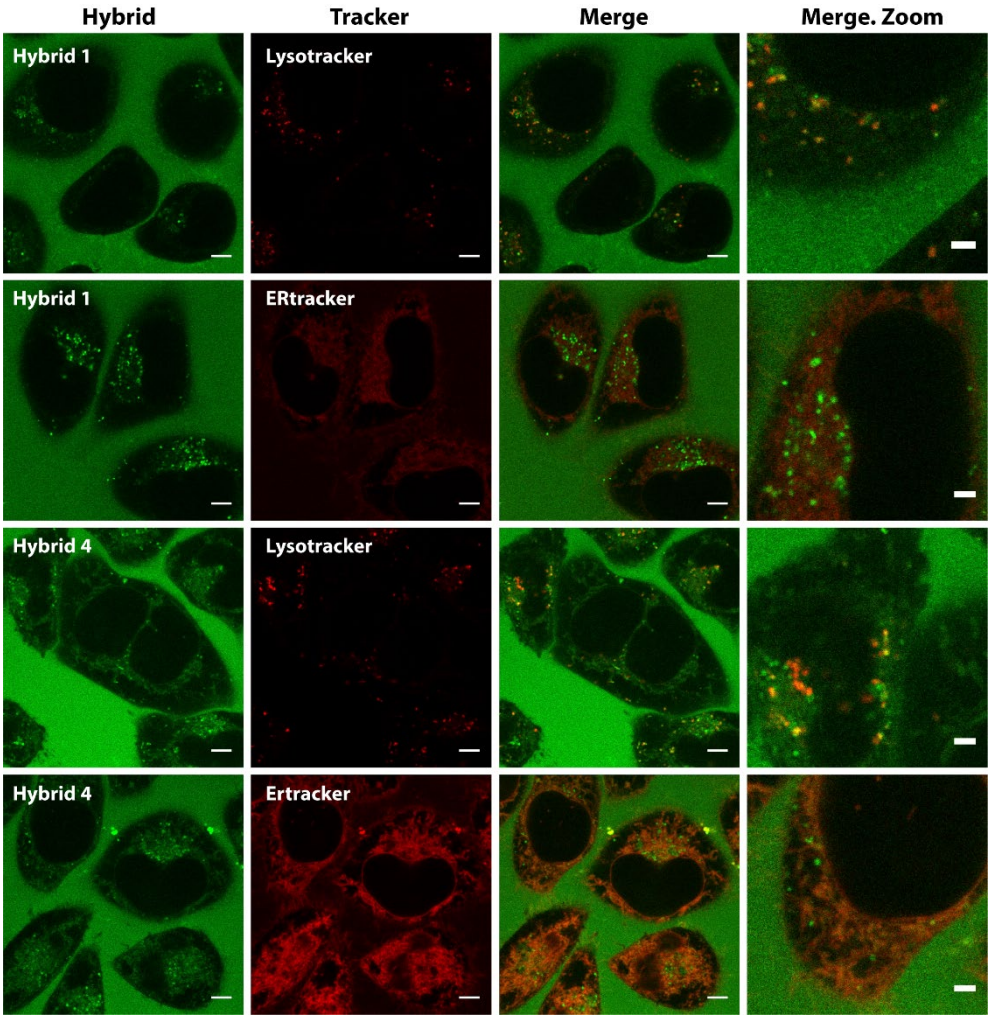

Figure 4.17 The intracellular locations of hybrids 1 and 4 studied after 1 hour of incubation with HeLa cells. Hybrids were added at a concentration of 160 μM. ER or lysosomes were stained using ERtracker Red and Lysotracker Red, respectively. Hybrid signal is shown in green and tracker signals in red. Scale bar 5 μm and zoom in scale bar 2 μm.

adding the cellular markers. The acquired confocal images are shown in Figure 4.16. The images show that hybrid **4** co-localized with both Lysotracker and ERtracker (Figure 4.17). This indicates either a release from the lysosomes to the ER or, more likely, a parallel entrance

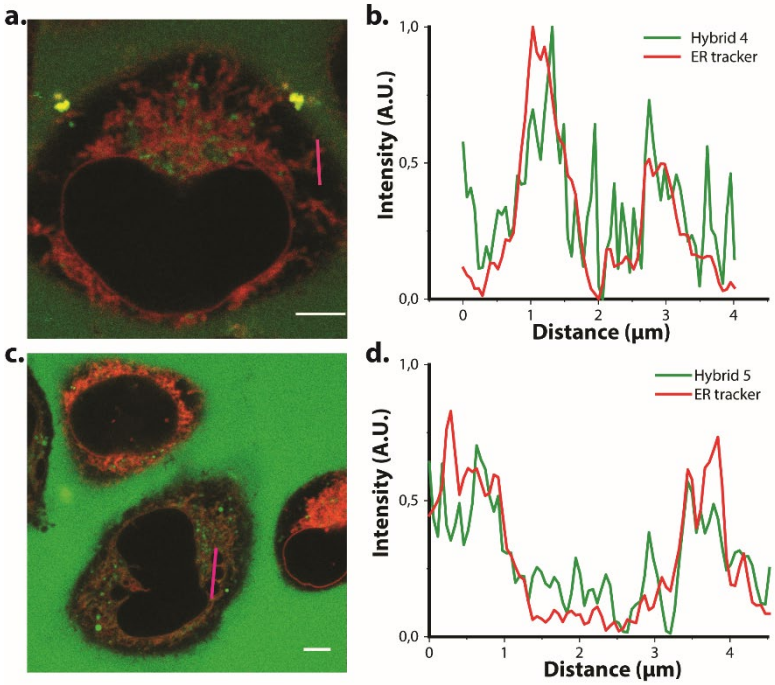

Figure 4.18 Confocal images of the localization of hybrid 4 (a and b) and hybrid 5 (c and d) in HeLa cell (green) after 1 hour incubation and addition of ERtracker (red). Scale bar 5 µm. The intensity profile of both hybrid and ER tracker in the pink line of the images have been plotted normalized to be able to compare both dyes fluorescence. The graphs show similar profiles for ER and hybrid which indicates colocalization.

through membrane permeability as hypothesized based on lambda stack images. These results suggested that monomers and micelles have different internalization mechanisms, micelles through endocytosis and monomers by direct cell permeability, resulting in two different intracellular localizations.

Interestingly, we confirmed membrane permeability of the monomer by performing the incubation of micelles for 1 hour followed by washing to remove the non-internalized structures before confocal imaging (Figure 4.18). Under these experimental conditions none of the hybrids co-localized with ERtracker but they did co-localize with the Lysotracker. These results suggest a high membrane permeability of the monomer, and a tendency to equilibrium of the monomer concentration in the ER and extracellularly, which produced the release of the hybrid. To further confirm the colocalization of the monomeric hybrids with ERtracker, we also performed the same experiment for hybrid **5** (Figure 4.17 and 4.19), which only co-

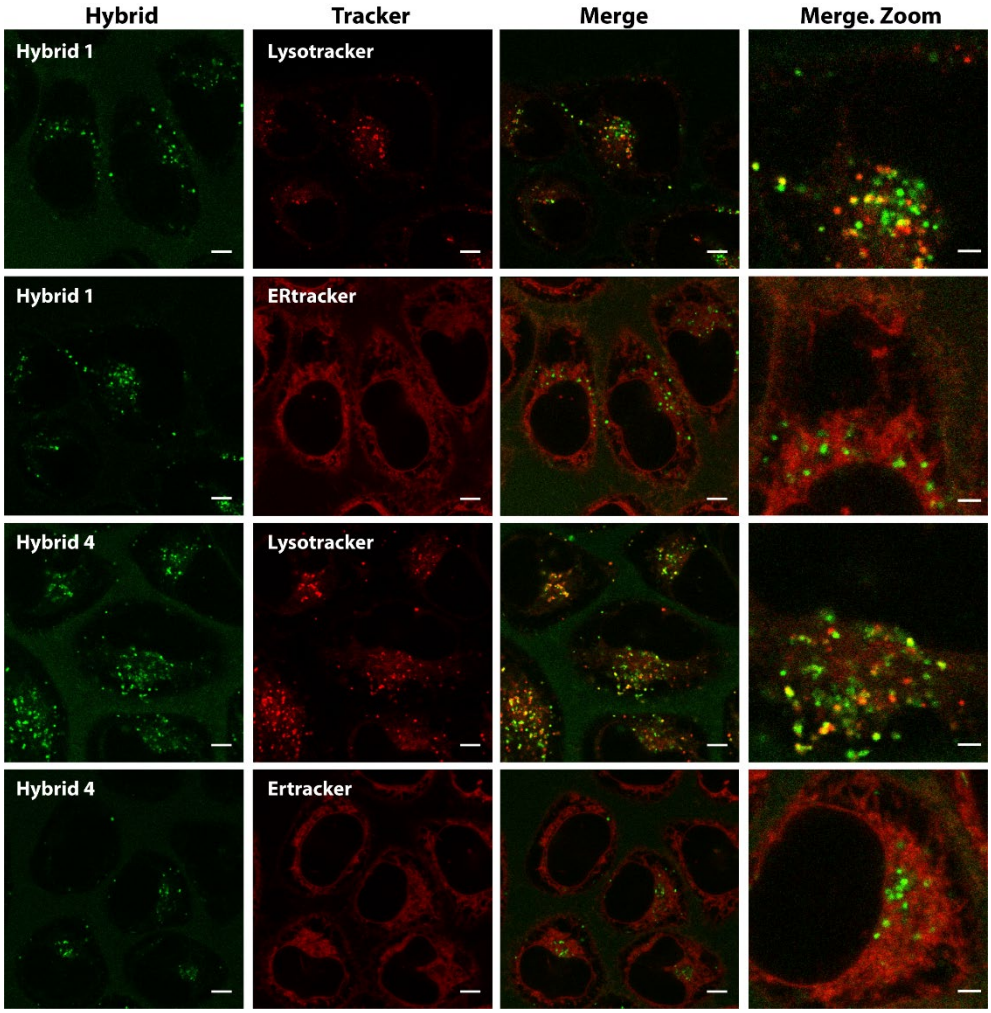

Figure 4.19 The intracellular location of Hybrid 4 and Hybrid 1 was studied after 1 hour of incubation in HeLa cells. Cells were washed and then ER or lysosomes were stained using Red ERtracker and Red Lysotracker respectively. Scale bar 5μm. Zoom in scale bar 2 μm

localized with ERtracker. In contrast, hybrid **1** co-localized with Lysotracker but not with ERtracker (Figure 4.16), suggesting a unique uptake mechanism of this hybrid by endocytosis. Based on these images, we assumed that hybrid **1,** which formed the most stable micelle, entered the cells only by endocytosis, followed by trafficking to the lysosome while slowly disassembling inside. These results show that the complex network of monomer-micelle equilibria is crucial for the intracellular localization of the carrier as illustrated in Scheme 1.

Overall, the present study suggests a complex equilibrium between the monomer, the micelles, and the serum proteins, which depending on the chemical structure of the hybrid

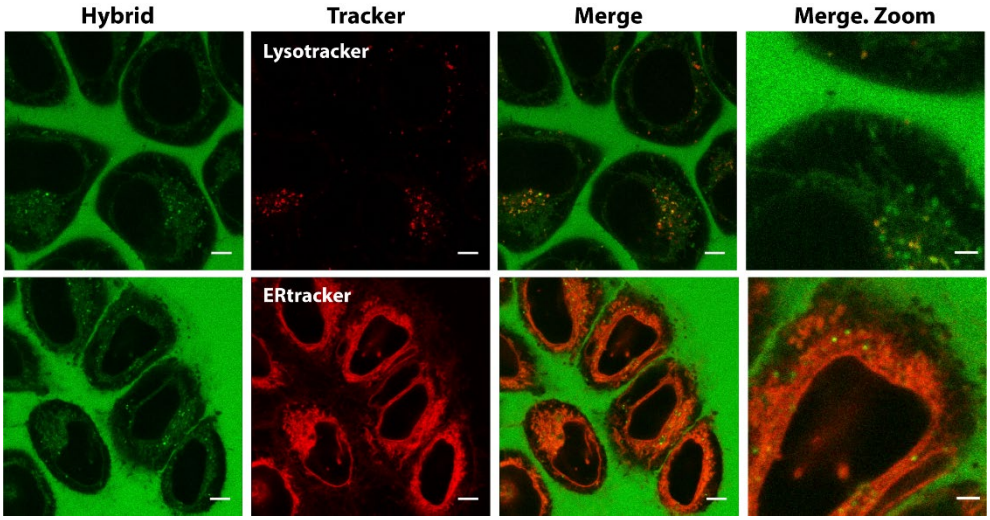

Figure 4.20 The intracellular localization of hybrid 5 in HeLa. Hybrid wasadded at a concentration of 160 μM. ER or lysosomes were stained using ERtracker Red and Lysotracker Red, respectively. Hybrid signal is shown in green and tracker signals in red. Scale bar 5 μm and zoom in scale bar 2 μm.

strongly affects the micelle stability and dictates the interaction with the cells. We observed different internalization pathways of the hybrids depending on assembly state. The monomer form intercalated through the membrane and localized in the ER but could also enter by endocytosis, whereas the micelles entered by the endolysosomal pathway and with time disassembled as illustrated in Scheme 1.

4.5. Conclusions

In this chapter, we showed the importance of thermodynamic and kinetic stability of dynamic polymeric micelles, which are the main determinants of their biological behavior. Using various in vitro measurements, we demonstrated that serum proteins interact with both the monomeric and the micellar states and that these interactions affect both the supramolecular and covalent stabilities of the structures. Therefore, the presence of serum will likely strongly shift the monomer-micelle equilibria by introducing protein-bound species into the equation. Micellar stability was studied by varying incubation times, micelle dilution, and protein concentration in order to mimic in vivo conditions. The obtained results clearly show that hybrid 1 forms the most stable system under the studied conditions. We observed a clear stability trend: hybrid **1** > hybrid **2** > hybrid **3** > hybrid 4**.** The utilization of

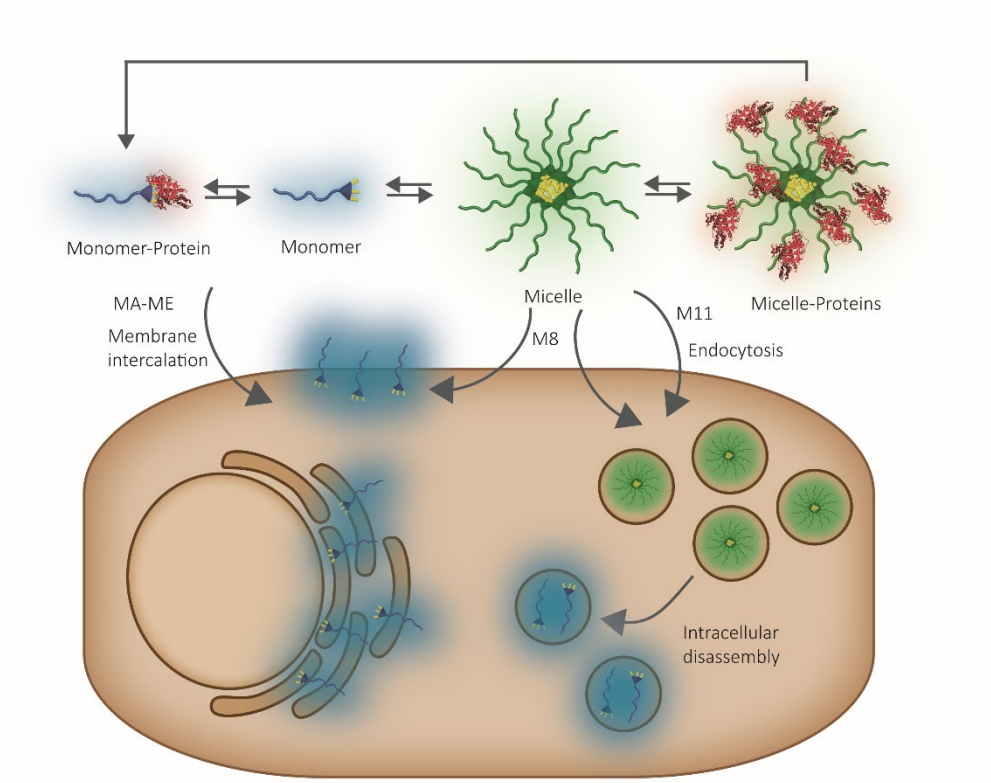

Figure 4.21 Stability of micelle in the presence of proteins and internalization pathways elucidated in this study. In complex media, such as serum, hybrids studied in this work are in equilibrium not only between their assembled and disassembled states but with serum proteins, which modifies the monomer-micelle balance and can induce dissociation of nanocarriers. Moreover, each state internalizes differently into cells, while micelle internalize by endocytosis the monomer can both intercalate through the membrane or use the endolysosomal pathway.

dendrons as the hydrophobic blocks allowed us to achieve unprecedented molecular control over these structures and to fine tune their amphiphilicities. This high molecular precision enabled us to precisely evaluate structure-stability relations for these polymer-dendron hybrids. Very interestingly, we showed that the cell internalization strongly depended on the stability of the micelles and that there are multiple possible internalization mechanisms that depend on the micellar stability. We observed that the monomeric state can intercalate with the membrane and directly enter the cell, mainly localizing at the ER. In contrast, assembled structures enter by endocytosis and are dissembled inside the endolysosomal system. Overall, hybrid **1** was the most promising system from the present study as it showed both supramolecular and covalent stability in vitro, entered the cell in its assembled state, and disassembled inside the cells to potentially release cargo. Moreover, the identification of

different mechanisms of internalization for the monomer and the micelle paves the way towards the design of novel delivery strategies where the cargo could be delivered to different intracellular locations depending on the internalization mechanism. In this framework, stable micelles can be loaded non-covalently to release the payload after endocytosis, and covalent loading of monomers with drug molecules may be an effective strategy in which slightly less stable micelles disassemble outside the cell and the cell-permeability of the drug-linked monomers will result in delivery of the drug directly into the cytosol.

4.6. Experimental section

6.1.1. Instrumentation

HPLC: All measurements were recorded on a Waters Alliance e2695 separations module equipped with a Waters 2998 photodiode array detector. All solvents were purchased from Bio-Lab Chemicals and were used as received. All solvents are HPLC grade.

1H and 13C NMR: spectra were recorded on Bruker Avance I and Avance III 400MHz spectrometers. Chemical shifts are reported in ppm and referenced to the solvent. The molecular weights of the PEG-dendron hybrids were determined by comparison of the areas of the peaks corresponding to the PEG block (3.63 ppm) and the protons peaks of the dendrons. GPC: All measurements were recorded on Viscotek GPCmax by Malvern using refractive index detector and PEG standards (purchased from Sigma-Aldrich) were used for calibration. DMF + 25mM NH4Ac was used as mobile phase. Infrared spectra: All measurements were recorded on a Bruker Tensor 27 equipped with a platinum ATR diamond. Absorbance and fluorescence spectra (including CMC measurements): Spectra were recorded on an Agilent Technologies Cary Eclipse Fluorescence Spectrometer using quartz cuvettes or on TECAN Infinite M200Pro plate reader device. MALDI-TOF MS: Analysis was conducted on a Bruker AutoFlex Speed MALDI-TOF- TOF MS (Germany). DHB matrix was used. DLS: All measurements were recorded on a VASCO-3 Particle Size Analyzer. Confocal imaging: All images were recorded using Zeiss LSM780 Spectral Confocal Microscope.

6.1.2. Reagents

Poly (Ethylene Glycol) methyl ether 5kDa, 2,2-dimethoxy-2-phenylacetophenone (DMPA, 99%), Esterase from porcine liver (PLE), Allyl bromide (99%), N,N'-dicyclohexylcarbodiimide (DCC, 99%), Fmoc-Lys(Boc)-OH (98%), Octanoic acid (98%), Undecanoic acid (98%) and Sephadex® LH20 were purchased from Sigma-Aldrich. Cystamine hydrochloride (98%) and DIPEA were purchased from Merck. O-(Benzotriazol-1-yl)-N,N,N′,N′-tetramethyluronium hexafluorophosphate (HBTU, 99.9%) was purchased from Chem-Impex. Trifluoroacetic acid (TFA) and 2-Mercaptoethanol (99%) were purchased from Alfa Aesar and phenyl acetic acid was purchased from Fluka. Sodium hydroxide and all solvents were purchased from Bio-Lab

and were used as received. Deuterated solvents for NMR were purchased from Cambridge Isotope Laboratories, Inc. Bovine Serum Albumin (lyophilized powder 96%) and Triton X-100 were purchased from Sigma-Aldrich. Fetal Bovine Serum was purchased from Thermofisher, it was stored at – 22 ºC and was only defreeze before used. Cy-5 was purchased from Lumiprobe. PrestoBlue was purchased from Thermofisher.

6.1.3. Synthesis

General procedure for MeO-PEG5kDa-Lys(Boc)-dendron-(Aliphatic)4. MeO-PEG5kDa-Lys(Boc)-dendron-(OH)41 (5a) was dissolved in DCM (1mL, per 0.1g). Aliphatic acid (20 eq.) were added. The flask was cooled to 0°C followed by the addition of DCC (20 eq.) and DMAP (0.1eq.) dissolved in DCM (1mL). The reaction was stirred for 1 hour at room temperature. The crude mixture was filtered and the organic solution was evaporated to dryness. The residue was re-dissolved in DCM (5mL per 1g) and the product was precipitated by the drop wise addition of Ether (50mL per 1g). The precipitate underwent centrifugation and was separated from the organic solvent. The precipitate was collected and residual of solvents were evaporated under vacuum. The residue was dissolved in MeOH and loaded on a MeOH based LH20 SEC column. The fractions that contained the product were unified and the MeOH was evaporated in vacuum to yield an oily residue. In order to facilitate the removal of residual MeOH and solidification of the product, the oily residue was re-dissolved in DCM (1mL) followed by addition of Hexane (3mL). DCM and Hexane were evaporated to dryness and the obtained solid was dried under high vacuum.

General procedure for MeO-PEG5kDa-Lys(Labeled)-dendron-(Aliphatic)4. MeO-PEG5kDa-Lys(Boc)-dendron-(Aliphatic)4 (1a or 2a) was dissolved in DCM (1mL) and TFA was added (1mL). After 30 minutes the solution was evaporated to dryness and dried in vacuum. The labeling moiety with a carboxylic acid functional group (2eq.) and HBTU (2eq.) were dissolved in DCM:DMF 1:1 (1mL) followed by addition of DIPEA (20eq.). The solution was added to the deprotected hybrid (MeO-PEG5kDa-Lys(NH2)-dendron-(Aliphatic)4) dissolved in DCM (1mL, per 0.1g). The reaction was stirred for 1 hour in room temperature. The crude mixture was concentrated under vacuum and loaded on a MeOH based LH20 SEC column. The fractions that contained the product were unified and the DCM and MeOH were evaporated in vacuum to yield an oily residue. In order to facilitate the removal of residual MeOH and solidification of the product, the oily residue was re-dissolved in DCM (1mL) followed by addition of Hexane (3mL). DCM and Hexane were evaporated to dryness and the obtained solid was dried under high vacuum.

6.1.4. Characterization of hybrids

Gel permeation chromatography (GPC). Hybrids were dissolved in mobile phase (DMF + 25mM NH4Ac) to give final concentrations of 10mg/ml. Solution was filtered through a 0.22μm PTFE syringe filter. The columns used were 2 x PSS GRAM 1000Å + PSS GRAM 30Å

at 50ºC. 50 µL of mobile phase were injected at a flow rate of 0.5ml/min. Refractive index detector was set at 50°C (Figures S9 and S10).

Critical micelle concentration (CMC) measurements: Diluent solution was prepared as followed; 10 mL Phosphate buffer solution (pH 7.4), 4.5µL of Nile red stock solution (0.88mg/mL in Ethanol) were mixed to give a final concentration of 1.25µM. To measure CMC for compounds 1 and 2 a 500µM solution of each hybrid was prepared in diluent and sonicated for 15 minutes. This solution was repeatedly diluted by a factor of 1.5 with diluent. 150µL of each solution were loaded onto a 96 wells plate. The fluorescence emission intensity was scanned for each well, by exciting at 550 nm and measuring the emission spectra from 580 to 800nm. Maximum emission intensity was plotted vs. hybrid concentration in order to determine the CMC. All measurements were repeated 3 times.

Dynamic Light Scattering (DLS). Hybrids 1 - 5 were separately dissolved in phosphate buffer (pH 7.4) to give final concentration of 160µM. The Solutions were sonicated for 15 minutes and filtered through a 0.22µm nylon syringe filter. Measurements were performed (t=0 before addition of enzyme). All measurements were repeated 3 times (Figure S12).

Transmission Electron Microscopy (TEM). Hybrid 1 was prepared at a concentration of 160 µM and 0.5 µM in MiliQ water and let stabilize for 72 hours. Then, samples were deposited onto a glow discharged C-only grids and negative staining was performed using uranyl acetate at 2%. All electron micrographs were obtained with a Jeol JEM 1010 MT electron microscope (Japan) operating at 80 kV. Images were obtained on a CCD camera Megaview III (ISIS), Münster, Germany.

Comparing HPLC and fluorescence monitoring of enzymatic degradation. For the HPLC analysis of degradation a Phenomenex, Aeris WIDEPORE, C4, 150x4.6mm, 3.6µm column was used at a temperature of 30ºC, and the UV detector set at 256nm, 2Hz detection rate. Three mobile phase were used i) solution A: 0.1% HClO4 in H2O:Acetonitrile 95:5 V/V, ii) solution B: 0.1% HClO4 in H2O:Acetonitrile 5:95 V/V and iii) solution C: THF. A gradient program in time was used were percentage of solutions A/B/C was changed from 95/0/5 at 1 min to 0/95/5 at 20 min and from 0/95/5 at 23 minutes to 95/0/5 at 23.1 minutes. For HPLC monitoring hybrids 1 and 2 were separately dissolved in phosphate buffer to give a concentration of 160µM. Each solution was sonicated for 15 minutes. 30µL of hybrid solution were injected to the HPLC as t=0 injection. PLE enzyme stock solution (36.0µM or 72.0µM in phosphate buffer pH 7.4) were added to each solution of the tested hybrid (160µM) and mixed for 10 seconds (vortex mixer) to give final PLE concentration of 685nM or 2µM. Enzymatic degradation was monitored by

repeating 30μL injections from the same vail over 15 hours. All measurements were repeated 3 times (Figures S17-S20)[b].

The fluorescence monitoring of micelle disassembly rate by enzymes was performed using an Agilent Technologies Cary Eclipse Fluorescence Spectrophotometer. Hybrids 1 and 2 were prepared the same as for HPLC measurements (160μM, PBS). For each hybrid 600μL were accurately transferred to a quartz cuvette. A fluorescence emission scan was performed (t=0). For enzymatic degradation 600μL were transferred to quarts cuvette and mixed with the enzymes at either 685nM or 2μM final concentration. Hybrids were excited at 420 nm and emission scan was measured from 440 to 700 nm at a scan rate of 590 nm/min, all measurements were carried out at 37ºC (Figures S13 and S14). Repeating fluorescence scans were performed either every 30 minutes or 2 hours for about 15 hours or 160 hours respectively. All measurements were repeated 3 times (Figures S13-S16).

6.1.5. Micelle – blood proteins interaction

Interaction of monomer and blood proteins. Hybrid 4 was prepared at 2 μM in filtered Phosphate Buffered Saline (PBS) 0.16M, the fluorescence emission spectrum of the micelles was monitor using Tecan infinite M200Pro microplate reader. The measured emission wavelength ranged from 450 nm to 650 nm, using an excitation wavelength of 420 nm. BSA was added at a final concentration of 10 mg/ml, modifying the micelle concentration to 1,82 μM. The Fluorescence emission spectrum was measured for 9 cycles every 40 s.

Förster Resonance Energy Transfer (FRET) was used to measure the interactions between the dye of the hybrids (coumarin) and Cy5 conjugated. Micelles at a final concentration of 145,5 μM were mixed with BSA (10% v/v Cy5 labelled) at a final concentration of 5.5 mg/mL. The sample was excited at 420 nm wavelength (coumarin excitation, donor), and the fluorescence emission spectra was measured from 450 nm to 750 nm to include Cy5 emission. The spectra were measured before the addition of BSA and 3 more times every 15 minutes after the addition.

6.1.6. Supramolecular stability

BSA titration. All hybrids were prepared at a final concentration of 40 μM (in PBS). BSA was added at increasing concentrations from 0 to 1mM in PBS. Emission fluorescence spectra of each condition was measured using Tecan infinite M200Pro microplate reader. Samples were excited at 420 nm and emission spectra was collected from 450 nm to 650 nm.

[b] All HPLC, CMC and GPC characterization analysis were performed by M. Buzhor from R. Amir group in Tel Aviv University.

Stability in time. To perform studies on stability of micelles in time, hybrids solutions were prepared at a concentration of 160 μM of monomer (in PBS). Each hybrid was mixed with BSA at a final concentration of 10 mg/mL in PBS, FBS at a final concentration of 10% v/v or PBS as a control. Then, Tecan infinite M200Pro microplate reader was used to measure emission fluorescence spectra in time every hour, for 12 hours. Samples were excited at 420 nm and emission spectra was collected from 450 nm to 650 nm.

Resistance to dilution. To determine the stability of micelles against dilution each hybrid was prepared at a concentration of 160 μM (in PBS). Then, it was sequentially diluted either in PBS or FBS up to 78 nM. Then, Tecan infinite M200Pro microplate reader was used to measure emission fluorescence spectra every 15 min for 4 hours. Samples were excited at 420 nm and emission spectra was collected from 450 nm to 650 nm.

6.1.7. Enzymatic response

The enzymatic response of the micelles was studied in presence of BSA and FBS comparing to control conditions without proteins. Each hybrid was prepared at a concentration of 160 μM (in PBS). Then, each hybrid was mixed with BSA at a final concentration of 10 mg/mL, FBS at a final concentration of 10% v/v or PBS as a control and let stabilize for 1 hour. Fluorescence emission spectra were measured for each condition before and after the addition of the protein. Then, PLE at a concentration of 5 μM in the ester responsive micelles and PGA at a concentration of 50 μM in the amidase responsive sample were added to a final concentration of 270 nM and 910 nM respectively. Following by the measurement in time of the spectrum for 15 hours. The enzyme concentration was selected considering the concentrations used in previous works1.

6.1.8. Hybrids- cell interactions

Cytotoxicity. The cytotoxicity of all the samples was evaluated with PrestoBlue assay on HeLa cells culture. HeLa cells were seeded in a 96-well plate at a density of 5.000 cells/well and cultured overnight at 37ºC and 5% CO2. Hybrids were added to the cells in full medium to a concentration of 160 μM, the same volume of PBS was added to the negative controls, Triton X-100 0,1 %v/v was added to the positive controls. The hybrids were incubated for 24 hours at 37º and 5% CO2.Then, PrestoBlue reactive was added at 10 % v/v. The emitted fluorescence at 600 nm of each well was measured after exciting at 550 nm.The wells at the boundary remained untested with micelles. Each sample had 3 replications. Fluorescent signal was normalized with negative and positive controls to 0 and 100% respectively.

Internalization. HeLa cells were seeded in a 8-wells Nunc™ Lab-Tek™ II Chamber Slide™ (ThermoFisher) and cultured overnight at 37ºC and 5% CO2, 17000 cells/well. Hybrids at a final concentration of 160 μM in complete medium supplemented with 20 mM Hepes were added and live imaging of cells at a 37ºC was performed in a Zeiss LSM780 Spectral Confocal

Microscope. Hybrids were excited using 405 nm laser and emission spectra was collected after 10 and 30 minutes of incubation using two approaches. i) Two different PMT detectors were used to collect emission of monomer and micelle separately and simultaneous, windows of detection were set as following, monomer 446-500 nm and micelle 526-589nm. ii) Spectral images were acquired using a 32 PMT GaAsP array detector, with allowed to collect a lambda stack with steps of 9 nm from 411 nm to 695 nm. Ratiometric images were obtained from dividing the monomer image by the micelle image, after applying a mask to each image were noise was removed. Experiments were localization of micelles was studied micelles were incubated for 1 hour and then a cellular compartment tracker was added, LysoTracker was used at a concentration of 1nM and ER-Tracker at a concentration of 40 nM. Confocal images were acquired by exciting hybrids with 405 nm laser and Red Tracker with 561 nm laser.

4.7. References

(1) Movassaghian, S.; Merkel, O. M.; Torchilin, V. P. Applications of Polymer Micelles for Imaging and Drug Delivery. *Wiley Interdiscip. Rev. Nanomed. Nanobiotechnol.* **2015**, *7* (5), 691–707. https://doi.org/10.1002/wnan.1332.

(2) Torchilin, V. P. Micellar Nanocarriers: Pharmaceutical Perspectives. *Pharm. Res.* **2007**, *24* (1), 1. https://doi.org/10.1007/s11095-006-9132-0.

(3) Werner, M. E.; Cummings, N. D.; Sethi, M.; Wang, E. C.; Sukumar, R.; Moore, D. T.; Wang, A. Z. Preclinical Evaluation of Genexol-PM, a Nanoparticle Formulation of Paclitaxel, as a Novel Radiosensitizer for the Treatment of Non-Small Cell Lung Cancer. *Int. J. Radiat. Oncol. Biol. Phys.* **2013**, *86* (3), 463–468. https://doi.org/10.1016/j.ijrobp.2013.02.009.

(4) Shi, Y.; Lammers, T.; Storm, G.; Hennink, W. E. Physico-Chemical Strategies to Enhance Stability and Drug Retention of Polymeric Micelles for Tumor-Targeted Drug Delivery. *Macromol. Biosci.* **2017**, *17* (1), 1600160. https://doi.org/10.1002/mabi.201600160.

(5) Photos, P. J.; Bacakova, L.; Discher, B.; Bates, F. S.; Discher, D. E. Polymer Vesicles in Vivo: Correlations with PEG Molecular Weight. *J. Controlled Release* **2003**, *90* (3), 323–334. https://doi.org/10.1016/S0168-3659(03)00201-3.

(6) Owen, S. C.; Chan, D. P. Y.; Shoichet, M. S. Polymeric Micelle Stability. *Nano Today* **2012**, *7* (1), 53–65. https://doi.org/10.1016/j.nantod.2012.01.002.

(7) Lu, J.; Owen, S. C.; Shoichet, M. S. Stability of Self-Assembled Polymeric Micelles in Serum. *Macromolecules* **2011**, *44* (15), 6002–6008. https://doi.org/10.1021/ma200675w.

(8) Aguilar-Castillo, B. A.; Santos, J. L.; Luo, H.; Aguirre-Chagala, Y. E.; Palacios-Hernández, T.; Herrera-Alonso, M. Nanoparticle Stability in Biologically Relevant Media: Influence of Polymer Architecture. *Soft Matter* **2015**, *11* (37), 7296–7307. https://doi.org/10.1039/C5SM01455G.

(9) Gravier, J.; Sancey, L.; Hirsjärvi, S.; Rustique, E.; Passirani, C.; Benoît, J.-P.; Coll, J.-L.; Texier, I. FRET Imaging Approaches for in Vitro and in Vivo Characterization of Synthetic Lipid Nanoparticles. *Mol. Pharm.* **2014**, *11* (9), 3133–3144. https://doi.org/10.1021/mp500329z.

(10) Chen, H.; Kim, S.; He, W.; Wang, H.; Low, P. S.; Park, K.; Cheng, J.-X. Fast Release of Lipophilic Agents from Circulating PEG-PDLLA Micelles Revealed by in Vivo Förster Resonance Energy Transfer Imaging. *Langmuir* **2008**, *24* (10), 5213–5217. https://doi.org/10.1021/la703570m.

(11) Ma, S.; Zhou, J.; Zhang, Y.; He, Y.; Jiang, Q.; Yue, D.; Xu, X.; Gu, Z. Highly Stable Fluorinated Nanocarriers with IRGD for Overcoming the Stability Dilemma and Enhancing Tumor Penetration in an Orthotopic Breast Cancer. *ACS Appl. Mater. Interfaces* **2016**, *8* (42), 28468–28479. https://doi.org/10.1021/acsami.6b09633.

(12) Kessenbrock, K.; Plaks, V.; Werb, Z. Matrix Metalloproteinases: Regulators of the Tumor Microenvironment. *Cell* **2010**, *141* (1), 52–67. https://doi.org/10.1016/j.cell.2010.03.015.

(13) Blum, A. P.; Kammeyer, J. K.; Rush, A. M.; Callmann, C. E.; Hahn, M. E.; Gianneschi, N. C. Stimuli-Responsive Nanomaterials for Biomedical Applications. *J. Am. Chem. Soc.* **2015**, *137* (6), 2140–2154. https://doi.org/10.1021/ja510147n.

(14) Chien, M.-P.; Thompson, M. P.; Lin, E. C.; Gianneschi, N. C. Fluorogenic Enzyme-Responsive Micellar Nanoparticles. *Chem. Sci.* **2012**, *3* (9), 2690–2694. https://doi.org/10.1039/C2SC20165H.

(15) Daniel, K. B.; Callmann, C. E.; Gianneschi, N. C.; Cohen, S. M. Dual-Responsive Nanoparticles Release Cargo upon Exposure to Matrix Metalloproteinase and Reactive Oxygen Species. *Chem. Commun.* **2016**, *52* (10), 2126–2128. https://doi.org/10.1039/C5CC09164K.

(16) Samarajeewa, S.; Shrestha, R.; Li, Y.; Wooley, K. L. Degradability of Poly(Lactic Acid)-Containing Nanoparticles: Enzymatic Access through a Cross-Linked Shell Barrier. *J. Am. Chem. Soc.* **2012**, *134* (2), 1235–1242. https://doi.org/10.1021/ja2095602.

(17) Samarajeewa, S.; Zentay, R. P.; Jhurry, N. D.; Li, A.; Seetho, K.; Zou, J.; Wooley, K. L. Programmed Hydrolysis of Nanoassemblies by Electrostatic Interaction-Mediated Enzymatic-Degradation. *Chem. Commun.* **2013**, *50* (8), 968–970. https://doi.org/10.1039/C3CC46013D.

(18) Thornton, P. D.; Heise, A. Bio-Functionalisation to Enzymatically Control the Solution Properties of a Self-Supporting Polymeric Material. *Chem. Commun.* **2011**, *47* (11), 3108–3110. https://doi.org/10.1039/C0CC03647A.

(19) Habraken, G. J. M.; Peeters, M.; Thornton, P. D.; Koning, C. E.; Heise, A. Selective Enzymatic Degradation of Self-Assembled Particles from Amphiphilic Block Copolymers Obtained by the Combination of N-Carboxyanhydride and Nitroxide-Mediated Polymerization. *Biomacromolecules* **2011**, *12* (10), 3761–3769. https://doi.org/10.1021/bm2010033.

(20) Raghupathi, K. R.; Azagarsamy, M. A.; Thayumanavan, S. Guest-Release Control in Enzyme-Sensitive, Amphiphilic-Dendrimer-Based Nanoparticles through Photochemical Crosslinking. *Chem. – Eur. J.* **2011**, *17* (42), 11752–11760. https://doi.org/10.1002/chem.201101066.

(21) Azagarsamy, M. A.; Sokkalingam, P.; Thayumanavan, S. Enzyme-Triggered Disassembly of Dendrimer-Based Amphiphilic Nanocontainers. *J. Am. Chem. Soc.* **2009**, *131* (40), 14184–14185. https://doi.org/10.1021/ja906162u.

(22) Wang, H.; Raghupathi, K. R.; Zhuang, J.; Thayumanavan, S. Activatable Dendritic 19F Probes for Enzyme Detection. *ACS Macro Lett.* **2015**, *4* (4), 422–425. https://doi.org/10.1021/acsmacrolett.5b00199.

(23) Rosenbaum, I.; Harnoy, A. J.; Tirosh, E.; Buzhor, M.; Segal, M.; Frid, L.; Shaharabani, R.; Avinery, R.; Beck, R.; Amir, R. J. Encapsulation and Covalent Binding of Molecular Payload in Enzymatically Activated Micellar Nanocarriers. *J. Am. Chem. Soc.* **2015**, *137* (6), 2276–2284. https://doi.org/10.1021/ja510085s.

(24) Segal, M.; Avinery, R.; Buzhor, M.; Shaharabani, R.; Harnoy, A. J.; Tirosh, E.; Beck, R.; Amir, R. J. Molecular Precision and Enzymatic Degradation: From Readily to Undegradable Polymeric Micelles by Minor Structural Changes. *J. Am. Chem. Soc.* **2017**, *139* (2), 803–810. https://doi.org/10.1021/jacs.6b10624.

(25) Harnoy, A. J.; Slor, G.; Tirosh, E.; Amir, R. J. The Effect of Photoisomerization on the Enzymatic Hydrolysis of Polymeric Micelles Bearing Photo-Responsive Azobenzene Groups at Their Cores. *Org. Biomol. Chem.* **2016**, *14* (24), 5813–5819. https://doi.org/10.1039/C6OB00396F.

(26) Molla, M. R.; Prasad, P.; Thayumanavan, S. Protein-Induced Supramolecular Disassembly of Amphiphilic Polypeptide Nanoassemblies. *J. Am. Chem. Soc.* **2015**, *137* (23), 7286–7289. https://doi.org/10.1021/jacs.5b04285.

(27) Guo, J.; Zhuang, J.; Wang, F.; Raghupathi, K. R.; Thayumanavan, S. Protein AND Enzyme Gated Supramolecular Disassembly. *J. Am. Chem. Soc.* **2014**, *136* (6), 2220–2223. https://doi.org/10.1021/ja4108676.

(28) Hawker, C. J.; Frechet, J. M. J. Preparation of Polymers with Controlled Molecular Architecture. A New Convergent Approach to Dendritic Macromolecules. *J. Am. Chem. Soc.* **1990**, *112* (21), 7638–7647. https://doi.org/10.1021/ja00177a027.

(29) Hawker, C.; Fréchet, J. M. J. A New Convergent Approach to Monodisperse Dendritic Macromolecules. *J. Chem. Soc. Chem. Commun.* **1990**, *0* (15), 1010–1013. https://doi.org/10.1039/C39900001010.

(30) Buzhor, M.; Harnoy, A. J.; Tirosh, E.; Barak, A.; Schwartz, T.; Amir, R. J. Supramolecular Translation of Enzymatically Triggered Disassembly of Micelles into Tunable Fluorescent Responses. *Chem. – Eur. J.* **2015**, *21* (44), 15633–15638. https://doi.org/10.1002/chem.201502988.

(31) Chandel, A. K.; Rao, L. V.; Narasu, M. L.; Singh, O. V. The Realm of Penicillin G Acylase in β-Lactam Antibiotics. *Enzyme Microb. Technol.* **2008**, *42* (3), 199–207. https://doi.org/10.1016/j.enzmictec.2007.11.013.

(32) Gillies, E. R.; Jonsson, T. B.; Fréchet, J. M. J. Stimuli-Responsive Supramolecular Assemblies of Linear-Dendritic Copolymers. *J. Am. Chem. Soc.* **2004**, *126* (38), 11936–11943. https://doi.org/10.1021/ja0463738.

(33) Bai, H.; Qian, J.; Tian, H.; Pan, W.; Zhang, L.; Zhang, W. Fluorescent Polarity Probes for Identifying Bovine Serum Albumin: Amplification Effect of Para-Substituted Benzene. *Dyes Pigments* **2014**, *103*, 1–8. https://doi.org/10.1016/j.dyepig.2013.11.018.

(34) Walkey, C. D.; Chan, W. C. W. Understanding and Controlling the Interaction of Nanomaterials with Proteins in a Physiological Environment. *Chem. Soc. Rev.* **2012**, *41* (7), 2780–2799. https://doi.org/10.1039/C1CS15233E.

(35)Feiner-Gracia N.; Beck M.; Pujals S.; Tosi S.; Mandal T.; Buske C.; Linden M.; Albertazzi L. Super-Resolution Microscopy Unveils Dynamic Heterogeneities in Nanoparticle Protein Corona. *Small* **2017**, *13* (41), 1701631. https://doi.org/10.1002/smll.201701631.

(36) Harnoy, A. J.; Buzhor, M.; Tirosh, E.; Shaharabani, R.; Beck, R.; Amir, R. J. Modular Synthetic Approach for Adjusting the Disassembly Rates of Enzyme-Responsive Polymeric Micelles. *Biomacromolecules* **2017**, *18* (4), 1218–1228. https://doi.org/10.1021/acs.biomac.6b01906.

(37) Harnoy, A. J.; Rosenbaum, I.; Tirosh, E.; Ebenstein, Y.; Shaharabani, R.; Beck, R.; Amir, R. J. Enzyme-Responsive Amphiphilic PEG-Dendron Hybrids and Their Assembly into Smart Micellar Nanocarriers. *J. Am. Chem. Soc.* **2014**, *136* (21), 7531–7534. https://doi.org/10.1021/ja413036q.

Chapter 5 .

Real-time Ratiometric Imaging of Micelles Assembly State in a Microfluidic Cancer-on-a-chip

The performance of supramolecular nanocarriers as drug delivery systems depends on their stability in the complex and dynamic biological media. After being administered, nanocarriers are challenged by confronting different barriers such as shear stress and proteins present in blood, tight endothelial walls, extracellular matrix (ECM) and eventually cancer cells. While early disassembly will result in a premature drug release, extreme stability of the nanocarriers can lead to poor drug release and lack of effectivity. One of the key challenges is that current 2D in vitro models do not provide exhaustive information, as they do not fully recapitulate the 3D tumor microenvironment. This deficiency in complexity of the 2D models is the main reason for the differences observed in vivo when testing the performance of supramolecular nanocarriers. Herein, taking advantage of spectrally active polymeric amphiphiles, we present a real-time monitoring study of self-assembled micelles stability and extravasation, combining spectral confocal microscopy and a microfluidic tumor-on-a-chip. The combination of advanced imaging and a reliable organ-on-a-chip model allow us to track micelle disassembly by following the spectral properties of the amphiphiles in space and time during the crucial steps of drug delivery. Using this method, a small library of micelles composed of fluorescently labeled PEG-dendron amphiphiles, has been studied, revealing the interplay between carrier structure, micellar stability and extravasation. Integrating the ability of the micelles to change their fluorescent properties when disassembled, spectral confocal imaging and 3D microfluidic tumor blood vessel-on-a-chip, resulted in the establishment of a robust testing platform, suitable for real-time imaging and evaluation of supramolecular drug delivery carrier's stability.

10.1. Introduction

One of the main challenges with the use of supramolecular nanocarriers is the control of their dynamic nature, i.e. their assembly-disassembly equilibrium, which can determine *in vivo* success, as reviewed in Chapter 1. Nanocarriers have to withstand an exposure to diverse environments affecting their properties during their life in the body. Interactions with blood proteins, high dilution in blood, the continuous flow present in the vessels[1,2], but also the interactions with endothelial barrier[3] or the ECM can compromise the stability of supramolecular systems[4] . Therefore, it is important to optimize the properties of the nanocarriers to be able to ensure the stability once they are injected into the body, avoiding premature disassembly and drug release. The predictability and understanding of supramolecular assemblies' stability within these changing conditions, can pave the way to an improved design of nanosystems to be translated into the clinics. Therefore, a comprehensive study of NPs behavior in complex and dynamic environment requires a reliable, precise and versatile method.

Due to the difficulties in real-time monitoring and studying of NPs in physiologically relevant milieu many aspects are not addressed when screening new nanocarriers. In Chapter 4 we have studied the stability of PEG-dendron micelles in blood-like conditions using spectroscopy and microscopy techniques thanks to the inner fluorescent properties of the system. As explained in Chapter 4, few other stability studies had been carried on in other supramolecular systems exposed to serum proteins in vitro[5–8]. Nevertheless, all these in vitro assays consisted mainly of 2D systems, which lack the dynamic and spatial/geometrical arrangement of environment present in human body. Despite of being high throughput and rapid, they did not provide complete information reflecting the *in vivo* conditions. To overcome these limitations, microfluidic technology emerged few years ago as a new advancement to re-create cancer-on-a-chip models, which may lead to a real paradigm shift in preclinical trials and drug (carrier) development[9,10]. Microfluidic technology aims to enrich conventional 2D studies by investigating 3D arrangement and transport phenomena in blood vessel and tumor microenvironment (TME) to provide additional screening before use of animal models[11–13].

The first studies showed new microfluidic models in which only some of the barriers had been recreated[13–15]. Recently, more complex healthy and tumor blood vessel-on-a-chip have been designed in order to assess the differences in nanoparticles permeability in various conditions[16–18], demonstrating the appearance of increased endothelial permeability when cancer cells were present[16]. However, all microfluidics models developed up to now, were used for studying only the end time point of nanoparticles incubation, lacking time-resolved monitoring of their performance. We believe that it is very important to close the gap in

understanding the crucial changes occurring in the supramolecular nanocarriers throughout their journey.

Herein, we continuously monitored real-time the spectrally active polymeric micelles used in Chapter 4 under flow using ratiometric confocal microscopy imaging combined with a 3d cancer blood vessel-on-a-chip model. The major aim of this Chapter was to reveal the stability of micelles in the various barriers and screen for the best performing candidate. We prepared a chip with a perfusable blood vessel and 3D arranged tumor cells, separated by endothelial cells' wall. We designed the method to map the nanocarrier stability in time and space using spectral confocal microscopy thanks to the unique fluorescent properties of the micelles. The designed cancer-on-a-chip setup with our mapping method opens the way towards a new testing tool for optimizing the pre-clinical screening of nanoparticles.

10.2. The system

10.2.1. Amphiphilic PEG-dendron micelles

The stability of three of the amphiphilic PEG-dendron hybrids used in chapter 4, **1-3**, differing by their lipophilic end group in the hydrophobic block has been studied 34,35. . The micelles were labeled with a responsive dye, 7-diethylamino-3-carboxy coumarin, which forms and excimer when the hybrids self-assemble into micelles. The excimer formation causes a red-shift of the emission spectra of the dye allowing us to discriminate the assembled state (micelle) from the disassembled state (monomers), as shown in Figure 5.1. The

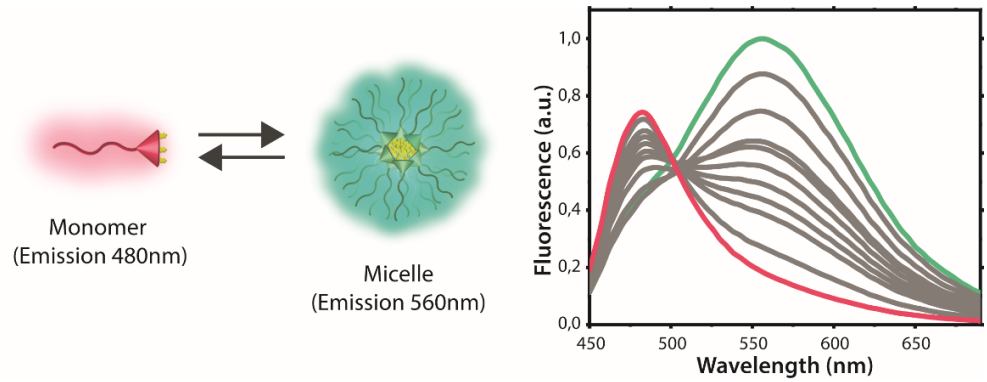

Figure 5.1 Schematic representation of the properties of our supramolecular system. Micelle-monomer equilibrium together with their emission spectra. In magenta monomer (fully disassembled structure) and in green fully assembled micelle.

responsive properties of these micelles in serum and cells, have been demonstrated in Chapter 4. Here we aim to exploit these spectrally active micelles as a model system to study stability in a more complex cancer-on-a-chip platform.

10.2.2. *Microfluidic cancer-on-a-chip*

With the microfluidic cancer-on-a-chip we aimed to recapitulate the four important barriers that the micelles will have to overpass when injected into the body: 1) the blood vessel circulation; 2) the endothelial barrier; 3) the ECM, and 4) the tumor spheroids (Figure 5.2). To

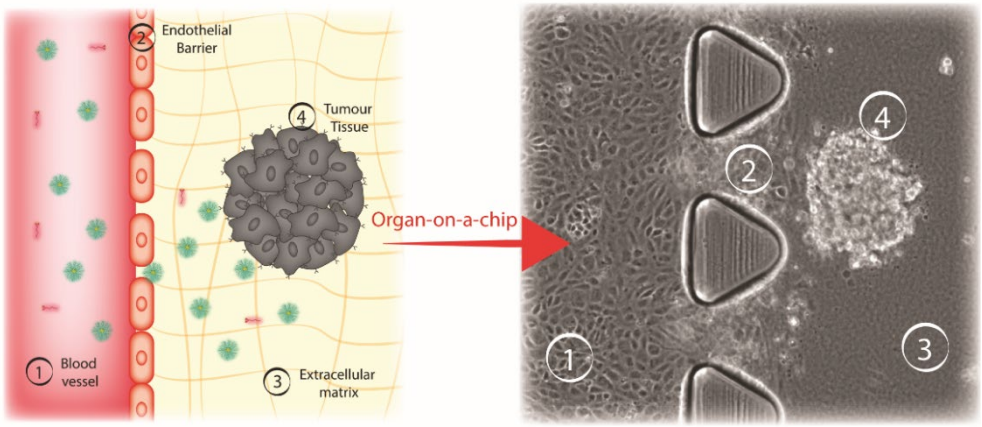

Figure 5.2 Cancer blood vessel-on-a-chip model with the reconstructed barriers marked. Left shows an schematic drawing of the model and in the right the microfluidic chip with the barriers recreated, blood vessel, endothelial barrier, ECM and solid tumour.

establish our platform and recreate these environments we used 3D cell culture chip[19], consisting of 3 microfluidic channels: the central channel with 1.3 x 0.25 mm (w x h) and the two media channels with 0.5 x 0.25 mm (w x h) dimensions (see Figure 5.3). The middle channel is separated from the two lateral channels by rows of triangular posts distant by 100 μm from one another, as shown in Figure 1b right. In our model, one of the lateral channels represents the blood vessel and the interface between the pillars reconstitutes the endothelial barrier. Human Umbilical Vein Endothelial Cells (HUVECs) were seeded on the upper and lower plane of the channel which induced the formation of a lumen-alike geometry. The

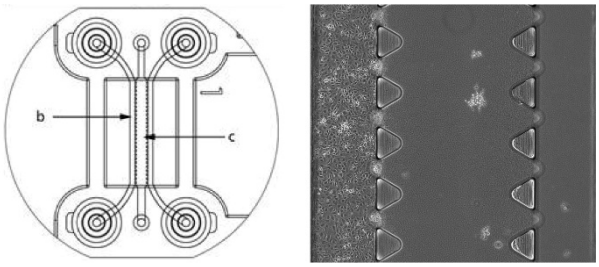

Figure 5.3 Microfluidic chip used to reproduce cancer-on-a-chip. It consists of three microfluidic channels the central channel with 1.3 x 0.25 mm (w x h) and the two media channels with 0.5 x 0.25 mm (w x h) dimensions. The middle channel is separated from the two lateral channels by rows of triangular posts distant by 100 μm from one another

created EB separates the inner lumen of the blood vessel from the central microchannel, where we introduced preformed HeLa spheroids embedded into the Type 1 Collagen Gel. Importantly, co-culture of endothelial and cancer cells in the same systems adds complexity to the model, therefore, growth kinetics of HeLa cells and HUVEC cells were previously evaluated to determine the optimal medium for the healthy growth of both cell lines (Figure 5.4). HUVEC cells did not grow in DMEM medium but they did using both HUVEC optimized media. While, HeLa cells grow was similar using both endothelial cell optimized media. Therefore, HUVEC media was chosen to be used for co-culture experiments. Overall, we recreated a cancer-on-a-chip microenvironment where micelles stability can be evaluated during perfusion through the blood vessel channel. Moreover, the geometry of our model, where one channel is parallel to the other, enables continuous imaging of the interactions of nanosystems with all barriers. This real time imaging cannot be done in other channels conformations proposed previously in which only end time points studies could be performed[18].

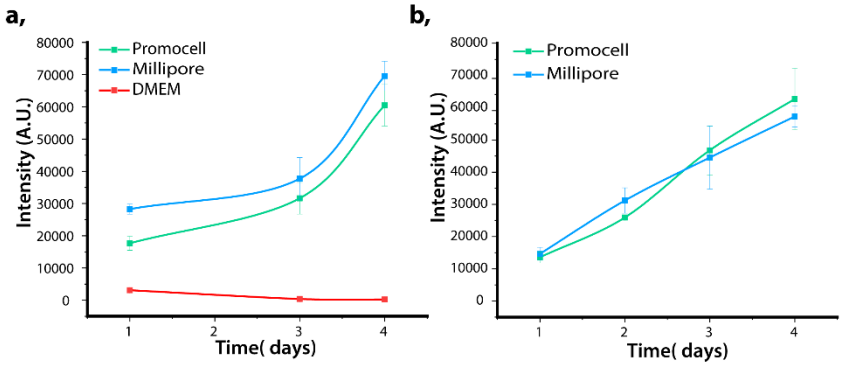

Figure 5.4 Growth kinetics of HUVEC and HeLa. a. HUVEC cell viability test performed after 24, 72 and 96 hours. The absorbance at 570 nm is plotted as a function of time. **b**. HeLa cells viability test was performed at 24, 48, 72, 96 hours. The graph shows the absorbance intensity as a function of time. Every condition was performed in sextuplicate, error bar represents S.D. between wells.

10.3. Reconstructing the barriers in microfluidic cancer-on-a-chip

The evaluation of supramolecular stability using organ-on-a-chip requires a thorough design and characterization of the 3D model prior to further studies. Therefore, we performed a series of experiments aiming to validate the integrity and functionality of our chip. Figures 5.5 show transmission images of our model focusing on the two different channels with Figure 5b upper zooming into the vessel channel and Figure 5b lower into the gel embedded cancer spheroid, while Figure 5.5a shows a zoom-out image of the two channels.

To validate our model, first we aimed to characterize the formation of an endothelial barrier separating both channels. The magnified transmission image of the vessel channel,

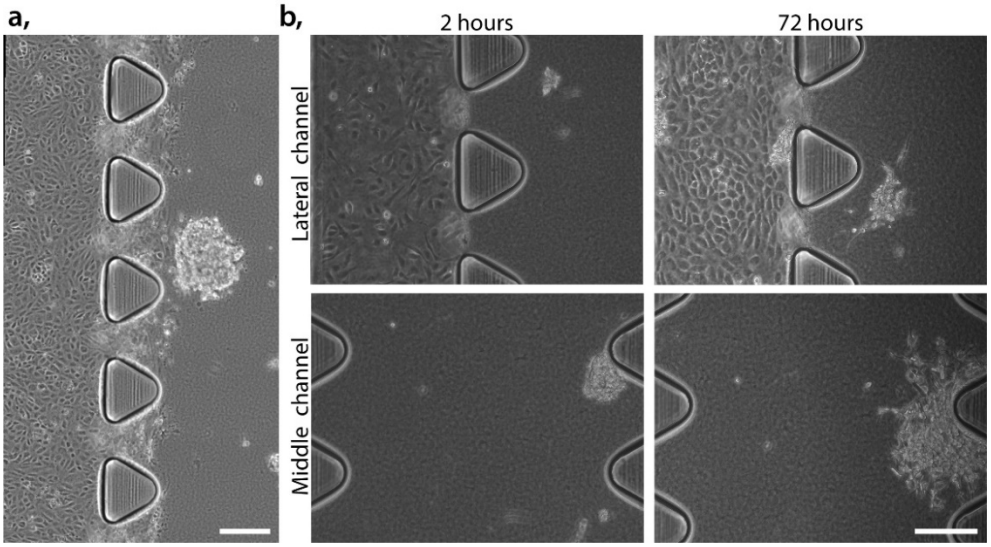

Figure 5.5 Tumor vessel-on-a-chip model. a, Transmission image showing central and lateral channel of the chip with HUVEC in lateral and HeLa in central channel. Scale bar 200 μm **b,** Cell growth in the microfluidic chip after 2 hours, and 72 hours. Transmission images of the same chip are shown: upper row is a magnified image of the lateral channel were HUVECs were seeded to form the 'blood vessel' and part of the middle channel. Lower row shows magnified images of the middle channel consisting on the ECM and the HeLa spheroids. Scale bar 200 μm

(Figure 5.5b) demonstrates the arrangement of a HUVEC monolayer after 3 days of unidirectional medium perfusion, which provided nutrients in a dynamic manner, mimicking physiological conditions, in both the lower and the upper plane of the channel. The formation of the confluent endothelial monolayer was further validated by fixating and staining the cells as shown in confocal image in Figure 5.6, where actin, nucleus and formation of tight junction can be observed. The endothelial cell to cell contact results in the expression of tight junction zonula occludens-1 (ZO-1, green) protein, which is essential in forming these junctions and corroborate the creation of a healthy endothelial barrier. Moreover, 3D confocal imaging allowed us to demonstrate the appearance of the EB on the interface of the blood vessel and ECM channel (Figure 5.6b). This vertical endothelial monolayer physically separates the lumen of the vessel channel from the collagen gel, mimicking the *in vivo* barrier. Interestingly, HUVECs in our chip aligned parallel to the flow direction due to the shear stress mimicking physiological conditions[20,21](Figure 5.7). In contrast, cells cultured in static conditions show random arrangement following similar observations reported previously[22] . Subsequently, we tested the structural integrity of the HUVECs barrier by measuring the retention of fluorescently labeled 10 kDa Dextran perfused through the "blood vessel". The fluorescence signal was detected in the lumen of the lateral channel but not in the collagen gel (Figure 5.7c) indicating proper functionality of the endothelial barrier. Altogether, these measurements indicate the formation of a functional EB with good structural intergity.

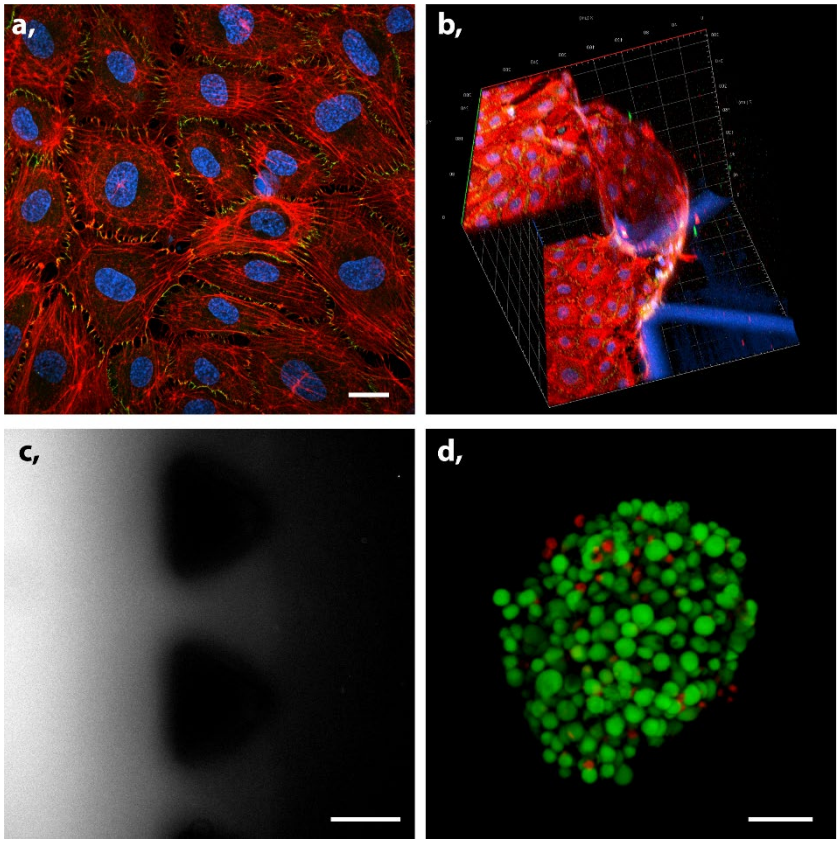

Figure 5.6 Integrity and functionality of cancer-on-a-chip. a, Confocal image of HUVEC confluent monolayer (red: Phalloidin, blue: Hoechst, green: ZO-1). Scale bar 20 μm, **b,** 3D confocal image of HUVECs/gel interface (red: Phalloidin, blue: Hoechst, green: ZO-1), scale: axis ticks 40 μm, **c,** Epi fluorescence image of Dextran perfused during 10 minutes into the lateral channel lined with HUVEC monolayer, retaining the 10 kDa Dextran. In this experiment there were no HeLa cells in the collagen gel. Scale bar 150 μm, **d,** Confocal image of stained HeLa spheroid live – green (calcein), dead – red (Propidium iodide). Scale bar 50 μm

Finally, the transmission image of gel-embedded HeLa cells allowed us to observe their 3D spheroid conformation (Figure 5.5) This arrangement implies less available surface area per cell, than in 2D cell culture models[23] and it recapitulates important aspects of geometry present in physiological conditions that cannot be studied in 2D cultures. The spheroids were introduced into the chip with sizes of 50-100 μm, and after 3 days of culturing they grew up 2-3 times of their original size, as shown in Figure 5.5b. A live/dead staining assay revealed that the cells are viable within the spheroid after 3 days of culture (Figure 5.7d), indicating that the nutrients of the culture medium and oxygen diffuse through the spheroids and are able to sustain the cell growth. Overall, we recreated a functional, microfluidic platform of a 3D tumor microenvironment, with perfusable blood vessel and cancer cells conformed into

spheroid, more accurately resembling physiological conditions than previously proposed platforms [16–18,24].

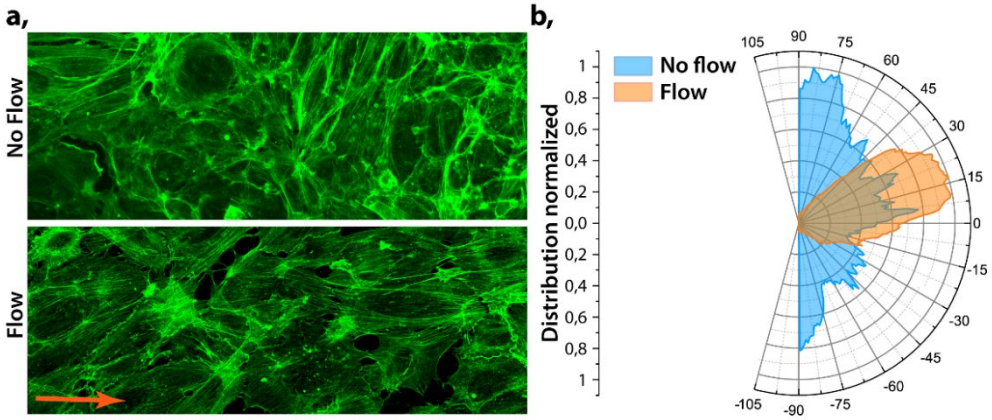

Figure 5.7 HUVECs align with the direction of the flow. Two independent chips were prepared as explained, however, one of the chips was incubated in static conditions, with medium change every 24h, meanwhile the other was continuously perfused with cell medium. After 72 hours the cells were fixated and actin stained, confocal images of actin were acquired using Zeiss LSM 800. The images were analyzed using the OrientationJ plugin of ImageJ to obtain the distribution of the orientation's graphs. It can be observed that the cells without flow are oriented randomly having components in all directions, while the cells cultured under flow have a dominant direction.

10.4. Increased extravasation of micelles is induced in cancer blood vessel chip

Having established our cancer vessel-on-a-chip microfluidic model, we aimed to investigate the ability of the micelles to permeate the blood vessel into the ECM channel. Previous studies using microfluidic models reported enhanced permeability of endothelial cells when exposed to specific molecules such as TNF-α[18] or when co-cultured with cancer cells[16], leading to the formation of "leaky vessels" which recapitulate the EPR effect. However, the majority of these microfluidics models were used for studying only the end time point of nanoparticles permeation, lacking the intermediate progress of their extravasation. Herein, taking advantage of the design of our chip, we could continuously monitor the perfusion of our micelle system under three different experimental conditions: i) no HUVECs as negative control; ii) HUVECs barrier, and iii) HUVECs barrier with proximate HeLa spheroids mimicking a tumor blood vessel.

First, we aimed to test the ability of the micelle to cross the endothelial barrier, therefore, we perfused hybrid **1** into the three different models. In Figure 5.8a it can be observed that the hybrid immediately penetrates the collagen gel in the negative control (without HUVEC). This experiment proves that the properties of our NPs (e.g. small size of the micelles of about

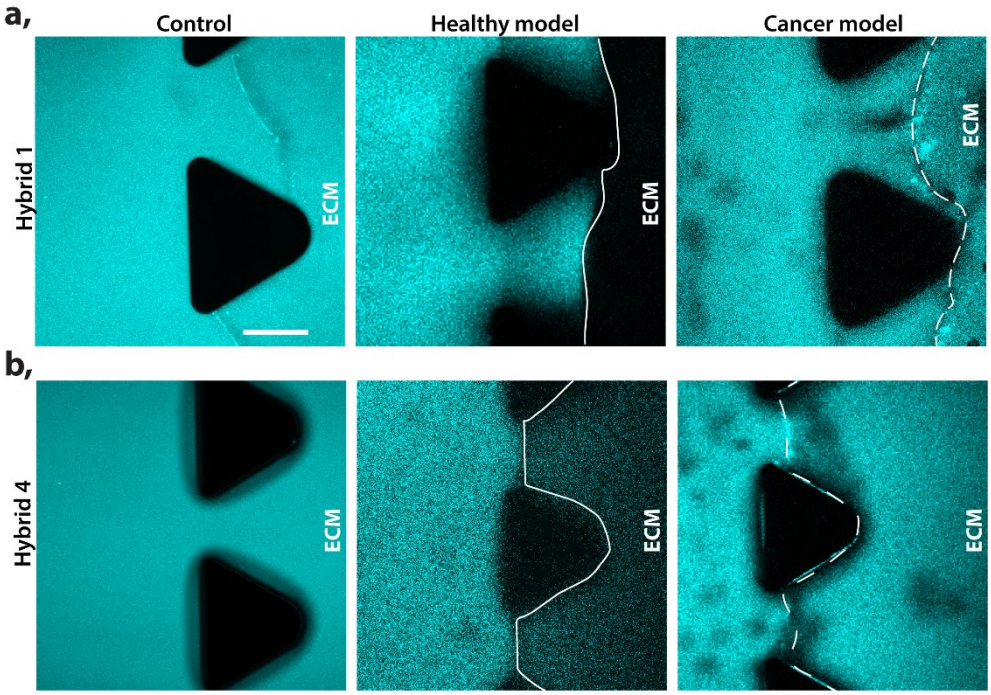

Figure 5.8 Extravasation of PEG-dendron hybrids in healthy and cancer models. Confocal image of hybrid 1 extravasation in a control chip (no HUVEC barrier), a healthy model (HUVEC barrier formed in the interface of the collagen gel) and cancer model (HUVEC barrier formed with presence of HeLa spheroids in the collagen gel). The images show emitted intensity between 446-700 nm, which include both monomer and micelle signal. Scale bar 100 μm **b.** Confocal image of hybrid 4 extravasation in the 3 corresponding models. Scale bar 100 μm

20 nm[25]) allow their free diffusion through the ECM[4]. In contrast, hybrid **1** was successfully retained in the healthy blood vessel channel where HUVEC barrier blocks the permeation. Finally, if cancer cells were cultured in the collagen gel (mimicking the TME), we observed diffusion of hybrid **1** through the EB into the ECM channel after few minutes of infusion. These observations resemble experiments performed by Tang and co-workers where co-culture of cancer endothelial cells and breast cancer cells increased the permeation of nanoparticles through the EB[16]. Using quantitative analysis, we could define the percentage of polymer able to cross the barrier in each model as a function of the detected fluorescence intensity in the perfused channel. We observed that close to 100% of the labeled hybrid fluorescence was detected in the collagen gel after less than a minute when there was no endothelial barrier. However, within the first 30 minutes of hybrid perfusion only an equivalent of 10% of the perfused polymer intensity was detected across the endothelial wall in the case of the healthy blood vessel, while at the same time point about 80% of the hybrid was detected in the ECM region in the tumor blood vessel. These results indicate that the HUVEC monolayer in the healthy model significantly restricts the hybrid from crossing the

EB and penetrating the ECM. However, however the barrier function is undoubtedly affected, even when HeLa spheroids are present in the gel (tumor model), where only a fraction of the perfused hybrid was retained by the endothelial wall. Interestingly, we hypothesized that the 10% of hybrid detected in collagen gel of the healthy model could origin from the permeation of the smaller monomer form (~3-5 nm) and not the assembled micelle (~20 nm), considering the healthy EB permeability[26].

To investigate this proposed possibility of the monomer form to extravasate in the healthy model we perfused hydrophilic hybrid **4**, which has four hydroxyl end-groups and hence doesn't self-assemble into micelles, as reported previously[25]. This hybrid was used as a control to study the behavior of the labeled monomeric form. The perfusion of hybrid **4** was followed in time in the three different models and the experiment was ended when the hybrid was observed to infiltrate into the collagen gel (like in Figure 5.8b). As expected, the monomer penetrates into the ECM in the control and the cancer models, but also, in the healthy one. HUVEC barrier partially retained the monomer in healthy blood vessel model for 25 minutes

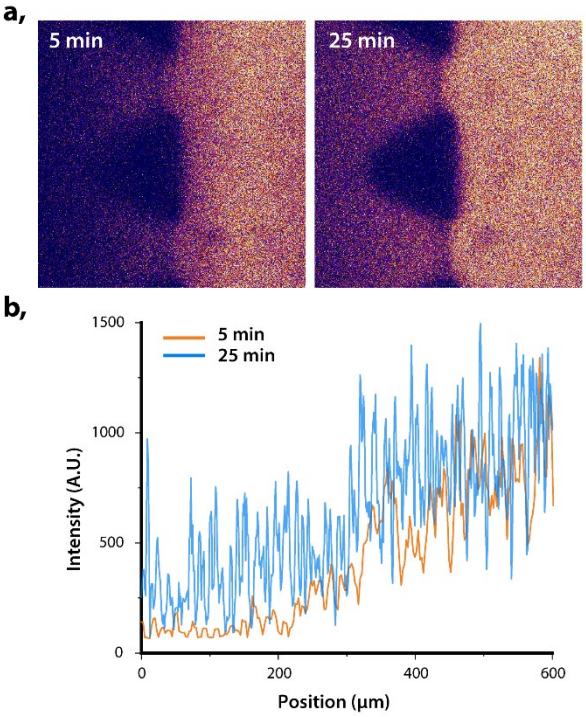

Figure 5.9 Extravasation of hybrid 4 in healthy model already occurs after 5 minutes of continuous perfusion. A healthy microfluidic model was prepared and hybrid 4 was flow for 25 minutes to study its extravasation a. Confocal images of the hybrid 4 being flow through the 'blood vessel' at 5 and 25 minutes. In the images the 'blood vessel' channel (right) and part of the ECM (left) can be observed. b. Plot profile of a horizontal line across each image showing the intensity detected in each position. After 5 minutes hybrid was detected in both the gel and the channel, but the intensity in the gel was only 15% the channel one while after 25 minutes it was 40%.

of continuous perfusion, limiting its concentration in the gel to ~40% of its concentration in the blood vessel channel. It is worth noting that after 5 minutes some hybrid could already be detected in the gel of healthy blood vessel (Figure 5.9). However, the time required was significantly shorter when HeLa cells were co-cultured in the gel. In case of tumor blood vessel, the penetration of hybrid **4** was almost immediate after inflow started, we measured similar concentrations of the hybrid in all regions after 5 minutes. Therefore, we hypothesize that the monomer form can cross into the ECM even in the healthy blood vessel model due to its small size, which may allow it to penetrate the ECM region through paracellular transport.

Next, we aimed to visually determine the morphological effect of co-culturing cancer cells on the structural integrity of the endothelial monolayer, to understand if a loss of integrity was the reason for the increased micelles permeation in the tumor blood vessel model. Tight junctions and adherent junctions are crucial structural elements formed between endothelial cells, they are essential part of the endothelial barrier, regulating paracellular diffusion. These junctions' main function is to restrict the permeation of molecules bigger than ~2 nm[27] from

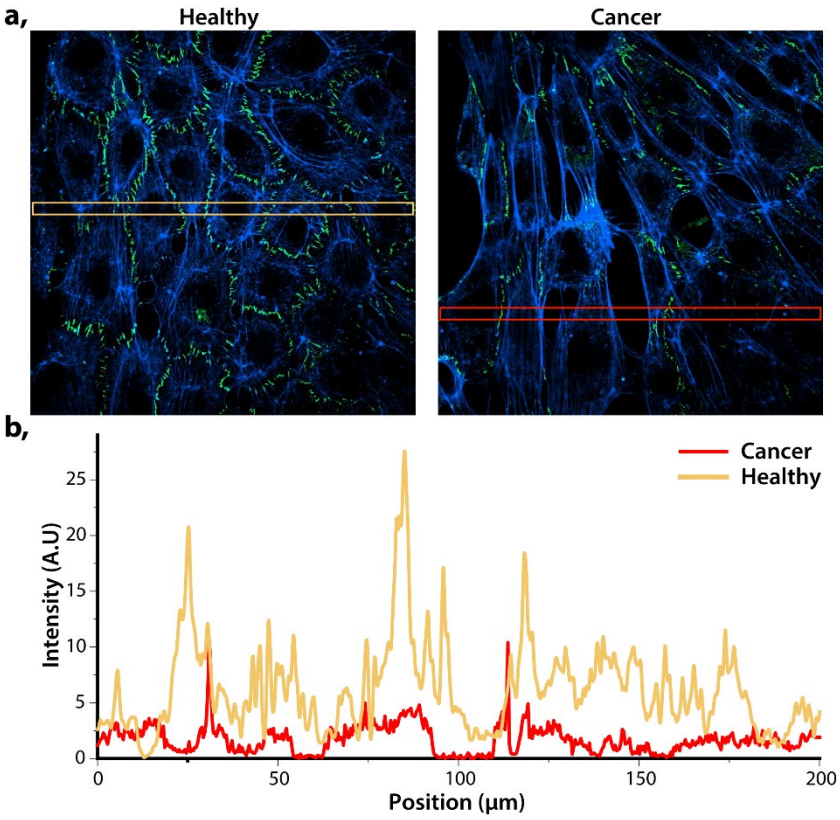

Figure 5.10 Confocal images of monolayer of HUVECs formed lining the healthy (left) and cancer (right) blood vessel channel. Actin (blue) and ZO-1 (green). b. Plot profile of ZO-1 expression of the section highlighted in (a) of cancer vs healthy model

extravasation outside blood vessels. To further confirm that the enhanced permeability of the barrier in our microfluidic model was induced by the presence of cancer cells, we studied the expression of ZO-1, an essential protein forming tight junctions. Both, healthy and cancer blood vessel models were prepared as mentioned previously. After 3 days of continuous cell culture medium flow the cells were fixed in the chip and ZO-1 protein stained as shown in Figure 5.10. ZO-1 was clearly and uniformly expressed in the interface between HUVECs of our healthy model. However, the expression of ZO-1 was reduced when HeLa spheroids were co-cultured with endothelial cells (cancer blood vessel-on-a-chip model). These observations indicated that cancer cells impact the HUVEC cell-cell interaction, reducing the tight junction formation, therefore, making the blood vessels leakier. All these observations further confirm the existence of an enhanced permeability in our cancer models. Similarly to previous studies by Kaji et al.[28] reporting that HUVEC and HeLa coculture affects the endothelial cells growth through either direct cell-cell contact as well as transmission of information via culture medium (paracrine communication). The cytokines excreted by HeLa can repulse HUVECs from their proximity and released reactive oxygen species lead to malfunction and even death of HUVECs, thus inducing leakiness of the endothelial barrier, permitting transportation of normally retained particles. However, it is worth noting that the permeation of micelles in the tumor blood vessel model was heterogenous and not always occurred at the same time point. We observed that small differences in number of spheroids or the proximity between spheroid and HUVECs monolayer impairs their retention capacity, which could be due to a variable concentration of signaling molecules. These observations reflect the heterogeneity of the EPR effect, which has been extensively discussed recently and is related not only to the type of cancer but also to the stage of the diseases[29].

10.5. Time- and space-resolved micelle stability revealed in 3D tumor microenvironment model

The major aim of the current work was to study the stability of our micelles systems when introduced into our microfluid based 3D TME model. In our previous work, it was possible to detect the micelles and monomer inside cells due to the ability of the labeling coumarin dyes to change their emission wavelength upon disassembly. This self-reporting capabilities allow us to use confocal fluorescence microscopy to study the internalization pathway of different hybrids and correlate to them to their assembled state[25]. Herein, we hypothesized that the added complexity and dynamicity of the vessel-on-a-chip model may induce premature disassembly due to multiple possible interactions. To evaluate these critical interactions, we perfused hybrid 1, which was previously reported as the most stable system, in culture medium into the blood vessel channel. Then, we monitored in real time the micelles' stability in key regions: the "blood vessel", the endothelial barrier, the ECM and the HeLa spheroids as shown in Figure 5.11. Notably, micelles are represented in cyan and monomers (disassembled form) in magenta.

In the first minutes of perfusion fluorescence was detectable only in the lateral perfused channel, coated with the monolayer of HUVECs (Figures 5.11 and 5.12), and indicated assembled micelles (Figure 5.12). Progression of hybrid penetration into the depth of the ECM

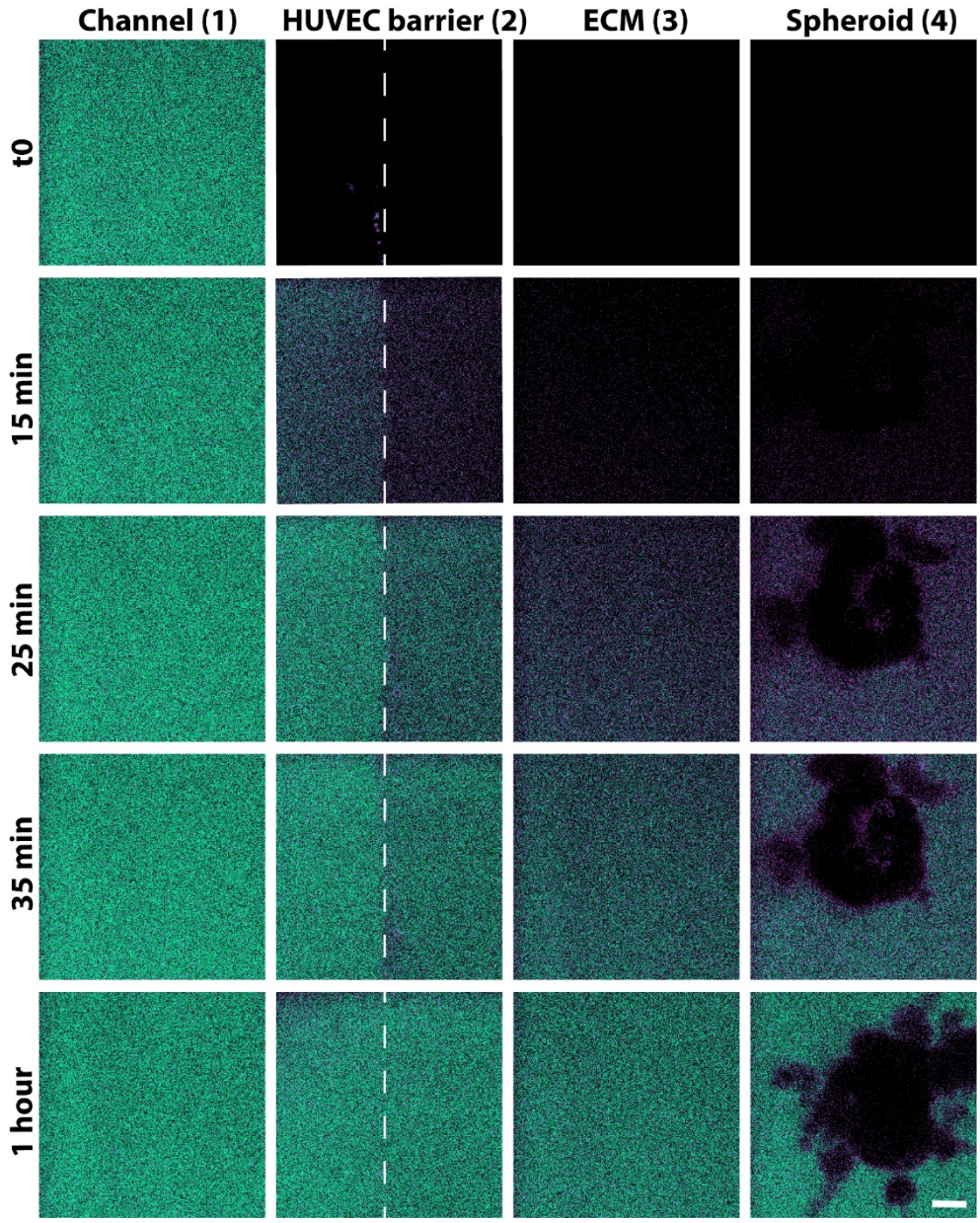

Figure 5.11 Space and time-resolved stability of hybrid 1. a. Ratiometric confocal images of real-time monitored presence of micelle (green) and monomer (magenta) at reconstructed barriers (1 - blood vessel, 2 - HUVECs barrier, 3 - ECM and 4 - cancer Spheroid) during constant perfusion of the hybrid 1, scale bar 15 μm.

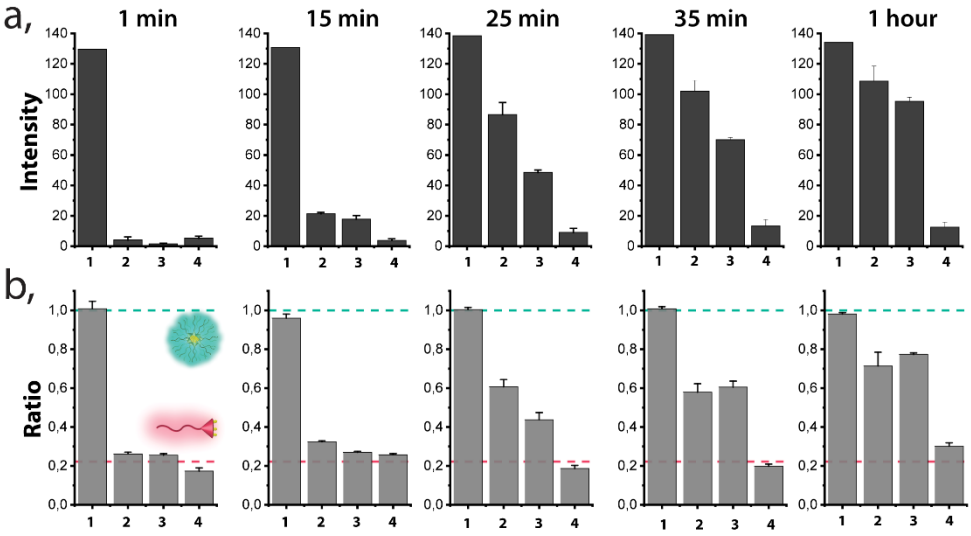

Figure 5.12 a,Time-resolved intensity of fluorescence signal originating from the sum up of both micelle and monomer channels at each barrier. c. Normalized ratio of fluorescence signal between micellar and monomer form monitored in time at different barriers. Green dashed line indicates the ratio of fully formed micelles in equilibrium and the magenta dashed line indicates the ratio of fully disassembled (monomer) form.

was observed over time. After 15 minutes of continuous flow the hybrid started to reach the endothelial barrier but based on the fluorescent intensity at the wave length corresponding to the monomeric coumarin, we could observe that mostly the monomer prevailed in passing through the ECs wall and entering the ECM as shown by the prevalence of the magenta signal in the central compartment. This is likely related to the smaller size of the monomer, allowing much better passage through the EB. After 25 minutes we observed the assembled micelles starting to traverse the EB, while the deep penetration into ECM (towards the tumor area) was still achieved mostly by the disassembled polymers. This observation could be attributed to two factors: i) the micelles progressively overcame the endothelial barrier or ii) the monomer form, which entered the ECM through the EB previously, accumulated and reached the critical micelle concentration (CMC), thus re-assembling into micelles. Figure 4b demonstrates that both, micelle and monomer forms coexist in the endothelial barrier, and in the ECM as the mean ratio is 0.6 and 0.4 respectively, not corresponding to the completely assembled neither the completely disassembled form. The assembled structures were not detected in the surroundings of the spheroids until more than half an hour of continuous perfusion. In addition, we observed only a weak penetration of the hybrid **1** into the depth of HeLa cells spheroids after 1 hour, but also after 2 hours of constant perfusion of micelles through the cancer blood vessel, as presented in Supplementary Figures 5.13. We observed

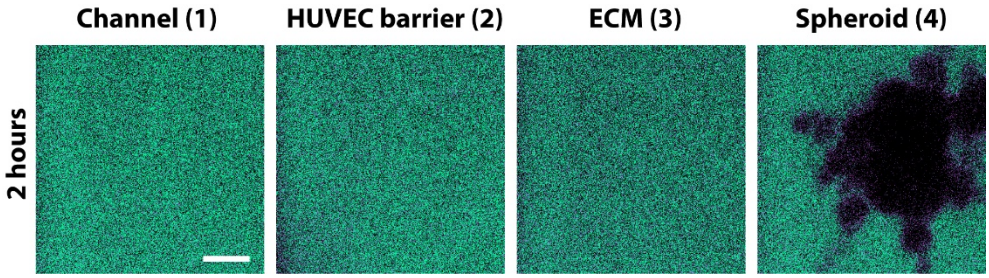

Figure 5.13 Space resolved stability of hybrid 1 after 2 hours of continuous perfusion. Ratiometric confocal images of real-time monitored presence of micelle (green) and monomer (magenta) at reconstructed barriers (1 - blood vessel, 2 - HUVECs barrier, 3 - ECM and 4 - cancer Spheroid). Scale bar 20μm.

the stabilization monomer/micelle equilibrium in all monitored regions after 1h from the beginning of the perfusion, excluding the spheroid.

Interestingly, hybrid **1** in contact or in close proximity to HeLa cells was always detected as monomer, Figure 5.14. This observation contrasts to previously reported internalization behavior in 2D cell cultures where it was demonstrated that assembled hybrid **1** was taken up by HeLa cell via endocytosis, and its disassembly progressed in time[25]. This discrepancy can be attributed to the 3D conformation of the cells, as spheroids, which could promote different endocytosis processes related to the new 3D cells confluency and conformation, highlighting the importance of going beyond 2D cell culture models. Other preceding works investigated the penetration of nanosystems into tumor spheroids as a function of nanocarrier size, shape, charge and functionalization[30–32]. Likewise, the penetration of cross-linked and non-cross-linked micelles into spheroids has been compared, showing an improved tumor penetration for the cross-linked ones, which was linked with their higher stability[48–50] . Therefore, we hypothesized that the lower penetration into our model can be caused by a premature disassembly in the periphery of the spheroid.

Here, for the first time, we can demonstrate the real-time interactions of dynamic supramolecular systems with cells in a dynamic 3D environment., which are different than the interactions in a static 2D cell cultures. Therefore, the system stability at different physiological barriers can be evaluated and correlated to its final penetration into the cancer cells. These results highlight the importance of selecting adequate screening models, which resemble to much greater extent the *in vivo* cell arrangement and features, to rationally evaluate and optimize supramolecular nanocarriers design. This approach sheds light on how nanocarriers stability affects their accumulation in solid tumors *in vivo.* Overall, by combining confocal imaging and a microfluidic 3D cancer-on-a-chip model we could demonstrate the high stability of hybrid **1** against induced flow shear stress and interactions with the ECM, while we prove a low stability/penetration in contact with 2D arranged cancer cells. This

impedes the assembled state to penetrate the solid tumor in the current more realistic model along with general low penetration of the perfused structures into the HeLa spheroids.

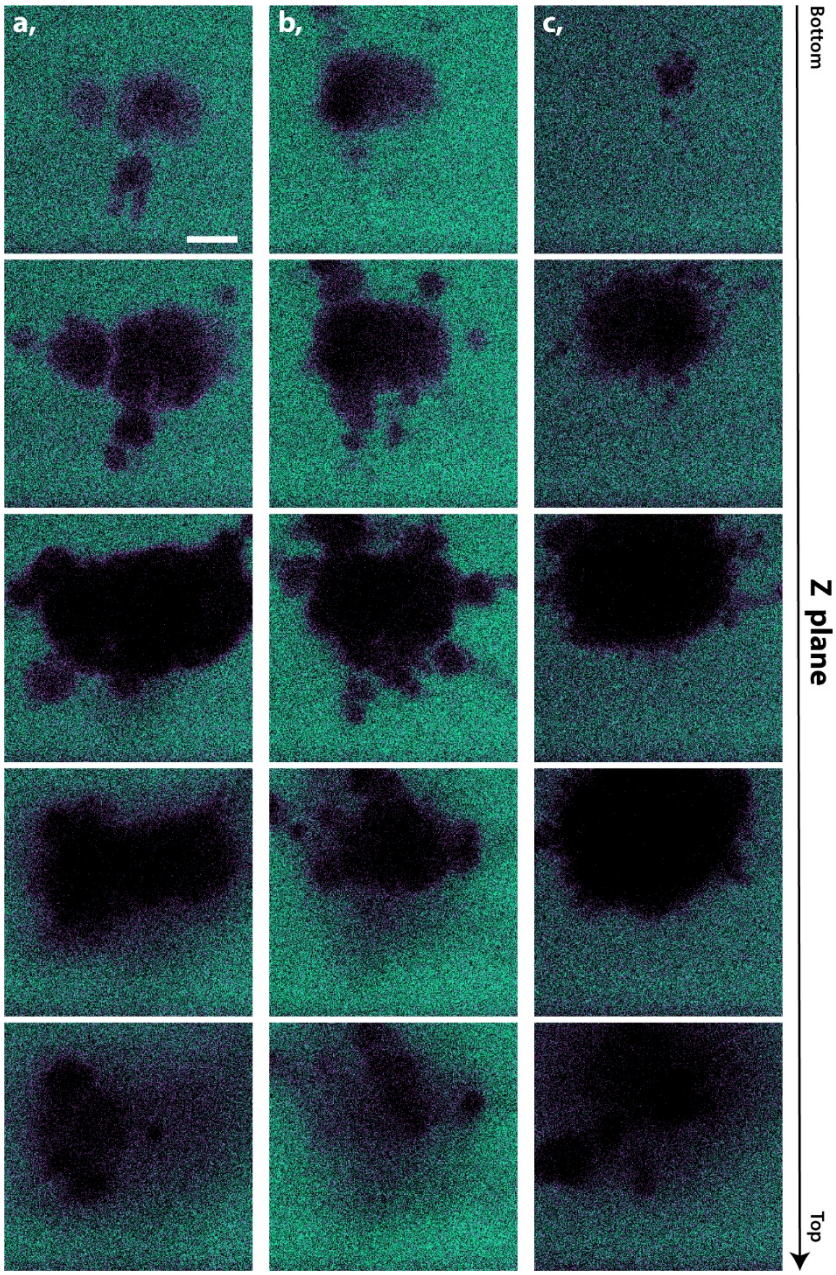

Figure 5.14 Penetration and stability of hybrid 1 in the HeLa spheroids after 2 hours of continoius perfusion. Ratiometric confocal images of real-time monitored presence of micelle (green) and monomer (magenta). a. Z-stack images of spheroid 1 b. Z-stack images of spheroid 2 c. Z-stack images of spheroid 3. Scale bar 20μm

10.6. Stability of hybrids dictates their infiltration/extravasation

Finally, we aimed to investigate the interplay between molecular structure and micellar stability and the consequent ability to extravasate. Therefore, we compared the stability of three hybrids, with decreasing length of the hydrophobic end-groups starting from four undecanoate tails for hybrid **1** to four octanoate alkyl chains for hybrid **2** and four phenyl acetate for hybrid **3**, which have also eight carbons but differ by the presence of the more polar aromatic ring. Using the cancer vessel-on-a-chip model, we wanted to identify the factors affecting their performance in the new 3D system. In our previous studies[25], we demonstrated that stabilities of hybrid **2** and **3** were similar when diluted with serum, however, the kinetics of their disassembly were significantly different. While hybrid **3** disassembles rapidly upon dilution, hybrid **2** needed hours to reach the equilibrium. In contrast, hybrid **1** was stable both in the presence of serum proteins and upon dilution. Here, we aimed to understand how these differences in thermodynamic and kinetic stability are reflected in a complex model, where the micelles face the reconstructed barriers of the tumor microenvironment. Experiments with each one of the three hybrid systems were performed by perfusing a solution of culture media containing the micelles through the blood vessel channel of the chip. In Figure 5 we show representative images of two different areas of the chip for each of the perfused micelles. First, we investigated the ability of each hybrid to cross the endothelial barrier. We observed extravasation of all hybrids **1-3** when HeLa spheroids were located close to HUVECs (Figure 5b). In contrast, in the regions where spheroids were further away (hundreds of microns), only hybrid **3**, which has the least hydrophobic dendron in comparison with hybrids **2** and **1**, was able to significantly extravasate to the ECM. Thus, we conclude the endothelial barrier "leakiness" can be heterogenous, depending on the amount, distance and distribution of tumor spheroids in the ECM.

We next tested the stability of the three hybrids, under flow conditions when perfused through the vessel-like channel (Figure 5a and c). Based on the ratios between the emitted intensity of the coumarin dye at 480 nm and 550 nm, corresponding to the disassembled and assembled state of the labeled polymers, we could study the assembled states of the different hybrids. We did not observe disassembly of hybrid **1** in the vessel channel, with mean ratio of fluorescence signal between micellar and monomer form equal to 1, which is indicative of the presence of micelles, while we observed slight disassembly of hybrid **2** and significant disassembly of hybrid **3**, with mean ratios of 0.8 and 0.5 respectively. Previous investigations[25] showed hybrid **2** and **3** were slightly unstable in presence of serum proteins, but the degree of disassembly based on the fluorescent ratio was the same for both. Therefore, we hypothesized the enhanced disassembly rate of hybrid **3** is not only due to interactions with serum proteins but also affected by the flow. This result indicates that the flow-induced shear stress can drastically affect the stability of supramolecular nanocarriers.

Further, we monitored the stability of each hybrid at the previously defined barriers and observed significant differences among them. Interestingly, in regions far from spheroids only

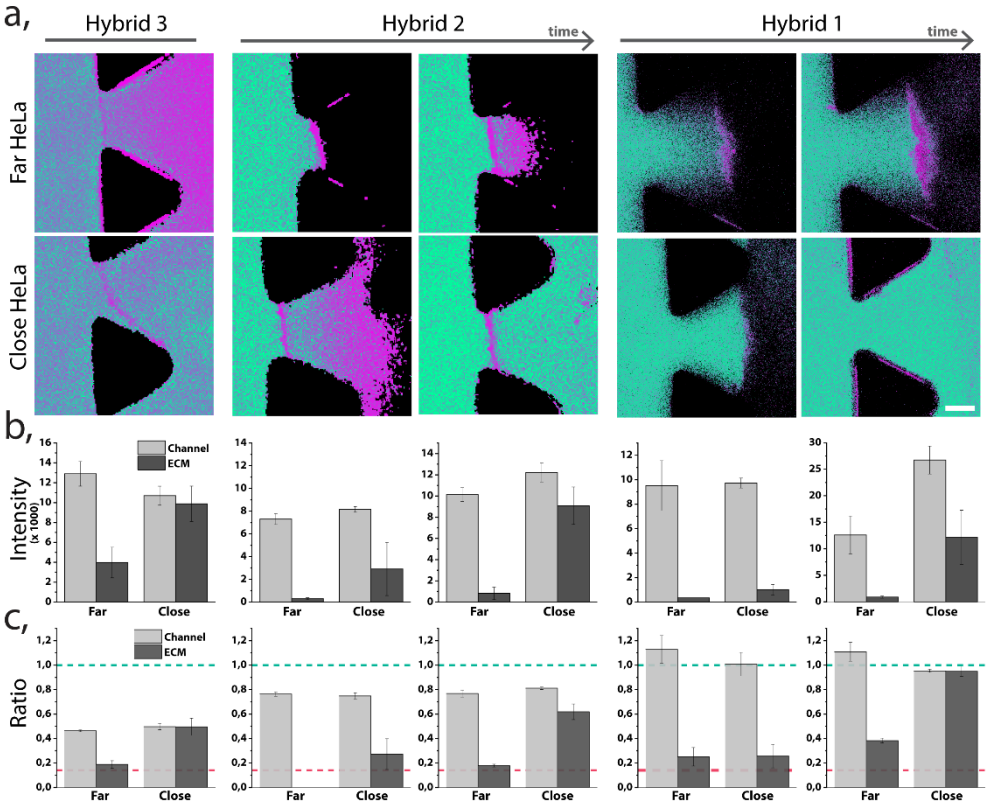

Figure 5.15 Stability of different hybrids in blood vessel-on-a-chip. a. Ratiometric confocal images of the different hybrids inside the chip in two different regions. Hybrid 1 and 2 are shown at 2 different time points: less than 15 minutes and after more than 30 minutes of continuous perfusion. Scale bar 75 μm. **b.** Intensity of fluorescence signal originating from the sum up of the intensity of both the monomer and the micelle channels. Intensity was measure in the vessel channel and in the ECM region **c.** Normalized ratio of fluorescence signal between micellar and monomer form for each hybrid and in each region. Green dashed line indicates the ratio of fully formed micelles in equilibrium and the magenta dashed line indicates the ratio of fully disassembled (monomer) form.

the monomeric form of hybrid **3** was able to efficiently extravasate. This phenomenon could occur due to the increased disassembly of the micelle in contact with the HUVEC barrier, which allowed the monomer i) to paracellularly extravasated due to its small size or ii) to transcellularly cross the EB. Noticeably, among all the tested hybrids only monomer of hybrid **3** extravasates efficiently, most likely due to the low stability of this hybrid in contact with cells. In contrast to that, in regions close to HeLa, hybrid **3** crossed the EB mostly in the semi-assembled state (as it appeared in the blood vessel channel), probably due to the increased wall leakiness. These results indicated that the disappearance of the tight junctions allowed the assembled micelles to cross the barrier. Differently, extravasation of micelles formed from hybrid **2** in regions close to HeLa, had a time dependent response; first only monomer crossed the EB whereas, assembled micelles were detected in the ECM only after more than 30 minutes. Finally, we observed that hybrid **1** behaves similarly to the hybrid **2**, where

monomer molecules extravasated first, followed by the later penetration of the assembled micelles. Interestingly, while hybrid **2** and **3** accumulated in the endothelial barrier only as a monomer, hybrid **1** monomeric form accumulated only in areas far away from the HeLa cells. We hypothesize a relationship between the micelles' stability and the different internalization behavior of hybrids, while **3** and **2** were observed to internalize as monomer in the previous work, **1** internalized as a micelle and disassembled over time[25]. These results corroborate our previous observations, where hybrid **1** is proven to be the most stable system, but also, demonstrate the high stability of hybrid **2** in complex systems. Overall, we could correlate the interplay between stability of the micelles and their performance in a 3D model, as well as their ability to extravasate to reach the tumor regions.

10.7. Conclusions

In the present work, we introduced the combination of spectral confocal imaging and a microfluidic 3D cancer-on-a-chip model as a new approach to study the stability of supramolecular nanocarriers. The unique fluorescence properties of our micelles allowed us to track their assembly state across the changing conditions and correlate their stability with the ongoing biological interaction. The cancer-on-a-chip introduced here, enriches the study thanks to its similarities to physiological conditions, introduced especially via the 3D dimension in cellular distribution and through active flow in the blood vessel channel. This approach helps to recapitulate the barriers to be overcome (e.g. blood flow, endothelial wall, ECM and 3D cancer spheroids) that cannot be successfully reconstructed in a 2D cell culture. The results obtained show the formation of leaky vasculature in the presence of cancer cells, but also, a high heterogeneity among different chips or even across distant regions of the same chip, related to number of cancer cells and distance from the endothelial cells. Importantly, these features resemble to a great extent the *in vivo* pathologies of many tumors. Moreover, we obtained a precise and direct information about the performance and stability of the micelles in each of the barriers, thanks to the time and space-resolved imaging. We demonstrate the ability of hybrids **1** and **2** to extravasate from 'blood vessel' as assembled micelles, while the complex interactions of EB and the ECM induce the disassembly of micelles of hybrid **3**. Interestingly, we observed the loss of stability of hybrid **1** in close proximity to spheroids, as well as, a very low penetration into the tumor. These results demonstrated the importance of screening nanocarriers stability in more complex 3D based systems to accurately predict their potential to be translated into the clinic. Our approach of combining spectrally responsive supramolecular structures with a platform reconstructing cancer-on-a-chip has the capacity to provide new knowledge about nanoparticles performance, stability and accumulation in tumor, which will allow to bridge the gap between *in vitro* and *in vivo* testing of new drug delivery systems.

.

10.8. Experimental Section

10.8.1. Microfluidic device

Microfluidic 3D culture chip DAX-1 (AIM Biotech) was used as a platform to reconstruct tumor microenvironment. LUC-1 connectors (AIM Biotech) were used to connect the chip inlets with luer connector ended PTFE tubing. The other end of the tubbing was connected to a syringe placed in a double syringe pump (Nexus Fusion 200) and filled with HUVEC (EndoGRO, Millipore) basal medium, used to constantly perfuse the chip for 48 – 72h.

10.8.2. Cells and reagents

Human Umbilical Vein Endothelial Cells (Promocell) were used to recreate blood vessel lining and HeLa cells were used in to create tumor spheroids. HUVECs were cultured in EndoGRO Basal Medium (Millipore) supplemented with SCME001 kit (EndoGRO-LS Supplement 0.2%, rh EGF 5 ng/mL, Ascorbic Acid 50 μg/mL, L-Glutamine 10 mM, Hydrocortisone Hemisuccinate 1 μg/mL, Heparin Sulfate 0.75 U/mL, FBS 2%) and penicillin/streptomycin 1% (Biowest). HeLa cells were cultured in DMEM (as received with L-Glutamine, 4.5 g/L D-glucose and pyruvate, Gibco) supplemented with FBS 5% (Gibco) and penicillin/streptomycin 1% (Biowest). HUVEC were cultured in 75 cm2 flasks and HeLa in 25 cm2 flasks at 37^{0}C and 5% CO2. Cells were harvested using trypsin-EDTA (0.25%, Gibco) when reached 70-80% confluence.

10.8.3. Growth kinetics of HUVEC and HeLa

HUVEC cells or HeLa were seeded in a 96 well plate at a density of 2500 cells/well and incubated with three different medium types: DMEM medium 10%FBS which is used for HeLa cell grown and Promocell or Millipore media optimized for HUVEC. PrestoBlue cell viability test was performed after 24, 72 and 96 hours. The absorbance at 570 was measured after PresoBlue reagent addition using Tecan Microplate Reader.

10.8.4. Cell culture in the Microfluidic device

Collagen gel at concentration of 2.5-3.0 mg/mL was prepared, introduced and polymerized according to the general protocol v5.3 (AIM Biotech). In brief, Rat tail collagen Type I (Corning Life Science) was mixed on ice with 10x PBS (Sigma Aldrich) and Phenol Red (Sigma Aldrich), and pH of the mixture was adjusted between 7-8 using 0.5 M NaOH (NaOH in pellets PanReac dissolved in MiliQ water), final volume was adjusted with MiliQ water (for healthy model) or suspension of HeLa clusters (for cancer model).

For preparation of cancer model microfluidic chip HeLa cells were seeded into 96-well ultra-low attachment plate (Corning) at 0.5 – 1.5 k cells/well and cultured for 48-96h. Formed cell spheroids were harvested, centrifuged and resuspended in previously prepared collagen

gel, resulting in few clusters (30-200 μm) per 10 μL of the gel. Prepared collagen was inserted into the central channel of 3D culture chip and allowed to polymerize during 30 min at 37^{0}C and 5% CO_2. After gel polymerization one of the lateral channels was prepared for HUVECs culture, by coating the channel with 50 μg/mL fibronectin (FN) from bovine plasma (Sigma Aldrich) during about 2h at 37^{0}C. Remaining lateral channel was filled in with DMEM (HeLa culture medium) and closed using luer caps.

After the incubation time, the FN was washed away using 1x PBS (Gibco) and EndoGRO HUVEC medium. HUVECs were seeded to the prepared lateral channel at a density of 2.5-3.5M cells/mL. The 3D culture chip was flipped upside down to allow cell adhesion to the upper plane during 1.5-2.5h at 37^{0}C and 5% CO_2. Second batch of HUVECs cultured in another flasks was harvested and introduced to the same lateral channel at the same concentration as previously. The cells were then incubated for minimum 2h at 37^{0}C and 5% CO_2 in the upright placed chip to allow their attachment to the lower plane. Next, the chip was perfused with EndoGRO HUVEC medium at a flow rate 3-5 μL/min during 48 - 72 hours (as described above), until HUVECs reached confluency.

10.8.5. Hybrids perfusion setup

Hybrids were prepared at a concentration of 480 μM in filtered PBS, sonicated for 5 minutes and let to equilibrate for at least 10 minutes. Prior to hybrid flowing into the chip they were mixed with EndroGRO HUVEC medium resulting in final concentration of 160 μM.

The microfluidic chip was placed into the on-stage incubator of a Zeiss LSM 800 Confocal microscope at a temperature of 37^{0}C and 5% CO_2, and connected to peristaltic pump (Ismatec, Reglo Digital, ISM597) with a silicon tubing (Tygon, Kinesis) to perfuse hybrids at real-time, at 15 uL/min, while imaging. Hybrids were excited using 405 nm laser and emission spectra was collected using two different PMT detectors to detect both monomer and micelle separately and simultaneous. The windows of detection were set as following: i) monomer 446-500 nm and ii) micelle 500-700 nm. Ratiometric images were obtained from dividing the micelle image by the monomer image, after applying a mask to each image were noise was removed.

To calculate the amount of hybrid able to extravasate we first sum up the signal of both windows. Next, we calculated the mean intensity signal of the vessel channel and used this value as the maximum concentration. Next the mean intensity signal of the gel channel was calculated and divided by the maximum signal concentration.

10.8.6. Dextran perfusion

10kDa Dextran labelled with AlexaFluor568 (Thermo Fisher Scientific) was diluted in HUVEC (EndoGRO) medium at a final concentration of 1 μg/mL. The solution was perfused into the "blood vessel" of the chip at a flow rate of 5 μL/min using a syringe pump. The

perfusion of dextran was monitored using Nikon Eclipse Ti2 epifluorescent microscope. The chip was placed in the on-stage incubator (Okolab) at a temperature of 37^{0}C and 5% CO_2, the perfused fluorophore was excited at 525 nm and emission collected at 650 nm.

10.8.7. HeLa spheroid viability assay

The viability of HeLa cells within the spheroids were evaluated using Calcein (Fluka, Sigma Aldrich) and Propidium Iodide (Sigma Aldrich) to stain live and dead cells, respectively. First, cells were incubated with 10 μM Calcein solution for 20 min. at 37^{0}C and 5% CO_2 and then. Next, the cells were incubated with 10 μg/mL Propidium Iodide solution for 5 min. at 37^{0}C and 5% CO_2 and then washed with 1x PBS (Sigma Aldrich). The imaging was performed using Zeiss LSM 800 Confocal microscope. The Calcein and Propidium Iodide stained spheroids were excited at laser wavelength of 488 nm and 561 nm respectively and detection windows set at 400 – 600 nm for Calcein and 600 – 700 nm for Propidium Iodide. The 3D image was reconstructed (ZEN, Confocal microscope software) from slices acquired in a Z-stack mode with a plane interval of 1,5 μm.

10.8.8. Immunostaining, labelling and Confocal Microscopy (Confocal Imaging Labelling)

Cells in the microfluidic chip were washed with 1x PBS (Gibco) and fixed with 4wt% solution of paraformaldehyde (PFA, Sigma Aldrich) in 1x PBS. After 10 minutes the fixative was washed away with 1x PBS, cells were permeabilized during 10 minutes with 0.1% solution of Triton X-100 (Sigma Aldrich) in 1x PBS and exposed for 1h to a 3% Bovine Serum Albumin (BSA, Sigma Aldrich) blocking solution in 1x PBS.

Next, the HUVECs' tight junctions were stained using 5 μg/mL ZO-1 (Zonula Occludens-1) Monoclonal Antibody conjugated with Alexa Fluor 488 (Thermo Fisher Scientific) solution in previously prepared 3% BSA during O/N incubation at 4^{0}C. In the next step the cells were washed with 3% BSA solution and incubated with 1x Phalloidin-iFluor594 (Abcam, stock 1000x) solution (in 1% BSA) for 30 min. at RT to stain actin filaments. The cell nuclei were stained after washing the cells with 1x PBS, using Hoechst 33258 stain at concentration 5 μg/mL. After 10 min. of incubation at RT the cells were washed with 1x PBS and imaged at RT using Zeiss LSM 800 Confocal microscope. Nuclei, tight junctions and actin were excited using 405 nm, 488 nm and 561 nm laser, respectively. The 3D images were acquired scanning the sample in a Z-stack mode, with an acquisition plane each 1 to 10 μm and later reconstructed into 3D image using the ZEN (Confocal microscope) software.

10.9. References

(1) Owen, S. C.; Chan, D. P. Y.; Shoichet, M. S. Polymeric Micelle Stability. Nano Today 2012, 7 (1), 53–65. https://doi.org/10.1016/j.nantod.2012.01.002.

(2) Holme, M. N.; Fedotenko, I. A.; Abegg, D.; Althaus, J.; Babel, L.; Favarger, F.; Reiter, R.; Tanasescu, R.; Zaffalon, P.-L.; Ziegler, A.; et al. Shear-Stress Sensitive Lenticular Vesicles for Targeted Drug Delivery. *Nat. Nanotechnol.* **2012**, *7* (8), 536–543. https://doi.org/10.1038/nnano.2012.84.

(3) Barua, S.; Mitragotri, S. Challenges Associated with Penetration of Nanoparticles across Cell and Tissue Barriers: A Review of Current Status and Future Prospects. *Nano Today* **2014**, *9* (2), 223–243. https://doi.org/10.1016/j.nantod.2014.04.008.

(4) Jain, R. K.; Stylianopoulos, T. Delivering Nanomedicine to Solid Tumors. *Nat. Rev. Clin. Oncol.* **2010**, *7* (11), 653–664. https://doi.org/10.1038/nrclinonc.2010.139.

(5) Chen, H.; Kim, S.; He, W.; Wang, H.; Low, P. S.; Park, K.; Cheng, J.-X. Fast Release of Lipophilic Agents from Circulating PEG-PDLLA Micelles Revealed by in Vivo Förster Resonance Energy Transfer Imaging. *Langmuir* **2008**, *24* (10), 5213–5217. https://doi.org/10.1021/la703570m.

(6) Lu, J.; Owen, S. C.; Shoichet, M. S. Stability of Self-Assembled Polymeric Micelles in Serum. *Macromolecules* **2011**, *44* (15), 6002–6008. https://doi.org/10.1021/ma200675w.

(7) Gravier, J.; Sancey, L.; Hirsjärvi, S.; Rustique, E.; Passirani, C.; Benoît, J.-P.; Coll, J.-L.; Texier, I. FRET Imaging Approaches for in Vitro and in Vivo Characterization of Synthetic Lipid Nanoparticles. *Mol. Pharm.* **2014**, *11* (9), 3133–3144. https://doi.org/10.1021/mp500329z.

(8) Aguilar-Castillo, B. A.; Santos, J. L.; Luo, H.; Aguirre-Chagala, Y. E.; Palacios-Hernández, T.; Herrera-Alonso, M. Nanoparticle Stability in Biologically Relevant Media: Influence of Polymer Architecture. *Soft Matter* **2015**, *11* (37), 7296–7307. https://doi.org/10.1039/C5SM01455G.

(9) Ravi, M.; Paramesh, V.; Kaviya, S. R.; Anuradha, E.; Solomon, F. D. P. 3D Cell Culture Systems: Advantages and Applications. *J. Cell. Physiol.* **2015**, *230* (1), 16–26. https://doi.org/10.1002/jcp.24683.

(10) Doshi, N.; Prabhakarpandian, B.; Rea-Ramsey, A.; Pant, K.; Sundaram, S.; Mitragotri, S. Flow and Adhesion of Drug Carriers in Blood Vessels Depend on Their Shape: A Study Using Model Synthetic Microvascular Networks. *J. Controlled Release* **2010**, *146* (2), 196–200. https://doi.org/10.1016/j.jconrel.2010.04.007.

(11) Gupta, N.; Liu, J. R.; Patel, B.; Solomon, D. E.; Vaidya, B.; Gupta, V. Microfluidics-Based 3D Cell Culture Models: Utility in Novel Drug Discovery and Delivery Research. *Bioeng. Transl. Med.* **2016**, *1* (1), 63–81. https://doi.org/10.1002/btm2.10013.

(12) Pampaloni, F.; Reynaud, E. G.; Stelzer, E. H. K. The Third Dimension Bridges the Gap between Cell Culture and Live Tissue. *Nat. Rev. Mol. Cell Biol.* **2007**, *8* (10), 839–845. https://doi.org/10.1038/nrm2236.

(13) Jeon, J. S.; Zervantonakis, I. K.; Chung, S.; Kamm, R. D.; Charest, J. L. In Vitro Model of Tumor Cell Extravasation. *PLOS ONE* **2013**, *8* (2), e56910. https://doi.org/10.1371/journal.pone.0056910.

(14) Kim, M.-C.; Whisler, J.; Silberberg, Y. R.; Kamm, R. D.; Asada, H. H. Cell Invasion Dynamics into a Three Dimensional Extracellular Matrix Fibre Network. *PLOS Comput. Biol.* **2015**, *11* (10), e1004535. https://doi.org/10.1371/journal.pcbi.1004535.

(15) Kalchman, J.; Fujioka, S.; Chung, S.; Kikkawa, Y.; Mitaka, T.; Kamm, R. D.; Tanishita, K.; Sudo, R. A Three-Dimensional Microfluidic Tumor Cell Migration Assay to Screen the Effect of Anti-Migratory Drugs and Interstitial Flow. *Microfluid. Nanofluidics* **2013**, *14* (6), 969–981. https://doi.org/10.1007/s10404-012-1104-6.

(16) Tang, Y.; Soroush, F.; Sheffield, J. B.; Wang, B.; Prabhakarpandian, B.; Kiani, M. F. A Biomimetic Microfluidic Tumor Microenvironment Platform Mimicking the EPR Effect for Rapid Screening of Drug Delivery Systems. *Sci. Rep.* **2017**, *7* (1), 9359. https://doi.org/10.1038/s41598-017-09815-9.

(17) Ho, Y. T.; Adriani, G.; Beyer, S.; Nhan, P.-T.; Kamm, R. D.; Kah, J. C. Y. A Facile Method to Probe the Vascular Permeability of Nanoparticles in Nanomedicine Applications. *Sci. Rep.* **2017**, *7* (1), 707. https://doi.org/10.1038/s41598-017-00750-3.

(18) Wang, H.-F.; Ran, R.; Liu, Y.; Hui, Y.; Zeng, B.; Chen, D.; Weitz, D. A.; Zhao, C.-X. Tumor-Vasculature-on-a-Chip for Investigating Nanoparticle Extravasation and Tumor Accumulation. *ACS Nano* **2018**, *12* (11), 11600–11609. https://doi.org/10.1021/acsnano.8b06846.

(19) Shin, Y.; Han, S.; Jeon, J. S.; Yamamoto, K.; Zervantonakis, I. K.; Sudo, R.; Kamm, R. D.; Chung, S. Microfluidic Assay for Simultaneous Culture of Multiple Cell Types on Surfaces or within Hydrogels. *Nat. Protoc.* **2012**, *7* (7), 1247–1259. https://doi.org/10.1038/nprot.2012.051.

(20) Sinha, R.; Le Gac, S.; Verdonschot, N.; van den Berg, A.; Koopman, B.; Rouwkema, J. Endothelial Cell Alignment as a Result of Anisotropic Strain and Flow Induced Shear Stress Combinations. *Sci. Rep.* **2016**, *6*. https://doi.org/10.1038/srep29510.

(21) Aird, W. C. Spatial and Temporal Dynamics of the Endothelium. *J. Thromb. Haemost.* **2005**, *3* (7), 1392–1406. https://doi.org/10.1111/j.1538-7836.2005.01328.x.

(22) Tzima, E.; Irani-Tehrani, M.; Kiosses, W. B.; Dejana, E.; Schultz, D. A.; Engelhardt, B.; Cao, G.; DeLisser, H.; Schwartz, M. A. A Mechanosensory Complex That Mediates the Endothelial Cell Response to Fluid Shear Stress. *Nature* **2005**, *437* (7057), 426. https://doi.org/10.1038/nature03952.

(23) Baker, B. M.; Chen, C. S. Deconstructing the Third Dimension: How 3D Culture Microenvironments Alter Cellular Cues. *J. Cell Sci.* **2012**, *125* (Pt 13), 3015–3024. https://doi.org/10.1242/jcs.079509.

(24) Lazzari, G.; Couvreur, P.; Mura, S. Multicellular Tumor Spheroids: A Relevant 3D Model for the in Vitro Preclinical Investigation of Polymer Nanomedicines. *Polym. Chem.* **2017**, *8* (34), 4947–4969. https://doi.org/10.1039/C7PY00559H.

(25) Feiner-Gracia, N.; Buzhor, M.; Fuentes, E.; Pujals, S.; Amir, R. J.; Albertazzi, L. Micellar Stability in Biological Media Dictates Internalization in Living Cells. *J. Am. Chem. Soc.* **2017**, *139* (46), 16677–16687. https://doi.org/10.1021/jacs.7b08351.

(26) Tight Junctions https://www.crcpress.com/Tight-Junctions/Cereijido-Anderson/p/book/9780849323836 (accessed Jul 10, 2019).

(27) Tarbell, J. M. Shear Stress and the Endothelial Transport Barrier. *Cardiovasc. Res.* **2010**, *87* (2), 320–330. https://doi.org/10.1093/cvr/cvq146.

(28) Kaji, H.; Yokoi, T.; Kawashima, T.; Nishizawa, M. Controlled Cocultures of HeLa Cells and Human Umbilical Vein Endothelial Cells on Detachable Substrates. *Lab Chip* **2009**, *9* (3), 427–432. https://doi.org/10.1039/B812510D.

(29) Maeda, H. Toward a Full Understanding of the EPR Effect in Primary and Metastatic Tumors as Well as Issues Related to Its Heterogeneity. *Adv. Drug Deliv. Rev.* **2015**, *91*, 3–6. https://doi.org/10.1016/j.addr.2015.01.002.

(30) Albanese, A.; Lam, A. K.; Sykes, E. A.; Rocheleau, J. V.; Chan, W. C. W. Tumour-on-a-Chip Provides an Optical Window into Nanoparticle Tissue Transport. *Nat. Commun.* **2013**, *4*, 2718. https://doi.org/10.1038/ncomms3718.

(31) Tchoryk, A.; Taresco, V.; Argent, R. H.; Ashford, M.; Gellert, P. R.; Stolnik, S.; Grabowska, A.; Garnett, M. C. Penetration and Uptake of Nanoparticles in 3D Tumor Spheroids. *Bioconjug. Chem.* **2019**, *30* (5), 1371–1384. https://doi.org/10.1021/acs.bioconjchem.9b00136.

(32) Agarwal, R.; Jurney, P.; Raythatha, M.; Singh, V.; Sreenivasan, S. V.; Shi, L.; Roy, K. Effect of Shape, Size, and Aspect Ratio on Nanoparticle Penetration and Distribution inside Solid Tissues Using 3D Spheroid Models. *Adv. Healthc. Mater.* **2015**, *4* (15), 2269–2280. https://doi.org/10.1002/adhm.201500441.

(33) Lu, H.; Utama, R. H.; Kitiyotsawat, U.; Babiuch, K.; Jiang, Y.; Stenzel, M. H. Enhanced Transcellular Penetration and Drug Delivery by Crosslinked Polymeric Micelles into Pancreatic Multicellular Tumor Spheroids. *Biomater. Sci.* **2015**, *3* (7), 1085–1095. https://doi.org/10.1039/C4BM00323C.

(34) Du, A. W.; Lu, H.; Stenzel, M. Stabilization of Paclitaxel-Conjugated Micelles by Cross-Linking with Cystamine Compromises the Antitumor Effects against Two- and Three-Dimensional Tumor Cellular Models. *Mol. Pharm.* **2016**, *13* (11), 3648–3656. https://doi.org/10.1021/acs.molpharmaceut.6b00410.

(35) Arranja, A.; Denkova, A. G.; Morawska, K.; Waton, G.; van Vlierberghe, S.; Dubruel, P.; Schosseler, F.; Mendes, E. Interactions of Pluronic Nanocarriers with 2D and 3D Cell Cultures: Effects of PEO Block Length and Aggregation State. *J. Controlled Release* **2016**, *224*, 126–135. https://doi.org/10.1016/j.jconrel.2016.01.014.

Conclusions.

Nanoscopy study of nanoparticles biological interactions

The main aim of the present thesis was to exploit the use of new methodologies based on advance optical microscopy, to understand the interactions of nanoparticles in biological environments, focusing on the interactions occurring under circulation in the blood vessels. The success of the field of nanomedicine for drug and gene delivery has been profoundly discussed in the last years due to the low success in clinical translation. One of the reasons of this is believed to be the lack of knowledge of the nanoparticles interactions occurring in complex biological systems. This low understanding is mainly due to the lack of proper techniques exploiting these phenomena. In this thesis new techniques which have the ability to unveil the interactions of nanoparticles in complex media have been introduced as a guidance for the rational design of new nanocarriers to favour their clinical success.

Heterogeneity of individual nanoparticles

One of the main limitations in the study of nanoparticles interactions with biological environments is the small size of the nanocarriers, which limit the number of techniques able to provide information at a single nanoparticle level. Nowadays, most of the studies are performed using ensemble techniques, studying a complete population, which make the results blind to any degree of heterogeneity. In the present thesis, dSTORM a SMLM technique has been introduced as a new tool to study the nanoparticles behaviour at a single particle level. The possibility to overpass the optical resolution limit, one of the main restrictions in the use of optical microscopy to study nanomaterials, allows to identify individual nanoparticles. Moreover, the molecular specificity of the technique, the possibility to label each component of the system with different fluorophores, provides molecular information to the imaging, not possible to obtain with electron microscopy techniques which have also nanoparticle resolution.

As an example of such an approach, in Chapter 3 the structural and molecular differences of single nanoparticles have been studied. The molecular specificity of the technique allowed to study the molecular composition of polyplexes. Polyplexes are mainly composed by electrostatic interactions of a cationic polymer and nucleic acids, and the optimal composition is believed to be those complexing all the genetic molecules. However, the complexation is currently studied using ensemble techniques. In Chapter 3 the molecular composition of polyplexes was studied as a function of the composition used in the synthesis. The molecular specificity of dSTORM allowed to determine the necessary ratio of cationic molecules to nucleic acid to form the complexes. While it also revealed a significant number of non-complexed cationic molecules, which cannot be observed using traditional methods such as gel electrophoresis. Moreover, the possibility to study the composition of single structures revealed heterogeneities in the molecular ratio of individual complexes. This heterogeneity cannot be determined using other techniques, which highlight the benefits of using dSTORM as a complementary characterization method. We believe that both, the free species, and the molecular heterogeneity may be responsible of the low success in the transfection efficiency *in vitro*. It could be that only a small population of the systems has the right composition to

internalize and release the nucleic acid molecules inside the cell, which will influence the final performance of the designed system. Up to now it was not possible to determine which is the composition of the outstanding system. However, in Chapter 3 we have exploited the possibility to characterize this molecular structure not only *in vitro* but inside cells. Further studies, correlating the transfection efficiency with the molecular composition of the internalized gene delivery system revealed by super resolution microscopy will improve the design of clinical translatable systems.

dSTORM revealed not only a heterogeneity in nanocarriers composition but in their biological interactions. In Chapter 2 the nanometric resolution of the technique have enable the observation of protein corona formation into individual nanoparticles, which was not possible with other techniques broadly utilised. The study of the protein corona at this level have revealed also a heterogeneity in the adsorption of serum proteins: we detected NPs with almost no corona coexisting with others with a immense number of molecules adsorbed. This heterogeneity can be related to structural differences of individual nanoparticles that are impossible to observe when studying a full population. We believe this discovery is of utmost importance and could be one of the causes of the low number of nanoparticles reaching the tumour cells *in vivo*. The possibility that only the population with no corona is able to escape from the blood vessels reflects the importance of understanding the structural differences between nanoparticles with adsorbing and non-adsorbing proteins. Future experiments using correlation microscope as proposed in Chapter 2, can shine more light into this heterogeneity. The possibility to correlate physicochemical properties of the NP, such as shape or porosity, using electron microscopy resolution, to the molecular composition of the protein corona using SMLM can predict the eminent NPs with high chances of success.

Overall, we have revealed the existence of surface and composition heterogeneities within the same population, which have also recently been shown for other nanoparticle properties, although their characterization is challenging. Differences in size, surface chemistry, composition, functionalization or encapsulation efficiency within a same population can be one of the causes of the low performance *in vivo*. Thus, dSTORM can be a useful methodology to characterize these differences and determine the properties of the most optimal nanocarrier.

Protein interactions: a complex phenomenon

The complex molecular environment present in the blood leads to multiple biological interactions. One of the more studied and more critical is the interactions with blood proteins which can result into i) the formation of a biomolecular corona adsorbed in the nanocarrier surface, as studied in Chapter 2 or ii) the loss of stability of the system, studied in Chapter 3 and 4. The complexity of the environment makes very challenging the understanding and recognition of single molecular interactions. In dSTORM the image reconstruction is based on

the localization of individual molecules separated in time, which provides additional quantitative information. Thus, in Chapter 2, the protein corona has been demonstrated to be a dynamic phenomenon as it evolves and grow in time. In addition, we have demonstrated that changes in the surface chemistry of nanoparticles induces changes in protein adsorption. Moreover, the composition of the protein corona evolves in time, while more abundant proteins adsorb first, low abundant but high affinity molecules substitute the previous. This dynamic and changing protein corona has been gaining more and more interest, with recent studies proposing that the changing biological environments through the nanoparticle journey in the body will also modify the corona composition. Although PEG and other antifouling molecules can reduce the protein adsorption it is almost impossible to completely avoid it. Thus, the focus should be directed to characterize the corona formation in more real environments such as flow, or human blood, as way to predict and guide the interactions *in vivo*. The guidance of desired protein interactions though modification of the NPs physicochemical properties can be the trigger to exploit the protein corona. Finally, recent studies have shown the importance of reproducibility and of using control measurements when performing protein corona analysis. It has been demonstrated that some protein species are detected in bulk experiments without nanoparticles due to interactions with the devices, or materials used. Thus, most protein corona studies may have led to misunderstandings on protein corona composition. Advantageous, our dSTORM studies focus only on proteins directly adsorbed into localized nanoparticles, and therefore, the obtained results are not influenced by no-specific interactions.

In Chapter 3, dSTORM have also demonstrated the complex interactions between blood proteins and polyplexes, leading to a loss of stability of supramolecular systems. The possibility to image both molecular components of the polyplexes has granted the determination of stability as a function of time and serum composition. We have disclosed a complex interplay between proteins and polyplexes, where we observed that first peptide is decomplexed from the complex probably due to increasing protein adsorption that exchange for the peptide. Interesting in this moment mRNA molecules were still compacted within nanometric structures; however, longer times or higher serum concentrations completely destabilize the polyplexes, leading to release of mRNA molecules.

Stability of nanocarriers in space and time

Interactions with serum proteins led to a loss of stability of supramolecular nanosystems which reduce their possibilities of success due to a premature release of therapeutic molecules. We have already demonstrated the relevance of protein interactions, yet the stability can be compromised by many other interactions through the long journey of the NPs inside the human body. The use of spectral imaging can provide functional information and at the same time operate in complex dynamic systems thanks to its low time resolution of seconds, and its minimal phototoxicity which allow live-cell imaging. These makes possible to follow stability changes not only in time but spatially, due to the importance of discerning

which interaction is the one triggering disassembly. In Chapter 4 and 5 we have demonstrated the utility of spectral imaging to follow the stability of supramolecular systems in complex media, in combination with the unique fluorescence properties of our PEG-dendron hybrids. The fluorescence of the hybrids self-reports their self-assembled state by a shift in the emission spectra due to excimer formation during assembling. This property favoured the study of these supramolecular systems in contact with serum proteins and cells, demonstrating small and molecularly precise changes in their amphiphilicity can lead to substantial differences of their stability.

Another important parameter to consider when designing new supramolecular systems is the need to use complex 3d models to accurately predict the interactions mimicking *in vivo* conditions. In Chapter 5 a new 3d cancer-on-a-chip device have been established, consisting on a blood vessel channel and an ECM channel, that prove the exitance of leaky vasculature in presence of cancer cells. Different critical barriers that can led to undesired interactions and loss of stability have been recreated, the continuous flow, the endothelial barrier, the ECM and the 3d tumour arrangement of the cancer cells. Spectral imaging has allowed to follow these changing conditions and correlate the stability of supramolecular systems with the ongoing biological interaction. The micelles studied in the present thesis, which appeared to be a promising system after the studies in Chapter 4, because their high stability in serum conditions and in contact with cells, showed a loss of stability in 3d cell arrangements in Chapter 5. This loss of stability could not be predicted from 2d *in vitro* studies demonstrating the importance of using complex systems to test the NPs under study, thus, bridging the gap between *in vitro* and *in vivo* testing. Finally, we demonstrated a very low penetration of our polymeric hybrids into the 3d tumour, which could be caused for the low stability of the system. But also, for a different biological behaviour of cells in 3d organization, 2d cell culture endocytosis can be very different than 3d where cells are in close contact to each other and not fully exposed to the medium.

Overall, in the present thesis we have introduce the use of two new microscopy techniques, dSTORM and spectral imaging, to study the interactions of nanocarriers in complex biological media. At the same time, we have proved the importance of studying these interactions in individual nanoparticles considering the heterogeneity in composition and physicochemical properties that lead to different outcomes. Moreover, we have demonstrated the importance of studying the biological interactions in 3d complex cellular models, and therefore, the need for proper techniques, such as, spectral imaging which allow to track the temporally and spatially behaviour of nanocarriers. We believe that the use of both SMLM and spectral imaging, in combination with other investigations, to understand and predict biological interactions will expand the clinical translation of nanocarriers.

Appendix 1.

Resum en català

1 Introducció

1.1.1 *Nanomedicina pel tractament de càncer*

El càncer és una de les principals causes de mort a tot el món, el nombre de casos augmenta cada any principalment a causa de l'incrementt de l'esperança de vida. Els tractaments actuals a part de la cirurgia inclouen quimioteràpia, radioteràpia i immunoteràpia que, en molts casos, tenen un èxit limitat degut a la seva toxicitat o poca efectivitat. L'ús de nanopartícules (NPs) per el tractament de tumors sòlids aporta un conjunt d'avantatges com per exemple i) una major solubilitat del fàrmac, ii)protecció envers la degradació, cosa que també millora la dosi efectiva, iii)major circulació de NPs en comparació amb medicaments lliures i finalment iv) alliberament controlat i sostingut de molècules[1–3].

El 1995 es va aprovar la primera NP per al tractament del càncer, Doxil, un liposoma que encapsula Doxorubicina anomenat [4,5]. L'aprovació d'aquests sistema es va convertir en una fita en el món de la nanomedicina, demostrant els beneficis promesos, per al tractament del càncer. Des de llavors, altres teràpies basades en liposomes també han estat aprovades per al tractament de diferents càncers. Tot i el gran nombre d´estructures i materials investigats, només un sistema que consisteix en nanopartícules de proteïnes[6] i un altre formulat a partir de polímers[7] s'han aprovat per ús clínic. En general, tots aquests sistemes redueixen els efectes secundaris del tractament i/o permeten utilitzar una dosis reduïda amb la mateixa eficàcia.. No ha sigut fins recentment s'ha aprovat el primer sistema que millora l'esperança de vida, CPX-351, un liposoma millora de 5 a 9 mesos l'esperança de vida en pacients amb leucèmia[8].

Aquests èxits han demostrat el potencial que té la nanomedicina per tractar el cancer, però tot i així, el nombre de sistemes aprovats és molt baix en comparació amb els milers de milions invertits en investigacions preclíniques. En els darrers 15 anys, l'interès en el camp ha crescut contínuament, un exemple d´això és el nombre de publicacions que han passat de 100 per any a més de 4.000 el 2018. Aquestes diferències en investigacions i nombre de sistemes que arriben a utilitzar-se demostren la importància d'identificar i superar els reptes que limiten l'aplicació de nanomedicina[9,10].

1.1.2 *Vida d'una nanopartícula dins del cos*

Les NPs injectades per via intravenosa tenen un llarg viatge a l'interior del cos abans que puguin identificar a les cèl·lules canceroses. En cada pas d'aquest recorregut, es poden produir diferents interaccions amb components biològics[11,12]. A més, les barreres biològiques estan dissenyades per restringir l'entrada de material no desitjat. En general, són sistemes essencials per a la defensa de l'organisme contra patògens i virus, però, aquestes barreres també restringeixen la penetració de les NPs. Per tant, s'han de realitzar estudis complets i específics per pre-seleccionar els sistemes amb resultats més favorables i que, per tant, poden tenir més èxit. La primera barrera que es troba una NPs quan s'injecta per via intravenosa (i.v)

és la circulació. A la circulació, l'estabilitat de les NPs es pot veure afectada a causa de l'estrès a la cisalla o l'adsorció de proteïnes a la seva superfície que, a més a més, poden activar el sistema immune[13,14]. Una NP capaç de superar totes aquestes interaccions d' arribar a les parets dels vasos sanguinis i poder-los creuar, on l'efecte EPR té un paper important[15,16]. Abans d´arribar al tumor sòlid, es poden produir bio-interaccions intratumorals que afecten al sistema. Les NPs poden interaccionar amb les cèl·lules no malignes (per exemple, fibroblasts), o la matriu extracel·lular (ECM)[17]. Finalment, les NPs hauran de detectar i penetrar el tumor sòlid per tal de ser més efectives el què, en la majoria dels casos, és molt difícil[18].

La majoria de les interaccions de les NPs amb els diferents components biològics són poc entesos, el què limita el seu disseny. Per tal de poder dissenyar NPs efectives és necessari comprendre detalladament i a nivell molecular les característiques estructurals que impulsen les interaccions del nanomaterial amb les cèl·lules cancerígenes i amb el seu medi biològic. Fins al moment, totes aquestes interaccions s'estan estudiant mitjançant tècniques que avaluen una solució de NPs com un conjunt. Però, al mateix temps, s'ha suggerit que d'una població de NPs hi ha polidispersitat que pot provocar diferents interaccions en cada partícula dins d'un mateix lot. La possibilitat d'identificar la subpoblació efectiva de NPs, permetria optimitzar-les i augmentar la seva acumulació en el tumor. Per tant, el desenvolupament de tècniques i mètodes nous per visualitzar i investigar les interaccions biològiques de nanopartícules individuals en models més complexos jugarà un paper fonamental per predir l'efectivitat del sistema.

1.1.3 *Noves tècniques per estudiar les interaccions biologiques de les nanopartícules*

Adquisisió dímatges espectrals

La microscòpia d'imatge espectral es basa en l'adquisició de l'espectre d'emissió dels fluoròfors a cada píxel. Això s'aconsegueix normalment amb un microscopi confocal equipat amb un prisma i capaç de diferenciar els diferents colors de manera seqüencial o simultània. Els principals avantatges són la possibilitat de detectar diferents fluoròfors que tenen un espectre d'emissió superposat, així com, distingir perfectament el senyal d'interès del fons o de l'autofluorescència[19–21]. A més, un ús molt útil de la imatge espectral és la seva combinació amb molècules sensores capaces de canviar la seva longitud d'ona d'emissió depenent d'un factor específic, per exemple el pH[22]. Aquesta és una característica clau ja que permet una imatge funcional: proporcionar informació complementària sobre l'estat i el comportament de les NP i no només la seva localització a l'espai. A part d´algunes investigacions previs en què s´investiguen la cinètica d'alliberament i el perfil de les drogues dins de les cèl·lules, es pot explotar la imatge espectral per respondre a moltes més preguntes sobre les interaccions biològiques de les NPs

*Microscopia de super-reosluci*ó

La microscòpia de fluorescència és una tècnica poderosa per analitzar les interaccions entre NPs i estructures biològiques i moleculars. Tanmateix, la seva resolució espacial està limitada per la difracció de la llum a uns quants centenars de nanòmetres segons els criteris d' Abbe. Aquesta restricció dificulta la observació de NPs més petites que la resolució. La microscòpia de gran resolució (SRM) o nanoscòpia ha aparegut recentment com una tècnica potent per complementar i superar la limitació actual de les tècniques de microscòpia òptica[23,24]. Una de les famílies de SRM és la microscòpia de localització de molècules úniques, dins la qual podem trobar la tècnica de reconstrucció òptica estocàstica directa de Microscòpia (dSTORM). dSTORM aconsegueix una resolució per sota el límit de difracció mitjançant la localització precisa de fluoròfors individuals, on la detecció de cada emissor està separada en el temps[25,26]. Durant l'adquisició d'imatges, la majoria dels fluoròfors es troben en un estat "desactivat". Després, d'un en un passen de forma estocàstica i reversible a un estat "activat", moment en què es localitza la molècula. Utilitzant dSTORM es pot aconseguir entre les millors resolucions espacials assolibles amb tècniques òptiques, fins a 20nm. A més, la possibilitat de localitzar esdeveniments d'una sola molècula pot proporcionar informació quantitativa.

Tot i que fins al moment només s'han publicat uns quants estudis que utilitzen dSTORM per estudiar nanomaterials[27], destaquen que la imatge òptica és una eina potent per visualitzar i estudiar les propietats de les NPs difícils d'estudiar amb altres tècniques. A més a més, originalment aquesta tècnica va ser creada per estudiar estructures cel·lulars nanomètriques, el que obra la possibilitat al estudi de les interaccions NP-cèl·lula[28].

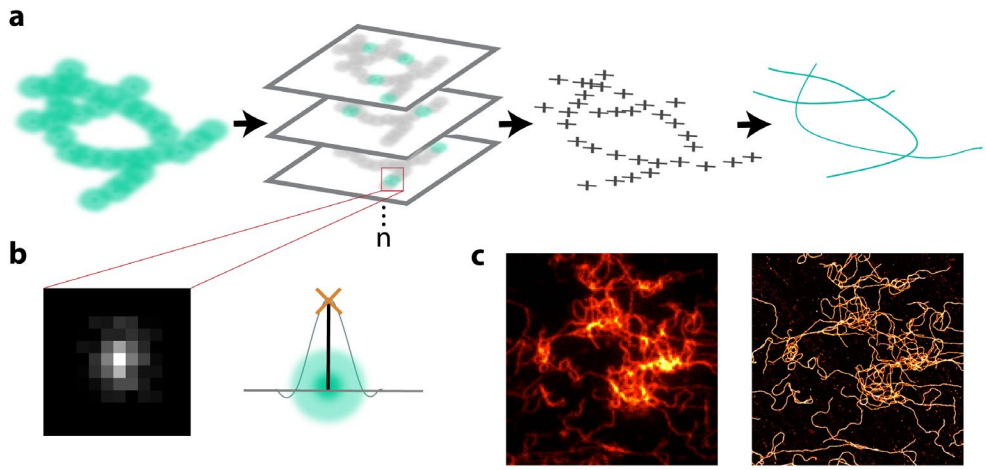

Figure 86 Principi de microscòpia de localització d'una sola molècula. a. Els fluoròfors s'activan i desactivan en diversos cicles, cosa que permet la localització específica de l'emissor en cada cicle. Aquest procés permet la reconstrucció de l'estructura amb resolució nanomètrica. b. Emissió d'un sol fluoròfor es pot ajustar a la funció gaussiana 2D per localitzar acuradament la seva posició. c. Exemple d' una imatge dSTROM de material sintètic.

2 Objectius

Les seccions anteriors han destacat la necessitat de comprendre les interaccions biològiques de les NPs que es produeixen durant la seva vida a l'interior del cos. La comprensió d'aquests passos crítics juntament amb un estudi en profunditat de la composició estructural de les nanopartícules guiarà un disseny racional dels sistemes, augmentant la seva translació a clínica. Actualment, la limitació principal d'aquestes investigacions és la manca de tècniques experimentals capaces de proporcionar informació sobre el comportament de les nanopartícules a nivell individual, així com, tècniques que es puguin realitzar en medis biològics complexos.

L'objectiu principal d'aquesta tesi és l'ús de noves tècniques de microscòpia òptica avançades per donar a conèixer les interaccions biològiques de les NPs en medis biològics complexes, visualitzar NPs individuals, així com, les seves interaccions amb molècules específiques.

3 La microscopia de super-resolució permet revel.la heterogenïtats dinàmiques en la corona proteica de les nanopartícules

Les nanopartícules (NPs) després de ser injectades *in vivo* interaccionen amb els fluids biològics com per exemple la sang, donant lloc a la formació d'una corona biomolecular que determina la identitat biològica del nanomaterial[29–32]1-5. L'adsorció de proteïnes, lípids i petits metabòlits presents a la sang afecta la seva estabilitat, les seves habilitats d'identificar les cèl.lules cancerígenes respecte les sanes, així com, la resposta del sistema immunitària a les NPs injectades. Totes aquestes alteracions no permeten que les NPs duguin a terme la seva funció terapèutica de forma correcta. Per aquesta raó, és de gran importància investigar la formació i la dinàmica de la corona proteica adsorbida en les NPs, per tal de dissenyar nanoestructures més efectives per a poder tractar el càncer[33–35].

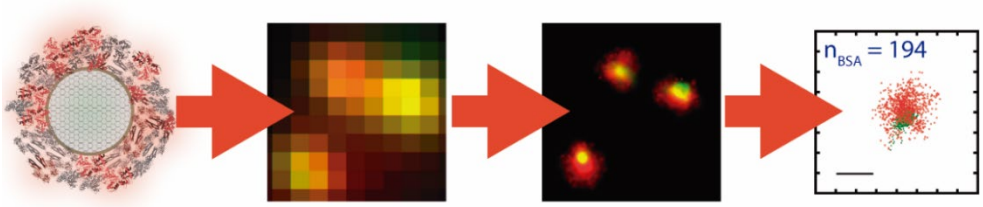

Figura 87. Representació esquemàtica del procediment utilitzat per obtenir imatges de la corona proteica. Les MSNs es van incubar amb una solució de proteïnes marcades durant un temps determinat a 37`C. A continuació es van adsorbir a un cobreobjectes i es van adquirir imatges dSTORM. Finalment, un anàlisis quantitatiu va permetre estimar el nombre de molècules adsorbides per NP.

En aquest treball, es va utilitzar la tècnica dSTORM per visualitzar i quantificar les proteïnes adsorbides en NPs mesoporoses de sílica (MSNs), una nanoestructura rellevant per a aplicacions mèdiques[36,37]. La figura 1 mostra una imatge de fluorescència convencional de MSNs (verd) incubades amb albúmina marcada amb Cy5 (vermell) en sèrum complet, en comparació amb la imatge dSTORM corresponent. Gràcies a la major resolució de la microscòpia dSTORM en aquesta imatge és possible diferenciar NPs individuals i visualitzar la capa de proteïna circumdant, cosa que no és possible utilitzant la tècnica de fluorescència convensional.

Després d'haver establert aquesta potent metodologia, es va estudiar l'evolució en el temps de la corona proteica, un factor clau tenint en compte els diferents temps de circulació *in vivo* de les NPs. El nombre de proteïnes adsorbides no va augmentar significativament en els primers 15 minuts, però si ho va fer posteriorment, observant una adsorció màxima pel temps d'incubació més llarg estudiat (12 hores), d'acord amb estudis anteriors11. Curiosament, les diferències entre les proteïnes adsorbides en cada partícula van augmentar enormement després d'1h. L'observació directa d'aquesta adsorció heterogènia de proteïnes posa de manifest la importància d'estudiar la corona biomolecular de forma individual per cada NP, i proporciona informació crucial sobre el comportament biològic d'aquestes partícules[38].

A continuació, es va estudiar si la càrrega superficial electrostàtica de partícules té una influencia en la formació de la corona. Sorprenentment, l'evolució del potencial zeta en el temps de les tres nanopartícules segueix la mateixa tendència que el canvi del comportament d'adsorció de proteïnes. Com a exemple, només quan el potencial zeta de MSNs va augmentar cap a la neutralitat, es va observar un augment de la corona. Aquests resultats indiquen que la formació i la dinàmica d'aquesta corona depenen fortament de la càrrega superficial, i que els canvis en la química superficial de les NPs a causa de la hidròlisi afecten clarament la composició de la corona. L'alteració de la química superficial de les NPs amb el temps introdueix un factor més d'heterogeneïtat en la formació de la corona, és a dir, una heterogeneïtat dinàmica.

El sèrum és un medi complex, on conviuen un nombre elevat de molècules que poden interaccionar amb les MSNs. Per aquesta raó s'ha utilitzat dSTORM per investigar els canvis en la composició de la corona de proteïna en funció del temps. Aquest mètode ens permet seguir una sola proteïna en sèrum complet (sèrum boví fetal, FBS). L'albúmina (BSA), el fibrinogen, la IgG i la transferrina s'han escollit per la seva alta concentració en sang, la seva rellevància biològica i la seva afinitat reportada per les NPs de sílice en estudis anterior 50-53. Les mostres es varen preparar utilitzat el mateix protocol que s'ha explicat anteriorment, però aquest cop la proteïna marcada de interès es va barrejar amb sèrum complet. Les molècules de BSA es van adsorbir a la superfície de MSNs en temps d'exposició curts, però la seva concentració va disminuir significativament després d'una hora d'incubació. En contra, el nombre mitjà de molècules de transferrina adsorbides va augmentar amb els temps

d'exposició; això indica que la transferrina té una afinitat més forta per a la superfície MSNs que l'albúmina, però degut a la seva baixa concentració necessita més temps per interaccionar amb les NPs.

Finalment vam correlacionar els resultats de la nostra investigació de super-resolució de la corona proteica amb les capacitats de les MSN funcionalitzades amb anticossos de detectar cèl·lules cancerígenes que sobrexpresin un antigen. Curiosament, primer vam observar que la formació de corona estava influenciada per la presència d'anticossos, ja que el perfil d'adsorció de molècules és diferent. Aquesta observació demostra la importància d'estudiar la corona proteïna directament en les NPs modificades i que es preveu utilitzar *in vivo.* Paral·lelament, vam estudiar la pèrdua d'anticossos al llarg del temps, ja que la naturalesa biodegradable de la superfície de MSN pot induir canvis en el nombre d'anticossos per MSN en el temps. dSTORM ens va permetre observar una pèrdua mínima d'anticossos durant les primeres 12 hores (al voltant del 10%) que es va fer més significativa (fins al 40%) després de 18 hores. Per acabar vàrem correlacionar la pèrdua d'anticòs i el creixement de la corona proteïna amb les capacitats d'internalització de les MSN en les cèl·lules cancerígenes, demostrant la importància d'entendre aquest fenomen per dissenyar NPs funcionals.

4 Estudi de la composició molecular i l'estabilitat en sèrum de poliplexes

Les interaccions amb proteïnes poden afectar notablement l'estabilitat de nanosystemes supramoleculars. Per tant, és important estudiar la seva estabilitat en entorns complexes similars al sanguini per predir el seu comportament *in vivo*. Un exemple molt rellevant és l'ús de sistemes d'administració de gens com ara els polipexes. Els polipexes són NPs caracteritzades per les interaccions electrostàtiques entre el polímer i l'àcid nucleic, les quals guien la seva formació. L'estudi de l'eficàcia de complexació de polipexes en medis biològics complexes requereix una comprensió prèvia de les propietats i les variacions estructurals dels polipexes formulats. Avui en dia, el coneixement sobre aquestes propietats estructurals és molt limitat[39,40]. En aquesta tesi hem volgut explotar la possibilitat d'utilitzar dSTORM per entendre l'organització d'aquests complexes, formats per pèptids (r9)[39,41,42] i ARN missatger (ARNm)[43,44]. Posteriorment, hem volgut utilitzar aquesta informació per predir la seva estabilitat en condicions similars a la sang. Un cop optimitzats tots els paràmetres, les imatges obtingudes van revelar complexos de radi de 50-75 nm, d'acord amb les mesures de dispersió dinàmica de llum (DLS), Figura 2. Curiosament, les imatges dSTORM van revelar una gran quantitat de pèptid lliure, el què indica que no tot el pèptid utilitzat en el procediment de complexació s'incorpora a l'estructura dels poliplexes, fenomen que no és possible observar utilitzant altres tècniques. A més, la imatge dSTORM va permetre estudiar la distribució del pèptid (verd) i de l'ARN missatger (vermell). El solapament observat dels dos colors indica que les molècules d'ARNm i r9 s'encreuen homogèniament dins del complex, per tant, les molècules d'ARNm no estan exposades a la superfície sinó que estan amagades dins l'estructura, de forma que queden protegides dels agents externs.

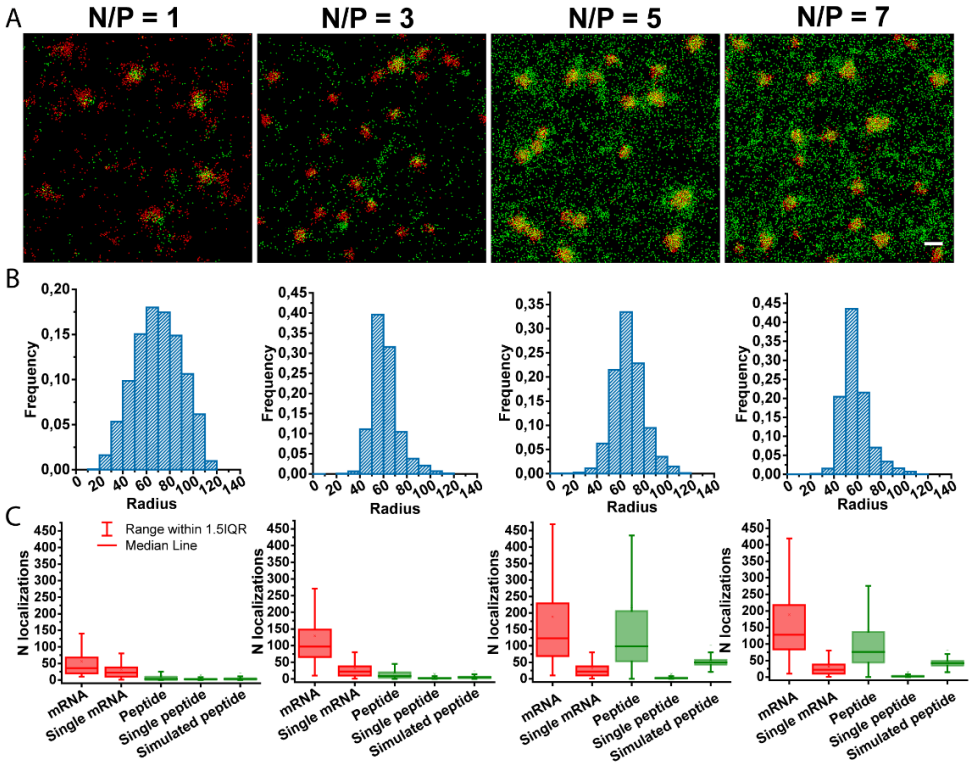

Figura 88. Estudi de la composició estequiomètrica dels poliplexes a diferents relacions N/P. a. Imatges adquirides utilitzant dSTORM de les diferents N/P, en vermell es mostra el ARNm i en verd el pèptid r9. **b.** Radi dels complexes mesurats a partir de les imatges dSTORM. **c.** Analysis quantitatiu del nombre de localitzacions per poliplèx tant del ARNm com del pèptid r9 obtingut de les imatges en comparació amb el nombre de localitzacions d'una sola molècula i del nombre de localitzacions obtingudes utilitzant la simulació creada per predir el comportament estocastic en l'activació dels fluoròfors.

Un dels graus experimentals de llibertat més importants en la formació de poliplexes és la relació entre el nombre de molècules catiòniques i els àcids nucleics, que ve determinada per la relació entre les càrregues positives i negatives, relació N/P. Aquesta relació determina propietats clau dels polipexes com ara la seva càrrega neta, mida i estabilitat[39,45]. Degut a la importància d'aquest paràmetre, en aquesta tesis es va voler comparar l'estructura i la distribució de molècules d'ARNm i de r9 per a diferents relacions N/P. Gracies a les imatges obtingudes es va demostrar que és necessari un excés de pèptid per condensar l'ARNm en polipexes ja que a N/P 1 no es van poder observar complexes definits, en canvi, a N/P 3, el nombre de pèptids era suficient per empaquetar l'ARNm en polipexes compactes, com mostra la Figura 2a. Amb un augment de N/P a 5, el contingut de r9 i la relació de pèptids - ARNm dels polipexes van augmentar encara més fins arribar a un màxim al voltant de N/P 5.

En treballs previs s´ha demostrat que simulacions estocàstiques poden predir el nombre i la distribució esperada de localitzacions d'un nombre fix de molècules. Per tant, la comparació del nombre de localitzacions per poliplex detectades experimentalment amb dades simulades pot proporcionar una estimació més precisa de la composició de cada complex. Per aquesta raó en aquesta tesis s'ha utilitzat un programa capaç de simular el procés subjacent de la fotoactivació estocàstica per comparar els resultats obtinguts de les imatges, com mostren els gràfics en la Figura 2c. Amb tot això vam poder entendre la composició molecular en cada relació N/P. En resum, r9 s'uneix a l'ARNm a N/P 1, però només a partir de N/P 3 aquesta unió és suficient per condensar l'ARNm en complexes. Els poliplexes de N/P 3 a N/P 7 són similars en mida i quantitat d'ARNm, però canvien significativament respecte a la quantitat de pèptid present en les partícules. A més, hi ha una heterogeneïtat significativa de la composició molecular, especialment a N/P 5 i 7. Notablement, les diferències entre les tres últimes condicions i l'heterogeneïtat de les mostres haurien estat difícils o impossibles de mesurar amb altres mètodes, mostrant el potencial de dSTORM per complementar les tècniques existents per a la caracterització de poliplexes.

Després d'haver establert la metodologia per mesurar la mida i la composició estructural de poliplexes, vam explotar la capacitat de dSTORM per realitzar anàlisis en medis complexos com el sèrum sanguini. Per fer-ho, vàrem incubar complexes formulats a N/P 5 a 37ºC amb sèrum a concentracions de l'1%, el 20% i el 100% durant 1 minut i 1 hora i, a continuació, vam adquirir imatges dSTORM dels complexos. Aquests estudis van permetre arribar a la conclusió que les proteïnes interaccionen amb els poliplexes en dues etapes: i) el sèrum elimina ràpidament els pèptids dels poliplexes sense comprometre l'ARNm compactat a l'interior de la partícula (escala de temps de minuts); ii) les proteïnes desestabilitzen els complexos provocant l'alliberament de molècules d'ARNm (escala de temps d'hores). Aquest estudi demostra la importància d'entendre l'estabilitat dels poliplexes o d'altres NPs formulades a partir d'interaccions electrostàtiques en medis complexos que imitin entorns *in vivo*, per tal de poder predir el seu comportament.

5 L'estabilitat micel·lar en medis biològics dicta la internalització cel·lular

La naturalesa dinàmica d'estructures supramoleculars polimèriques1,2 fa que la seva estabilitat en medis biològics sigui un paràmetre indispensable per al seu ús potencial com a sistemes de lliurament de medicaments *in vivo*. Per tant, és fonamental estudiar i comprendre el comportament d'aquest tipus d'estructures en condicions que es trobaran *in vivo*, com ara dilucions extremes i interaccions amb proteïnes i cèl·lules5,6,11. En aquesta tesis, s'ha utilitzat una combinació d'espectroscòpia de fluorescència i microscòpia per estudiar quatre híbrids amfifílics basats en una molècula PEG-dendró28,29 i les micel.les que formen quan s'autoensamblen per determinar les relacions estructura-estabilitat. L'alta precisió molecular del bloc dendrític va permetre ajustar sistemàticament la hidrofobicitat i l'estabilitat de les micel·les. A més a més, els híbrids utilitzats es van marcar fluorescentment amb coumarina,

aquest fluòrofor forma excimers quan els híbrids creen micel·les. Aquest fenomen indueix canvis significatius en el pic d'emissió (Em) que es mou cap al vermell, de 480 nm a aproximadament 560 nm. Aquesta propietat del fluòrof utilitzat permet distingir fàcilment entre les micel·les (Em ~ 560 nm) i els híbrids monomèrics (Em ~ 480 nm) fins i tot en medis biològics complexos gracis a la informació espectral obtinguda.

L'estabilitat supramolecular cap al desensemblatge de micel·les en condicions que imitin fluids com la sang és de màxima importància per optimitzar el rendiment *in vivo* dels sistemes. Per avaluar el potencial de les micel·les polimèriques estudiades, primer es va determinar l'estabilitat dels quatre tipus de micel·les en presència de concentracions creixents d'albúmina. A concentracions superiors a 100 μM, la proporció monòmer/micel.la per als híbrids **2**, **3** i **4** augmenta indicant que les micel·les es desfan. En canvi, la proporció per a l'híbrid **1** comença a augmentar lleugerament només per sobre dels 100 μM BSA, cosa que indica que aquestes micel·les són resistents a la interacció amb BSA. A continuació, es va estudiar l'estabilitat en el temps, en què els quatre tipus de micel·les van ser estables durant més de 14 hores en PBS, mentre que en un 10% de sèrum i en condicions de BSA es van desmuntar lleugerament. Per altre banda, cada subtipus de micel·la es va comportar diferent.

Quan s'administren micel·les per via intravenosa aquestes experimenten una forta dilució en la sang, que pot afectar greument la seva estabilitat supramolecular. Aprofitant les propietats fluorescents del nostre sistema, es va investigar la resistència de les micel·les en funció de la seva dilució en dos medis diferents: PBS i en sèrum. Com era d'esperar, les dades mostren diferències dramàtiques entre aquestes dues situacions. En sèrum, les micel·les es desestabilitzen a concentracions molt més elevades que en PBS. D'altra banda, els comportaments cinètics observats de les quatre micel·les són molt diferents. Mentre que els híbrids **3** i **4** es van desfer ràpidament després de la seva dilució, els híbrids **1** i **2** van necessitar fins a 12 hores per assolir el seu estat d'equilibri, demostrant una estabilitat cinètica més elevada. Sota les condicions mesurades, arribem a la conclusió que l'híbrid **1** és tant cinètic com termodinàmicament estable, l'híbrid **2** és cinèticament estable però no termodinàmicament, i els híbrids **3** i **4** no són estables.

Finalment, es va explorar el paper de l'estabilitat micel·lar en la internalització cel·lular mitjançant microscòpia d'escaneig làser confocal espectral. Aquesta eina ens va permetre obtenir els espectres de fluorescència complets i la relació monòmer/micel·la per a cada píxel de la imatge i, per tant, identificar els dos estats dels diferents sistemes en l'espai i el temps. Com era d'esperar, l'híbrid **5** estava en la seva forma monomèrica en els dos punts estudiats, 10 i 30 minuts, independentment de la seva localització. Els híbrids **3** i **4** estaven majoritàriament en estat monomèric després de 10 minuts amb algunes regions semblants a vesícules a la cèl·lula que contenien els híbrids autoensamblats (color blau-verd), i al cap de 30 minuts, totes les molècules estaven en la seva forma monomèrica. Aquests resultats suggereixen que els híbrids entren a les cèl·lules tant en el seu estat monomèric, probablement per intercalació a la membrana, com en el seu estat micel·lar, probablement per endocitosi, i

després es desmunten dins de les vesícules endocítiques. De manera molt diferent, l'híbrid **2** es va observar a la membrana tant com a monòmer com a micel·la després d'una incubació de 10 minuts, cosa que pot indicar que el sistema es va desmuntar una vegada en contacte amb la cèl·lula, tot i que també es van observar micel·les internalitzades en vesícules. Després de 30 minuts la majoria dels híbrids dins de la cèl·lula es van detectar en la seva forma monomèrica. Finalment, l'híbrid **1**, després de 10 minuts d'incubació, estava significativament menys interioritzat que els altres híbrids, això si, tot es trobava dins de vesícules i en forma de micel·la. Al cap de 30 minuts, la quantitat d'híbrids interioritzats va augmentar i es van detectar tant micel·les com molècules monomeriques Aquests resultats confirmen l'alta estabilitat micel·lar de l'híbrid **1** i el seu potencial per alliberar específicament la càrrega a l'interior de la cèl·lula.

6 Imatges espectrals en temps real de l'estabilitat micel·lar en un càncer en un xip de microfluídica

L'estabilitat de sistemes supramoleculars (i.e micel·les) no només es veu afectada per les dilucions extremes o les interaccions amb les molècules sanguínies, sinó que hi ha molts altres punts crítics que poden desencadenar el desensemblatge d'aquests sistemes abans d'arribar a

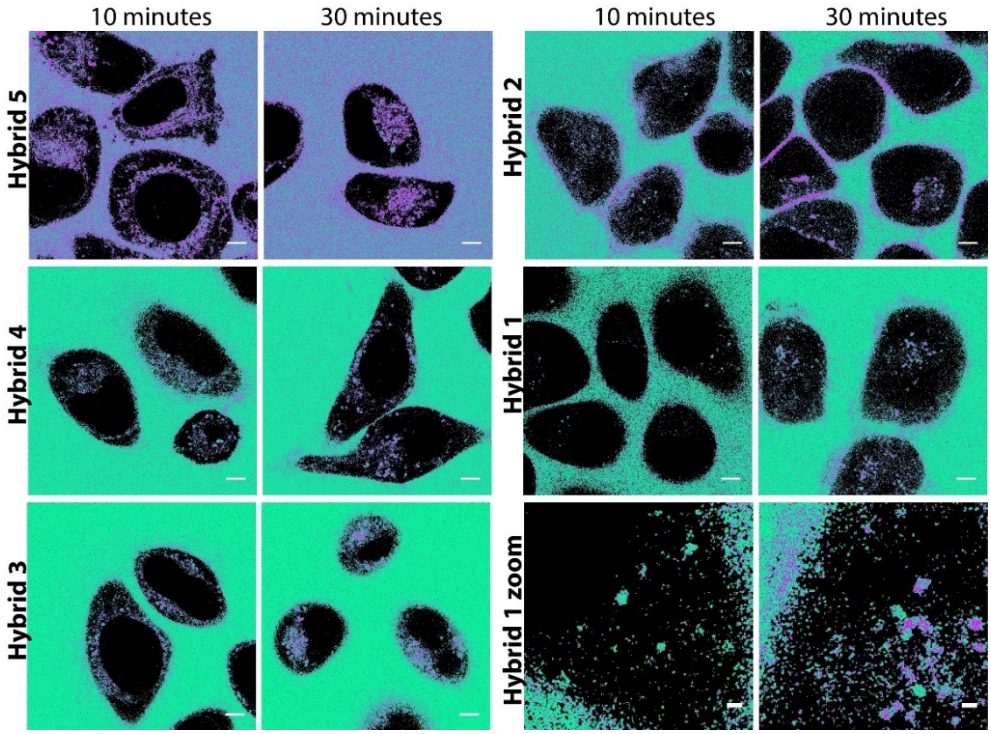

Figura 89. Imatges ratiometriques obtingudes a partir the microscopia confocal de la estabilitat de les miceles durnat internalització. Cada híbrid es va incubar a la mateixa concentració amb cultius cel.lulars i es van adquirir imatges després de 10 i 30 minuts per observar les diferències de l'estabilitat en el temps i en funció de la localització cel.lular.

les cèl·lules d'interès[46]. El flux sanguini continu present en els vasos indueix estrès de cisalla, el qual també pot desencadenar que l'estabilitat de les micel·les es perdi, i es desmontin[47]. A més a més, les micel·les necessiten extravasar a través de la capa de cèl·lules endotelials que revesteix la paret interna del vas sanguini. Aquestes cèl·lules estan fortament unides gracies a molècules que formen unions estretes, creant una barrera física que només permet la difusió de molècules petites[48,49]. Durant l'extravasació es poden produir interaccions amb la membrana de les cèl·lules endotelials, les quals poden comprometre l'estabilitat de la micel·la. Per tant, un estudi complet del comportament de les micel·les en entorns complexes i dinàmics requereix un mètode fiable, precís i versàtil. Aquí abordem aquest desafiament combinant imatges espectrals amb una plataforma d'òrgan en un xip.

Per establir la nostra plataforma i recrear aquests entorns vam fer servir un xip que consta de 3 canals microfluídics. El canal central està separat dels dos canals laterals per una fila de barreres triangulars distants de 100 μm els uns dels altres. En el nostre model, un dels canals laterals representava el vas sanguini i la interfície entre els pilars reconstituïa la barrera endotelial. Les cèl·lules endotelials de la vena umbilical humana (HUVEC) es van sembrar al pla superior i inferior del canal, el què va induir la formació d'una geometria similar al lumen. La barrera de cèl·lules endotelials creada separa el lumen intern del vas sanguini del microcanal central, on vam introduir esferoides de cèl·lules cancerígenes incrustades a un gel de col·lagen, el qual representa la matriu extracel·lular (ECM). L'avaluació de l'estabilitat supramolecular mitjançant òrgans en un xip requereix un disseny i una caracterització exhaustiva del model 3D abans de posteriors estudis. Per tant, vam realitzar una sèrie d'experiments amb l'objectiu de validar la integritat i la funcionalitat del nostre xip.

Després d'haver establert el nostre model de microfluídica ens vam proposar investigar la capacitat de les micel·les de penetrar des del vas sanguini fins a l'ECM. Primer, vam voler estudiar la capacitat de la micel·la per creuar la barrera endotelial, per tant, vam introduir l'híbrid 1 en tres models de microfluídica diferents: i) sense HUVEC com a control negatiu; ii) barrera HUVECs, imitant un vas sanguini sa i iii) barrera HUVECs amb cèl·lules cancerígenes pròximes per imitar un vas sanguini cancerigen. Els resultats obtinguts indiquen que la monocapa HUVEC restringeix parcialment el creuament lliure de l'híbrid quan hi ha cèl·lules cancerígenes, i gairebé totalment quan no hi són. Després de realitzar una sèrie d'experiments amb un híbrid que està sempre en la seva forma monomèrica, vam determinar que el monòmer podia creuar la paret endotelial fins i tot en el model de vas sanguini saludable degut a la seva mida petita, cosa que pot permetre que penetri a la regió ECM mitjançant un transport paracel·lular. Per confirmar que l'augment de la permeabilitat de la barrera en el nostre model microfluídic era induït per la presència de cèl·lules cancerígenes, es va estudiar l'expressió de zonula occludens-1 (ZO-1), una proteïna essencial que forma unions estretes entre cèl·lules endotelials. La ZO-1 s'expressava de manera clara i uniforme en la interfície entre les cèlules del nostre model saludable. No obstant això, es va observar una expressió reduïda quan hi havia cèl·lules cancerígenes. Aquestes observacions indiquen que les cèl·lules

cancerígenes afecten la interacció endotelial cèl·lula-cèl·lula, reduint la formació d'unions estretes, i per tant, fent que els vasos sanguinis siguin més permeables.

En aquest estudi vam poder demostrar en temps real que les interaccions dels sistemes supramoleculars amb cèl·lules que es troben en una conformació 3d són diferents de les interaccions en cultius de cèl·lules estàtiques 2d. Per tant, l'estabilitat del sistema en diferents barreres fisiològiques es pot correlacionar amb la seva penetració final a les cèl·lules canceroses, cosa que fins ara no era possible corroborar. Els resultats obtinguts demostren l'elevada estabilitat de l'híbrid **1** davant l'estrès de cisalla de flux induït i les interaccions amb

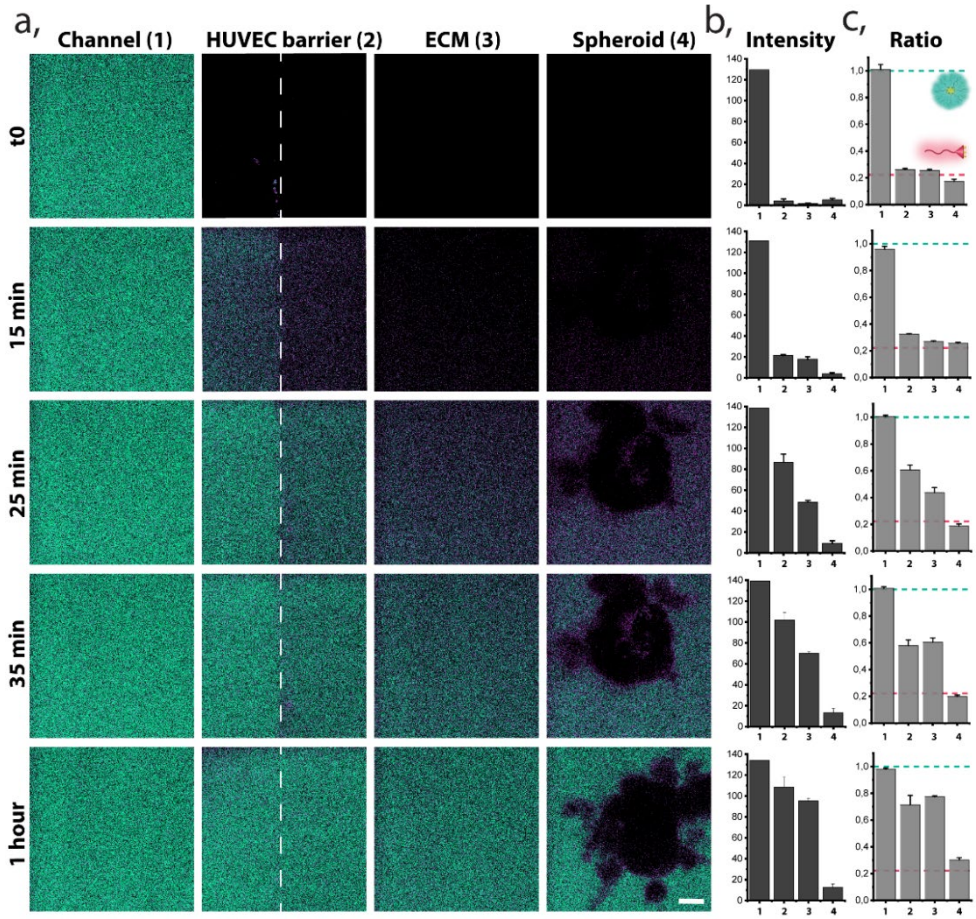

Figura 90. Espai i estabilitat resolta en temps de l'híbrid 1. a. Imatges confocals ratiomètriques en temps real de micel·les (verd) i monòmer (magenta) a les diferents barreres biologiques reconstruïdes (1 - vas sanguini, barrera 2 - HUVECs, 3 - ECM i 4 - càncer esferoide) durant la perfusió constant de l'híbrid 1, escala 15 μm. b. Intensitat resolta en temps de la senyal de fluorescència provinent de la suma de canals de micel.la i monòmer a cada barrera. c. Proporció normalitzada de senyal de fluorescència entre forma micel·lar i monòmera controlada a temps en diferents barreres. La línia guionada verda indica la proporcio en què les micel·les estan completament formades, en equilibri, i la línia guionada magenta indica la proporció en que l'hibrid només es troba en forma monomerica.

la barrera endotelial i la matriu extracel·lular, Figura 5. Al mateix temps demostrem una baixa estabilitat i penetració en contacte amb cèl·lules cancerígenes que formen una massa tumoral. Això impedeix que la micel·la penetri en el tumor sòlid de forma ensemblada i, per tant, que dugui a terme la seva funció en tota la massa tumoral, reduint així la seva efectivitat.

El càncer en un xip presentat aquí enriqueix l'estudi de l'estabilitat gràcies a les seves similituds amb les condicions fisiològiques, introduïdes especialment a través de la dimensió 3d en la distribució cel·lular i el flux continu al canal sanguini. Aquest enfocament ajuda a recapitular les barreres a superar (per exemple el flux sanguini, la paret endotelial, l'ECM i els esferoides en càncer 3d) que no es poden reconstruir amb èxit en un cultiu de cèl·lules 2d. Aquest estudi ens ha permès obtenir una informació directa i precisa sobre el rendiment i l'estabilitat de les micel·les a cadascuna de les barreres, gràcies a la possibilitat d'obtenir imatges en el temps i l'espai. A la vegada, els resultats han demostrat la importància d'estudiar l'estabilitat en sistemes més complexos per predir amb precisió el seu potencial a ser utilitzats en pacients.

7 Conclusions

L'ús de la microscòpia de superresolució ens ha permès visualitzar les interaccions de nanopartícules de forma individual. Aquesta observació a nivell individual ha demostrat la existència d'una gran heterogenitat dins d'un mateix lot. A més a més, hem demostrat que aquesta heterogenita produeix que cada NP es comporti de forma diferent en contacte, per exemple, de proteïnes, el què guiarà el comportament de la NP dins del cos i la seva acumulació en el tumor. Hem demostrat també la importància d'entendre l'estabilitat de sistemes supramoleculars en medis complexes, i no només en medis aquosos, com s'ha fet fins ara. La microscòpia confocal espectral ens ha permès estudiar no només en funció del temps sinó del espai l'estabilitat de micel·les. A més a més, l'ús de models 3d complexes, com és la microfluídica i els cultius cel·lulars 3d permeten un estudi del comportament molt més real, i proper al humà que els cultius 2d, el que pot ajudar a predir el comportament de les NPs i per tant a pre-seleccionar aquelles NP amb més bons resultats i que, per tant, tindran més possibilitats de funcionar *in vivo*.

8 References

(1) Petros, R. A.; DeSimone, J. M. Strategies in the Design of Nanoparticles for Therapeutic Applications. Nat. Rev. Drug Discov. 2010, 9 (8), 615–627. https://doi.org/10.1038/nrd2591.

(2) Lavik, E.; von Recum, H. The Role of Nanomaterials in Translational Medicine. ACS Nano 2011, 5 (5), 3419–3424. https://doi.org/10.1021/nn201371a.

(3) Ferrari, M. Cancer Nanotechnology: Opportunities and Challenges. Nat. Rev. Cancer 2005, 5 (3), 161–171. https://doi.org/10.1038/nrc1566.

(4) James, N. D.; Coker, R. J.; Tomlinson, D.; Harris, J. R. W.; Gompels, M.; Pinching, A. J.; Stewart, J. S. W. Liposomal Doxorubicin (Doxil): An Effective New Treatment for Kaposi's Sarcoma in AIDS. Clin. Oncol. 1994, 6 (5), 294–296. https://doi.org/10.1016/S0936-6555(05)80269-9.

(5) Barenholz, Y. (Chezy). Doxil® — The First FDA-Approved Nano-Drug: Lessons Learned. J. Controlled Release 2012, 160 (2), 117–134. https://doi.org/10.1016/j.jconrel.2012.03.020.

(6) Miele, E.; Spinelli, G. P.; Miele, E.; Tomao, F.; Tomao, S. Albumin-Bound Formulation of Paclitaxel (Abraxane® ABI-007) in the Treatment of Breast Cancer. Int. J. Nanomedicine 2009, 4, 99–105.

(7) Werner, M. E.; Cummings, N. D.; Sethi, M.; Wang, E. C.; Sukumar, R.; Moore, D. T.; Wang, A. Z. Preclinical Evaluation of Genexol-PM, a Nanoparticle Formulation of Paclitaxel, as a Novel Radiosensitizer for the Treatment of Non-Small Cell Lung Cancer. Int. J. Radiat. Oncol. Biol. Phys. 2013, 86 (3), 463–468. https://doi.org/10.1016/j.ijrobp.2013.02.009.

(8) Mayer, L. D.; Tardi, P.; Louie, A. C. CPX-351: A Nanoscale Liposomal Co-Formulation of Daunorubicin and Cytarabine with Unique Biodistribution and Tumor Cell Uptake Properties. Int. J. Nanomedicine 2019, 14, 3819–3830. https://doi.org/10.2147/IJN.S139450.

(9) Overchuk, M.; Zheng, G. Overcoming Obstacles in the Tumor Microenvironment: Recent Advancements in Nanoparticle Delivery for Cancer Theranostics. Biomaterials 2018, 156, 217–237. https://doi.org/10.1016/j.biomaterials.2017.10.024.

(10) Blanco, E.; Shen, H.; Ferrari, M. Principles of Nanoparticle Design for Overcoming Biological Barriers to Drug Delivery. Nat. Biotechnol. 2015, 33 (9), 941–951. https://doi.org/10.1038/nbt.3330.

(11) Shi, J.; Kantoff, P. W.; Wooster, R.; Farokhzad, O. C. Cancer Nanomedicine: Progress, Challenges and Opportunities. Nat. Rev. Cancer 2017, 17 (1), 20–37. https://doi.org/10.1038/nrc.2016.108.

(12) Anchordoquy, T. J.; Barenholz, Y.; Boraschi, D.; Chorny, M.; Decuzzi, P.; Dobrovolskaia, M. A.; Farhangrazi, Z. S.; Farrell, D.; Gabizon, A.; Ghandehari, H.; et al. Mechanisms and Barriers in Cancer Nanomedicine: Addressing Challenges, Looking for Solutions. ACS Nano 2017, 11 (1), 12–18. https://doi.org/10.1021/acsnano.6b08244.

(13) Ahsan, S. M.; Rao, C. M.; Ahmad, Md. F. Nanoparticle-Protein Interaction: The Significance and Role of Protein Corona. In Cellular and Molecular Toxicology of Nanoparticles; Saquib, Q., Faisal, M., Al-Khedhairy, A. A., Alatar, A. A., Eds.; Advances in Experimental Medicine and Biology; Springer International Publishing: Cham, 2018; pp 175–198. https://doi.org/10.1007/978-3-319-72041-8_11.

(14) Barbero, F.; Russo, L.; Vitali, M.; Piella, J.; Salvo, I.; Borrajo, M. L.; Busquets-Fité, M.; Grandori, R.; Bastús, N. G.; Casals, E.; et al. Formation of the Protein Corona: The Interface between Nanoparticles and the Immune System. Semin. Immunol. 2017, 34, 52–60. https://doi.org/10.1016/j.smim.2017.10.001.

(15) MAEDA, H. Vascular Permeability in Cancer and Infection as Related to Macromolecular Drug Delivery, with Emphasis on the EPR Effect for Tumor-Selective Drug Targeting. Proc. Jpn. Acad. Ser. B Phys. Biol. Sci. 2012, 88 (3), 53–71. https://doi.org/10.2183/pjab.88.53.

(16) Golombek, S. K.; May, J.-N.; Theek, B.; Appold, L.; Drude, N.; Kiessling, F.; Lammers, T. Tumor Targeting via EPR: Strategies to Enhance Patient Responses. Adv. Drug Deliv. Rev. 2018, 130, 17–38. https://doi.org/10.1016/j.addr.2018.07.007.

(17) Walker, C.; Mojares, E.; del Río Hernández, A. Role of Extracellular Matrix in Development and Cancer Progression. Int. J. Mol. Sci. 2018, 19 (10). https://doi.org/10.3390/ijms19103028.

(18) Lazzari, G.; Couvreur, P.; Mura, S. Multicellular Tumor Spheroids: A Relevant 3D Model for the in Vitro Preclinical Investigation of Polymer Nanomedicines. Polym. Chem. 2017, 8 (34), 4947–4969. https://doi.org/10.1039/C7PY00559H.

(19) Gautier, J.; Munnier, E.; Paillard, A.; Hervé, K.; Douziech-Eyrolles, L.; Soucé, M.; Dubois, P.; Chourpa, I. A Pharmaceutical Study of Doxorubicin-Loaded PEGylated Nanoparticles for Magnetic Drug Targeting. Int. J. Pharm. 2012, 423 (1), 16–25. https://doi.org/10.1016/j.ijpharm.2011.06.010.

(20) Gautier, J.; Munnier, E.; Soucé, M.; Chourpa, I.; Eyrolles, L. D. Analysis of Doxorubicin Distribution in MCF-7 Cells Treated with Drug-Loaded Nanoparticles by Combination of Two Fluorescence-Based Techniques, Confocal Spectral Imaging and Capillary Electrophoresis. Anal. Bioanal. Chem. 2015, 407 (12), 3425–3435. https://doi.org/10.1007/s00216-015-8566-9.

(21) Stracke, F.; Weiss, B.; Lehr, C.-M.; König, K.; Schaefer, U. F.; Schneider, M. Multiphoton Microscopy for the Investigation of Dermal Penetration of Nanoparticle-Borne Drugs. J. Invest. Dermatol. 2006, 126 (10), 2224–2233. https://doi.org/10.1038/sj.jid.5700374.

(22) Weyland, M.; Manero, F.; Paillard, A.; Grée, D.; Viault, G.; Jarnet, D.; Menei, P.; Juin, P.; Chourpa, I.; Benoit, J.-P.; et al. Mitochondrial Targeting by Use of Lipid Nanocapsules Loaded with SV30, an Analogue of the Small-Molecule Bcl-2 Inhibitor HA14-1. J. Controlled Release 2011, 151 (1), 74–82. https://doi.org/10.1016/j.jconrel.2010.11.032.

(23) Huang, B.; Bates, M.; Zhuang, X. Super-Resolution Fluorescence Microscopy. Annu. Rev. Biochem. 2009, 78 (1), 993–1016. https://doi.org/10.1146/annurev.biochem.77.061906.092014.

(24) Schermelleh, L.; Heintzmann, R.; Leonhardt, H. A Guide to Super-Resolution Fluorescence Microscopy. J. Cell Biol. 2010, 190 (2), 165–175. https://doi.org/10.1083/jcb.201002018.

(25) Hess, S. T.; Girirajan, T. P. K.; Mason, M. D. Ultra-High Resolution Imaging by Fluorescence Photoactivation Localization Microscopy. Biophys. J. 2006, 91 (11), 4258–4272. https://doi.org/10.1529/biophysj.106.091116.

(26) Rust, M. J.; Bates, M.; Zhuang, X. Sub-Diffraction-Limit Imaging by Stochastic Optical Reconstruction Microscopy (STORM). Nat. Methods 2006, 3 (10), 793–796. https://doi.org/10.1038/nmeth929.

(27) Albertazzi, L.; Zwaag, D. van der; Leenders, C. M. A.; Fitzner, R.; Hofstad, R. W. van der; Meijer, E. W. Probing Exchange Pathways in One-Dimensional Aggregates with Super-Resolution Microscopy. Science 2014, 344 (6183), 491–495. https://doi.org/10.1126/science.1250945.

(28) van der Zwaag, D.; Vanparijs, N.; Wijnands, S.; De Rycke, R.; De Geest, B. G.; Albertazzi, L. Super Resolution Imaging of Nanoparticles Cellular Uptake and Trafficking. ACS Appl. Mater. Interfaces 2016, 8 (10), 6391–6399. https://doi.org/10.1021/acsami.6b00811.

(29) Lazarovits, J.; Chen, Y. Y.; Sykes, E. A.; Chan, W. C. W. Nanoparticle–Blood Interactions: The Implications on Solid Tumour Targeting. Chem. Commun. 2015, 51 (14), 2756–2767. https://doi.org/10.1039/C4CC07644C.

(30) Monopoli, M. P.; Åberg, C.; Salvati, A.; Dawson, K. A. Biomolecular Coronas Provide the Biological Identity of Nanosized Materials. Nat. Nanotechnol. 2012, 7 (12), 779–786. https://doi.org/10.1038/nnano.2012.207.

(31) Schöttler, S.; Landfester, K.; Mailänder, V. Controlling the Stealth Effect of Nanocarriers through Understanding the Protein Corona. Angew. Chem. Int. Ed. 2016, 55 (31), 8806–8815. https://doi.org/10.1002/anie.201602233.

(32) Nel, A. E.; Mädler, L.; Velegol, D.; Xia, T.; Hoek, E. M. V.; Somasundaran, P.; Klaessig, F.; Castranova, V.; Thompson, M. Understanding Biophysicochemical Interactions at the Nano–Bio Interface. Nat. Mater. 2009, 8 (7), 543–557. https://doi.org/10.1038/nmat2442.

(33) Mahmoudi, M.; Lynch, I.; Ejtehadi, M. R.; Monopoli, M. P.; Bombelli, F. B.; Laurent, S. Protein−Nanoparticle Interactions: Opportunities and Challenges. Chem. Rev. 2011, 111 (9), 5610–5637. https://doi.org/10.1021/cr100440g.

(34) Saptarshi, S. R.; Duschl, A.; Lopata, A. L. Interaction of Nanoparticles with Proteins: Relation to Bio-Reactivity of the Nanoparticle. J. Nanobiotechnology 2013, 11 (1), 26. https://doi.org/10.1186/1477-3155-11-26.

(35) Walkey, C. D.; Chan, W. C. W. Understanding and Controlling the Interaction of Nanomaterials with Proteins in a Physiological Environment. Chem. Soc. Rev. 2012, 41 (7), 2780–2799. https://doi.org/10.1039/C1CS15233E.

(36) Mamaeva, V.; Sahlgren, C.; Lindén, M. Mesoporous Silica Nanoparticles in Medicine—Recent Advances. Adv. Drug Deliv. Rev. 2013, 65 (5), 689–702. https://doi.org/10.1016/j.addr.2012.07.018.

(37) Slowing, I. I.; Vivero-Escoto, J. L.; Wu, C.-W.; Lin, V. S.-Y. Mesoporous Silica Nanoparticles as Controlled Release Drug Delivery and Gene Transfection Carriers. Adv. Drug Deliv. Rev. 2008, 60 (11), 1278–1288. https://doi.org/10.1016/j.addr.2008.03.012.

(38) Lartigue, L.; Wilhelm, C.; Servais, J.; Factor, C.; Dencausse, A.; Bacri, J.-C.; Luciani, N.; Gazeau, F. Nanomagnetic Sensing of Blood Plasma Protein Interactions with Iron Oxide Nanoparticles: Impact on Macrophage Uptake. ACS Nano 2012, 6 (3), 2665–2678. https://doi.org/10.1021/nn300060u.

(39) van Asbeck, A. H.; Beyerle, A.; McNeill, H.; Bovee-Geurts, P. H. M.; Lindberg, S.; Verdurmen, W. P. R.; Hällbrink, M.; Langel, Ü.; Heidenreich, O.; Brock, R. Molecular Parameters of SiRNA–Cell Penetrating Peptide Nanocomplexes for Efficient Cellular Delivery. ACS Nano 2013, 7 (5), 3797–3807. https://doi.org/10.1021/nn305754c.

(40) Scomparin, A.; Polyak, D.; Krivitsky, A.; Satchi-Fainaro, R. Achieving Successful Delivery of Oligonucleotides — From Physico-Chemical Characterization to in Vivo Evaluation. Biotechnol. Adv. 2015, 33 (6, Part 3), 1294–1309. https://doi.org/10.1016/j.biotechadv.2015.04.008.

(41) Wu, R. P.; Youngblood, D. S.; Hassinger, J. N.; Lovejoy, C. E.; Nelson, M. H.; Iversen, P. L.; Moulton, H. M. Cell-Penetrating Peptides as Transporters for Morpholino Oligomers: Effects of Amino Acid Composition on Intracellular Delivery and Cytotoxicity. Nucleic Acids Res. 2007, 35 (15), 5182–5191. https://doi.org/10.1093/nar/gkm478.

(42) Futaki, S.; Ohashi, W.; Suzuki, T.; Niwa, M.; Tanaka, S.; Ueda, K.; Harashima, H.; Sugiura, Y. Stearylated Arginine-Rich Peptides: A New Class of Transfection Systems. Bioconjug. Chem. 2001, 12 (6), 1005–1011. https://doi.org/10.1021/bc015508l.

(43) Debus, H.; Baumhof, P.; Probst, J.; Kissel, T. Delivery of Messenger RNA Using Poly(Ethylene Imine)–Poly(Ethylene Glycol)-Copolymer Blends for Polyplex Formation: Biophysical Characterization and in Vitro Transfection Properties. J. Controlled Release 2010, 148 (3), 334–343. https://doi.org/10.1016/j.jconrel.2010.09.007.

(44) Sahin, U.; Karikó, K.; Türeci, Ö. MRNA-Based Therapeutics — Developing a New Class of Drugs. Nat. Rev. Drug Discov. 2014, 13 (10), 759–780. https://doi.org/10.1038/nrd4278.

(45) Ezzat, K.; EL Andaloussi, S.; Zaghloul, E. M.; Lehto, T.; Lindberg, S.; Moreno, P. M. D.; Viola, J. R.; Magdy, T.; Abdo, R.; Guterstam, P.; et al. PepFect 14, a Novel Cell-Penetrating Peptide for

Oligonucleotide Delivery in Solution and as Solid Formulation. Nucleic Acids Res. 2011, 39 (12), 5284–5298. https://doi.org/10.1093/nar/gkr072.

(46) Owen, S. C.; Chan, D. P. Y.; Shoichet, M. S. Polymeric Micelle Stability. Nano Today 2012, 7 (1), 53–65. https://doi.org/10.1016/j.nantod.2012.01.002.

(47) Holme, M. N.; Fedotenko, I. A.; Abegg, D.; Althaus, J.; Babel, L.; Favarger, F.; Reiter, R.; Tanasescu, R.; Zaffalon, P.-L.; Ziegler, A.; et al. Shear-Stress Sensitive Lenticular Vesicles for Targeted Drug Delivery. Nat. Nanotechnol. 2012, 7 (8), 536–543. https://doi.org/10.1038/nnano.2012.84.

(48) Barua, S.; Yoo, J.-W.; Kolhar, P.; Wakankar, A.; Gokarn, Y. R.; Mitragotri, S. Particle Shape Enhances Specificity of Antibody-Displaying Nanoparticles. Proc. Natl. Acad. Sci. 2013, 110 (9), 3270–3275. https://doi.org/10.1073/pnas.1216893110.

(49) Maeda, H.; Wu, J.; Sawa, T.; Matsumura, Y.; Hori, K. Tumor Vascular Permeability and the EPR Effect in Macromolecular Therapeutics: A Review. J. Controlled Release 2000, 65 (1), 271–284. https://doi.org/10.1016/S0168-3659(99)00248-5.

Appendix 2.

Glossary

Ab	Antibody
AFM	Atomic Force Microscopy
APA	Amphiphilic alkylated poly(α)glutamate amine
BCA	Bradford Protein Assay
BSA	Bovine Serum Albumin
CD	Circular Dichroism
CLEM	Correlative Light and Electron Microscopy
CMC	Critical Micelle Concentration
CPPs	Cell-penetrating peptides
DLS	Dynamic light scattering
dSTORM	direct Stochastic Optical reconstruction Microscopy
ECM	Extracellular Matrix
EM	Electron Microscopy
EPR effect	Enhanced Permeability and Retention effect
ER	Endoplasmic Reticulum
FBS	Fetal Bovine Serum
FCS	Fluorescence Correlation Spectroscopy
FRAP	Fluorescence Recovery After Photobleaching
FRET	Fröster Resonance Energy Transfer
HPLC	High Performance Liquid Chromatography
IgG	Immunoglobulin G
ITC	Isothermal titration calorimetry
LC-MS	Liquid Chromatography Mass Spectrometry
LDL	Low-density Lipoprotein
MMPs	Matrix metalloproteinases
MRI	Magnetic Resonance Imaging
MSN	Mesoporous silica nanoparticles
N/P ratio	Ratio of positive over negative charge in complexes
NPs	Nanoparticles
PEG	Polyethylene glycol
PGA	Enzyme penicillin G amidase
PLE	Esterase enzyme

PSMA	Prostate-Specific Membrane Antigen
r9	L-nona-arginine
SDS-PAGE	Sodium dodecyl sulfate polyacrylamide gel electrophoresis
SEM	Scanning Electron Microscopy
SIM	Structured Illumination Microscopy
SLS	Static Light Scattering
SMLM	Single Molecule Localization Microscopy
SRM	Super Resolution Microscopy
STED	Stimulated Emission Depletion
Tf	Transferrin

Appendix 3.
Publications and Conferences

8.1 Publications

8.1.1 *Thesis period*

N. Feiner-Gracia*, A. Glinkowska*, M. Buzhor, R. Amir, J. Samitier and L. Albertazzi. Real-time ratiometric imaging of supramolecular nanocarriers stability in perfusable 3D tumor vessel-on-a-chip. *In preparation.*

A. Boloix N. Feiner-Gracia, N. Segovia, A. Soriano, J. Roma, J. Sánchez de Toledo, S. Gallego, J, Veciana, L. Albertazzi, M.F. Segura, N. Ventosa. Quatsomes as novel nanocarrier for clinical delivery of small RNAs *In preparation.*

N. Feiner-Gracia, A. Boloix, R. Pascarella, J. Repetto, N.Ventosa, M.F. Segura, L. Albertazzi. Follow the miRNA: tracking the release of genetic material from Quatsomes using FRET imaging. *In preparation.*

R. Riera*, N. Feiner-Gracia*, C. Fornaguera, A. Cascante, S. Borrós, L. Albertazzi. Tracking DNA complexation state of pBAE polyplexes in cells with super resolution microscopy. *Nanoscale,* **2019**

N. Feiner-Gracia*, R. A. Olea*, R. Fitzner, N. El Boujnouni, A. H. van Asbeck, R. Brock, L. Albertazzi. Super-resolution imaging of structure, molecular composition and stability of single oligonucleotide polyplexes. *Nano Letters*, **2019**

S. Pujals, N. Feiner-Gracia, P. Delcanale, I. Voets, L. Albertazzi. Super-resolution microscopy as a powerful tool to study complex synthetic materials. *Nature Review Chemistry*, **2019**: 3 (2), 68-84.

Ardizzone A., Kurhuzenkau S., Illa-Tuset S., Faraudo J., Bondar M., Hagan D., Van Stryland EW., Painelli A., Sissa C., Feiner N., Albertazzi L., Veciana J., Ventosa N. Nanostructuring Lipophilic Dyes in Water Using Stable Vesicles, Quatsomes, as Scaffolds and Their Use as Probes for Bioimaging. *Small*. **2018**: 14(16), e1703851

T. Patino*, N. Feiner-Gracia*, X. Arque, A. Miguel-Lopez, A. Jannasch, T. Stumpp, E. Schaffer, L. Albertazzi, S. Sanchez. Influence of Enzyme Quantity and Distribution on the Self-Propulsion of Non-Janus Urease-Powered Micromotors. *JACS*. **2018**: (25), 7896-7903

N. Feiner-Gracia, S. Pujals, P. Delcanale, L. Albertazzi. Smart nanoparticles for Biomedicine. Chapter 15: Advance optical microscopy techniques for the investigation of cell-nanoparticle interactions. *Elsevier*. **2018**, Edited by Gianni Ciofani.

Krivitsky A., Polyak .1, Scomparin A., Eliyahu S., Ofek P., Tiram G., Kalinski H., Avkin-Nachum S., Feiner Gracia N, Albertazzi L., Satchi-Fainaro R. Amphiphilic poly(α)glutamate polymeric micelles for systemic administration of siRNA to tumors. *Nanomedicine.* **2018**: 14(2), 303-315

S. Pujals, N. Feiner-Gracia and L. Albertazzi. Self-Assembling Biomaterials: Molecular Design, Characterization and Application in Biology and Medicine Chapter 16: Unveiling complex structure and dynamics in supramolecular biomaterials using super-resolution microscopy *Elsevier*. **2018.** Edited by Riccardo da Silva.

N. Feiner-Gracia*, M. Buzhor*, E. Fuentes, R. J. Amir and L. Albertazzi. Micellar stability in biological media dictates internalization in living cells. *JACS.* **2017**:139 (46), 16677–16687.

N. Feiner-Gracia, M. Beck, S. Pujals, S. Tosi, T. Mandal, C. Buske, M. Linden, L. Albertazzi. Super-Resolution Microscopy Unveils Dynamic Heterogeneities in Nanoparticle Protein Corona. *Small*. **2017**: 13, 1701631.

A. Duro-Castano, V.J. Nebot, A. Niño-Pariente, A. Armiñán, J.J. Arroyo-Crespo, A. Paul, N. Feiner-Gracia, L. Albertazzi, M. J. Vicent. Capturing "Extraordinary" Soft-Assembled Charge-Like Polypeptides as a Strategy for Nanocarrier Design. *Adv Materials* **2017**: 29, 1702888

H. Li, K. Fierens, Z. Zhang, N. Vanparijs, M. J. Schuijs, K.Van Steendam, N. Feiner Gracia, R. De Rycke, T. De Beer, A. De Beuckelaer, S. De Koker, D. Deforce, L. Albertazzi, J. Grooten, B. N. Lambrecht, B. De Geest. Spontaneous Protein Adsorption on Graphene Oxide Nanosheets Allowing Efficient Intracellular Vaccine Protein Delivery *ACS Appl Mater Interfaces*, **2016**, 8(2): 1147-55.

8.1.2 *Previous publications*

N. Feiner-Gracia, A. Dols-Perez, M. Royo, C. Solans, M.J. Garcia-Celma, C. Fornaguera. Cell penetrating peptide grafting of PLGA nanoparticles to enhance cell uptake. *European Polymer Journal,* **2018**: 108, 429-438

C. Fornaguera, N. Feiner-Gracia, A. Dols-Perez, M. J. García-Celma, C. Solans. Versatile Methodology to Encapsulate Gold Nanoparticles in PLGA Nanoparticles Obtained by Nano-Emulsion Templating. *Pharm Res.* **2017,** 34(5):1093-1103.

C. Fornaguera, N. Feiner-Gracia, G. Calderó, M. J. García-Celma, C. Solans . PLGA nanoparticles from nano-emulsion templating as imaging agents: Versatile technology to obtain nanoparticles loaded with fluorescent dyes. *Colloids Surf B Biointerfaces.* **2016**, 147: 201-9

C. Fornaguera, N. Feiner-Gracia, G. Calderó, M. J. García-Celma, C. Solans. Galantamine-loaded PLGA nanoparticles, from nano-emulsion templating, as novel advanced drug delivery systems to treat neurodegenerative diseases. *Nanoscale*, **2015**, 7(28): 12076-84.

8.2 Conferences contribution

8.2.1 *Poster contributions*

10th IBEC Symposium (Barcelona, Spain) **2017**

"Super-resolution microscopy unveils dynamic heterogeneities in nanoparticle protein corona" **N. Feiner-Gracia**, M. Beck, S. Pujals, S Tosi, T.Mandal, C. Buske, M. Lindén, L. Albertazzi

"Stability in Biological Media of Molecularly-Precise Micelles Dictates Internalization in Living Cells" E. Fuentes**, N. Feiner-Gracia**, M. Buzhor, R. J. Amir, and L. Albertazzi

"A study of polyplexes as gene delivery vectors using super-resolution microscopy" R. Alis Olea, R. Riera, **N. Feiner-Gracia**, R. Brock, S. Borrós, L. Albertazzi

"Effect of enzyme quantity and distribution on the self-propulsion of urease-powered micromotors" T. Patiño, **N.Feiner-Gracia**, X. Arqué, L. Albertazzi, S. Sánchez

"NanoBio&Med2017" International Conference (Barcelona, Spain) **2017**

"Super-resolution microscopy study of protein corona composition and evolution in single nanoparticles". **Natalia Feiner-Gracia**, Michaela Beck, Sílvia Pujals, Sébastien Tosi, Tamoghna Mandal, Christian Buske, Mika Linden, Lorenzo Albertazzi.

8th Single Molecule Localization Microscopy Symposium (Berlin, Germany) **2018**

"Unveiling structure, molecular composition and stability of nanoparticles using Single Molecule Localization Microscopy" **N. Feiner-Gracia**, M. Beck, S. Pujals, S Tosi, T.Mandal, C. Buske, M. Lindén, L. Albertazzi

Orals

11th IBEC Symposium (Barcelona, Spain). **2018**

"Evaluating the Stability and Extravasation of Supramolecular Nanocarriers in Biological Conditions" **N. Feiner-Gracia**, A.Glinkowska, M. Buzhor, E. Fuentes, J. Samitier, R. J. Amir, and L. Albertazzi

Chains: Chemistry as Innovating Science (Veldhoven, The Netherlands) **2018**

"Micellar Stability in Biological Media Dictates Internalization in Living Cells". **N. Feiner-Gracia**, M. Buzhor, E. Fuentes, R. J. Amir, and L. Albertazzi

Dutch Biophysics (Veldhoven, The Netherlands) **2019**

"Single Molecule Localization Microscopy revels structure and molecular composition of polyplexes". **N. Feiner-Gracia**, R. A. Olea, R. Fitzner, N. El Boujnouni, A. H. van Asbeck, R. Brock, L. Albertazzi.

International Conference on Nanomedicine And Nanobiotechnology – ICONAN 2019 (Munich, Germany) **2019**

"Imaging the stability and extravasation of micelles using a microfluidic platform mimicking tumor microenvironment". **N. Feiner-Gracia**, A.Glinkowska, M. Buzhor, R. J. Amir, J. Samitier, and L. Albertazzi